A Measurement of the Neutron Electromagnetic Form Factor Ratio from a Rosenbluth Technique with Simultaneous Detection of Neutrons and Protons

Ezekiel Woodrow Eberly Wertz

Lebanon, Pennsylvania

Master of Science, William & Mary, 2020
Bachelor of Science, Lebanon Valley College, 2018

A Dissertation presented to the Graduate Faculty of
The College of William and Mary in Virginia in Candidacy for the Degree of
Doctor of Philosophy

Department of Physics

The College of William and Mary in Virginia
August, 2025

APPROVAL PAGE

This Dissertation is submitted in partial fulfillment of
the requirements for the degree of

Doctor of Philosophy

Ezekiel Woodrow Eberly Wertz

Approved by the Committee, July 2025

Committee Chair
David S. Armstrong, Chancellor Professor, Physics
College of William & Mary

Todd Averett, Professor, Physics
College of William & Mary

Joshua Erlich, Professor, Physics
College of William & Mary

Justin Stevens, Associate Professor, Physics
College of William & Mary

Holly Szumila-Vance, Assistant Professor, Physics
Florida International University

ABSTRACT

The internal structure of protons and neutrons provides insight into both the dynamical behavior of the constitute quarks and gluons, and emergent properties of the nucleons (such as mass, spin, and electromagnetic distributions). Elastic electron-nucleon scattering can probe the elastic electromagnetic form factors of the nucleon. The electric and magnetic form factors, respectively, encode information about the internal charge and magnetization distributions within the nucleon. Precision data for these form factors, over a broad range of the four-momentum transfer squared, Q^2, can benchmark theoretical models describing the strong interaction of nuclear physics.

The Super BigBite Spectrometer (SBS) program in Hall A at Jefferson Lab, is a series of high-precision experiments which seek to significantly extend the Q^2 reach of previous data for the nucleon electromagnetic form factors. The first two experiments of this program are known as G_M^n and the neutron Two Photon Exchange (nTPE) and the data were collected from October 2021 to February 2022. Both experiments were conducted with the simultaneous measurement of D(e,e'n) and D(e,e'p) reactions for quasi-elastic electron-deuteron scattering. The scattered electrons were detected in the BigBite Spectrometer, which features multiple large-acceptance Gas Electron Multiplier (GEM) detectors. The Super BigBite Spectrometer provided simultaneous detection of scattered nucleons, and utilized a large acceptance dipole magnet and Hadron Calorimeter (HCal).

The G_M^n experiment provides precision measurements of the neutron magnetic form factor, via the ratio method, over a Q^2 range of 3.0 to 13.5 $(\mathrm{GeV/c})^2$. From this data analysis, preliminary values for $G_M^n/\mu_n G_D$ are extracted. For $Q^2 = 4.48$ $(\mathrm{GeV/c})^2$ we find $G_M^n/\mu_n G_D = 0.9546 \pm 0.0132$ and for $Q^2 = 4.476$ $(\mathrm{GeV/c})^2$ we find $G_M^n/\mu_n G_D = 0.9563 \pm 0.0110$. These preliminary $G_M^n/\mu_n G_D$ values are more precise than existing world data in this Q^2 regime and are consistent with the most recent parameterization of the $G_M^n/\mu_n G_D$ world data.

The nTPE experiment provides a first measurement of the neutron Rosenbluth slope and seeks to quantify the two-photon exchange(TPE) contribution to elastic electron-neutron scattering at a fixed $Q^2 = 4.5$ $(\mathrm{GeV/c})^2$ with two different beam energies and scattering angle values. For data of the proton form factor ratio, $\mu_p G_E^p/G_M^p$, significant discrepancies exist between values obtained from Rosenbluth Separation and polarization transfer measurement, particularly at large Q^2, and TPE contributions are thought to resolve this discrepancy. The impacts of TPE contributions have not yet been experimentally established for the neutron. From the data analysis presented in this dissertation, a preliminary result for the neutron Rosenbluth slope is found as $S^n = (G_E^n)^2/\tau_n (G_M^n)^2 = 0.0916 \pm 0.0476$ for $Q^2 = 4.48$ $(\mathrm{GeV/c})^2$. This value of the neutron Rosenbluth slope is consistent with the world data extrapolation and the absence of large TPE corrections.

TABLE OF CONTENTS

ACKNOWLEDGMENTS

This dissertation marks a decade-long journey pursuing a career as a scientist. Specifically, it reflects the contributions from a large number of people who have helped me become a better person and better researcher and without whom this dissertation would not be possible. I would like to take this opportunity to recognize as many people as possible, both people I met along the way and those who are foundational in my support network. I have no intention of forgetting anyone; if there are any omissions please know I am grateful for your support beyond what is expressed here.

First, I would like to start by thanking my parents, my mother Anne Riffle and and my father Brad Wertz. From a young age, they fostered a sense of curiosity and promoted a multitude of opportunities to further all levels of my education. They instilled in my brothers and I that honesty, perseverance, and resourcefulness are essential attributes for approaching life. Their guidance, commitment, and continued support have made me the person I am today. It is hard to express the depth of gratitude I have for their support, which has led to this achievement.

I would like to extend a warm thank you to my advisor, David Armstrong. You have been an outstanding mentor. Your vast experience and dedication foster an environment of growth for all of your students. With your kind encouragement you guide students through challenging research, using the central principles of insightful teaching and thoughtful learning. I am incredibly grateful for the time I spent in your group and the opportunities you provided. Your mentorship has given me a solid foundation for my future as a scientist.

I would like to thank all of my colleagues in the nuclear physics groups at William & Mary. I will always be appreciative of their support, guidance, and insightful discussions and I cherish the shared experiences with Kate Evans, Maria Satnik, Jack Jackson, Tasneem Raza, Ben Spaude, Eric Fuchey, Carrington Metts, Quinn Campagna, and Victoria Owen. I want to give a special mention to Todd Averett who helped me get started with the GEM project and introduced me to the SBS program. Besides myself and David, Todd has been the most invested in my data analysis and acted as a second mentor.

I want to thank all of my colleagues from Jefferson Lab. I am grateful to the members of the PREX-II and CREX collaboration. When I was a young graduate student they showed me how a nuclear physics experiment is run. Particularly, the teachings and memories with Chandan Ghosh, Ciprian Gal, Eric King, Sangwha Park, Cameron Clark, Don Jones, Caryn Palatchi, Allison Zec, Dave Gaskell, Paul King, and Kent Paschke.

There are a large number of people from the SBS collaboration at JLab that I want to thank. I will start with the graduate students, since we learned from one another, collaborated on analysis, and installed a complicated and new set of spectrometers together. The G_M^n/nTPE folks: Maria Satnik, John Boyd, Provakar Datta, Anuruddha Rathnayake, Sebastian Seeds, Ralph Marinaro, and Nathaniel Lashley. The G_E^n folks: Kate Evans, Jack Jackson, Sean Jeffas, Gary Penman, Vimukthi Gamage, and Hunter Presley. I want to thank many folks who were part of the SBS GEM group and were tasked with installing a complex and delicate detector subsystem. I have learned much from all of you, both about detector hardware and about running experiments. Specifically, my colleagues from INFN, in Italy: Evaristo Cisbani, Roberto Perrino, and Paulo Musico. Additionally, the members of the UVA GEM group: Nilanga Liyanage, Kondo Gnanvo, Huong Nguyen, Xinzhan Bai, John Boyd, Anuruddha Rathnayake, Sean Jeffas, Vimukthi Gamage, Bhasitha Dharmasena. The folks at JLab who also made significant efforts to the success of the GEM include Holly Szumila-Vance, Saru Dhital, Malinga Rathnayake, Manjukrishna Suresh, and Thir Guatam.

I would like to acknowledge the SBS Collaboration as a whole for their efforts in putting a brand new apparatus on the floor of Hall A and collecting the data used in my dissertation. I would especially like to thank Mark Jones, Bogdan Wojtsekhowski, Andrew Puckett, Carlos Ayerbe Gayoso, Arun Tadepalli, Alexandre Camsonne, Ben Raydo, Bryan Moffit, Brad Sawatzky, and Gordon Cates. I would also like to acknowledge the members of the technical staff of Hall A for their hardwork in installing and running the experiment: Jack Segal, Jessie Butler, Andrew Lumanog, Travis Dodge, Ellen Becker, Heidi Fansler, Bob Tucker, Marc McMullen, and Chuck Long.

I would like to thank members of the defense committee: Todd Averett, Joshua Erlich, Justin Stevens, and Holly Szumila-Vance. I appreciate the time everyone put into reading the dissertation and providing thoughtful feedback.

This work was supported by the National Science Foundation grants: PHY-1714792, PHY-2012738, and PHY-2412825, as well as the JSA/JLab Graduate Fellowship program.

I want to thank Lorelei Carlson at JLab. It was a great experience serving on the JLUO board with you. You are an advocate and indispensable source of knowledge for all users at Jefferson Lab.

I would like to acknowledge a couple of staff at William & Mary who have been central to my graduate experience. Sarah Glosson has been a great friend and has provided me with many unique opportunities for personal and professional development as a graduate student. She goes above and beyond by creating spaces

and advocating for graduate students in Arts & Sciences. I am indebted to the administrative staff of the physics department for making my graduate experience straightforward and pleasant, thanks to Carol Hankins, Paula Perry, Ellie Wilkinson, Belmari Bello, Yvette Osorio-Valdez, and Melinda Kerins.

I would like to thank the professors in the physics department during my time at Lebanon Valley College, who contributed greatly to my growth as scientist: Michael Day, Barry Hurst, David Lyons, and Scott Walck. I'd also like to thank Nathan Hansell and Shane Thomas of Cedar Crest High School for insightful introductory courses in physics and mathematics, which convinced me to change from a business administration to a physics major as I entered college.

On a more personal note I would like to recognize particular members of my family. To my brothers Gabe and Nate Wertz, you both have been constantly supportive as I endeavored on this journey. I am grateful for the time we get together now and for you both being the best brothers I could ask for. To my stepdad Brad Riffle, thank you for your encouragement and wit over cups of coffee and for reminders to give context for those not as educated. I would like to recognize my maternal cousins: Steffan Bomberger, Hannah Pouffary, and Ethan Hentz, who permit my discussions of physics and ultimately remind me that there are activities beyond the lab. I would like to further recognize members of my family who were central to my upbringing: Aunt Sue and Uncle Scott Hentz, Aunt Jen and Uncle Barry Wertz, and Rose Kiefer (Mimi). I shall not try to name all members of my extended family, there are simply too many folks. Please know that I am grateful and appreciative of your support over the years.

During my time at Lebanon Valley College I was fortunate to form friendships with a group of folks and we have done well to be part of each others lives, beyond our collective undergraduate education. These people are worth recognizing as they are some of my oldest friends, who encourage good fun and challenge my personal notions. In no particular order: Samantha & Matt Schoeller, Carly & Taylor Hutchison, Alex Marchi & Darrly McClish, Nick & Hannah Pollak, Alec Whitsett, Trevor Dugan, Justin Cammarota, and Quinn Girasek. Special recognition to Justin Cammarota for following me to William & Mary for graduate school, rooming with me for six years, and encouraging me to attend social activities outside the apartment.

Lastly to my wonderful girlfriend, Shelby Arrigo, I am grateful for your support and kindness. This has been a challenging and time-consuming task and your patience and understanding has been greatly appreciated.

To my grandmothers
Sarah Mae Eberly (Kerr) and Anna Mary Wertz (Lerch)
for their dedication to building families

and to my nephews
Matthias Alexandro Wertz Ochoa, Elian Theodore Wertz Ochoa,
and Montana Ephraim Wertz Ochoa
for they are our future

LIST OF TABLES

LIST OF FIGURES

Chapter 1

Introduction

Nuclear physics is the field of study which seeks to empirically investigate and theoretically model the constituents and interactions of atomic nuclei. Modern nuclear and particle physics are historically intertwined, as the two fields grow from the discipline of atomic physics. Particle physics represents the study of matter from the most elementary components. Distinctly, modern atomic physics is the study of an isolated system (an atom) of electrons and an atomic nucleus, including the interactions between atoms. Two subatomic particles of fundamental importance in nuclear physics are the proton and neutron (collectively the nucleon). The protons and neutrons serve as the building blocks for atomic nuclei, and with the inclusion of the electron, form most ordinary matter in the universe.

There is a remarkable history, spanning the last two centuries, of atomic physics which progresses to the individual and unique fields of nuclear physics and particle physics. Instead of comprehensively recounting this history, we will emphasize parts of this larger story to help contextualize the continued study of the nucleon. The electron was discovered in 1897 by J.J. Thomson [1] and its discovery provided the first evidence for the internal structure of the atom. The experiments conducted by Rutherford, Geiger, and Marsden, published in 1909 and 1911, [2, 3] involving the deflection of alpha particles from a gold foil led to the conclusion that a dense, positively-charged, core is present at the center of atoms, and thus the discovery of the atomic nucleus. Rutherford continued these atomic

scattering experiments and this effort led to the discovery of the proton, published in 1919 [4]. James Chadwick extended the understanding of the atomic nucleus by discovering the neutron in 1932 [5]. During the early 20^{th} century there was significant developments in theoretical quantum mechanics, notably in 1928, Paul Dirac proposed a relativistic wave equation to describe the behavior of structureless massive spin-1/2 particles [6]. This "Dirac equation" predicts the magnetic moment of such a particle to be

$$\mu = g\left(\frac{e}{2m}\right)\frac{\hbar}{2}, \tag{1.1}$$

where g is the so called g-factor, e is the particle's charge, m is the particle's mass, and $\hbar$ is Planck's constant divided by 2π. Initially, the proton and the neutron were considered point-like massive spin-1/2 particles, consistent with Dirac's theory, and as such were expected to have $g = 2$ and therefore magnetic moments of

$$\text{proton} : \mu_p = \mu_N = \frac{e\hbar}{2m_p}, \tag{1.2}$$

and

$$\text{neutron} : \mu_n = 0, \tag{1.3}$$

μ_N is more commonly called the nuclear magneton. In 1933 Otto Stern measured the proton magnetic moment and the value was found to be $\mu_p = 2.79\mu_N$ [7]. Additionally, in 1940, the neutron magnet moment was measured by Alvarez and Bloch and the value was found to be $\mu_n = -1.91\mu_N$ [8]. The significant deviations of the proton and neutron magnetic moments from that of a point-like massive spin-1/2 particle provide the first evidence for an internal structure of the nucleon. In the 1950's Hofstadter and collaborators [9] pioneered the use of electron scattering experiments as probes of the nucleon internal structure. These scattering experiments demonstrated that the electron-proton scattering cross-section deviated significantly from that of a point-like particle. It is now well-accepted that protons and neutrons are composite particles, each with internal struc-

ture and dynamics.

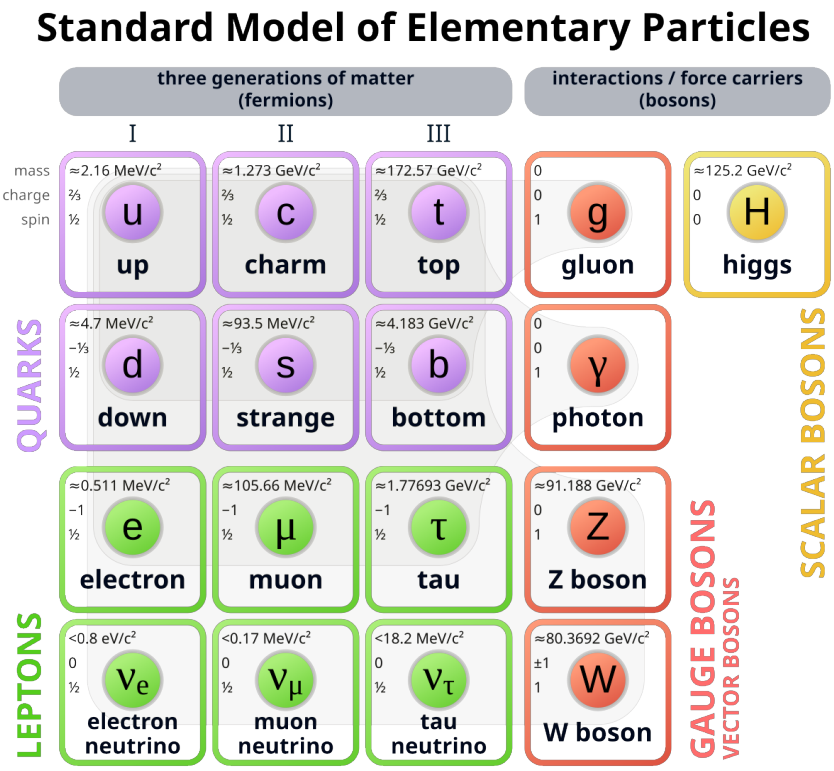

Figure 1.1: All known elementary particles of the Standard Model. Particles are categorized as quarks, leptons, or bosons. The respective particle's mass, charge, and spin are labeled. Image Credit: Wikimedia Commons.

The Standard Model of particle physics (Standard Model, SM) is a well-established quantum field theory, formulated in the 1970s, which describes all known elementary particles and three of the four fundamental interactions in nature: electromagnetic, weak, and strong. The Standard Model is a renormalizable and mathematically self-consistent non-abelian quantum field theory, subject to the local gauge symmetry of the $\mathrm{SU}(3)\times\mathrm{SU}(2)\times\mathrm{U}(1)$ unitary product group. The electromagnetic force, described by Quantum Electrodynamics (QED), describes all phenomena involving electrically charged particles with interactions mediated by the photon. The weak interaction is the mechanism responsible for the radioactive decay of atoms; this interaction is mediated by the W and Z bosons, and

is described by the unified electroweak theory by Glashow, Salam, and Weinberg. The strong interaction, described by Quantum Chromodynamics, confines quarks into hadrons and is responsible for binding protons and neutrons into atomic nuclei; it is mediated by the gluon.

The elementary particles of the Standard Model are visualized in Fig. 1.1, and are categorized as three different types: quarks, leptons, and bosons. The quarks come in six different "flavors:" up (u), down (d), charm (c), strange (s), top (t), and bottom (b). The leptons are the electron (e), muon (μ), tau (τ), and their corresponding neutrinos (ν). Additionally, the integer spin force carrier particles are the photon (γ), gluon, W and Z bosons, and the Higgs boson. The quarks are the only elementary particles that experience all fundamental interactions. In Quantum Chromodynamics, each quark is assigned a quantum number called "color" (or color charge) and is one of three varieties: blue, green, or red. Within a given generation of quarks, one quark has an electric charge of $+2/3$, and one quark has an electric charge of $-1/3$. Quarks and leptons are both fermions, in that they are spin $1/2$ particles. Leptons are distinct as they only experience the electromagnetic and weak interactions and do not undergo strong interactions. The quarks and leptons are grouped together in three generations, by increasing mass, as shown in Fig. 1.1. Leptons exist as free particles in nature, in contrast with quarks which occur as composite "colorless" particles known as hadrons. Hadrons are categorized by their number of constituent quarks, most of which fall into two categories:

1. Mesons are bound states of a quark-antiquark pair (e.g. pions)

2. Baryons are bound states of three quarks (e.g. protons and neutrons).

Increasing experimental evidence of other kinds of "exotic" hadrons, beyond mesons and baryons, implies that there may be bound-states of four (tetraquark) or five (pentaquark) quarks [10]. Within the framework of the Standard Model, the proton and neutron are composed of three "valence quarks" in the combinations of uud and udd, respectively. The proton and neutron are the most stable baryons.

The Standard Model has been successful in predicting the existence of many particles and their properties, prior to their respective experimental discoveries. Notably this includes the W and Z bosons, top quark, charm quark, gluon, and Higgs boson. While the Standard Model as a theory is mathematically self-consistent, it has not been mathematically proven from first-principles. Furthermore the Standard Model is not an all-encompassing theory, as some physical phenomena remain unexplained in its framework. Gravity is not described by the Standard model, due to contradictions arising when attempting to incorporate general relativity. The graviton is postulated as the force carrier, though it has yet to be experimentally discovered. The Standard Model also does not allow for massive neutrinos, while there is experimental evidence for neutrinos to have mass [10]. The Standard Model is also unable to explain the observed phenomena called "dark matter" or "dark energy" [11]. Also it is difficult to accommodate the observed predominance of matter over antimatter within the universe in the Standard Model.

Quantum Chromodynamics (QCD) is the modern quantum field theory of the strong interaction, and thus describes the interacting behavior of quarks mediated by gluons. QCD was originally formulated in the early 1960s, and is now an important part of the Standard Model. QCD is a non-abelian gauge theory, that is invariant under the SU(3) color symmetry group (called color SU(3)). As already noted, the strong force is mediated by a massless gauge boson called a gluon, the gluon also carries color charge and can self-interact. The strong coupling constant, α_s, varies as a function of the energy scale of the interaction, and therefore is a running coupling constant [12]. From the theoretical formulation, QCD exhibits two unique properties:

1. Color Confinement: The attractive force between two quarks increases as their separation increases (or at larger distances). This phenomena (known as color confinement) suggests that the amount of energy required to separate two quarks is infinite, exceeding the quark mass. While there is not yet an analytical proof of color confinement in any non-abelian gauge theories, quarks are always bound in color neutral

hadrons. Free quarks cannot be isolated experimentally, their existence has been established through deep-inelastic electron-nucleon scattering experiments, where an electron interacts with a single quark inside the nucleon.

2. Asymptotic Freedom: At shorter distances between quarks, the strength of the strong coupling constant decreases. Shorter distances scales are probed via higher-energy processes. Thus the interaction between the quarks and gluons is asymptotically weaker as the energy scale increases, and the corresponding length scale decreases. Asymptotic Freedom enables perturbative treatments of the strong interaction and α_s, which is known as Perturbative QCD (pQCD).

Presently, a complete and mathematically self-consistent description of nuclear structure and dynamics is not obtainable from the first-principles of QCD. Due to the behavior of the strong coupling constant, α_s, in the low- to medium-energy (non-perturbative) regime exact calculations involving the lightest quarks (up and down), and therefore the nucleon, are extremely difficult. Furthermore, from the features of QCD it is known that valence quarks are not the only particles contributing to the structure of the nucleon. Rather, QCD predicts that hadrons also contain "sea quarks," which are quark-antiquark pairs splitting from a gluon, and "sea gluons," quark-antiquark pairs annihilating to produce a gluon. This so called parton sea is expected to significantly contribute to the emergent properties of the respective hadron, in our case the nucleon.

Most ordinary matter in the universe, in the form of protons and neutrons, arises from QCD interactions, and understanding the structure and properties of the nucleon from the constituent quarks and gluons of QCD is a major research effort. A large body of experimental data exists in the high energy regime (from deep inelastic scattering, and Jet Production at colliders) and this confirms the validity of QCD, particular in the perturbative regime. A central challenge in nuclear physics is understanding the transition region from the low- and medium-energy non-perturbative regime to energy scales where pQCD is valid.

At present, exact calculations in this non-perturbative regime of QCD, are not possible due to the complexity of the theory. Various techniques have been developed to study QCD as a theory. QCD-inspired models and effective field theory techniques have been successful in studying aspects of QCD. However, these QCD-inspired models and and effective field theories are only valid in certain energy ranges. Lattice QCD is a well-established non-perturbative approach to formulating QCD which uses a discrete set of spacetime points (called the lattice). Lattice QCD also has limitations, notably, that it is computationally intensive and requires the use of advanced computers to perform calculations.

Experimental data pertaining to properties of the nucleon serves to validate and guide the theoretical interpretation of the strong interaction. One of the most straightforward experimental techniques for studying the nucleon's structure is by using electrons as a probe. An advantage is that the theoretical framework of QED is well-understood and electrons are point-like particles, and electron-nucleon scattering still provides significant information about the nucleon structure. The downside of electron scattering probes is that they are largely insensitive to a portion of the nucleon structure, that of the gluons. The elastic electromagnetic form factors encode information about the internal charge and magnetization distributions within the nucleon. Precision measurements of the elastic nucleon electromagnetic form factors from electron-nucleon scattering experiments, over a broad range of four-momentum transfer, provide a way for benchmarking theories describing the strong interaction; such a measurement is the focus of this dissertation.

1.1 Quantum Electrodynamics and Scattering Theory

Quantum Electrodynamics (QED) is the relativistic quantum field theory describing electromagnetic interactions. One of the most powerful features of QED is that interactions may be expanded perturbatively with the fine-structure constant α as the development parameter. The perturbative framework of QED allows practical calculations of observable phenomena to be completed to an arbitrary degree of accuracy. Further, QED provides a

powerful method to describe interactions and processes with the implementation of Feynman Diagrams.

An entire rigorous characterization of QED is beyond the scope of this dissertation; one can find such a treatment presented by Halzen & Martin [12] or Peskin & Schroeder [13]. For the purposes of this dissertation, we will cover theory related to this analysis which involves the study of the nucleon electromagnetic form factors. Specifically, we are interested in the scattering of a point-like spin $1/2$ charged particle from an arbitrary target, with our particular application being electron scattering from a neutron or deuterium target. For a point-like spin $1/2$ charged particle, with only an electromagnetic interaction, the wavefunction is governed by the Dirac Equation

$$(i\gamma^{\mu}\partial_{\mu} - m)\psi = 0, \tag{1.4}$$

where m is the rest mass of the particle, ψ is the four component Dirac spinor, μ indexes from $0 \ldots 3$ over the implied summation, and γ^{μ} is the set of 4×4 Dirac matrices. The Dirac γ^{μ} matrices must satisfy the anticommutation relations

$$\{\gamma^{\mu}, \gamma^{\nu}\} \equiv \gamma^{\mu}\gamma^{\nu} + \gamma^{\nu}\gamma^{\mu} = 2g^{\mu\nu}I_{n\times n}, \tag{1.5}$$

where $g^{\mu\nu}$ is the Minkowski metric tensor, and $I_{n\times n}$ the $n \times n$ identity matrix. The Dirac γ^{μ} matrices may be written in the form

$$\gamma^0 = \begin{pmatrix} I & 0 \\ 0 & -I \end{pmatrix}, \qquad \gamma^i = \begin{pmatrix} 0 & \sigma_i \\ -\sigma_i & 0 \end{pmatrix}, \tag{1.6}$$

where the σ_i are the Pauli matrices and I is the 2×2 identity matrix. By deriving a continuity equation $\partial_{\mu}j^{\mu} = 0$ from the Dirac Equation in Eq. 1.4, one can determine a charge-current density j^{μ} associated with ψ

$$j^{\mu} = -e\bar{\psi}\gamma^{\mu}\psi, \tag{1.7}$$

where $\bar{\psi}$ is the adjoint spinor:

$$\bar{\psi} = \psi^{\dagger}\gamma^{0}, \tag{1.8}$$

and e is the unit charge. In order to describe interactions, we will introduce the free particle solution to the Dirac Equation

$$\psi = u(p)e^{-ip\cdot x}, \tag{1.9}$$

where u is a four component spinor, and p is the four momentum of the particle. Substituting the free particle solution into the Dirac Equation, Eq. 1.4, yields

$$(\gamma^{\mu}p_{\mu} - m)\psi = 0. \tag{1.10}$$

Since we are interested in point-like spin $1/2$ charged particles, the equation for an electron in an electromagnetic field A^{μ}, where A^{μ} is a four component electromagnetic potential, is determined by the substitution of

$$p^{\mu} \rightarrow p^{\mu} + eA^{\mu}, \tag{1.11}$$

into Eq. 1.10. Applying the substitution yields the following equations of motion

$$(\gamma_{\mu}p^{\mu} - m)\psi = (-e\gamma_{\mu}A^{\mu})\psi = \gamma^{0}V\psi, \tag{1.12}$$

and we will treat $\gamma^{0}V$ as the perturbation parameter. From the first-order perturbation, the transition amplitude for the scattering of an electron from initial state ψ_i to ψ_f is

$$T_{fi} = ie\int \bar{\psi}_f\gamma_{\mu}A^{\mu}\psi_i\, d^4x = -i\int j_{\mu}^{fi}A^{\mu}\, d^4x, \tag{1.13}$$

where we have defined the transition current

$$j_{\mu}^{fi} \equiv -e\bar{\psi}_f\gamma_{\mu}\psi_i. \tag{1.14}$$

For the purposes of this work, we are interested in scattering two point-like spin 1/2 charged particles one from the other as presented in Fig. 1.2, rather than a particle interacting with a fixed potential. The deviation from the point-like scattering, in the case of a target nucleon with structure, is parameterized by the nucleon form factors which provide information about the structure of the nucleon. For scattering of two point-like spin 1/2 charged particles, the electromagnetic field A^μ associated with the current j^μ must, in Lorenz gauge, obey Maxwell's Equations

$$\Box^2 A^\mu = j^\mu, \tag{1.15}$$

where $\Box$ is the four-dimensional Laplacian operator which is defined to be the invariant contraction $\Box \equiv \partial_\mu \partial^\mu$. For the transition current $j_\mu^{fi} = -e\bar{u}_f \gamma_\mu u_i e^{(p_f - p_i)\cdot x}$ it is known that the solution for A^μ is

$$A^\mu = -\frac{j_{fi}^\mu}{(p_i - p_f)^2} = -\frac{j_{fi}^\mu}{q^2}, \tag{1.16}$$

where the four momentum transfer $q = p_i - p_f$. From the same formalism as for Eq. 1.13, the transition amplitude for scattering between two charge-current distributions j_1^μ and j_2^μ is

$$T_{fi} = -i \int j_\mu^1 \left(-\frac{1}{q^2}\right) j_2^\mu \, d^4x = -ie^2 \int \bar{\psi}_{1,f} \gamma_\mu \psi_{1,i} \left(\frac{1}{q^2}\right) \bar{\psi}_{2,f} \gamma^\mu \psi_{2,i} \, d^4x. \tag{1.17}$$

One needs to relate this formalism to physical observables; in our case of scattering we are interested in relating the transition amplitude to the differential scattering cross-section. The differential cross-section is a measure of the probability that a specific scattering process will occur. In order to motivate the differential cross-section for scattering between two point-like spin 1/2 charged particles, we will first consider the transition rate per unit volume W_{fi}:

$$W_{fi} = \frac{|T_{fi}|^2}{TV}, \tag{1.18}$$

where T_{fi} is the transition amplitude, T is the time interval of the interaction, and V is the volume. The differential cross-section $d\sigma$, in symbolic form, is directly related to the

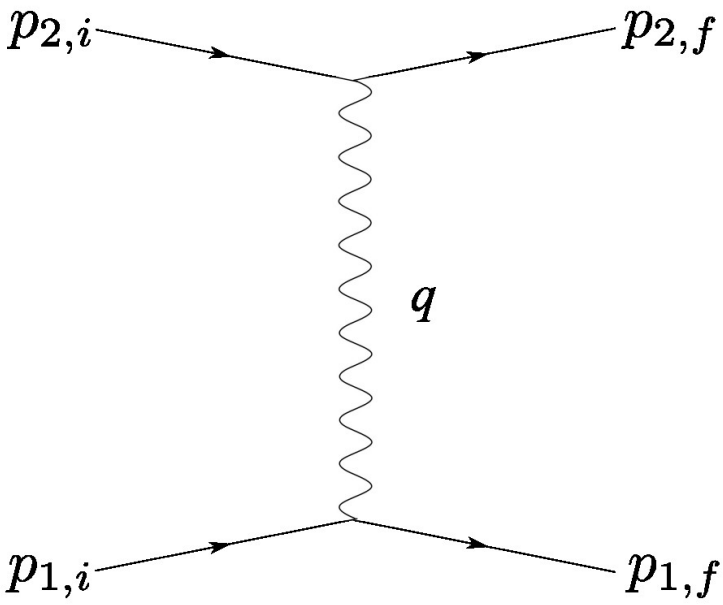

Figure 1.2: First-order Feynman diagram for scattering between two point-like spin 1/2 charged particles. Four momenta for each point-like spin 1/2 charged particle are indicated by p_1 and p_2, respectively. The incoming and outgoing momenta are indicated by i and f, respectively.

transition rate per unit volume W_{fi} and is

$$d\sigma = \frac{W_{fi}}{\Phi} dQ \tag{1.19}$$

where Φ is the initial flux of particles, and dQ is the Lorentz-invariant phase space factor. The calculation of the differential cross-section for many scattering processes, to leading order, are well-known; in this work we will not reproduce these derivations. The differential cross-section for the scattering of two distinguishable spin 1/2 point particles in the lab frame is

$$\frac{d\sigma}{d\Omega} = \left.\frac{d\sigma}{d\Omega}\right|_{\text{Mott}} \frac{E'}{E} \left(1 - \frac{q^2}{2M^2} \tan^2 \frac{\theta}{2}\right), \tag{1.20}$$

where the Mott cross-section describes the scattering of an electron from a structureless

spinless target,

$$\left.\frac{d\sigma}{d\Omega}\right|_{\text{Mott}} = \frac{\alpha^2 \cos^2 \frac{\theta}{2}}{4E^2 \sin^4 \frac{\theta}{2}}, \tag{1.21}$$

θ is the scattering angle of the electron, M is the mass of the target, E is the initial energy of the electron, E' is the final energy of the electron, and $q = p_i - p_f$ is the four momentum transfer.

1.2 Particles with Structure

The model from Sec. 1.1 for scattering between two point-like spin 1/2 charged particles is a good starting place for extending to the scattering of an electron from an arbitrary target. This section will describe scattering of an electron from a particle with structure. Ultimately the goal of this section is to consider the differential cross-section of scattering an electron from a particle with structure, so that the differential cross-section can be parameterized for the case of the nucleons. In particular, we are interested in the scattering of an electron from a nucleon, as shown in Fig. 1.3. We will start with a modified version of Eq. 1.17, which describes the transition amplitude for two interacting currents,

$$T_{fi} = -i \int j_\mu \left(-\frac{1}{q^2}\right) J^\mu \, d^4x, \tag{1.22}$$

where we will take j^μ as defined in Eq. 1.14 to be the current for the electron, and J^μ to be the current for the nucleon. We are interested in the general form for J^μ, which is a Lorentz invariant four-vector, and must consider an exhaustive list of linearly independent four-vector quantities that can describe the interaction. In general J^μ is some expression that involves p^μ, p'^μ, and γ^μ; but combinations of contracted quantities like $p^\mu \gamma_\mu p^\nu$, etc. should also be considered. We consider all possible 4×4 matrices that can be constructed from the 16 linearly independent matrices

$$I, \gamma^\mu, \sigma^{\mu\nu}, \gamma^\mu\gamma^5, \gamma^5, \tag{1.23}$$

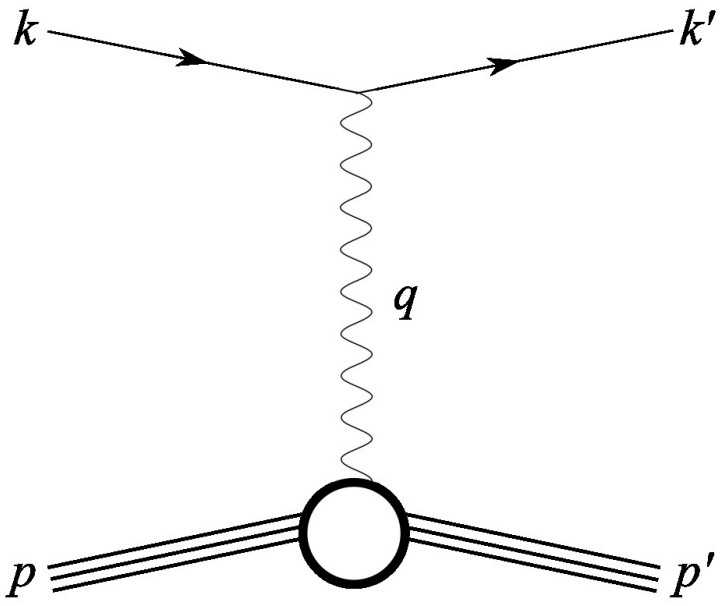

Figure 1.3: First-order Feynman diagram for elastic electron-nucleon scattering. Four momenta for the electron and the nucleon are indicated as k and p, respectively. The incoming and outgoing momenta are denoted as unprimed and primed, respectively.

where two new objects have been introduced,

$$\gamma^5 = i\gamma^0\gamma^1\gamma^2\gamma^3 \tag{1.24}$$

and

$$\sigma^{\mu\nu} = \frac{i}{2}\left(\gamma^\mu\gamma^\nu - \gamma^\nu\gamma^\mu\right). \tag{1.25}$$

A known property of the γ^5 matrix is that it anticommutes with the parity operator and is therefore a pseudo-scalar. Since the electromagnetic interaction conserves parity, we can eliminate any terms involving γ^5. The only remaining four-vectors available are the incoming momentum p^μ, the outgoing momentum p'^μ, and γ^μ. Any coefficients in the expression of J^μ must be functions of Lorentz scalars; the only nontrivial scalar available is $q^2 = -2p\cdot p' + 2m^2$. Taking all of this information into account and using the combinations $(p'^\mu + p^\mu)$ and $(p'^\mu - p^\mu)$ for convenience, the most general form of the hadronic current,

J^ν, is

$$J^\nu = e\bar{u}\left(p'\right)\left[A\left(q^2\right)\gamma^\nu + B\left(q^2\right)\left(p'^\nu + p^\nu\right) + C\left(q^2\right)\left(p'^\nu - p^\nu\right)\right]u\left(p\right)e^{i(p'-p)\cdot x}. \tag{1.26}$$

By enforcing current conservation, $\partial_\mu J^\mu = 0$ or in this case in the form $q_\mu J^\mu = 0$ from the Ward Identity, any terms which do not vanish for an arbitrary coefficient must have the coefficient itself equal to zero. We can write the enforcement of current conservation directly

$$\begin{aligned} q_\mu J^\mu = \Big(&A\left(q^2\right)\bar{u}\left(p'\right)\gamma^\mu\left(p'_\mu - p_\mu\right)u\left(p\right) + B\left(q^2\right)\bar{u}\left(p'\right)u\left(p\right)\left(p'^\mu - p^\mu\right)\left(p'_\mu + p_\mu\right) \\ &+ C\left(q^2\right)q^2\Big)e^{i(p'-p)\cdot x}. \end{aligned} \tag{1.27}$$

For the term proportional to A,

$$A\left(q^2\right)\bar{u}\left(p'\right)\gamma^\mu q_\mu u\left(p\right) = A\left(q^2\right)\bar{u}\left(p'\right)\gamma^\mu\left(p'_\mu - p_\mu\right)u\left(p\right) = A\left(q^2\right)\bar{u}\left(p'\right)(m-m)u\left(p\right) = 0, \tag{1.28}$$

which directly follows from the Dirac equation, in Eq. 1.10, so this term will vanish. For the term proportional to B, $p^2 = p'^2 = m^2$, and

$$B\left(q^2\right)\bar{u}\left(p'\right)u\left(p\right)\left(p'^\mu - p^\mu\right)\left(p'_\mu + p_\mu\right) = B\left(q^2\right)\bar{u}\left(p'\right)u\left(p\right)\left(m^2 - m^2\right) = 0, \tag{1.29}$$

thus this term will vanish as well. For the term proportional to C, if the photon is not on-shell, $q^2 \neq 0$, therefore to preserve current conservation $C\left(q^2\right) = 0$ and there is no $(p'^\mu - p^\mu)$ term. Hence the hadronic current actually takes the form,

$$J^\nu = e\bar{u}\left(p'\right)\left[A\left(q^2\right)\gamma^\nu + B\left(q^2\right)\left(p'^\nu + p^\nu\right)\right]u\left(p\right)e^{i(p'-p)\cdot x}. \tag{1.30}$$

From the Gordon Identity

$$\bar{u}\left(p'\right)\gamma^\mu u\left(p\right) = \frac{1}{2M}\bar{u}\left(p'\right)\left(p'_\mu + p_\mu + i\sigma^{\mu\nu}q_\nu\right)u\left(p\right), \tag{1.31}$$

so the $(p'^{\mu} + p^{\mu})$ term can now be written using $i\sigma^{\mu\nu}q_{\nu}$ instead. Applying the Gordon Identity and rewriting the arbitrary functions in J^{ν} yields:

$$J^{\nu} = e\bar{u}\left(p'\right)\left[F_1\left(q^2\right)\gamma^{\nu} + \frac{\kappa}{2M}F_2\left(q^2\right)i\sigma^{\nu\mu}q_{\mu}\right]u\left(p\right)e^{i(p'-p)\cdot x}, \tag{1.32}$$

where κ is the anomalous magnetic moment of the target. From the hadronic current in Eq. 1.32, there are two independent functions of q^2 which parameterize the structure of the target particle. They are F_1 and F_2, which are known as the Dirac and Pauli form factors, respectively. To restate the original goal, we are focused on electron nucleon scattering and now can use the formalism of the Pauli and Dirac form factors to parameterize the structure of nucleons. By using the hadronic current from Eq. 1.32, one can then write the differential cross-section for electron nucleon scattering as

$$\frac{d\sigma}{d\Omega} = \frac{\alpha^2}{4E^2\sin^4\frac{\theta}{2}}\frac{E'}{E}\left[\left(F_1^2 - \frac{\kappa^2 q^2}{4M^2}F_2^2\right)\cos^2\frac{\theta}{2} - \frac{q^2}{2M}\left(F_1 + \kappa F_2\right)^2\sin^2\frac{\theta}{2}\right], \tag{1.33}$$

this is known as the Rosenbluth formula. For the limit of $q^2 \to 0$ we are not sensitive to the nucleon structure, instead we effectively see a particle with a total charge and a Dirac magnetic moment plus an anomalous moment κ. Therefore, in this limit, values for the form factors in Eq. 1.33 for the proton and neutron are

$$F_1^p(0) = 1, F_2^p(0) = 1, \tag{1.34}$$

$$F_1^n(0) = 0, F_2^n(0) = 1. \tag{1.35}$$

Further if we consider the case where the nucleon was actually a point-like particle, then $\kappa = 0$ and $F_1(q^2) = 1$ for all q^2 and the Rosenbluth formula in Eq. 1.33 recovers the differential cross-section for scattering between two charged spin 1/2 point-like particles as presented in Eq. 1.20.

The Pauli and Dirac form factors in Eq. 1.33 parameterize our understanding of the differential cross-section for protons and neutrons, and more generically spin 1/2 particles

with structure. In Chapter 2 we will provide a different interpretation of form factors in terms of the electric charge and magnetization distributions. The primary experimental measurement techniques, current global nucleon form factor data, and some relevant theoretical models will also be presented. In Chapter 3, a discussion of the experimental extraction technique will be provided for the SBS G_M^n and nTPE experiments. Chapter 4 will describe the CEBAF accelerator and the experimental apparatus used for the SBS G_M^n and nTPE experiments. Chapter 5 will overview Gas Electron Multiplier (GEM) tracking detectors and provide information on GEMs specific to the SBS program. The data analysis of the SBS G_M^n and nTPE experiments will be described in detail in Chapter 6, as well as, the methodology for experimental observables. Chapter 7 will present preliminary physics results from this analysis of the SBS G_M^n and nTPE data.

Chapter 2

Nucleon Electromagnetic Form Factors

In the previous chapter we described how to parameterize electron scattering from a spin-1/2 particle with structure. We arrived at the Rosenbluth Formula, Eq. 1.33, which relates the differential scattering cross-section to two independent functions, the Dirac and Pauli electromagnetic form factors. In the scope of this dissertation, when the nucleon electromagnetic form factors are described we are specifically referring to the spacelike nucleon electromagnetic form factors. The spacelike nucleon electromagnetic form factors can be extracted from processes like $e^- N \to e^- N$. The spacelike electromagnetic form factors provide information about the electric and magnetization distributions within the nucleon, and therefore present insights about the strong interaction. However, the spacelike electromagnetic form factors do not encompass the entire description for the structure of the nucleon. To provide a more complete description, the timelike nucleon electromagnetic form factors should also be considered. Measurements of the timelike nucleon electromagnetic form factors can be accessed from collider experiments investigating nucleon pair production, $e^+e^- \to N\bar{N}$, or nucleon annihilation, $N\bar{N} \to e^+e^-$. Understanding the nucleon electromagnetic form factors in the timelike region could provide information on the long-range behavior of strong interactions. A complete review of the timelike nucleon elec-

tromagnetic form factors is beyond the scope of this dissertation, a recent review of this matter is provided in Ref. [14].

In this chapter we will first describe how the Dirac and Pauli form factors are related to the electric charge and magnetization distributions in the nucleon. The second and third sections of this chapter will examine techniques for extracting the nucleon electromagnetic form factors. We will consider nucleon Two-Photon Exchange and other Radiative Corrections in the fourth section. The fifth section will describe the current status of world data on nucleon electromagnetic form factors. The sixth section of this chapter will summarize current relevant theoretical models of the nucleon electromagnetic form factors. The final section will describe how the nucleon electromagnetic form factors can be decomposed into their contributions arising from the individual quark flavors.

2.1 Sachs Form Factors

Sachs first suggested writing the nucleon electromagnetic form factors as two linear combinations of the Pauli and Dirac form factors around 1960 [15, 16], such that these combinations could be related to the electric charge and current distributions in the nucleon. Subsequently in 1963 Hand, Miller, and Wilson [17] showed that the two functions G_E and G_M are reasonable alternatives to the traditional Dirac and Pauli form factors. Further Hand, Miller, and Wilson suggested that if one considered the Breit frame (or the "brick-wall" frame) the two functions G_E and G_M could be related to the Fourier transforms of the electric charge and magnetization distributions. These functions are known as the electric and magnetic form factors

$$G_E = F_1 + \frac{\kappa q^2}{4M^2} F_2, \tag{2.1}$$

and

$$G_M = F_1 + \kappa F_2, \tag{2.2}$$

where κ is the anomalous magnetic moment. Rewriting the differential scattering cross-section, Eq. 1.33, in terms of the electric and magnetic form factors gives the following form

$$\begin{aligned}\left(\frac{d\sigma}{d\Omega}\right)_{\text{exp}} &= \left(\frac{d\sigma}{d\Omega}\right)_{\text{Mott}} \frac{E'}{E}\left(\frac{G_E^2+\tau G_M^2}{1+\tau}+2\tau G_M^2\tan^2\frac{\theta}{2}\right) \\ &= \left(\frac{d\sigma}{d\Omega}\right)_{\text{Mott}} \frac{E'}{E}\frac{1}{1+\tau}\left(G_E^2+\frac{\tau}{\epsilon}G_M^2\right),\end{aligned} \tag{2.3}$$

where τ is the dimensionless four-momentum transfer defined as

$$\tau = \frac{-q^2}{4M^2}, \tag{2.4}$$

and ϵ is the longitudinal polarization of the virtual photon defined as

$$\epsilon = \frac{1}{1+2(1+\tau)\tan^2\frac{\theta}{2}}. \tag{2.5}$$

The electric and magnetic form factors can be physically interpreted best in the frame of zero energy transfer, also known as the Breit frame. In the Breit frame, the electric and magnetic form factors are closely related to the Fourier transforms of the charge and magnetization distributions, respectively [12, 18]. However, the definition of the Breit frame is different for each value of q^2, therefore this leads to difficulties generating three dimensional representations of the electric and magnetic distributions for the nucleon using Fourier transforms.

If we instead consider the non-relativistic limit of $q^2 \to 0$, each form factor is the Fourier transform of the corresponding charge or magnetization spatial distribution function in the nucleon rest frame. If we consider the particular case of the electric form factor G_E, for short distances, we can expand the exponential that appears in the transform of the charge

distribution in powers of $|\vec{q}|^2$

$$\begin{aligned} G_E(q) &= \int \rho(\vec{x})\, e^{i\vec{q}\cdot\vec{x}} d^3x = \int \left(1 + i\vec{q}\cdot\vec{x} - \frac{(\vec{q}\cdot\vec{x})^2}{2} + \cdots\right) \rho(\vec{x})\, d^3x \\ &= \left(\int \rho(\vec{x})\, d^3x\right) - \frac{1}{6}|\vec{q}|^2 \left\langle r^2_{charge}\right\rangle + \frac{1}{120}|\vec{q}|^4 \left\langle r^4_{charge}\right\rangle + \cdots \\ \therefore G^p_E(q) &= 1 - \frac{1}{6}|\vec{q}|^2 \left\langle r^2_{charge}\right\rangle + \frac{1}{120}|\vec{q}|^4 \left\langle r^4_{charge}\right\rangle + \cdots \end{aligned} \tag{2.6}$$

The first term of the expansion in Eq. 2.6 is simply the total charge of the particle. By matching the q^2 terms in Eq. 2.6 and considering only small $|\vec{q}|^2$, we can obtain the mean-square charge radius from the derivative of Eq. 2.6

$$\frac{dG^p_E}{dQ^2} = \frac{-1}{6}\left|r^2_{charge}\right|_{Q^2=0}, \tag{2.7}$$

and thus it follows that

$$\left\langle r^2_{charge}\right\rangle = -6\left|\frac{dG^p_E}{dQ^2}\right|_{Q^2=0}. \tag{2.8}$$

Similar relations can be derived for the magnetic form factor of the nucleon G_M and the mean-square magnetic radius $\left\langle r^2_{magnetic}\right\rangle$, however, the extraction of $\left\langle r^2_{magnetic}\right\rangle$ is more difficult to do as its contribution to the cross-section is suppressed by the mass scaling factor τ (see Eq 2.3). In the limit of $q^2 \to 0$, one can determine behavior for the nucleon electromagnetic form factors, similar to the expressions in Eqs. 1.34 and 1.35,

$$G^p_E(0) = 1, G^p_M(0) = \mu_p, \tag{2.9}$$

$$G^n_E(0) = 0, G^n_M(0) = \mu_n, \tag{2.10}$$

where $\mu_p \approx 2.793\mu_N$ and $\mu_n \approx -1.913\mu_N$ are the magnetic moments of the proton and neutron, respectively, and μ_N is the standard nuclear magneton. The non-relativistic limit combined with the formalism of the electromagnetic form factors provides a reasonable method for parameterizing the macroscopic properties of the nucleon. G_E and G_M encode information about the distribution of charge and magnetization in the nucleon.

2.2 Rosenbluth Separation

The electric and magnetic form factors of the nucleon can be separately extracted from measurements of scattering cross-sections at a constant Q^2 by varying both the beam energy and the electron scattering angle over the experimental kinematic range. This extraction is known as the Rosenbluth separation technique [18] and was the primary technique available to obtain separated values for the electromagnetic form factors of the proton and neutron until the 1990s. The differential cross-section for eN scattering, written in terms of the electric and magnetic form factors G_E and G_M, is presented in Eq. 2.3 and the version containing τ and ϵ is a useful notation. The modern version of the Rosenbluth separation technique takes advantage of the linear dependence in ϵ of the reduced cross-section, based on Eq. 2.3, and is defined as follows

$$\begin{aligned}\left(\frac{d\sigma}{d\Omega}\right)_{\text{reduced}} &= \frac{\epsilon\,(1+\tau)}{\tau}\frac{E}{E'}\left(\frac{d\sigma}{d\Omega}\right)_{\text{exp}} \Big/ \left(\frac{d\sigma}{d\Omega}\right)_{\text{Mott}} \\ &= G_M^2 + \frac{\epsilon}{\tau}G_E^2.\end{aligned} \tag{2.11}$$

The linearity of the reduced cross-section assumes the dominance of one-photon exchange in the elastic electron-nucleon scattering process. The Rosenbluth separation technique is also called an L/T separation, for the longitudinal and transverse components of the reduced cross-section. In principle, to determine the slope, G_E^2/τ, and the intercept, G_M^2, from Eq. 2.11 one only needs two different ϵ points. Typically experiments have measured more than two ϵ points for a given Q^2. From a practical experimental perspective, more ϵ points allow better understanding and checks of systematic errors. From a theoretical perspective, more data points provides a better investigation of the predicted linearity of the ϵ dependence of the reduced cross-section. One possible sign of a two-photon exchange contribution to the cross-section would be a nonlinearity in the ϵ dependence of the reduced cross-section. However, the two-photon exchange contribution might also have a linear ϵ dependence, which would be difficult to separate experimentally. Therefore, theoretical

calculations of two-photon exchange contributions to the cross-section would need to be considered if an experimental evaluation of two-photon effects exhibited a linear behavior in ϵ.

2.3 Double-Polarization Methods

Separation using the Rosenbluth technique is inherently challenging due to the τG_M^2 term dominating the differential cross-section, particularly for large values of Q^2, thereby making the separation of the G_E^2 term practically impossible. Such extraction is further complicated by corrections from higher-order effects. In 1968, Akhiezer and Rekalo [19] described the shortcomings of the use of elastic electron-proton scattering with an unpolarized electron beam and introduced the idea that the best way to obtain the proton electric form factor is with polarization experiments, specifically by measuring the polarization of the recoil proton. Furthermore in 1974, Akhiezer and Rekalo [20] discussed the interest in measuring an interference term of the form $G_E G_M$ by observing the transverse component of the recoiling proton polarization in the $\vec{e}p \rightarrow e'\vec{p}$ process at large Q^2, to obtain G_E in the presence of the dominating G_M. In a review paper from 1969, Dombey [21] described measuring polarization observables in elastic and inelastic lepton scattering and emphasized measurements involving the use of polarized lepton beams on polarized targets. The description of measuring polarization was continued in 1981 by Arnold, Carlson, and Gross [22] who explained that the best way to measure the neutron and proton form factors would be to use the $^2\mathrm{H}(\vec{e}, e'\vec{n})p$ and $^1\mathrm{H}(\vec{e}, e'\vec{p})$ reactions, respectively. A description, in the sections directly following, of two methods for extracting nucleon form factors from polarization transfer observables will be provided.

2.3.1 Recoil Polarization Method

The scattering of a longitudinally polarized electron beam from an unpolarized nucleon target, where the polarization of the incoming electron is transferred to the nucleon via

exchange of a single virtual photon, as shown in Fig. 2.1, is known as the Recoil Polarization method [18]. For this consideration of eN scattering, with a longitudinally polarized

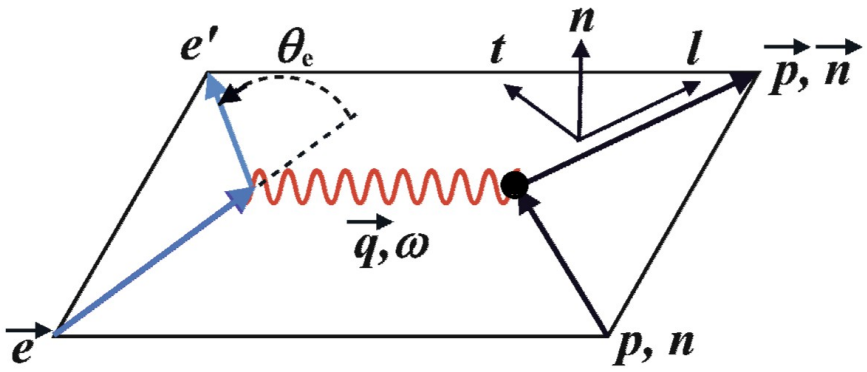

Figure 2.1: An illustration of the kinematics and polarization of the recoil nucleon for $\vec{e}p \to e'\vec{p}$ and $\vec{e}n \to e'\vec{n}$. Reproduced from [18].

electron beam and unpolarized target, the only nonzero polarization transfer components are the longitudinal and the transverse. The longitudinal polarization transfer component, P_l, is along the momentum transfer. The transverse polarization transfer component, P_t, is perpendicular to the momentum transfer in the scattering plane. The normal polarization transfer component, P_n, is zero. For single photon exchange, the polarization transfer components can be written in terms of the Sachs form factors as

$$\begin{aligned} I_O P_n &= 0 \\ I_O P_l &= h P_e \frac{(E_{\text{beam}} + E_e)}{M} \sqrt{\tau\,(1+\tau)} \tan^2 \frac{\theta_e}{2} G_M^2 \\ I_O P_t &= -h P_e 2 \sqrt{\tau\,(1+\tau)} \tan \frac{\theta_e}{2} G_E G_M \\ \text{where} \quad I_O &= G_E^2 + \frac{\tau}{\epsilon} G_M^2, \end{aligned} \tag{2.12}$$

where the incident electron (beam) and scattered electron energies are denoted E_{beam} and E_e, respectively, $h = \pm 1$ are the beam helicity states, P_e is the magnitude of the beam polarization, and θ_e is the electron scattering angle. Helicity is the projection of the spin onto the direction of the momentum, in this case of the electron. The ratio G_E/G_M can

then be directly obtained from the ratio of the two polarization components P_t and P_l as follows

$$\frac{G_E}{G_M} = -\frac{P_t}{P_l}\frac{(E_{\text{beam}} + E_e)}{2M}\tan\frac{\theta_e}{2}. \tag{2.13}$$

The experimental Recoil Polarization method is based on spin-precession in a magnetic spectrometer and the instrumentation of a nucleon polarimeter (traditionally the nucleon is a proton). The nucleon polarimeter depends on the spin-orbit interaction of the initial incident nucleon with a secondary target nucleon or nucleus, which produces an azimuthal angular effect on the scattering cross-section. The first major advantage of the Recoil Polarization method, compared to a Rosenbluth Separation, is that, in the Born approximation, for each value of Q^2 a single measurement gives both the longitudinal and transverse polarization components. Therefore the ratio G_E/G_M is obtained directly from a simultaneous measurement of the two recoil polarization components using a secondary (recoil) polarimeter. The second major advantage is that the knowledge of the beam polarization and the analyzing power of the recoil polarimeter is not needed to extract the ratio G_E/G_M. This greatly reduces the systematic uncertainties.

2.3.2 Asymmetry Method with Polarized Targets

The formalism associated with scattering longitudinally polarized electrons off a polarized nucleon target, as shown in Fig. 2.2, in order to obtain asymmetries and subsequently extract nucleon electromagnetic form factors will be summarized in this section. The method for this type of double-polarization technique is the Asymmetry Method with polarized targets [18, 23]. In the one-photon exchange approximation, the elastic electron-nucleon scattering cross-section can be written as a sum of two parts: Σ, which corresponds to the unpolarized elastic differential cross-section given by Eq. 2.3, and a polarized part, Δ, which is nonzero only if the electron beam is longitudinally polarized (helicity $h = \pm 1$),

$$\sigma_h = \Sigma + hP_e\Delta. \tag{2.14}$$

The polarized part of the cross-section, Δ, with two terms related to the directions of the

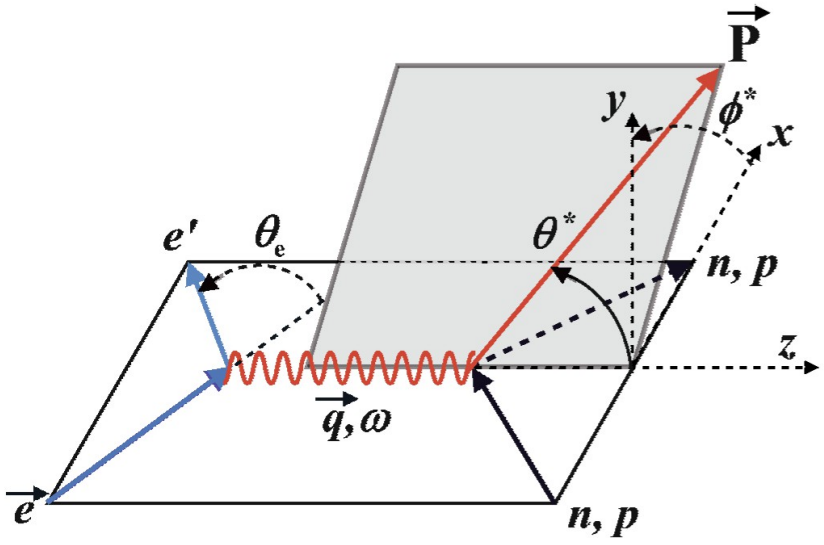

Figure 2.2: An illustration of the kinematics and the orientation of the target polarization $\vec{P}$, for the reactions $\vec{e}\,\vec{n} \to e'n$ and $\vec{e}\,\vec{p} \to e'p$. Reproduced from [18].

target polarization $\vec{P}(\theta^*\phi^*)$, is given by

$$\begin{aligned}\Delta = -2\left(\frac{d\sigma}{d\Omega}\right)_{\text{Mott}} \frac{E_e}{E_{\text{beam}}} \tan\frac{\theta_e}{2}\sqrt{\frac{\tau}{1+\tau}} \\ \times\left(\sin\theta^*\cos\phi^* G_E G_M + \sqrt{\tau\left[1+(1+\tau)\tan^2\frac{\theta_e}{2}\right]}\cos\theta^* G_M^2\right)\end{aligned} \tag{2.15}$$

where θ^* and ϕ^* are the polar and azimuthal laboratory angles of the target polarization vector. Here, the $\vec{z}$-direction is defined to be the direction of $\vec{q}$ and $\vec{y}$ normal to the electron scattering plane, as shown in Fig. 2.2. The physical asymmetry for the e-N scattering cross-section is defined as

$$A_{\text{phys}} = \frac{\sigma_+ - \sigma_-}{\sigma_+ + \sigma_-} \tag{2.16}$$

where σ_+ and σ_- are the scattering cross-sections for the two beam helicity states.

For a longitudinally-polarized electron beam and a polarized nucleon target, the mea-

sured asymmetry, A_{meas} is related to the physical asymmetry, A_{phys} by

$$A_{\text{meas}} = hP_e P_{\text{target}} A_{\text{phys}} \tag{2.17}$$

where P_e and P_{target} are the electron beam and target polarization, respectively. At the luminosity scales in which nucleon form factors experiments are performed, there are no practical free neutron targets. An alternative, in the case of asymmetry measurements with polarized targets, is a polarized ^{3}He target. The total spin of a polarized ^{3}He target is mainly carried by the neutron and thus polarized ^{3}He presents an effective polarized neutron target. It is worth noting that the spins of the protons in polarized ^{3}He approximately cancel, and this leads to the use of polarized ^{3}He as an effective polarized neutron target. Furthermore, it is known that the protons inside the polarized ^{3}He are not completely unpolarized and carry a small polarization. If one is interested in the measured experimental asymmetry for the $^3\overrightarrow{\text{He}}\,(\vec{e}, e'n)\,pp$ reaction, the measured asymmetry is modified compared to the ideal $\vec{n}\,(\vec{e}, e'n)$ or $\vec{p}\,(\vec{e}, e'p)$ reactions due to a number of effects. The following effects must be accounted for in the measured asymmetry: the limited polarization of the electron beam P_e, the polarization of the ^{3}He target $P_{^3\text{He}}$, the effective polarization of the neutrons in the ^{3}He target P_n, the addition of nitrogen in ^{3}He target D_{N_2}, contributions from inelastic pion production D_π, and reductions from nuclear effects D_{FSI}. The measured asymmetry for the $^3\overrightarrow{\text{He}}\,(\vec{e}, e'n)\,pp$ reaction can now be expressed (excluding proton polarization and other nuclear effects) as

$$A_{\text{meas}} = P_e P_{^3\text{He}} P_n D_{\text{N}_2} D_\pi D_{\text{FSI}} A_{\text{phys}}. \tag{2.18}$$

For either of the respective reactions considered, A_{phys} can be obtained by using Eqs. 2.3

and 2.15,

$$A_{\text{phys}} = -\frac{2\sqrt{\tau\,(1+\tau)}\tan\frac{\theta_e}{2}}{G_E^2 + \frac{\tau}{\epsilon}G_M^2}\left[\sin\theta^*\cos\phi^* G_E G_M + \sqrt{\tau\left[1+(1+\tau)\tan^2\frac{\theta_e}{2}\right]}\cos\theta^* G_M^2\right]. \tag{2.19}$$

From Eq. 2.19, if the target polarization in the laboratory frame is perpendicular with respect to the momentum transfer vector $\vec{q}$ and is within the reaction plane, with $\theta^* = \pi/2$, and $\phi^* = 0°$or $180°$, then one gets the perpendicular asymmetry

$$A_{\text{perp}} = \frac{-2\sqrt{\tau\,(1+\tau)}\tan\frac{\theta_e}{2}\frac{G_E}{G_M}}{\left(\frac{G_E}{G_M}\right)^2 + \frac{\tau}{\epsilon}}. \tag{2.20}$$

As $(G_E/G_M)^2$ is quite small, A_{perp} is approximately proportional to G_E/G_M. If one is interested in extracting only one of the two electromagnetic form factors from A_{perp} for a particular nucleon, knowledge of the respective form factor not being extracted is necessary. For the case of some detectors with a large acceptance, the longitudinal component (the second term) of Eq. 2.19 is not strictly zero. However, these finite acceptance effects are small and to first order depend only on kinematics and can be corrected for in the extraction of G_E/G_M. From Eq. 2.19, the longitudinal component [24] of A_{phys} can be expressed as

$$A_{\text{para}} = -\frac{2\tau\sqrt{1+\tau+(1+\tau)^2\tan^2\frac{\theta_e}{2}}\tan\frac{\theta_e}{2}}{\left(\frac{G_E}{G_M}\right)^2 + \frac{\tau}{\epsilon}}. \tag{2.21}$$

The description above is applicable to free electron-nucleon scattering and the case of quasi-elastic electron scattering from ^{3}He. For quasi-elastic electron scattering from ^{2}H similar corrections are required for several nuclear effects.

2.4 Nucleon Two-Photon Exchange

Most of the formalism presented thus far in Chapters 1 and 2 is exact only in the one-photon exchange (OPE) approximation, which in many cases provides an accurate and reasonable theoretical description of physical observables. However, for the consideration

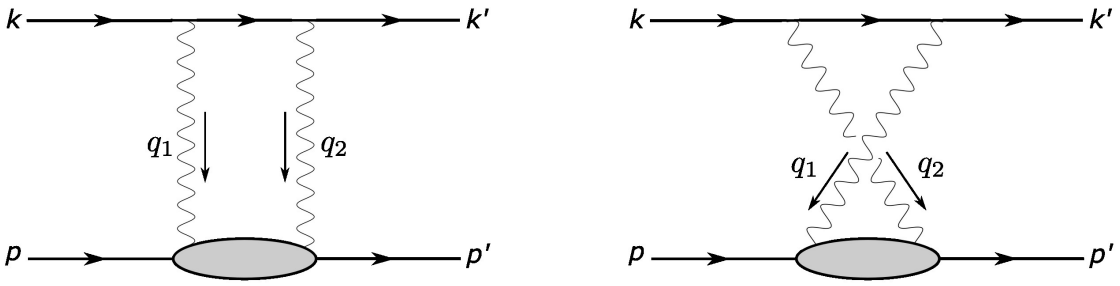

Figure 2.3: Box and crossed-box two-photon exchange Feynman diagrams, which contribute to elastic electron-nucleon scattering. Here k and k' are the momenta of the incident and outgoing electron, respectively. Similarly, p and p' are the momenta of the incident and outgoing nucleon, respectively. The momenta of the first and second virtual photons, respectively, is denoted as q_1 and q_2. The overall four-momentum transferred to the nucleon is $q = k - k' = q_1 + q_2$

of the nucleon electromagnetic form factors, understanding higher-order contributions to elastic electron-nucleon scattering cross-sections is of significant interest. The OPE approximation neglects to include radiative corrections to the cross-section; specifically these radiative corrections include one-loop virtual corrections (vacuum polarization, electron vertex corrections and self energy, nucleon vertex corrections and self energy), and inelastic scattering processes involving the emission of real bremsstrahlung photons.

In addition to these radiative corrections we need to consider the box and crossed-box two-photon exchange (TPE) contribution diagrams which are shown in Fig. 2.3. The TPE contributions are of particular importance for two main reasons. Firstly, the hadronic contributions, represented by the gray blob in Fig. 2.3, are extremely difficult to calculate and often have a large relative uncertainty. Secondly, the OPE consideration may not be a sufficiently good approximation for the extraction of the nucleon electromagnetic form factors from unpolarized cross-sections at large values of Q^2.

A full treatment of the TPE contributions and radiative corrections to electron-nucleon scattering is beyond the scope of this dissertation; more rigorous and complete characterizations are available in recent literature [25–27]. For the purposes of this dissertation, we will describe modifications to the formalism presented in Chapters 1 and 2, but now

include some higher-order corrections. This Section will summarize modifications to the scattering cross-sections and explain how TPE contributions are potentially quantified.

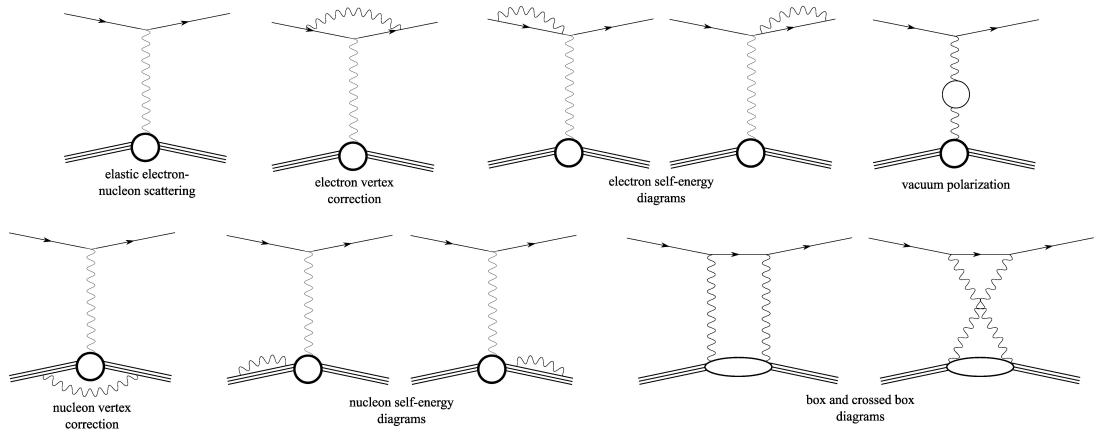

Figure 2.4: Diagrams contributing to the electron-nucleon scattering cross-section from virtual processes and TPE effects, to order α^2. Adapted from [25].

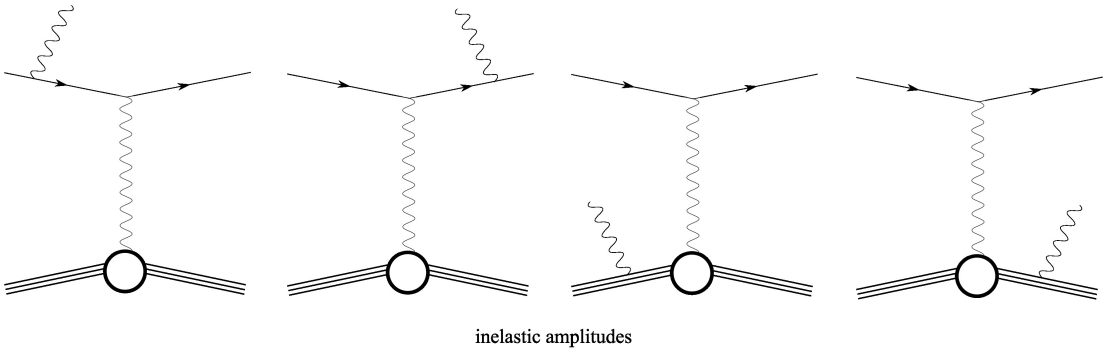

Figure 2.5: Diagrams contributing to the electron-nucleon scattering cross-section from bremssttrahlung (inelastic) processes, to order α^2. Adapted from [25].

To modify the formalism presented in Chapters 1 and 2, higher-order corrections beyond the one-photon exchange reduced cross-section, Eq. 2.11, will be considered

$$\left(\frac{d\sigma}{d\Omega}\right)_{\mathrm{R}} = \left(\frac{d\sigma}{d\Omega}\right)_{\mathrm{R}}^{\mathrm{OPE}} (1 + \delta_{\mathrm{virt}} + \delta_{\mathrm{brem}}) \,, \tag{2.22}$$

where δ_{virt} and δ_{brem} are radiative corrections arising from the exchange of a second virtual photon, and inelastic bremsstrahlung for real photon emission, respectively. When

considering the virtual corrections for eN scattering, it is convenient to separate terms into "soft" parts, which are independent of hadronic structure, and "hard" parts, which are model dependent. If we consider the scattering amplitude for all one-loop corrections, $\mathcal{M}_{1-\text{loop}}$, by accounting for all diagrams in Figs. 2.4 and 2.5 then $\mathcal{M}_{1-\text{loop}}$ can be written as a sum of a "factorizable" soft term, proportional to the OPE amplitude $\mathcal{M}_\gamma$, and a non-factorizable "hard term" $\mathcal{M}_{\text{hard}}$,

$$\mathcal{M}_{1-\text{loop}} = f(Q^2, \epsilon)\mathcal{M}_\gamma + \mathcal{M}_{\text{hard}}, \tag{2.23}$$

where $f(Q^2, \epsilon)$ is strictly a kinematic factor. Therefore δ_{virt} is given by

$$\delta_{\text{virt}} = 2f(Q^2, \epsilon) + \frac{2\text{Re}\left(\mathcal{M}_\gamma^* M_{\text{hard}}\right)}{|\mathcal{M}_\gamma|^2} \equiv \delta_{\text{soft}} + \delta_{\text{hard}}. \tag{2.24}$$

The virtual processes included in Fig. 2.5 contribute to the δ_{soft} term of δ_{virt}. The terms which depend on hadronic structure are contained within $\mathcal{M}_{\text{hard}}$, and arise from the nucleon vertex and TPE correction diagrams present in Fig. 2.4. Characterizations and computations of both δ_{virt} and δ_{brem} are provided in recent literature [25–27].

Ultimately, the leading-order relative TPE correction to the OPE reduced cross-section arises from the interference terms between one-photon and two-photon amplitudes as shown in Figs. 1.3 and 2.3, respectively, and is given by

$$\delta_{\text{TPE}} = \frac{2\text{Re}\left(\mathcal{M}_\gamma^* M_{2\gamma}\right)}{|\mathcal{M}_\gamma|^2}, \tag{2.25}$$

where $\mathcal{M}_\gamma$ is the OPE scattering amplitude, and $M_{2\gamma}$ is the scattering amplitude from TPE contributions. The higher-order TPE contributions effectively modify the reduced cross-section, at order α^2, so the measured reduced cross-section can be written as follows

$$\left(\frac{d\sigma}{d\Omega}\right)_{\text{R}}^{\text{meas}} \simeq \left(\frac{d\sigma}{d\Omega}\right)_{\text{R}}^{\text{OPE}} (1 + \delta_{\text{TPE}})\,. \tag{2.26}$$

A methodology and description of the extraction of TPE effects from the present experimental analysis will be further discussed in Chapter 3.

2.5 Global Nucleon Form Factor Data

The data and fits described in this Section are predominantly either adapted or reproduced from the most recent literature [28] on nucleon electromagnetic form factors. The data presented in Figs. 2.6a, 2.6b, 2.7a, and 2.7b captures the state of empirical knowledge of the proton and neutron electromagnetic form factors, respectively, at the time of writing this dissertation. Throughout this description of nucleon electromagnetic form factors we will include the magnetic moment of the proton, $\mu_p \approx 2.793\mu_N$, and the magnetic moment of the neutron, $\mu_n \approx -1.913\mu_N$, where μ_N is the standard nuclear magneton. The content of this Section will first provide a description of relevant fits of the world data, and second summarize the data included in the plots of the world data.

2.5.1 Fit Parameterizations

Traditionally, the proton form factors G_E^p and G_M^p/μ_p, and the neutron magnetic form factor G_M^n/μ_n are found to be roughly consistent, within the measured Q^2 range, with a parameterization known as the "standard dipole" form factor defined as

$$G_D = \left(1 + \frac{Q^2}{\Delta^2}\right)^{-2}, \tag{2.27}$$

where $\Delta^2 = 0.71$ (GeV/c)^2 is the scale parameter. The neutron electric form factor G_E^n has a markedly different Q^2-dependence, which is not consistent with the standard dipole form factor. The neutron has zero net charge, that is $G_E^n(0) = 0$, and this condition impacts the overall behavior of G_E^n. The existing measurements of G_E^n, shown in Fig. 2.7a, exhibit a rapid rise with Q^2 to a value that is approximately half the value of G_D, at the highest Q^2. To a level of reasonable agreement, a better parameterization for G_E^n is the Galster

fit [29] as defined by

$$G_E^n(Q^2)_{\text{Galster}} = \frac{\mu_n \tau}{1 + 5.6\tau} G_D(Q^2), \tag{2.28}$$

where μ_n is the magnetic moment of the neutron, τ is the dimensionless four-momentum transfer as presented in Eq. 2.4, and G_D is the dipole form factor. A phenomenological fit by Kelly [30] attempted to parameterize the nucleon form factors using data that were available in the early 2000's. The Kelly fit is useful in producing continuous values of the nucleon form factors and their uncertainties with greater accuracy than that of the dipole. The proton form factors G_E^p and G_M^p/μ_p, and the neutron magnetic form factor G_M^n/μ_n are taken to have the form

$$G(Q^2) \propto \frac{\sum_{k=0}^{n} a_k \tau^k}{1 + \sum_{k=1}^{n+2} b_k \tau^k}, \tag{2.29}$$

where numerator and denominator are both polynomials in τ and the degree of the denominator is larger than that of the numerator to ensure the $G \sim Q^{-4}$ behavior for large Q^2. Here, a_k and b_k are fitting parameters. However, since the existing data, at that time, were limited, Kelly implemented for G_E^n the general form of the Galster fit [30], which is defined as

$$G_E^n(Q^2) = \frac{A\tau}{1 + B\tau} G_D(Q^2), \tag{2.30}$$

where A and B are fitted parameters.

The most current parameterization of the world data comes from an article in 2018 by Ye *et al.* [31]. The methodology for the general fit procedure is detailed completely in [32], and the updated version in the article by Ye *et al.* [31]. For completeness, the Ye 2018 fit methodology will be described in this dissertation in some detail. For the proton form factors, the Ye 2018 procedure simultaneously fits G_E^p and G_M^p to the available cross-section and polarization data. For the neutron case, the procedure performs separate fits of G_E^n and G_M^n to the extractions of the individual form factors. For all form factor

considerations, the fit is a bounded polynomial z-expansion,

$$G(Q^2) = \sum_{k=0}^{k_{\max}} a_k z^k, \quad z = \frac{\sqrt{t_{\rm cut} + Q^2} - \sqrt{t_{\rm cut} - t_0}}{\sqrt{t_{\rm cut} + Q^2} + \sqrt{t_{\rm cut} - t_0}}, \tag{2.31}$$

where G stands for the proton and neutron form factors G_E^p, G_E^n, G_M^p/μ_p, G_M^n/μ_n, $t_{\rm cut} = 4m_\pi^2$, and a_k are fitting parameters. The Ye 2018 fit chooses a fixed value of $t_0 = -0.7$ $(\mathrm{GeV/c})^2$ for all four nucleon form factors so that there is a single definition of z in all cases. This choice in the value of $t_0 = -0.7$ $(\mathrm{GeV/c})^2$ is a compromise between the wide Q^2 range for the proton cross-section data ($Q^2 \sim 0 - 30$ $(\mathrm{GeV/c})^2$) and the limited Q^2 range for G_E^n form factor data ($Q^2 \sim 0 - 3.5$ $(\mathrm{GeV/c})^2$). The Ye 2018 fit applied sum-rule constraints on each nucleon form factor to ensure appropriate behavior in the limits of small and large Q^2. One sum-rule is applied to enforce the correct normalization at $Q^2 = 0$ $(\mathrm{GeV/c})^2$. The four additional sum-rules ensure the asymptotic scaling $G \sim Q^{-4}$ at large Q^2. With these five sum-rules enforced, the number of free parameters is $k_{\max} - 4$. The fit coefficients a_k are bounded in size and in a manner such that they must decrease at large k. By ensuring bounds on the coefficients, the Ye 2018 fit could add an arbitrary number of fit parameters. Specifically, what the bounds on the coefficients ensure is that while varying $k_{\max}$ in 2.31 the fit uncertainties do not grow out of control. In the Ye 2018 parameterization the protons fit are obtained with $k_{\max} = 12$ and the neutron fits have $k_{\max} = 10$. This ensures that the fit is not strongly influenced by the $k_{\max}$ truncation, and still retains a manageable number of independent fit parameters.

The analysis and Monte Carlo simulation, in Chapter 6, of this dissertation will reference the dipole form factor, the Galster parameterization, the Kelly fit, and the Ye parameterization.

2.5.2 Proton Data Description

The data presented in Figs. 2.6a and 2.6b encapsulate most of the existing data for the proton electric and magnetic form factors G_E^p and G_M^p/μ_p, respectively, normalized to G_D

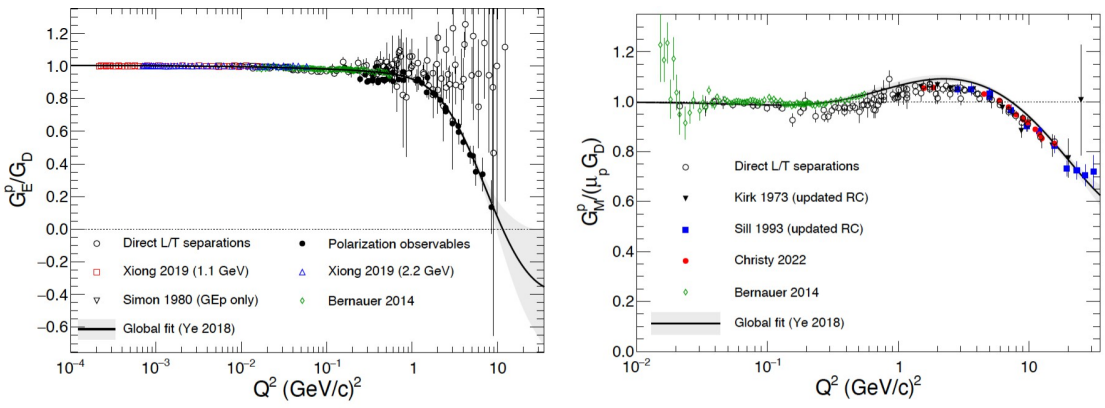

(a) (b)

Figure 2.6: The plots and descriptions within this figure are reproduced from the current literature [28], at the time of writing this dissertation, and are the status of the proton electromagnetic form factors. Left: A collection of World data for G_E^p/G_D "Direct L/T separations" are published point extractions of G_E^p from Rosenbluth plots. The points labeled "Bernauer 2014" are the direct Rosenbluth extractions from the Mainz A1 dataset [33, 34]. The data labeled "Xiong 2019" are from the PRad Experiment [35]. The global fit to the data is from [31]. Right: A collection of World data for $G_M^p/(\mu_p G_D)$. The "Direct L/T separations" are published point extractions from Rosenbluth plots. The Kirk 1973 data [36] and the Sill 1993 data [37] are point G_M^p extractions from single cross-section measurements, with updated radiative corrections as described in Ref. [38]. The data points labeled "Bernauer 2014" are the direct Rosenbluth extractions from the Mainz A1 dataset [33, 34]. The global fit to the data is from [31]. See text for complete sources of data.

over the measured Q^2 range. Though the data presented are not all-encompassing, the data shown are sufficiently representative of the Q^2 coverage and the precision of the entire world data. The data points shown as empty circles in Figs. 2.6a and 2.6b are published point extractions of G_E^p and G_M^p based on direct L/T separations from Rosenbluth plots, and are taken from Refs. [38–46]. The data based on direct L/T separations are not entirely independent of each other in terms of cross-section input, as several of the analyses combined data from multiple experiments at similar Q^2 values.

The data points shown as filled circles in Fig. 2.6a are based on direct measurements of the ratio G_E^p/G_M^p using polarization observables, converted to G_E^p/G_D values using the global fit to G_M^p from Ref. [31]. The polarization data for G_E^p include measurements based

on the polarization transfer technique described in Sec. 2.3.1, specifically using Eq. 2.13, and are taken from Refs. [47–60]. The polarization data for G_E^p also include measurements based the beam-target double-spin asymmetry method described in Sec. 2.3.2, particularly using Eqs. 2.20 and 2.21, and are taken from Refs. [61–63].

The points labeled "Bernauer 2014" in Figs. 2.6a and 2.6b are direct Rosenbluth separations from the Mainz A1 dataset [33, 34]. The data points at very low Q^2 labeled "Simon 1980" and "Xiong 2019" in Fig. 2.6a are direct extractions of G_E^p from individual cross-section measurements based on the assumption of form factor scaling ($G_M^p = \mu_p G_E^p$) in the case of Ref. [64], or using the Kelly fit to G_M^p ([30]) in the case of Ref. [35]. In Fig. 2.6b, the G_M^p values extracted from the cross-sections published in Refs. [36, 37] are based on the updated analysis in Ref. [38], which at that time used the most current radiative corrections described in Ref. [65]. It must also be noted that the global fits shown in Figs. 2.6a and 2.6b include phenomenological two-photon exchange corrections. These corrections have not been applied to the published form factor extractions. Therefore it is expected that a small, of the order 2-3% for G_M^p, discrepancy will exist between the extracted form factor values and the global fits.

2.5.3 Neutron Data Description

The neutron electromagnetic form factors are much more difficult to measure accurately than those of the proton, due primarily to the absence of free neutron targets of sufficient density for electron scattering experiments at large Q^2 values. As such, essentially all knowledge of neutron electromagnetic form factors, at meaningfully large Q^2 values, comes from measurements of electron scattering on bound neutrons in light nuclear targets such as deuterium and ^{3}He. The data presented in Figs. 2.7a and 2.7b encompass most of the existing data for G_E^n and G_M^n, respectively, excluding extractions based on elastic *ed* cross-section measurements.

For G_E^n, essentially all reliable data of reasonable precision come from measurements of polarization observables, since the quasi-elastic $(e,e'n)$ cross-section has relatively low

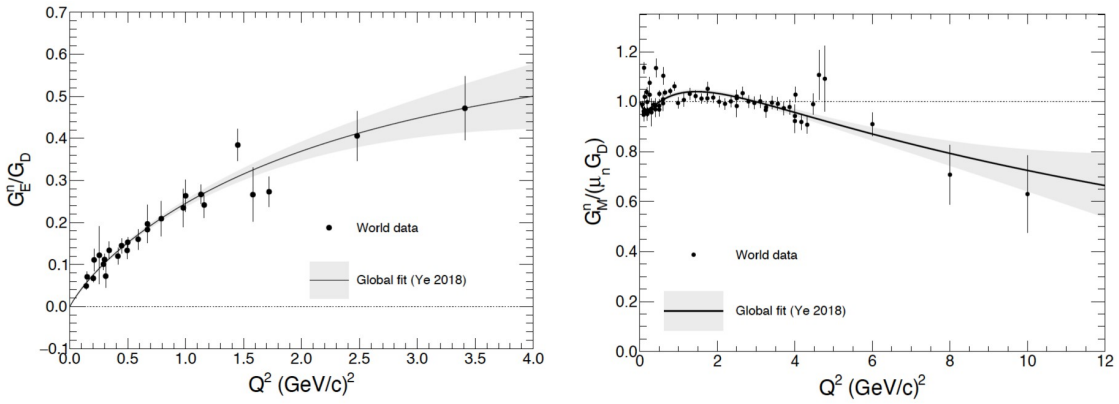

(a) (b)

Figure 2.7: The plots and descriptions within this figure are reproduced from the current literature [28], at the time of writing this dissertation, and are the status of the neutron electromagnetic form factors. Left: World data for the neutron electric form factor G_E^n/G_D. Right: World data for the neutron magnetic form factor G_M^n/G_D. See text for complete sources of data.

sensitivity to G_E^n over the entire Q^2 range. The data shown in Fig. 2.7a include extractions from asymmetry measurements on polarized deuterium targets (from Refs. [66–69]), polarized ^{3}He targets (from Refs. [70–74]), and via recoil neutron polarization on unpolarized deuterium (from Refs. [75–77]). The most reliable known method to determine the neutron magnetic form factor G_M^n is the so-called "ratio" technique [78], in which "neutron-tagged" and "proton-tagged" quasi-elastic electron scattering on a deuterium target are measured simultaneously, and the ratio of cross-sections $^2\mathrm{H}\,(\mathrm{e},\mathrm{e}'\mathrm{n})\,\mathrm{p}/^2\mathrm{H}\,(\mathrm{e},\mathrm{e}'\mathrm{p})\,\mathrm{n}$ is measured. The "ratio" (also known as "Durand") technique will be described in detail, as it pertains to this analysis, in Chapter 3 and the advantages and challenges of this method will be explained as well. Of the data presented in Fig. 2.7b, Refs. [79–83] used the ratio method, Refs. [84–87] extracted G_M^n from the beam-target double-spin asymmetry in inclusive quasi-elastic electron scattering on polarized ^{3}He, and Refs. [88–90] extracted G_M^n from absolute cross-section measurements in either inclusive scattering on deuterium or coincidence $d(e,e'n)p$ scattering.

2.6 Theoretical Models

The spacelike electromagnetic form factors are among the simplest, most clearly interpretable, and best-known measurable dynamical properties of the nucleon. The nucleon form factors constitute important benchmarks for testing theoretical models. Figures 2.8a and 2.8b show the world data for the nucleon's spacelike elastic electromagnetic form factor ratios together with selected theoretical models and expected results from the form factor program in Hall A at Jefferson Lab by the Super BigBite Spectrometer (SBS) collaboration. A description of the SBS physics program will be provided in Chapter 3 and the SBS apparatus as it pertains to this dissertation will be detailed in Chapter 4. The remainder of this Section will focus on describing some of the relevant theoretical ways for modeling the nucleon electromagnetic form factors. Specifically the following theoretical models will be considered: Perturbative QCD (pQCD), Relativistic Constituent Quark Models (RCQM), Dyson-Schwinger Equations (DSE), and Generalized Parton Distributions (GPDs).

2.6.1 Perturbative QCD

An important property of Quantum Chromodynamics (QCD), known as asymptotic freedom, is the steady reduction in the strength of interactions between quarks and gluons as the energy scale of those interactions increases. For sufficiently large Q^2 ($Q^2 \gtrsim 1$ (GeV/c)^2) it is theoretically expected that the coupling constant of the strong force, α_s, becomes small enough that perturbation theory (pQCD) is expected to become applicable. However, the kinematic regime in which the transition occurs from hadronic degrees of freedom to quark degrees of freedom is still a topic of current research. The present available world data do not suggest a Q^2-dependent behavior for most observables consistent with such a transition region [97].

Alternatively, in the kinematic regime in which pQCD is applicable, pQCD should predict the scaling behavior of the nucleon form factors. If one considers pQCD based on constituent counting rules, helicity conservation, and three-quark valence structure, then

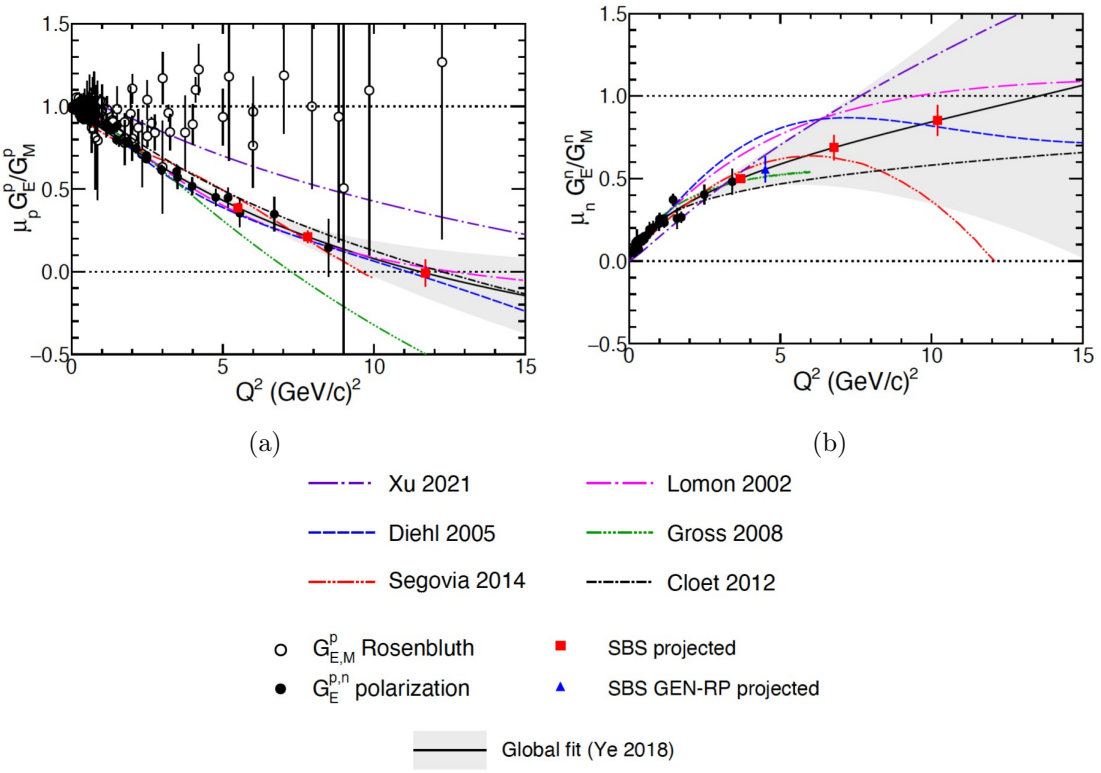

Figure 2.8: The plots and descriptions within this figure are adapted from the current literature [28], and are the status of the nucleon electromagnetic form factor ratios. The nucleon electromagnetic form factor ratio data is presented, along with selected theoretical models, the global fit from [31], and the projected results, with only statistical errors, from the ongoing SBS program at Jefferson Lab which are plotted arbitrarily at values of the global fit for the corresponding known value of Q^2. Theoretical curves presented are the BLFQ calculations of Ref. [91] (Xu 2021), the VMD-based model of Ref. [92] (Lomon 2002), the GPD-based model of Ref. [93] (Diehl 2005), the covariant spectator model of Ref. [94] (Gross 2008), the DSE-based calculation of Ref. [95] (Segovia 2014), and the quark-diquark model of Ref. [96] (Cloet 2012). Data references are the same as those given in the text and described in the captions of Figs. 2.6a, 2.6b, 2.7a, and 2.7b.

it is expected that for the nucleon form factors $F_1 \propto Q^{-4}$ and $F_2 \propto Q^{-6}$ [28]. Expressed differently, it is expected that the nucleon form factor ratio should scale as $F_2/F_1 \propto Q^{-2}$, at sufficiently large values of Q^2. However, experimental results as shown in Fig. 2.9a, are in clear disagreement with this suggested pQCD scaling of the nucleon form factors.

A more recent pQCD analysis from Ref. [98] considers both leading- and subleading-

twist light-cone wave functions of the nucleon, which include quark orbital angular momentum. This modified pQCD analysis predicts the following nucleon form factor scaling

$$\frac{F_2(Q^2)}{F_1(Q^2)} \propto \frac{\log^2(\frac{Q^2}{\Lambda^2})}{Q^2}, \tag{2.32}$$

where $\Lambda \approx 300$ MeV. This particular nucleon form factor scaling can be related to the electromagnetic form factors using Eqs. 2.1 and 2.2

$$\frac{G_E}{G_M} = \frac{Q^2 - \kappa\tau\alpha\log^2(Q^2/\Lambda^2)}{Q^2 + \kappa\tau\alpha\log^2(Q^2/\Lambda^2)}, \tag{2.33}$$

where α is a constant. It should be noted that the pQCD scaling presented in Eq. 2.32 is in reasonable agreement with the proton data analysis of $Q^2F_2^p/F_1^p$ as presented in Fig. 2.9a. However, in a similar analysis of the quark flavor decomposition for the neutron, the quantity $Q^2F_2^n/F_1^n$, as shown in Fig. 2.9a, does not follow the logarithmic scaling in Eq. 2.32, when considering similar values of Λ^2 as the proton. Since the data for the neutron electric form factor are the most limited of all the nucleon form factors, it is possible that the Q^2 value of 3.4 (GeV/c)^2 was not sufficiently large to demonstrate pQCD effects. It is anticipated that results which expand the Q^2 range of the nucleon electromagnetic form factors will allow better evaluations of pQCD models.

2.6.2 Relativistic Constituent Quark Model

QCD is now the accepted theory of the strong interaction, within the Standard Model. There exist models which predate QCD, which also describe the strong interaction, one type is the constituent quark models (CQMs). To explain dynamical properties of hadrons in terms of constituent quarks, a model for the confining quark-quark interaction and the resulting quark wavefunction is required. The "bare" up and down valence quark constituents of nucleons appearing in the QCD Lagrangian are almost massless, compared to the nucleon mass. For CQM, the nucleon is considered as the ground state of a bound

system of three light quarks and is characterized by a large ratio of binding energy to constituent mass. A fully relativistic treatment is mandatory to obtain realistic phenomenology and accurate descriptions consistent with data. A common feature of CQM calculations describing the nucleon structure is the "dressing" of the bare, almost massless valence quarks by gluons and quark-antiquark pairs. The "dressing" process leads to massive constituent quarks and/or diquarks as effective degrees of freedom, which have their own internal structure. Recent full reviews of relativistic constituent quark model (RCQM) calculations of the nucleon form factors are available in Refs. [18, 28].

One recent RCQM of importance is presented by Cloët and Miller [96]. The goal of the RCQM proposed by Cloët and Miller is to model the nucleon as consisting of three valence quarks and a pion cloud, constrained by Poincaré invariance. The basic concept of this RCQM is that the valence quarks are represented by quark-diquark combinations with the degrees of freedom of the nucleon. These valence quarks are then immersed in a cloud of pions. A complete description of the theoretical model, including the light-front wavefunction, a description of the model parameterization, and physical observable calculations is provided in [96]. The most recent theoretical prediction from the Cloët and Miller RCQM are presented in Figs. 2.8a and 2.8b with the label "Cloet 2012."

2.6.3 Dyson-Schwinger Equations

A recent review of Dyson-Schwinger Equations (DSEs) as a treatment of the strong interaction, and thereby an approximation of QCD, is provided in Ref. [28]. To summarize the fundamental method, the DSEs form an infinite set of coupled integral equations for the Green's function of a quantum field theory. The DSEs are exact, but for practical calculations the infinite set has to be truncated, often by a symmetry-preserving truncation. Formally, the equations can be derived from the matrix elements of the Lagrangian density, or in the path-integral formalism using functional derivatives. Alternatively, the DSEs can be described using Feynman diagram representations.

A recent set of theoretical predictions for continuum non-perturbative QCD, within

the framework of DSEs, is presented in Ref. [95]. The goal of Ref. [95] is to characterize the behavior of the running coupling and masses in the strong interaction sector of the Standard Model. To summarize the theoretical framework of this article, a confining symmetry-preserving treatment of vector contact interactions in a leading-order (rainbow-ladder) truncation of QCD's DSEs is employed. Particularly, this theoretical framework implements a Poincaré covariant Faddeev equation that sums all possible quantum field theoretical exchanges and interactions that can take place between three dressed-quarks. From this specific Faddeev equation one obtains the baryon's Faddeev amplitude, since in quantum field theory a baryon appears as a pole in a six-point quark Green function. Ultimately the primary result of Ref. [95] is a characterization of nucleon and $\Delta(1232)$-baryon elastic and transition form factors. The theoretical predictions for the nucleon elastic form factors are presented in in Figs. 2.8a and 2.8b with the label "Segovia 2014." An interesting behavior of the DSE-based approach from this article is the theoretical prediction that the proton and neutron electromagnetic form factor ratios have zero-crossings at approximately 10 and 12 $(\mathrm{GeV/c})^2$, respectively.

A more recent preprint [99] provides a similar DSE-based theoretical model that considers predictions for the nucleon elastic electromagnetic form factors and a flavor separation of the quark form factor contributions. A more detailed explanation of the flavor separation of quark contributions from nucleon form factors is presented in Sec. 2.7. Particularly, the preprint expands on the Q^2-range of previous theoretical predictions with the similar DSE-based method. The preprint uses a similar approach to that already described for Ref. [95], which considers a symmetry-preserving leading-order (rainbow-ladder) truncation all DSEs. The primary difference is that for the preprint's methodology a statistical Schelessinger point method (or multi-point Padé approximation scheme) is also implemented. The theoretical predictions for the nucleon electromagnetic form factor ratios $\mu_p G_E^p/G_M^p$ and $\mu_n G_E^n/G_M^n$, and the flavor separated quark contributions $F_1^{d,u}$ and $F_2^{d,u}$ are available in the figures of the preprint.

2.6.4 Generalized Parton Distributions

Generalized parton distributions (GPDs) represent an amplitude for removing a quark from the nucleon and replacing it with a quark of different momentum, possibly with different spin projection and flavor. GPDs are used to characterize the assembly of 3-dimensional tomographic images of the quark (and gluon). Therefore, GPDs provide insight to hadron structure in both perturbative and non-perturbative regimes. A recent review of GPDs in the context of nucleon elastic electromagnetic form factors is presented in Ref. [18]. GPDs can be extracted from Deeply Virtual Compton Scattering (DVCS) processes, where the in the interaction the perturbative and non-perturbative contributions can be factorized and considered separately.

From DVCS processes, the vector $H^q(x,\xi,Q^2)$ and the tensor $E^q(x,\xi,Q^2)$ GPDs can be extracted. Here x is the light-front momentum fraction and ξ is the skewness, which is the asymmetry between the quark momenta. It is known that GPDs are related to the quark form factors by the following expressions

$$F_1^q(Q^2) = \int_{-1}^{1} dx H^q(x,\xi,Q^2), \tag{2.34}$$

$$F_2^q(Q^2) = \int_{-1}^{1} dx E^q(x,\xi,Q^2), \tag{2.35}$$

where q is the quark flavor. With these relations between quark flavor form factors and GPDs, one is able to construct nucleon form factors in terms of quark form factors as follows

$$F_i^p = \frac{2}{3}F_i^u - \frac{1}{3}F_i^d - \frac{1}{3}F_i^s, \tag{2.36}$$

$$F_i^n = -\frac{1}{3}F_i^u + \frac{2}{3}F_i^d - \frac{1}{3}F_i^s, \tag{2.37}$$

where $i = 1, 2$ and $F_1^{u,d}$ are specifically for the proton.

With complete measurements or sufficient theoretical models of GPDs one is able to use these GPD and form factor relations to obtain nucleon electromagnetic form factors. However, current available GPD world data is very limited. So it is more useful to use the

available form factor world data to constrain GPD models and theoretical predictions, until GPD world data is updated in the necessary kinematic regions. A recent GPD model, which was informed by the available experimental data, that presents theoretical predictions for the nucleon electromagnetic form factors is from Ref. [93]. The theoretical prediction from the Diehl *et. al.* GPD model is in Figs. 2.8a and 2.8b with the label "Diehl 2005." A more recent article [100] was published, primarily including updated experimental data, which implements a similar GPD model and determines the quark flavor form factor. However, Ref [100] does not include a theoretical prediction for the nucleon elastic electromagnetic form factors.

2.7 Quark Flavor Decomposition

The theoretical formalism for the nucleon elastic electromagnetic form factors was summarized in Sec. 2.1, while the current empirical knowledge of these form factors was presented in Sec. 2.5. One motivation for studying the nucleon elastic electromagnetic form factors is the fact that, for large enough values of Q^2, the nucleon form factors can be used to extract information about quark behavior. By investigating quark behavior inside the nucleon we get a better understanding of the strong interaction and QCD as a whole, more importantly in the non-perturbative regime. Furthermore, experimental results in expanded kinematic regimes provides constraints on theoretical descriptions of nucleon structure.

A full quark flavor decomposition requires all elastic electric and magnetic form factors of the proton and neutron to be known at each value of Q^2. The neutron electric form factor, G_E^n, is the most data-limited and historically has been the most difficult to measure. By combining the available proton and neutron electromagnetic form factors, a quark flavor separation was completed to extract the elastic form factors for the up and down quarks up to $Q^2 = 3.4$ GeV^2. The most current description of the quark flavor decomposition is presented in Refs. [101, 102]; here we will summarize the method, results, and conclusions.

In the one-photon exchange approximation, it is known the amplitude for electron-

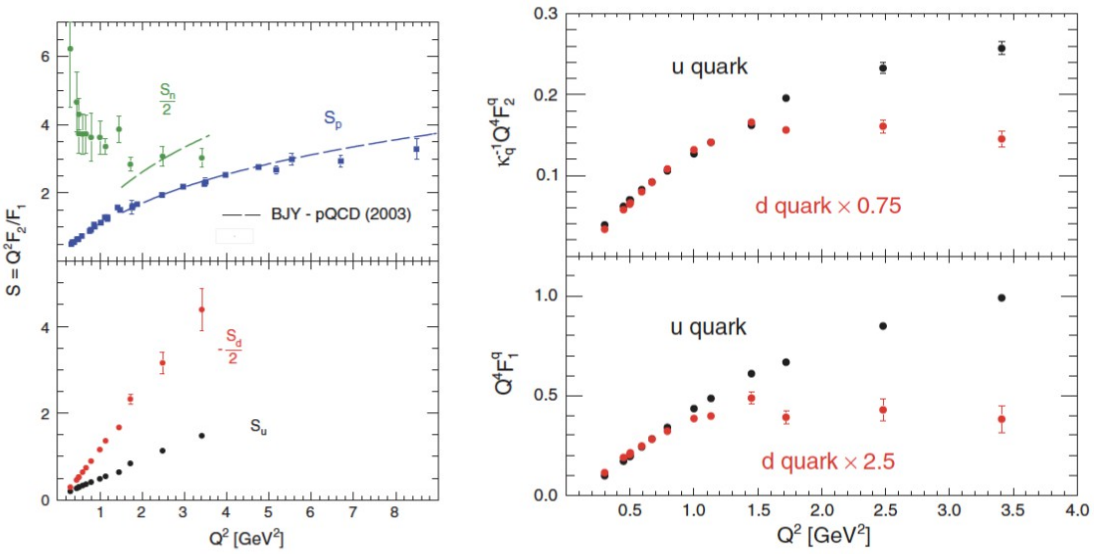

(a) (b)

Figure 2.9: Reproduced from [101]. Left: The ratio of the Pauli and Dirac form factors, multiplied by Q^2, $S_{p(n)} = Q^2F_2^{p(n)}/F_1^{p(n)}$ vs. the negative four momentum transfer squared, Q^2. The upper panel shows S_p for the proton and S_n for the neutron using the data available. In the upper panel the proton data points are overlaid with a pQCD scaling prediction. The bottom panel shows the individual flavor quantities S_u and S_d for the up and down quarks, respectively. Right: The extracted up (u) and down (d) quark contributions to the proton form factors (multiplied by Q^4), as dependent on Q^2. The 0.75 and 2.5 present in the top and bottom panels are the scale factors between up and down quark contributions. These scaling factors are only applicable up to a Q^2-value of approximately 1 GeV^2.

nucleon elastic scattering is proportional to $J_\mu^{\rm EM}$, where

$$J_\mu^{\rm EM} = \langle p(n)| \left(\frac{2}{3}\bar{u}\gamma_\mu u + \frac{-1}{3}\bar{d}\gamma_\mu d \right) |p(n)\rangle \tag{2.38}$$

is the hadronic matrix element of the electromagnetic current operators for the proton (neutron). In this hadronic matrix element the contributions from heavier quarks are not considered; it is possible that there are nonzero matrix element contributions due to strange quarks. The matrix elements: $\bar{u}\gamma_\mu u$ and $\bar{d}\gamma_\mu d$ cannot be described explicitly. Rather, from symmetry considerations, we know the hadronic matrix element in Eq. 2.38,

for the consideration of the proton, must have the form

$$J_\mu^{\rm EM} = \bar{p}(k')\left[\gamma^\mu F_1^p(Q^2) + \frac{i\sigma^{\mu\nu}q_\nu}{2M}F_2^p(Q^2)\right]p(k), \tag{2.39}$$

where $p(k)$ and $\bar{p}(k')$ are proton Dirac spinor for the initial and final momenta, respectively. A relation for the hadronic current involving the neutron form factors $F_1^n(Q^2)$ and $F_2^n(Q^2)$ has a similar form.

If we assume charge symmetry, thus implying $\langle p|\,\bar{u}\gamma_\mu u\,|p\rangle = \langle n|\,\bar{d}\gamma_\mu d\,|n\rangle$, and by comparing the hadronic matrix element of the electromagnetic operators for the proton and neutron, those present in Eqs. 2.38 and 2.39, we can arrive at the following relations

$$F_{1(2)}^p = \frac{2}{3}F_{1(2)}^u - \frac{1}{3}F_{1(2)}^d \quad \text{and} \quad F_{1(2)}^n = \frac{-1}{3}F_{1(2)}^u + \frac{2}{3}F_{1(2)}^d. \tag{2.40}$$

From Eq. 2.40 it is possible to perform a flavor decomposition of the proton (neutron) form factors $F_1^{p(n)}$ and $F_2^{p(n)}$, and construct form factors corresponding to the individual matrix elements of the separate up and down quarks. This separation is represented by the relations

$$F_{1(2)}^u = 2F_{1(2)}^p + F_{1(2)}^n \quad \text{and} \quad F_{1(2)}^d = 2F_{1(2)}^n + F_{1(2)}^p, \tag{2.41}$$

where $F_{1(2)}^u$ and $F_{1(2)}^d$ refer to the up and down quark contributions to the Dirac and Pauli form factors of the proton, respectively. Measured quantities of interest are $S_{p(n)} = Q^2F_2^{p(n)}/F_1^{p(n)}$; for the proton it is expected that S_p is constant at sufficiently high Q^2. Having introduced the flavor-separated Dirac and Pauli form factors, one can also define the quantities

$$S_u \equiv Q^2F_2^u/F_1^u \quad \text{and} \quad S_d \equiv Q^2F_2^d/F_1^d. \tag{2.42}$$

If we first consider the upper panel of Fig. 2.9a, both S_p and S_n are presented for the available data. For the proton case, S_p shows consistent behavior with the overlaid pQCD theoretical prediction, however, there is no clear evidence of a plateau at high Q^2. In the same plot, for S_n there is no clear scaling behavior at all. In the bottom panel of Fig. 2.9a,

both S_u and S_d are extracted and plotted for the available data. From the lower panel of Fig. 2.9a it is clear that both S_u and S_d exhibit a linear behavior in Q^2, and that there is no clear behavior consistent with saturation. In Fig. 2.9b the individual up and down quark contributions to the form factors of the proton: F_1^u, F_2^u, F_1^d, and F_2^d are plotted, with each multiplied by Q^4. For the down quark, above 1 GeV^2, F_1^d, and F_2^d appear to scale as $1/Q^4$, whereas for the up quark, F_1^u and F_2^u scale similar to $1/Q^2$, suggesting that the down quark contributions to the proton Dirac and Pauli form factors are suppressed at large Q^2.

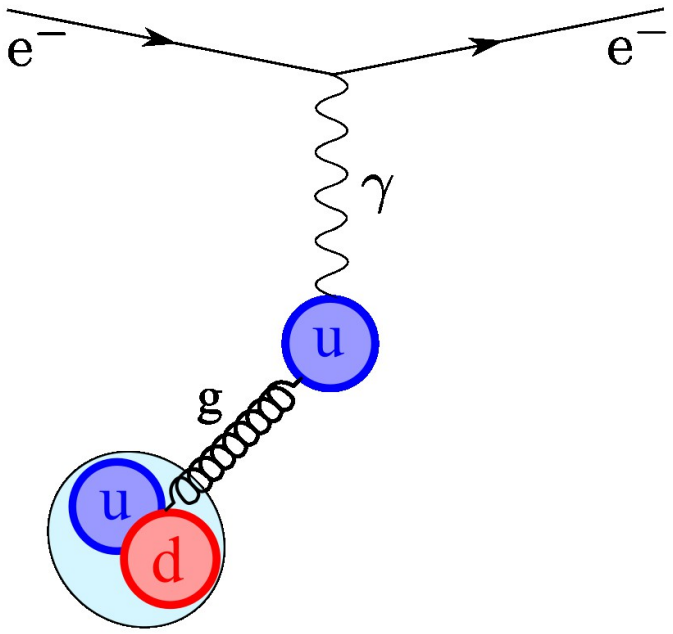

Figure 2.10: A simple diagram representing diquark correlations in the proton. In this particular case the down quark must be part of the diquark here.

A potential explanation for the difference in scaling between the quark contributions could be the importance of diquark degrees of freedom [103]. To motivate the diquark correlations as a possible explanation for the difference in scaling in the quark contributions to the proton form factors, consider the diagram in Fig. 2.10. In the consideration of Fig. 2.10, the nucleon would be dominated by a diquark containing a up and down quark, and a

single up quark. If elastic scattering off an up quark was dominated by the single up quark, the nucleon would seem like a composite of two constituents via 1 gluon contribution. Hence one would expect F_1^u would scale like $1/Q^2$. If instead one considers scattering off a down quark, this would necessarily involve the diquark and for the diquark to be held together during elastic scattering would require the interaction of a second gluon. Therefore the form factor F_1^d would be expected to similar to $1/Q^4$. Any experiments which expand the higher Q^2 reach of the nucleon elastic electromagnetic form factors will allow the further extraction of the quark contributions to those form factors and should provide a better understanding of the internal structure of the proton and neutron.

Chapter 3

SBS Experimental Program

In the previous chapter we introduced the Sachs treatment of the nucleon electromagnetic form factors, described various experimental methods for extracting those form factors, reviewed the state of form factor world data, and briefly summarized some theoretical models for nucleon electromagnetic form factors. In this chapter we will describe the Super BigBite Spectrometer (SBS) program in Hall A at Jefferson Lab. The primary goal of the SBS physics program is to provide precision measurements of all the nucleon electromagnetic form factors, in high Q^2 kinematic regimes. The second section will focus on an overview of the SBS G_M^n and neutron Two-Photon Exchange (nTPE) experiments (the topic of this thesis), and includes a detailed description of the method for extracting physics observables from measured experimental quantities.

3.1 The Super BigBite Spectrometer Physics Program

A core element of Jefferson Lab's research program is the study of the nucleon elastic electromagnetic form factors by precision measurements. Particularly, the elastic electromagnetic form factors are among the most interpretable observables describing the dynamic properties of the nucleon and are simultaneously able to be predicted from available theoretical models. A milestone, completed in 2015, for Jefferson Lab was the beam energy upgrade for the accelerator, CEBAF, which was increased from 6 GeV to 12 GeV. A

description of the accelerator facility in its current configuration, after the beam energy upgrade, is presented in Sec. 4.1. The combination of CEBAF's increase in beam energy and advances in detector technologies presents an opportunity for the nucleon electromagnetic form factors to be measured precisely at higher Q^2. The SBS nucleon electromagnetic form factor program at Jefferson Lab extends the Q^2 range of G_M^n, G_E^n, and G_E^p/G_M^p by precision measurements using multiple extraction methods. The experiments in the SBS nucleon electromagnetic form factor program will be referred to as SBS G_M^n [104], neutron Two-Photon Exchange (nTPE) [105], G_E^n-II [24], G_E^n-RP [106], and G_E^p-V [107]. All of these SBS experiments, at the time of this dissertation, have recently or in the near future will have completed data collection. There also remains a future program, besides the investigation of nucleon form factors, that could continue to use the SBS apparatus. The current proposed experiments in the SBS physics program, which could potentially be conducted in Hall C, include SBS Semi-Inclusive Deep Inelastic Scattering (SIDIS) [108], Tagged Deep Inelastic Scattering (TDIS) [109], proton strange form factor [110], and proton axial vector form factor [111].

The primary commonality between all the experiments in the SBS physics program is the shared spectrometer apparatus, albeit with some modifications or equipment reorganizations. This dissertation will focus on the measurements and analyses for the SBS G_M^n and nTPE experiments, and the state of the apparatus during that experimental run period is detailed in Chapter 4. Here we will compare and contrast the five experiments in the nucleon electromagnetic form factor program conducted in Hall A. All experiments collide an electron beam incident on a fixed target and investigate either elastic or quasi-elastic scattering. The SBS G_E^n-II, G_E^n-RP, and G_E^p-V experiments make use of the polarized electron beam from CEBAF. The SBS G_M^n and nTPE experiments have no requirements for beam polarization and therefore did not analyze polarization states of the electron beam. All measurements have an electron spectrometer and a hadron spectrometer. A conceptual diagram of a two spectrometer apparatus is shown in Fig. 3.1. For the SBS experiments G_M^n, nTPE, G_E^n-II, and G_E^n-RP, the scattered electrons are detected by the

BigBite Spectrometer and the scattered nucleons are detected by the Super BigBite Spectrometer. Descriptions of the BigBite Spectrometer and Super BigBite Spectrometer, as instrumented during the SBS G_M^n and nTPE experiments, are presented in Sec. 4.2.3 and Sec. 4.2.4, respectively. In the case of G_E^p-V the scattered nucleons are still detected by the Super BigBite Spectrometer, however, the electron spectrometer is replaced with only a particle tracking detector called the Coordinate Detector and a large acceptance Electron Calorimeter (ECal). A necessary caveat is that while all the experiments use the Super BigBite Spectrometer for detecting hadrons, some experiments require different configurations of the tracking detectors, known as Gas Electron Multipliers (GEMs), to be instrumented. A more detailed characterization of GEM detector fundamentals and the GEMs for the SBS program will be the focus of Chapter 5. The spectrometers for the SBS program were newly installed in Hall A before the SBS G_M^n and nTPE run period, therefore significant effort went into installing, commissioning, and calibrating the detector systems for the first time. This section will describe, in some detail, each of the 5 experiments in the SBS nucleon form factor program. A broader and more detailed overview of the SBS G_M^n and nTPE experiments will be presented in Sec. 3.2.

3.1.1 G_M^n and nTPE Experiments

The SBS G_M^n [104] and nTPE [105] are often considered together because the data for both experiments were collected during the same experimental run period, from October 2021 to February 2022. The G_M^n and nTPE experiments were the first experiments in the SBS program and were the first experiments to use both the newly installed BigBite Spectrometer and Super BigBite Spectrometer. The target used for production data collection was liquid deuterium and the instantaneous luminosity during running was approximately 10^{38} cm^{-2}/s. A milestone for this experimental run period, and the SBS program as a whole, was successfully operating and calibrating the entire apparatus. A critical instrumentation component of the SBS program are GEM tracking detectors. Large acceptance GEM tracking detectors have not been operated at Jefferson Lab in such high particle rate envi-

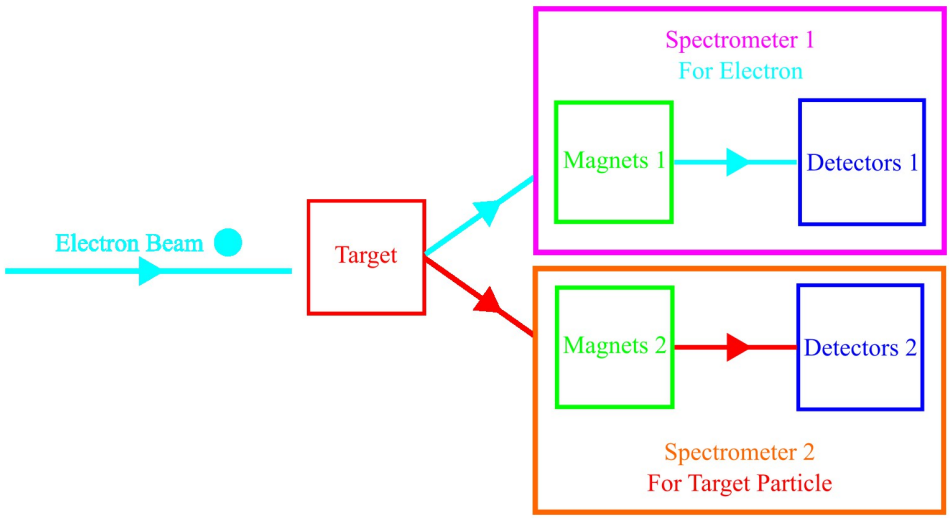

Figure 3.1: A conceptual diagram representing a two spectrometer apparatus. One spectrometer, represented in magenta, detects electrons. The second spectrometer, represented in orange, detects relevant scattered particles from the fixed target.

ronments, until the SBS program. A crucial element of the G_M^n and nTPE run period was simultaneously modifying and optimizing the GEM hardware and software for stable data collection, but moreover developing the GEM detectors for successful deployment in future higher luminosity experiments. To successfully install, operate, and collect data during the G_M^n and nTPE experimental run period, many challenges were overcome. These challenges included a reduced workforce and limited installation/commissioning schedule due to the COVID-19 pandemic, an inoperable Hall A overhead crane, a physical collision between the BigBite and Super BigBite magnets, multiple GEM detector replacements, and various failures with target components involving: vacuum, heaters, and target motion.

3.1.2 G_E^n-II Experiment

The goal of the SBS G_E^n-II [24] experiment is a measurement of the neutron electromagnetic form factor ratio, G_E^n/G_M^n, at three values of Q^2 = 5.0, 6.8, and 10.2 (GeV/c)^2. A measurement of the transverse asymmetry, $A_\perp$, of the cross-section in double polarized semi-inclusive $^3\overrightarrow{\text{He}}\,(\vec{e}, e'n)\,pp$ in quasi-elastic kinematics directly extracts the ratio G_E^n/G_M^n.

Furthermore, if precise high Q^2 data is available for G_M^n then it is straightforward to extract solely G_E^n.

G_E^n-II was the third experiment in the SBS program and the data were collected during two run periods: October 2022 to March 2023 and an extension during September to October 2023. The G_E^n-II experiment operated with a modified version of the G_M^n and nTPE apparatus; the main changes involved the target and the GEM trackers installed in the hadron spectrometer. The G_E^n-II experiment required polarized ^{3}He glass cell targets, with a target chamber of 60 cm in length. As a result of both known and still under investigation failure modes of the polarized ^{3}He glass cell targets, 6 targets were sequentially installed throughout both run periods of G_E^n-II. Throughout the entire data collection for the G_E^n-II experiment, target polarizations were typically in the range of 40-55%. As a commissioning phase for future experiments in the SBS program 8 GEM tracking detectors were installed as part of a new hadron spectrometer, prior to the start of the G_E^n-II experiment. It is imperative to note these GEM tracking detectors are not necessary for the analysis and physics extraction of the G_E^n-II experiment, rather they were intended to optimize hardware performance and software for future experiments in the SBS program, and also to implement for G_E^n-II analysis if beneficial. The detector particle occupancies found in the G_E^n-II data set were approximately 20% those observed during the G_M^n and nTPE data set. Therefore, the track search algorithm implemented for the GEM detectors had significantly fewer combinatorics and was more manageable.

3.1.3 G_E^n-RP Experiment

The purpose of the SBS G_E^n-RP [106] experiment is a measurement of the ratio of transverse and longitudinal components of the neutron spin polarization, P_t/P_l, in double polarized $^2\mathrm{H}(\vec{e}, e'\vec{n})p$ at a four momentum transfer $Q^2 = 4.5$ (GeV/c)^2. The ratio P_t/P_l will be measured by detecting the recoiling neutron from an incident longitudinally polarized electron. The ratio of the neutron electromagnetic form factors, G_E^n/G_M^n, will be extracted from the ratio of transverse and longitudinal components of the spin polarization.

G_E^n-RP was the fourth experiment in the SBS program and data were collected during the experimental run period from April to May 2024. The G_E^n-RP experiment operated with a modified version of the G_E^n-II apparatus. Instead of the ^{3}He target used in G_E^n-II, the G_E^n-RP experiment reinstalled a standard Hall A cryogenic target system, primarily to use liquid deuterium and liquid hydrogen. A key apparatus component for the G_E^n-RP experiment is a neutron polarimeter. To analyze the neutron polarization, for this experiment, the recoiling nucleon was detected for both $np \rightarrow pn$ (charge-exchange) and $np \rightarrow np$ scattering. The recoil polarimeter, in this case, consisted of 10 GEM tracker layers, a scintillator array, a copper analyzer, and the hadron calorimeter. Eight of the GEM trackers were instrumented such that they were inline with the trajectory of the scattered nucleons. Two of the GEM trackers and the scintillator array were located perpendicular to the focal plane of the scattered nucleons. A copper analyzer was inserted in the middle of the inline GEM layers in order to serve as the source of secondary recoiling nucleons. The copper analyzer enabled sufficient neutron polarimetry by reconstructing the neutron interaction position by tracking the protons produced after charge-exchange neutron-proton scattering.

3.1.4 G_E^p-V Experiment

The SBS G_E^p-V experiment [107] will measure the ratio of proton elastic electromagnetic form factors, G_E^p/G_M^p, to $Q^2 = 15$ (GeV/c)^2 using the recoil polarization technique. The G_E^p-V experiment will be the fifth experiment in the SBS program and is expected take its data during 2025. G_E^p-V will not use the BigBite Spectrometer for detecting scattered electrons. Rather, it will instrument a particle tracking detector called the Coordinate Detector and a large acceptance Electron Calorimeter (ECal), which together will constitute the electron spectrometer. The G_E^p-V experiment will use a 30 cm long liquid hydrogen target for production data collection. The Super BigBite Spectrometer will still have the Super BigBite magnet and HCal instrumented, but will also install 16 GEM tracking detector layers. Eight GEM layers will be installed in a front tracker, upstream of the CH_2

high density polyethylene analyzer. The remaining 8 GEM layers will be arranged in a rear tracker, downstream of the CH_2 high density polyethylene analyzer. G_E^p-V is notable because the expected luminosities are significantly higher than those for the G_M^n, nTPE, G_E^n-II, and G_E^n-RP experiments. The GEM tracking detector high luminosity studies completed during G_M^n, nTPE, G_E^n-II, and G_E^n-RP, along with the continued development of the GEM detector hardware and software, were ultimately essential for validating that the GEM detector system as a whole will be able to operate in the extreme particle rate environments of the G_E^p-V experiment.

3.2 G_M^n and nTPE Experimental Overview

The SBS G_M^n and nTPE experiments collected data in Hall A from October 2021 to February 2022, and the Jefferson Lab designations for these experiments are E12-09-019 and E12-20-010, respectively. G_M^n and nTPE collected data during the same experimental run period so the exact same apparatus was used for both experiments and is described in detail in Chapter 4. The experiments were performed by colliding an unpolarized electron beam with a fixed liquid deuterium target to simultaneously measure the neutron-tagged, D(e,e'n), and proton-tagged, D(e,e'p) quasi-elastic electron scattering from deuterium. The BigBite Spectrometer was used to detect scattered electrons, thereby measuring the momentum and angle of the scattered electrons. The Super BigBite Spectrometer was used to detect scattered nucleons, by measuring the particle's energy and position. A summary of the kinematic information for the G_M^n and nTPE experimental run period will be provided in Sec. 3.2.1. Descriptions of the experimental technique for the G_M^n and nTPE experiments will be presented in Sec. 3.2.2 and Sec. 3.2.3, respectively. A full extraction of physics observables from experimental analysis quantities for both G_M^n and nTPE will be presented in Chapter 7.

3.2.1 G_M^n and nTPE Kinematic Measurements

The completed experimental run plan for the G_M^n and nTPE period had a total of seven kinematic configurations known as SBS-1, SBS-4, SBS-7, SBS-8, SBS-9, SBS-11, and SBS-14. The naming convention implemented for the G_M^n and nTPE kinematics does not follow a standard, rather those listed here were initially in a draft run-plan that had more possible kinematic configurations. Hence, the kinematics presented in this dissertation do not follow a chronological or numerical ordering, nor is there a single kinematic parameter which uniquely distinguishes the different configurations. It is important to note that the kinematic SBS-1 was included strictly for experimental apparatus commissioning and will not be used to extract a physics result. The primary difference between each of these production kinematics is the Q^2 value, which had the range of $3.0 \leq Q^2 \leq 13.5$ $(\mathrm{GeV/c})^2$. The relevant kinematic information, for each configuration of the completed experimental run plan, is presented in Table 3.1. It should also be noted that though both experiments used the same apparatus, the BigBite and Super BigBite Spectrometers were physically reconfigured for various beam energies, scattering angles, and target-to-component distances to achieve the kinematics described. For G_M^n it is intended that the kinematics SBS-4, SBS-7, SBS-9, SBS-11, and SBS-14 will be used for the physics extraction. For nTPE the physics extraction will be completed with the kinematics SBS-8 and SBS-9. An important kinematic parameter for the SBS-8 and SBS-9 configurations is the longitudinal polarization of the virtual photon, ϵ, and has corresponding values of $\epsilon_{\mathrm{SBS8}} = 0.798$ and $\epsilon_{\mathrm{SBS9}} = 0.514$.

3.2.2 Experimental G_M^n Technique: The Ratio Method

The form factor G_M^n will be extracted via the "ratio method," originally proposed by L. Durand [78]. The ratio method requires the simultaneous measurement of both D(e,e'n) and D(e,e'p) reactions for quasi-elastic electron-deuteron scattering. The scattering from deuterium is critical as it allows access to bound neutrons, since there are no acceptable

Kine	Q^2 (GeV/c)^2	E_{beam} (GeV)	θ_e	θ_N	HCal Dist (m)	E' (GeV)	p_N (GeV/c)
SBS-1	1.55	1.9217	51.0°	34.5°	13.5	1.09	1.50
SBS-4	3.0	3.7393	36.0°	31.9°	11	2.11	2.35
SBS-8	4.5	5.9826	26.5°	29.4°	11	3.59	3.22
SBS-9	4.5	4.0268	49.0°	22.0°	11	1.63	3.22
SBS-14	7.4	5.9828	46.5°	17.3°	14	2.00	4.80
SBS-7	9.8	7.9308	40.0°	16.1°	14	2.67	6.20
SBS-11	13.5	9.889	42.0°	13.3°	14.5	2.67	8.10

Table 3.1: Nominal experimental information for each kinematic configuration for the G_M^n and nTPE experiments. To provide a description of the contents in this table: Q^2 is the central four-momentum transfer squared, E_{beam} is the initial energy of the electron beam, θ_e is the central electron scattering angle and is also known as θ_{BB}, θ_N is the central nucleon scattering angle and is also known as θ_{SBS}, HCal Dist is the length of the direct path from the center of the target scattering chamber to the face of HCal, E' is the average energy of the scattered electron, and p_N is the average momentum of the scattered nucleon.

sources of free neutrons. By simultaneously measuring both D(e,e'n) and D(e,e'p) quasi-elastic reactions, we can form the ratio

$$R = \frac{\left(\frac{d\sigma}{d\Omega}\right)_{\text{D(e,e'n)}}}{\left(\frac{d\sigma}{d\Omega}\right)_{\text{D(e,e'p)}}}. \tag{3.1}$$

The ratio R, ultimately, depends on all of the nucleon electromagnetic form factors. To extract the neutron magnetic form factor, G_M^n, information for the other electromagnetic form factors G_E^p, G_M^p, and G_E^n will be taken from the existing world data. The ratio method is far less sensitive to systematic errors, compared to techniques for previous electron-nucleon scattering experiments used to extract G_M^n. The primary advantage of the ratio method is that many systematic uncertainties associated with the apparatus should cancel in the cross-section ratio including: target thickness, density, and polarization; beam intensity, position, and polarization; data acquisition deadtime; electron trigger efficiency and acceptance; electron track reconstruction and efficiency; and knowledge of the magnetic fields. The advantages of the ratio method require the simultaneous measurement of both D(e,e'n) and D(e,e'p) reactions using a two spectrometer apparatus.

Some systematic effects are not expected to exactly cancel in the ratio. Quantities related to nuclear effects (primarily Fermi smearing and Final-State Interactions), radiative corrections, and nucleon detection efficiencies will not exactly cancel in the cross-section ratio, and therefore we will explicitly consider these systematic effects by applying corrections to R. We can relate Eq. 3.1 to the ratio of neutron to proton elastic cross-sections by including multiplicative corrections for known dominant effects, as follows

$$R = \frac{\left(\frac{d\sigma}{d\Omega}\right)_{\mathrm{D(e,e'n)}}}{\left(\frac{d\sigma}{d\Omega}\right)_{\mathrm{D(e,e'p)}}} = \frac{\left(\frac{d\sigma}{d\Omega}\right)_{\mathrm{n(e,e')}} \eta_{\mathrm{ne,n}}\eta_{\mathrm{rc,n}}\xi_{\mathrm{det,n}}}{\left(\frac{d\sigma}{d\Omega}\right)_{\mathrm{p(e,e')}} \eta_{\mathrm{ne,p}}\eta_{\mathrm{rc,p}}\xi_{\mathrm{det,p}}}. \tag{3.2}$$

In Eq. 3.2, the differential cross-section for elastic electron-neutron and electron-proton scattering, respectively, are defined by Eq. 2.3. In Eq. 3.2 the multiplicative corrections are applied to the corresponding neutron or proton, with $\eta_{\mathrm{ne,N}}$ accounting for nuclear effects, $\eta_{\mathrm{rc,N}}$ accounting for radiative corrections, and $\xi_{\mathrm{det,N}}$ quantifying nucleon detection efficiency. In order to extract the ratio of neutron to proton elastic cross-sections which directly relates to nucleon electromagnetic form factors, one can manipulate Eq. 3.2 and write the following expression, in terms of the measured quantity R,

$$R' = \frac{\left(\frac{d\sigma}{d\Omega}\right)_{\mathrm{n(e,e')}}}{\left(\frac{d\sigma}{d\Omega}\right)_{\mathrm{p(e,e')}}} = R \times \frac{\eta_{\mathrm{ne,p}}\eta_{\mathrm{rc,p}}\xi_{\mathrm{det,p}}}{\eta_{\mathrm{ne,n}}\eta_{\mathrm{rc,n}}\xi_{\mathrm{det,n}}}. \tag{3.3}$$

By explicitly writing the differential cross-sections for elastic electron-neutron and electron-proton scattering as defined by Eq. 2.3, one can rewrite Eq. 3.3 as follows

$$\begin{aligned} R' &= \frac{\left(\frac{d\sigma}{d\Omega}\right)_{\mathrm{Mott}} \left(\frac{E'}{E}\right)_n \frac{1}{1+\tau_n} \left(\left(G_E^n\right)^2 + \frac{\tau_n}{\epsilon_n}\left(G_M^n\right)^2\right)}{\left(\frac{d\sigma}{d\Omega}\right)_{\mathrm{Mott}} \left(\frac{E'}{E}\right)_p \frac{1}{1+\tau_p} \left(\left(G_E^p\right)^2 + \frac{\tau_p}{\epsilon_p}\left(G_M^p\right)^2\right)} \\ &= \frac{\frac{\tau_n}{\epsilon_n(1+\tau_n)} \left(\frac{\epsilon_n}{\tau_n}\left(G_E^n\right)^2 + \left(G_M^n\right)^2\right)}{\frac{\tau_p}{\epsilon_p(1+\tau_p)} \left(\frac{\epsilon_p}{\tau_p}\left(G_E^p\right)^2 + \left(G_M^p\right)^2\right)} \\ &= \frac{\frac{\tau_n}{\epsilon_n(1+\tau_n)} \left(\frac{\epsilon_n}{\tau_n}\left(G_E^n\right)^2 + \left(G_M^n\right)^2\right)}{\frac{\tau_p}{\epsilon_p(1+\tau_p)} \left(\left(\frac{d\sigma}{d\Omega}\right)_{\mathrm{reduced,p}}\right)}. \end{aligned} \tag{3.4}$$

It is important to note that in Eq. 3.4, the Mott cross-sections and the ratios of scattered electron energy to initial electron energy should cancel exactly. The ratios $\tau_{n/p}/(\epsilon_{n/p}(1+\tau_{n/p}))$ will be very close to a value of 1 in the ratio R', however, they will not exactly cancel and for now will be explicitly retained in R'. By straightforwardly manipulating Eq. 3.4, we can directly isolate the neutron magnetic form factor as follows

$$G_M^n = \sqrt{R' \times \frac{\epsilon_n(1+\tau_n)}{\tau_n}\frac{\tau_p}{\epsilon_p(1+\tau_p)}\left(\frac{d\sigma}{d\Omega}\right)_{\text{reduced,p}} - \frac{\epsilon_n}{\tau_n}\left(G_E^n\right)^2}. \tag{3.5}$$

From Eq. 3.5 one can extract a value for G_M^n; the details of how R' and is determined for this data extraction will be described in Chapter 6. The reduced cross-section for electron-proton scattering and the neutron electric form factor both can be calculated from parameterizations to current world data, and the $\tau_{n/p}$ or $\epsilon_{n/p}$ terms can be calculated if they do not exactly cancel.

3.2.3 Experimental Neutron Rosenbluth Slope Technique

The technique for the nTPE experiment combines the extraction method in Sec. 3.2.2, the ratio method, with a Rosenbluth Separation (also called an "LT Separation"), as described in Sec. 2.2, and therefore extracts the neutron Rosenbluth slope. The extracted neutron Rosenbluth slope directly relates to the neutron electromagnetic form factor ratio, G_E^n/G_M^n. For this technique to be implemented, one must consider two different measurements of both D(e,e'n) and D(e,e'p) reactions for quasi-elastic electron-deuteron scattering. In our case the two measurements are the SBS-8 and SBS-9 kinematics, which share the same Q^2-value and have sufficiently different values for ϵ. The Rosenbluth Separation technique exploits the linear-dependence in epsilon of the reduced cross-section, as expressed by (See Eq. 2.11)

$$\left(\frac{d\sigma}{d\Omega}\right)_R \equiv \sigma_R = \frac{\epsilon}{\tau}G_E^2 + G_M^2. \tag{3.6}$$

Fig. 3.2 shows an example plot of the neutron reduced cross-section vs. ϵ, to conceptualize how nucleon electromagnetic form factors are extracted using a Rosenbluth Separation.

One can extract important information from the reduced cross-section. If we consider σ_R when $\epsilon = 0$ then we find

$$\sigma_R(\epsilon = 0) = G_M^2, \tag{3.7}$$

which is the transverse component of the reduced cross-section, σ_T. Similarly if we consider the derivative (slope) of σ_R with respect to ϵ, we find

$$\frac{d\sigma_R}{d\epsilon} = \frac{1}{\tau} G_E^2, \tag{3.8}$$

which is the longitudinal component of the reduced cross-section, σ_L. Now by considering the longitudinal and transverse components we can rewrite the reduced cross-section in Eq. 3.6, as follows

$$\sigma_R = \frac{\epsilon}{\tau} G_E^2 + G_M^2 = \epsilon \sigma_L + \sigma_T. \tag{3.9}$$

By representing the reduced cross-section in terms of longitudinal and transverse components, we can construct a quantity known as "the Rosenbluth slope" as follows

$$S = \frac{G_E^2}{\tau G_M^2} = \frac{\sigma_L}{\sigma_T}, \tag{3.10}$$

(Hence the alternative name "L/T" separation).

To ultimately extract the neutron Rosenbluth slope S^n, we need to combine techniques from both the ratio method and a Rosenbluth Separation. We will begin by considering a "super-ratio" quantity called A which we shall define as follows

$$A \equiv \frac{R'_{\epsilon_1}}{R'_{\epsilon_2}}, \tag{3.11}$$

where $R'_{\epsilon_1/\epsilon_2}$ is the ratio of neutron to proton differential cross-sections for elastic electron-neutron or electron-proton scattering, respectively, as defined in Eqs. 3.3 and 3.4, and ϵ_1/ϵ_2 denotes two kinematic configurations with different values of the virtual photon polarization at the same value of Q^2. For clarity of this extraction, we will explicitly

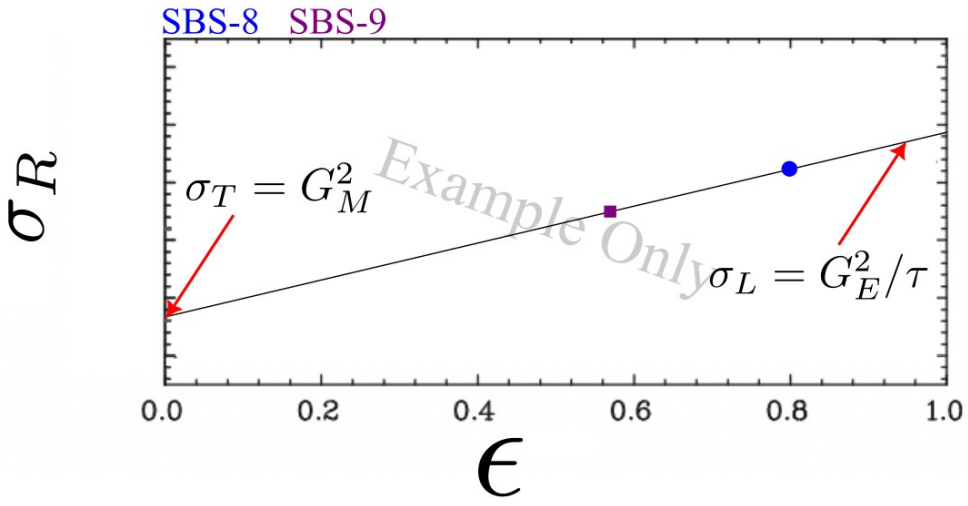

Figure 3.2: A conceptual example plot of the neutron reduced cross-section vs. ϵ. Here the neutron reduced cross-section is given arbitrary values, whereas the ϵ values are consistent with the nominal values for the SBS-8 and SBS-9 kinematics. In the OPE approximation, the reduced cross-section is linear in ϵ. Therefore from the slope and intercept of the linear fit, the longitudinal and transverse components of the neutron reduced cross-section can be extracted.

describe R'_{ϵ_1} and R'_{ϵ_2} as follows

$$R'_{\epsilon_1} = \frac{\frac{\tau_{n,\epsilon_1}}{\epsilon_{1,n}(1+\tau_{n,\epsilon_1})}\left(\frac{\epsilon_{1,n}}{\tau_{n,\epsilon_1}}\left(G_E^n\right)^2 + \left(G_M^n\right)^2\right)}{\frac{\tau_{p,\epsilon_1}}{\epsilon_{1,p}(1+\tau_{p,\epsilon_1})}\left(\frac{\epsilon_{1,p}}{\tau_{p,\epsilon_1}}\left(G_E^p\right)^2 + \left(G_M^p\right)^2\right)} = R_{\epsilon_1} \times \frac{\eta_{\mathrm{ne,p},\epsilon_1}\eta_{\mathrm{rc,p},\epsilon_1}\xi_{\mathrm{det,p},\epsilon_1}}{\eta_{\mathrm{ne,n},\epsilon_1}\eta_{\mathrm{rc,n},\epsilon_1}\xi_{\mathrm{det,n},\epsilon_1}}, \tag{3.12}$$

$$R'_{\epsilon_2} = \frac{\frac{\tau_{n,\epsilon_2}}{\epsilon_{2,n}(1+\tau_{n,\epsilon_2})}\left(\frac{\epsilon_{2,n}}{\tau_{n,\epsilon_2}}\left(G_E^n\right)^2 + \left(G_M^n\right)^2\right)}{\frac{\tau_{p,\epsilon_2}}{\epsilon_{2,p}(1+\tau_{p,\epsilon_2})}\left(\frac{\epsilon_{2,p}}{\tau_{p,\epsilon_2}}\left(G_E^p\right)^2 + \left(G_M^p\right)^2\right)} = R_{\epsilon_2} \times \frac{\eta_{\mathrm{ne,p},\epsilon_2}\eta_{\mathrm{rc,p},\epsilon_2}\xi_{\mathrm{det,p},\epsilon_2}}{\eta_{\mathrm{ne,n},\epsilon_2}\eta_{\mathrm{rc,n},\epsilon_2}\xi_{\mathrm{det,n},\epsilon_2}}, \tag{3.13}$$

Here $R_{\epsilon_1/\epsilon_2}$ is the ratio of D(e,e'n) and D(e,e'p) differential cross-sections for quasi-elastic electron-deuteron scattering, as defined in Eqs 3.1 and 3.2. Returning to the super-ratio

A in Eq. 3.11, we can rewrite A by considering the descriptions for R'_{ϵ_1} and R'_{ϵ_2}

$$
\begin{aligned}
A \equiv \frac{R'_{\epsilon_1}}{R'_{\epsilon_2}} &= \frac{\frac{\tau_{n,\epsilon_1}}{\epsilon_{1,n}(1+\tau_{n,\epsilon_1})}\left(\frac{\epsilon_{1,n}}{\tau_{n,\epsilon_1}}\left(G_E^n\right)^2+\left(G_M^n\right)^2\right)}{\frac{\tau_{p,\epsilon_1}}{\epsilon_{1,p}(1+\tau_{p,\epsilon_1})}\left(\frac{\epsilon_{1,p}}{\tau_{p,\epsilon_1}}\left(G_E^p\right)^2+\left(G_M^p\right)^2\right)} \\
&\quad \frac{\frac{\tau_{n,\epsilon_2}}{\epsilon_{2,n}(1+\tau_{n,\epsilon_2})}\left(\frac{\epsilon_{2,n}}{\tau_{n,\epsilon_2}}\left(G_E^n\right)^2+\left(G_M^n\right)^2\right)}{\frac{\tau_{p,\epsilon_2}}{\epsilon_{2,p}(1+\tau_{p,\epsilon_2})}\left(\frac{\epsilon_{2,p}}{\tau_{p,\epsilon_2}}\left(G_E^p\right)^2+\left(G_M^p\right)^2\right)}, \\
&= \frac{\frac{\tau_{n,\epsilon_1}}{\epsilon_{1,n}(1+\tau_{n,\epsilon_1})}\left(G_M^n\right)^2\left(\frac{\epsilon_{1,n}}{\tau_{n,\epsilon_1}}\left(G_E^n/G_M^n\right)^2+1\right)}{\frac{\tau_{p,\epsilon_1}}{\epsilon_{1,p}(1+\tau_{p,\epsilon_1})}\left(G_M^p\right)^2\left(\frac{\epsilon_{1,p}}{\tau_{p,\epsilon_1}}\left(G_E^p/G_M^p\right)^2+1\right)} \\
&\quad \frac{\frac{\tau_{n,\epsilon_2}}{\epsilon_{2,n}(1+\tau_{n,\epsilon_2})}\left(G_M^n\right)^2\left(\frac{\epsilon_{2,n}}{\tau_{n,\epsilon_2}}\left(G_E^n/G_M^n\right)^2+1\right)}{\frac{\tau_{p,\epsilon_2}}{\epsilon_{2,p}(1+\tau_{p,\epsilon_2})}\left(G_M^p\right)^2\left(\frac{\epsilon_{2,p}}{\tau_{p,\epsilon_2}}\left(G_E^p/G_M^p\right)^2+1\right)}, \\
&= \frac{\frac{\tau_{n,\epsilon_1}}{\epsilon_{1,n}(1+\tau_{n,\epsilon_1})}\frac{\sigma_{T,\epsilon_1}^n}{\sigma_{T,\epsilon_1}^p}\left(\epsilon_{1,n}S_{\epsilon_1}^n+1\right)}{\frac{\tau_{p,\epsilon_1}}{\epsilon_{1,p}(1+\tau_{p,\epsilon_1})}\left(\epsilon_{1,p}S_{\epsilon_1}^p+1\right)} \\
&\quad \frac{\frac{\tau_{n,\epsilon_2}}{\epsilon_{2,n}(1+\tau_{n,\epsilon_2})}\frac{\sigma_{T,\epsilon_2}^n}{\sigma_{T,\epsilon_2}^p}\left(\epsilon_{2,n}S_{\epsilon_2}^n+1\right)}{\frac{\tau_{p,\epsilon_2}}{\epsilon_{2,p}(1+\tau_{p,\epsilon_2})}\left(\epsilon_{2,p}S_{\epsilon_2}^p+1\right)},
\end{aligned}
\tag{3.14}
$$

where $\sigma_{T,\epsilon_1/\epsilon_2}^{n/p}$ is the corresponding neutron or proton transverse component of the reduced cross-section from Eq. 3.9, $S_{\epsilon_1/\epsilon_2}^{n/p}$ is the corresponding neutron or proton Rosenbluth slope from Eq. 3.10, and the ϵ_1/ϵ_2 denotes the two different kinematics. By manipulating Eq. 3.14 we can rewrite the super-ratio A as

$$
\begin{aligned}
A &= \frac{\frac{\tau_{n,\epsilon_1}}{\epsilon_{1,n}(1+\tau_{n,\epsilon_1})}}{\frac{\tau_{p,\epsilon_1}}{\epsilon_{1,p}(1+\tau_{p,\epsilon_1})}}\frac{\frac{\tau_{p,\epsilon_2}}{\epsilon_{2,p}(1+\tau_{p,\epsilon_2})}}{\frac{\tau_{n,\epsilon_2}}{\epsilon_{2,n}(1+\tau_{n,\epsilon_2})}}\frac{\sigma_{T,\epsilon_1}^n}{\sigma_{T,\epsilon_1}^p}\frac{\sigma_{T,\epsilon_2}^p}{\sigma_{T,\epsilon_2}^n}\frac{1+\epsilon_{2,p}S_{\epsilon_2}^p}{1+\epsilon_{1,p}S_{\epsilon_1}^p}\frac{1+\epsilon_{1,n}S_{\epsilon_1}^n}{1+\epsilon_{2,n}S_{\epsilon_2}^n}, \\
&= \frac{R'_{\epsilon_1}}{R'_{\epsilon_2}}.
\end{aligned}
\tag{3.15}
$$

To motivate the next step in the derivation of the nTPE physics extraction, consider the following common form of the Taylor Series

$$
\frac{1}{1+bx} = 1 - bx + (bx)^2 - (bx)^3 + (bx)^4 - (bx)^5 + \cdots . \tag{3.16}
$$

If we now apply this generic Taylor Series to Eq. 3.15 we can rewrite the super-ratio A as follows

$$
\begin{aligned}
A = & \frac{\frac{\tau_{n,\epsilon_1}}{\epsilon_{1,n}(1+\tau_{n,\epsilon_1})}}{\frac{\tau_{p,\epsilon_1}}{\epsilon_{1,p}(1+\tau_{p,\epsilon_1})}} \frac{\frac{\tau_{p,\epsilon_2}}{\epsilon_{2,p}(1+\tau_{p,\epsilon_2})}}{\frac{\tau_{n,\epsilon_2}}{\epsilon_{2,n}(1+\tau_{n,\epsilon_2})}} \frac{\sigma^n_{T,\epsilon_1}}{\sigma^p_{T,\epsilon_1}} \frac{\sigma^p_{T,\epsilon_2}}{\sigma^n_{T,\epsilon_2}} \frac{1+\epsilon_{2,p}S^p_{\epsilon_2}}{1+\epsilon_{1,p}S^p_{\epsilon_1}} \left(1+\epsilon_{1,n}S^n_{\epsilon_1}\right) \\
& \times \left(1-\epsilon_{2,n}S^n_{\epsilon_2} + \left(\epsilon_{2,n}S^n_{\epsilon_2}\right)^2 - \left(\epsilon_{2,n}S^n_{\epsilon_2}\right)^3 + \left(\epsilon_{2,n}S^n_{\epsilon_2}\right)^4 + \cdots\right), \\
= & \frac{\frac{\tau_{n,\epsilon_1}}{\epsilon_{1,n}(1+\tau_{n,\epsilon_1})}}{\frac{\tau_{p,\epsilon_1}}{\epsilon_{1,p}(1+\tau_{p,\epsilon_1})}} \frac{\frac{\tau_{p,\epsilon_2}}{\epsilon_{2,p}(1+\tau_{p,\epsilon_2})}}{\frac{\tau_{n,\epsilon_2}}{\epsilon_{2,n}(1+\tau_{n,\epsilon_2})}} \frac{\sigma^n_{T,\epsilon_1}}{\sigma^p_{T,\epsilon_1}} \frac{\sigma^p_{T,\epsilon_2}}{\sigma^n_{T,\epsilon_2}} \frac{1+\epsilon_{2,p}S^p_{\epsilon_2}}{1+\epsilon_{1,p}S^p_{\epsilon_1}} \\
& \times \left(1+\epsilon_{1,n}S^n_{\epsilon_1} - \epsilon_{2,n}S^n_{\epsilon_2} - \epsilon_{1,n}\epsilon_{2,n}S^n_{\epsilon_1}S^n_{\epsilon_2} + \left(\epsilon_{2,n}S^n_{\epsilon_2}\right)^2 - \epsilon_{1,n}\epsilon^2_{2,n}S^n_{\epsilon_1}\left(S^n_{\epsilon_2}\right)^2 + \cdots\right), \\
\simeq & \frac{\frac{\tau_{n,\epsilon_1}}{\epsilon_{1,n}(1+\tau_{n,\epsilon_1})}}{\frac{\tau_{p,\epsilon_1}}{\epsilon_{1,p}(1+\tau_{p,\epsilon_1})}} \frac{\frac{\tau_{p,\epsilon_2}}{\epsilon_{2,p}(1+\tau_{p,\epsilon_2})}}{\frac{\tau_{n,\epsilon_2}}{\epsilon_{2,n}(1+\tau_{n,\epsilon_2})}} \frac{\sigma^n_{T,\epsilon_1}}{\sigma^p_{T,\epsilon_1}} \frac{\sigma^p_{T,\epsilon_2}}{\sigma^n_{T,\epsilon_2}} \frac{1+\epsilon_{2,p}S^p_{\epsilon_2}}{1+\epsilon_{1,p}S^p_{\epsilon_1}} \\
& \times \left(1+\epsilon_{1,n}S^n - \epsilon_{2,n}S^n - \epsilon_{1,n}\epsilon_{2,n}\left(S^n\right)^2 + \left(\epsilon_{2,n}S^n\right)^2 - \epsilon_{1,n}\epsilon^2_{2,n}\left(S^n\right)^3 + \cdots\right).
\end{aligned}
\tag{3.17}
$$

For Eq. 3.17, in order to go from the last equals sign to the approximately equal to sign we must claim that $S^n \simeq S^n_{\epsilon_1} \simeq S^n_{\epsilon_2}$, which is not unreasonable if the two kinematic configurations have nearly identical values of Q^2. Since we anticipate S^n to have a small numerical value, we would expect higher order powers of S^n to have a smaller contribution. Therefore, we are able to truncate the expansion in Eq. 3.17 and use mathematical techniques to solve for S^n. By only considering first-order terms in S^n we can simplify (approximate) the super-ratio A as follows

$$
\begin{aligned}
A = & \frac{R'_{\epsilon_1}}{R'_{\epsilon_2}}, \\
\simeq & \frac{\frac{\tau_{n,\epsilon_1}}{\epsilon_{1,n}(1+\tau_{n,\epsilon_1})}}{\frac{\tau_{p,\epsilon_1}}{\epsilon_{1,p}(1+\tau_{p,\epsilon_1})}} \frac{\frac{\tau_{p,\epsilon_2}}{\epsilon_{2,p}(1+\tau_{p,\epsilon_2})}}{\frac{\tau_{n,\epsilon_2}}{\epsilon_{2,n}(1+\tau_{n,\epsilon_2})}} \frac{\sigma^n_{T,\epsilon_1}}{\sigma^p_{T,\epsilon_1}} \frac{\sigma^p_{T,\epsilon_2}}{\sigma^n_{T,\epsilon_2}} \frac{1+\epsilon_{2,p}S^p_{\epsilon_2}}{1+\epsilon_{1,p}S^p_{\epsilon_1}} \\
& \times \left(1+\Delta\epsilon S^n + O\left(S^n\right)^2\right),
\end{aligned}
\tag{3.18}
$$

where we define $\Delta\epsilon = \epsilon_{1,n} - \epsilon_{2,n}$. By not considering higher order terms in S^n one can

manipulate Eq. 3.18 to straightforwardly isolate, the extraction quantity, S^n, as follows

$$S^n \simeq \frac{1}{\Delta\epsilon} \frac{\frac{\tau_{p,\epsilon_1}}{\epsilon_{1,p}(1+\tau_{p,\epsilon_1})}}{\frac{\tau_{n,\epsilon_1}}{\epsilon_{1,n}(1+\tau_{n,\epsilon_1})}} \frac{\frac{\tau_{n,\epsilon_2}}{\epsilon_{2,n}(1+\tau_{n,\epsilon_2})}}{\frac{\tau_{p,\epsilon_2}}{\epsilon_{2,p}(1+\tau_{p,\epsilon_2})}} \frac{\sigma^p_{T,\epsilon_1}}{\sigma^n_{T,\epsilon_1}} \frac{\sigma^n_{T,\epsilon_2}}{\sigma^p_{T,\epsilon_2}} \frac{1+\epsilon_{1,p}S^p_{\epsilon_1}}{1+\epsilon_{2,p}S^p_{\epsilon_2}}$$
$$\left(\frac{R'_{\epsilon_1}}{R'_{\epsilon_2}} - \frac{\frac{\tau_{n,\epsilon_1}}{\epsilon_{1,n}(1+\tau_{n,\epsilon_1})}}{\frac{\tau_{p,\epsilon_1}}{\epsilon_{1,p}(1+\tau_{p,\epsilon_1})}} \frac{\frac{\tau_{p,\epsilon_2}}{\epsilon_{2,p}(1+\tau_{p,\epsilon_2})}}{\frac{\tau_{n,\epsilon_2}}{\epsilon_{2,n}(1+\tau_{n,\epsilon_2})}} \frac{\sigma^n_{T,\epsilon_1}}{\sigma^p_{T,\epsilon_1}} \frac{\sigma^p_{T,\epsilon_2}}{\sigma^n_{T,\epsilon_2}} \frac{1+\epsilon_{2,p}S^p_{\epsilon_2}}{1+\epsilon_{1,p}S^p_{\epsilon_1}} \right). \tag{3.19}$$

From Eq. 3.19 one can extract the neutron Rosenbluth slope: the $\Delta\epsilon$ term is directly calculable, the $\tau_{n/p,\epsilon_1/\epsilon_2}$ or $\epsilon_{1/2,n/p}$ terms are calculable if they do not exactly cancel, the $\sigma^{n/p}_{T,\epsilon_1/2}$ and $\epsilon_{1,2}S^p_{\epsilon_1/2}$ terms are calculable from parameterizations to current world data, and the details to how R' is determined for this data extraction will be described in Chapter 6. It should also be noted that though $\sigma^{n/p}_{T,\epsilon_1/2}$ terms can be calculated, these terms will almost cancel.

Chapter 4

G_M^n/nTPE Experimental Apparatus

The SBS G_M^n (E12-09-019) and neutron Two-Photon Exchange (nTPE or E12-20-010) experiments were both conducted in experimental Hall A at the Continuous Electron Beam Accelerator Facility (CEBAF), located at the Thomas Jefferson National Accelerator Facility (Jefferson Lab or JLab). The G_M^n and nTPE experiments together were the first stage of the SBS program and required the installation of two new detector packages. The detector packages used for the first stage of the SBS program are the BigBite Spectrometer and the Super BigBite Spectrometer. Hardware installation and commissioning of the SBS apparatus for the G_M^n and nTPE experiments occurred between May and October 2021. Data were collected for the G_M^n and nTPE experiments between October 2021 and February 2022.

This chapter will describe, in some detail, the experimental apparatus used for the G_M^n and nTPE experiments. The experimental apparatus and systems are organized into two categories, the first being the accelerator facility and the second being the Hall A equipment. In the following sections, we will discuss these topics in order.

4.1 The Continuous Electron Beam Accelerator Facility

CEBAF is the primary feature of Jefferson Lab. CEBAF was orignally brought online in 1994 with the capability of delivering polarized electrons, with beam energy up to 4 GeV,

to three experimental halls: Halls A, B, and C. In 2000 the maximum beam energy of CEBAF was increased to 6 GeV [112]. A significant upgrade to the accelerator started in 2012, which provided delivery of electrons to a fourth experimental hall, Hall D, and an increase in beam energy to 12 GeV [113, 114]. The present capability of CEBAF is simultaneous beam delivery to all four experimental halls, with a total beam current up to 200 μA and stable control of parameters including beam position, angle, and energy for individual experiments.

CEBAF is a recirculating electron accelerator that provides continuous wave beams and uses an injector source, two linear accelerators (Linacs), and multiple magnetic steering sections known as arcs. The layout of CEBAF and the experimental halls are shown in Fig. 4.1.

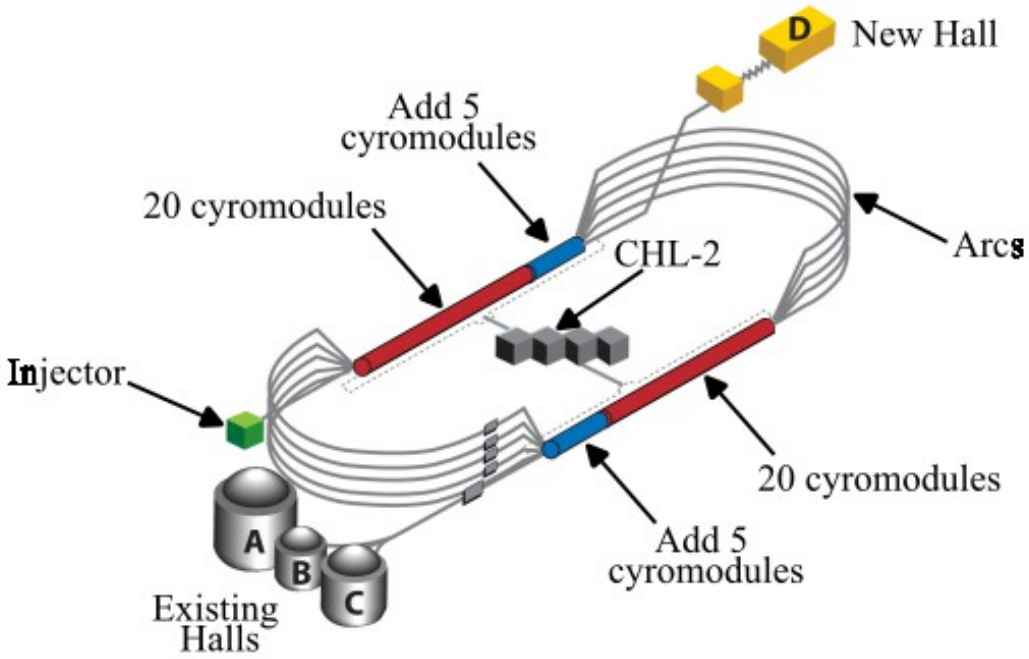

Figure 4.1: A schematic of the CEBAF complex, detailing components added during the 12 GeV updgrade, which represents the current state of the apparatus. Adapted from [114].

The electron beam delivery process begins in the injector, which is the source of the beam. The 123 MeV injector [115] contains many components; the components of most significance include: rf-gain-switched lasers, a single GaAs photocathode, and superconducting radio frequency (SRF) booster cyromodules. The accelerator is capable of producing both polarized (>85%) and unpolarized beams of electrons. The repetition rate of electrons to be delivered to the halls is 249.5 or 499 MHz. Once the electron beam leaves the injector it travels to the first of two Linacs, known as the North Linac.

Each Linac is composed of 25 cyromodules, two are shown Fig. 4.2, with each cyromodule containing 8 niobium SRF cavities [116]; one SRF cavity is shown in Fig. 4.3. The niobium SRF cavities in each cyromodule are maintained at a temperature of approximately 2 K by a bath of liquid helium. In the Linac the beam gains energy by passing through all the SRF cavities in the 25 cyromodules. Each Linac provides approximately 1.1 GeV of energy gradient to the electron beam. From the North Linac the electron beam proceeds to a steering section known as the East Arc. The electron beam continues to the second Linac, known as the South Linac. From the South Linac the electron beam is recirculated via the steering section known as the West Arc.

Both arcs, the West and the East, are composed of dipole magnets, quadrupole magnets, and diagnostic equipment. The primary function of the arcs is to steer the beam between the Linacs and provide a recirculating ability allowing multiple passes through the Linacs. The dipole magnets function to displace the electron beam either vertically or horizontally with respect to beam transport coordinates. A combination of quadrupole magnets either focus or defocus the electron beam. There are two main types of quadrupole magnets: 'F quadrupoles' which are horizontally focusing and vertically defocusing, and 'D quadrupoles' which are vertically focusing and horizontally defocusing. By using different combinations of both types of quadrupole magnets the electron beam can be either focused or defocused both vertically and horizontally with respect to beam transport coordinates. By circulating through the "racetrack" design of the entire accelerator the electron beam achieves an overall energy up to ≈12 GeV. Combining the energy of both Linacs provides

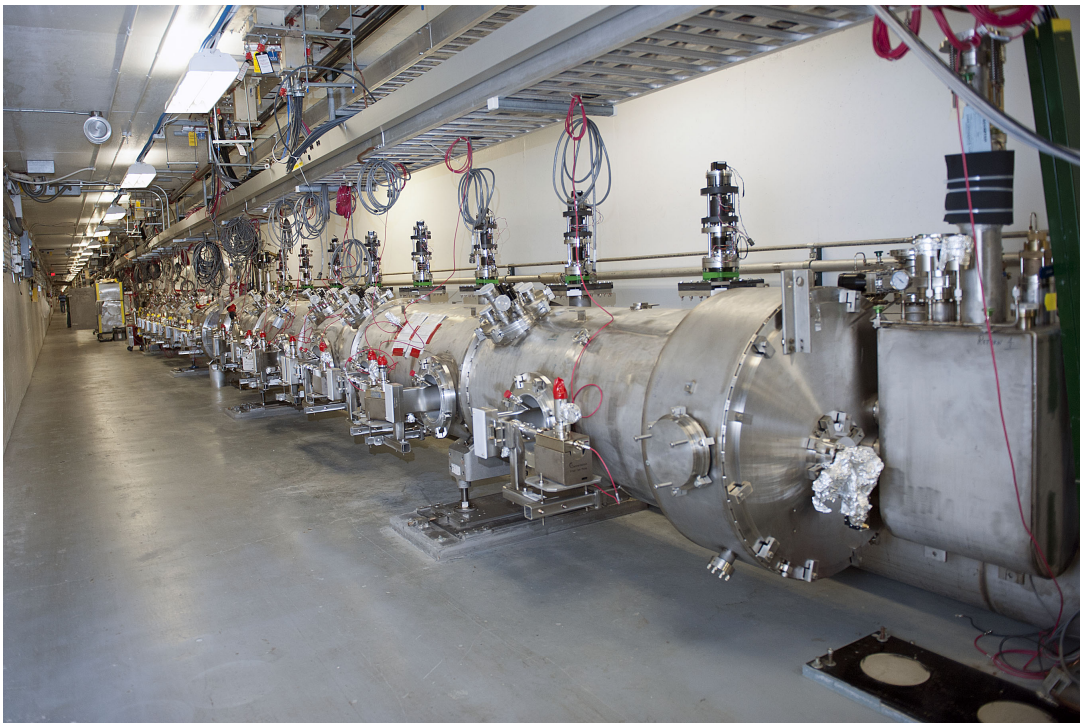

Figure 4.2: Two partially installed C-100 cryomodules.

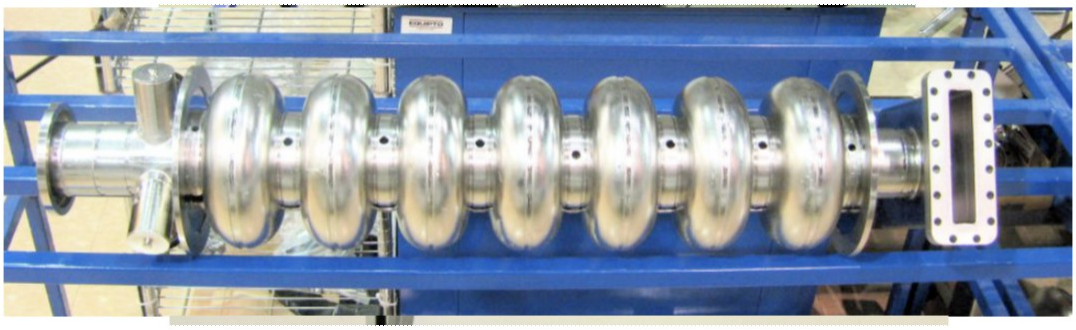

Figure 4.3: Seven-cell SRF Cavity. Adapted from [116].

an energy gain of approximately 2.2 GeV to the electron beam after one full circuit (pass) of the accelerator. The accelerator is able to deliver up to 5 passes to Halls A, B, and C, for a maximum total energy of approximately 11 GeV. For Hall D, 5.5 passes are available, for a maximum total energy of approximately 12 GeV.

After the electron beam has been circulated for the desired amount of energy, i.e. the desired number of passes, the beam is transferred to the beam switchyard. Here the

electron beam leaves the accelerator and takes a path to and through an experimental hall. For Halls B and D, this is a straight line path from the switchyard to the experimental hall. For Hall A and C, there are magnetic arcs after the switchyard which deliver the electron beam to the hall. The experimental hall then uses the electron beam for the installed experiment. The electron beam then is transported to the beam dump, where it is absorbed. The Hall A beam dump consists of water-cooled aluminum cylinders located in a tank that is located in a concrete tunnel at the end of the beam transport line [117].

4.2 Experimental Hall A

Experimental Hall A at Jefferson Lab is cylindrical with a radius of ∼26.5 m, and a height of 24 m at the center and 16 m at the edge. The beamline is positioned 3.05 m above the hall floor. The hall structures (wall, floor, and roof) are made of concrete. Hall A is separated from the accelerator in the beam switchyard by a retractable concrete shield wall. During the SBS G_M^n and nTPE experiments, Hall A was instrumented with the beamline, a target system, the BigBite Spectrometer, the Super BigBite Spectrometer, a trigger system, a data acquisition, and monitoring systems. The purpose of the Hall A beamline is to receive the electron beam through the accelerator and transport it through the experimental hall. The beamline also houses many diagnostic and machine protection systems. The Hall A beamline is described in more detail in Sec. 4.2.1. The target system contains the cryogenic and solid targets that the electron beam will scatter off of. A description of the target system is provided in Sec. 4.2.2. The BigBite Spectrometer obtains necessary information for the scattered electrons and is further detailed in Sec. 4.2.3. The Super BigBite Spectrometer detects important quantities for the scattered nucleons and is described in Sec. 4.2.4. The experimental trigger system was a single-arm trigger and determined when the apparatus should collect data; an explanation of the construction and logic is provided in Sec. 4.2.5. The data acquisition (DAQ) framework is used to collect and organize experimental physics events, the DAQ, known as CODA, is

specific to Jefferson Lab and is described in Sec 4.2.6. The monitoring systems known as EPICS, Slow Controls, and Panguin provide constant feedback about the status of almost every apparatus system; a summary of each of these systems is in Sec. 4.2.7.

4.2.1 Beamline

The Hall A beamlime is organized into two primary sections; the upstream portion which is located from the retractable concrete shield wall to the target scattering chamber and the downstream portion from the target scattering chamber to the beam dump. On the upstream portion of the beamline are important elements including polarimeters, beam position monitors, beam current monitors, and other diagnostic elements. On the downstream end of the beamline is a high-power beam dump. The beam dump serves to absorb any residual unscattered electron beam and contain radiation. Fig. 4.4 shows the configuration of Hall A during the G_M^n and nTPE experiments, and depicts some important experimental components.

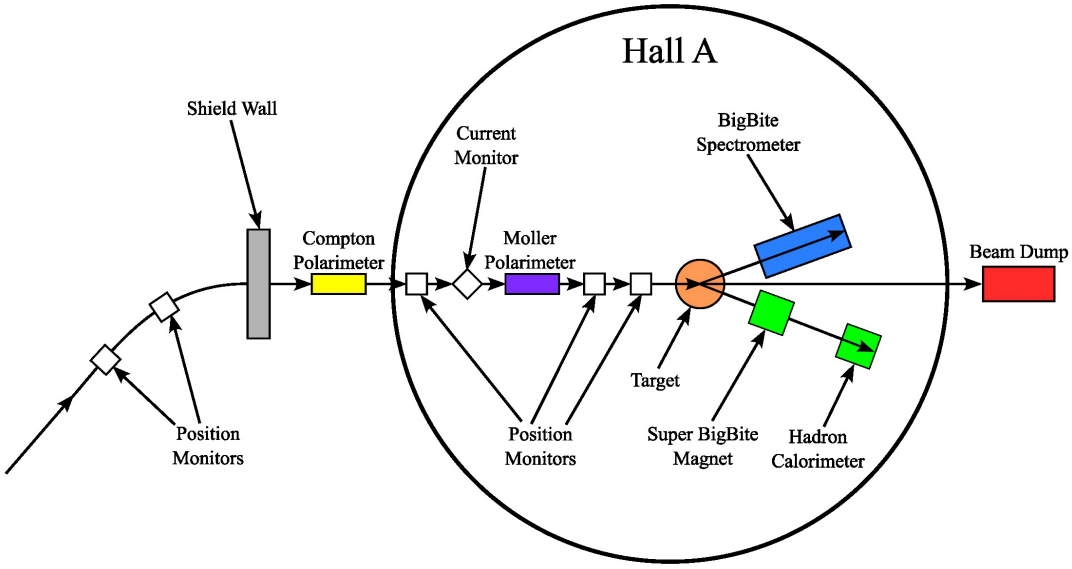

Figure 4.4: An overview of Hall A with relevant components. Not drawn to scale. Updated and adapted from [118].

Beam Current Monitors

The Hall A beamline includes a series of Beam Current Monitors (BCMs) [119] that measure the electron beam current. The BCM system is made of two components: a resonant RF cavity and a data acquisition system with corresponding electronics. The BCMs are designed for stable, low-noise, and non-intercepting beam measurements, with an accuracy of 0.2 %. Directly related to the BCMs is a device called the "Unser," which is a Parametric Current Transformer (PCT). The Unser is necessary for calibrating the BCMs. The Unser and two BCMS, one on each side known as IBC1H00 (upstream) and IBC1H00A (downstream), are housed in a magnetically isolated and thermally stabilized box approximately 25 m upstream of the target just before the fast raster. Other relevant BCMs are IBC1H01A, IBC1H01B, and IBC1H01C which are located downstream of the raster and upstream of the Møller Polarimeter. Another set of BCMs are IBC1H04A and IBC1H04B which are important because they are located upstream and in close proximity to the target scattering chamber. This experiment only needed to calibrate the BCMs during the beamline checkout within the commissioning stages of this experiment. The Unser monitor is the most accurate reference for the BCM calibration. The beam is passed through the Unser and a response is generated in a calibration wire which is proportional to the beam current. The BCM calibration is conducted by having alternating periods of beam-on and beam-off at various nominal beam currents in the range of 0-100 μA. Since the Unser Monitor can determine the beam current to high accuracy, this is used to calibrate the 2 RF cavities response to any given beam current. The two IBC1H00 and IBC1H00A RF cavities provide continuous current monitoring, unlike the Unser. Once calibrated, those two RF cavities were used throughout the experiment to monitor the current in the Hall A beamline, thereby providing one source of beam diagnostics and automatic safeguards in beam delivery. Given the physics extraction for this experiment, as described in Chapter 3, is a ratio of the neutron cross-section over the proton cross-section and this is experiment simultaneously measures neutrons and protons. We expect that the beam current

will cancel in the cross-section ratio and therefore is not required as an analysis parameter. Rather, the calibration of the BCMs was useful for this experiment to verify the integrity of signals from the BCMs.

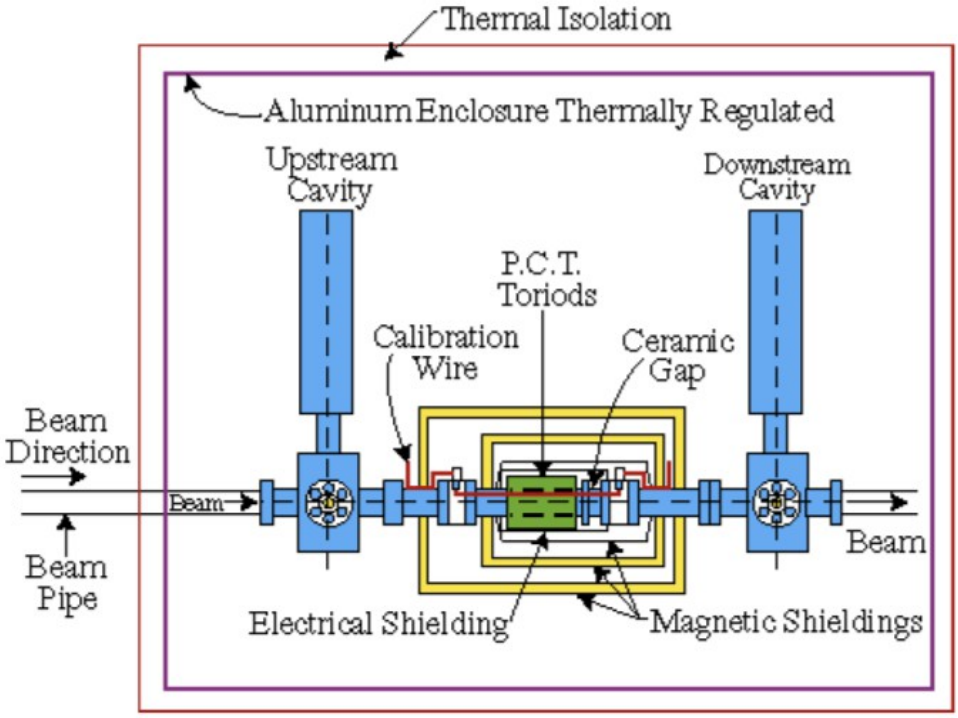

Figure 4.5: A diagram of the Unser and RF cavities of the BCM; electronics and data acquisition not included. Reproduced from [120].

Beam Position Monitors

The beam position monitor (BPM) [119] is a beamline diagnostic element used to determine the position and direction of the electron beam at a given location in the acclerator. The Hall A beamline has many BPMs placed in various locations along the beamline, particularly after any steering elements. Two BPMs of particular significance are IPM1H03A and IPM1H03B located upstream of the target position at a distance of 7.524 m and 1.286 m, respectively. A "stripline" BPM consists of a four-wire antenna array of thin wire striplines, each running parallel to the beamline (there are also newer "cavity" BPMs

that were not used during the G_M^n and nTPE experiments). A diagram of a typical BPM is show in Fig. 4.6. The basic function of the BPM is that when beam passes through the BPM the beam induces a current in each antenna, dependent on the position of the beam with respect to that antenna. The beam current-independent beam position in each direction can be computed from the signal in each of the four wires X_p, X_m, Y_p, and Y_m:

$$x_{rot} = C\frac{X_p - X_m}{X_p + X_m}, \qquad y_{rot} = C\frac{Y_p - Y_m}{Y_p + Y_m}, \tag{4.1}$$

where $C = 18.76$ mm is a calibration constant [118]. To convert the rotated positions to the hall coordinates, the positions must be rotated around the beam direction by $\theta = 45°$:

$$\begin{bmatrix} x \\ y \end{bmatrix} = \begin{bmatrix} \cos\theta & -\sin\theta \\ \sin\theta & \cos\theta \end{bmatrix} \begin{bmatrix} x_{rot} \\ y_{rot} \end{bmatrix}. \tag{4.2}$$

For this experiment the BPMs were used primarily for regular beam centering. To do this calibration one needs to align the center of the beam profile with the center of the carbon hole target, which represents the center of the production targets. This beam centering both ensures proper beam steering through the machine and also provides optimal interaction for the production targets. The relative beam position can be determined to within 100 μm for beam currents above 1 μA. Another calibration that was conducted less frequently was a BPM calibration to the wire scanners ("superharps") which are located adjacent to each one of the BPMs. This BPM calibration provides a determination of the absolute position of the electron beam. After proper calibration, the beam position information was used throughout the experiment and was stored for later analysis. Particularly precise information about the beam position was used for the experiment's optics calibration.

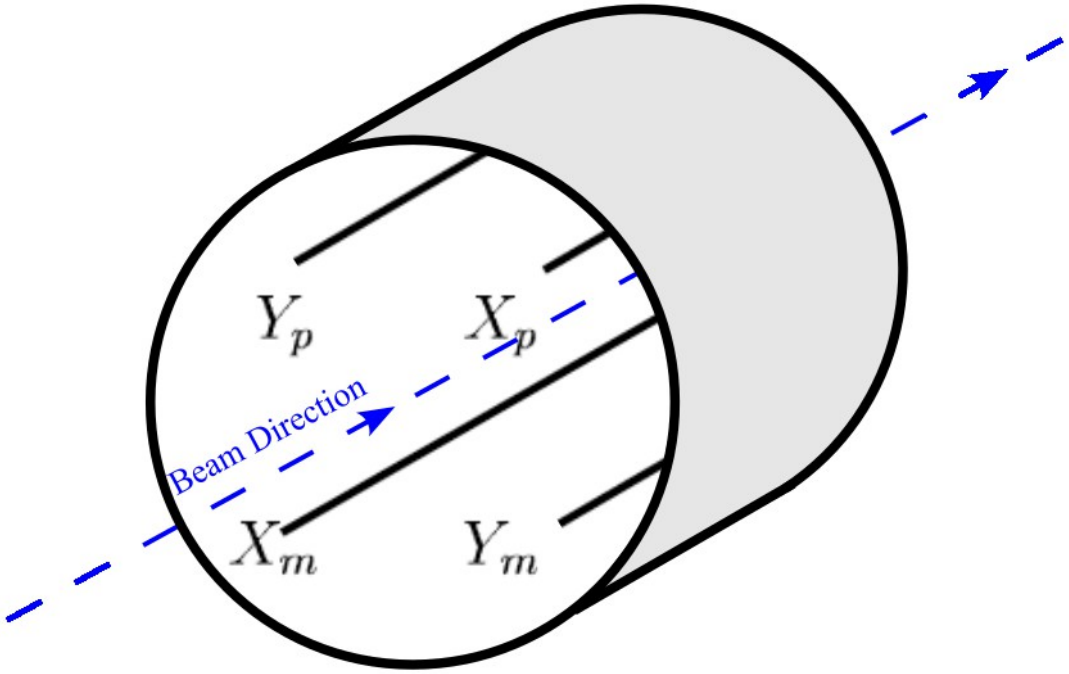

Figure 4.6: A schematic of a typical beam position monitor, including the four wires X_p, X_m, Y_p, and Y_m. Adapted from [119].

Fast Raster and Harps

For the SBS G_M^n and nTPE experiments the intrinsic beam size was about 100 μm when being delivered to Hall A. If an electron beam of this spot size with a typical intensity were to directly interact with the cryogenic liquid or the target cell walls there would be some form of harmful effects. The damage to the target system could be local heating of liquid cryogens or, at sufficient intensities, the melting of the thin aluminum windows of the target cells. Any heating of liquid cryogens can cause undesirable boiling and thus fluctuations in target density and uniformity. To protect against these detrimental conditions, a system was necessary to distribute the beam profile over the target.

The system that distributes the beam profile is known as the "fast raster." The raster is a set of magnetic coils located along the beamline approximately 23 m upstream of the target position. During beam delivery, when the raster is active, the two coils modulate

the beam steering at two different frequencies, one is not a simple multiple of the other, each of about 25 kHz [121]. The raster coils steer the beam in a rectangular pattern so that the beam profile at the target is 2×2 mm^2. To properly calibrate the size and shape of the raster pattern, the rastered electron beam is scattered off a carbon foil target with a 2 mm diameter hole in the center. By scattering the rastered beam off the carbon hole target one is able to compare the size of the raster pattern with the size of the hole of the carbon foil. A plot of a Raster Map showing the rastered beam, in vertical and horizontal raster coordinates, on a carbon hole target is displayed in Fig. 4.7. In this figure, the density gradient corresponds to the scattered electrons from the carbon hole target as detected by the BigBite Calorimeter. Since there is a 2 mm diameter hole in the target, one would expect to see very few scattered electrons from that region. However, at the circumference of the hole and other parts of the foil one would expect to see more scattered electrons in BBCal; since there was a target to scatter from. So by detecting electrons in BBCal from a carbon hole target, one is able to image the 2 mm hole. By iteratively comparing the raster size and position with the carbon hole target, the raster coil currents can be manipulated to reach the desired nominal size and shape of the raster pattern, and to verify the centering of the beam on target.

Additionally to the raster pattern, the intrinsic beam size before the raster must be calibrated. A small intrinsic beam size could cause damage to the target and a large spot size could cause beam transport problems. The intrinsic spot size of the beam is checked with an array of conductive wires called a "super harp." One uses a harp scan to assess the intrinsic beam spot size prior to beam rastering. Both the raster evaluations and harp scans are invasive to beam delivery and are only performed at low beam current to calibrate some beamline components either during beamline commissioning or if there is a significant change in the beam profile.

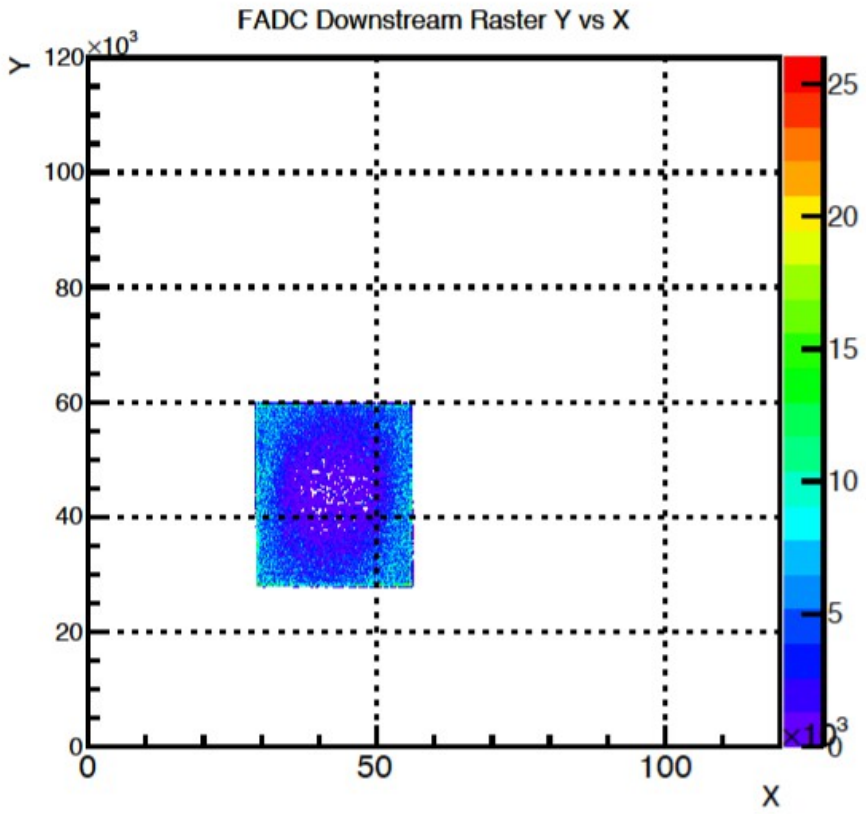

Figure 4.7: A typical plot of y vs x beam position of a rastered beam on the carbon hole target (Raster Map). In this case the raster is calibrated to match the size of the carbon hole.

Polarimeters

The Hall A beamline is outfitted with two forms of polarimetry devices, one is the Compton Polarimeter and the second is the Møller Polarimeter. For the SBS G_M^n and nTPE experiments only an unpolarized electron beam was necessary. Therefore the inclusion of operational polarimeters was not required and no polarimeters were used through the experiments. However, a brief description of each polarimeter and its general function will be included for completeness.

The Compton Polarimeter is located close to the entrance of Hall A by the shield wall. A diagram is shown in Fig. 4.8a. The Compton Polarimeter is unique in that it uses a chicane

to divert the electron beam along the beamline to do non-invasive measurements. The Compton Polarimeter [118] is composed of three major subsystems: the laser system, the photon detector, and the electron detector. The laser system is responsible for providing a circularly polarized photon beam and is composed of various standard optical instruments. A resonant Fabry-Pérot cavity is used to amplify the photon beam. The photon detector is responsible for generating a signal for Compton scattered photons and is a calorimeter. The electron detector is made of silicon strips and receives electrons that are lower in energy than the primary electron beam and is used to detect Compton scattered electrons. During regular beam delivery with the Compton Polarimeter in operation the electron beam is diverted through the chicane. From there it travels into the resonant cavity with the circularly polarized photon beam. The electron beam then passes through the photon beam and Compton scattering can occur. Compton scattered photons are then observed in the photon detector. The photon detector generates a signal which is used to measure the rate of the Compton scattering for each electron helicity state. From this measurement, one can calculate the asymmetry in the differential cross-section. The Compton Polarimeter is able to extract the electron beam polarization from this measured asymmetry because it is directly related to the polarization of the photons in the laser beam, the polarization of the electron beam, and the known Compton scattering analyzing power.

The Møller Polarimeter is located along the main beamline upstream of the target, in-between the raster and the BPMs. The Møller Polarimeter [122] has 5 major components: a target located in Helmholtz coils, 4 quadrupole magnets, an adjustable collimator, a dipole magnet, and shielded electron detectors. A diagram of these components and the Møller Polarimeter is displayed in Fig. 4.8b. Polarized target electrons are provided by the iron target foil, which is held in a saturated 4 T magnetic field by the superconducting Helmholtz coils. The electrons from the beam can scatter off polarized electrons from the target foil, a process known as Møller scattering. The four quadrupole magnets are used to align the two scattered outgoing electrons so that they are approximately parallel to each other along the beam axis. The adjustable collimator at the entrance to the dipole magnet is used to

restrict the azimuthal angle of scattering, with respect to the beam axis. The electrons then leave through the exit collimator and into the shielded detector hut containing the electron detectors. The electron detectors consist of two identical modules about the beam axis. A single module of the electron detector is made of four lead-scintillator calorimeter blocks, each 9×15 cm^2 and 30 cm long. Each of the lead calorimeter blocks is infused with a scintillating fiber. Each of the scintillating fibers is then connected to a photo-multiplier tube (PMT). The electron detectors generate a signal which is used to measure a helicity-correlated scattering asymmetry. The measured Møller asymmetry is directly related to the target polarization, the beam polarization, and the average analyzing power of the electron detectors, and so the polarization of the electron beam can be determined.

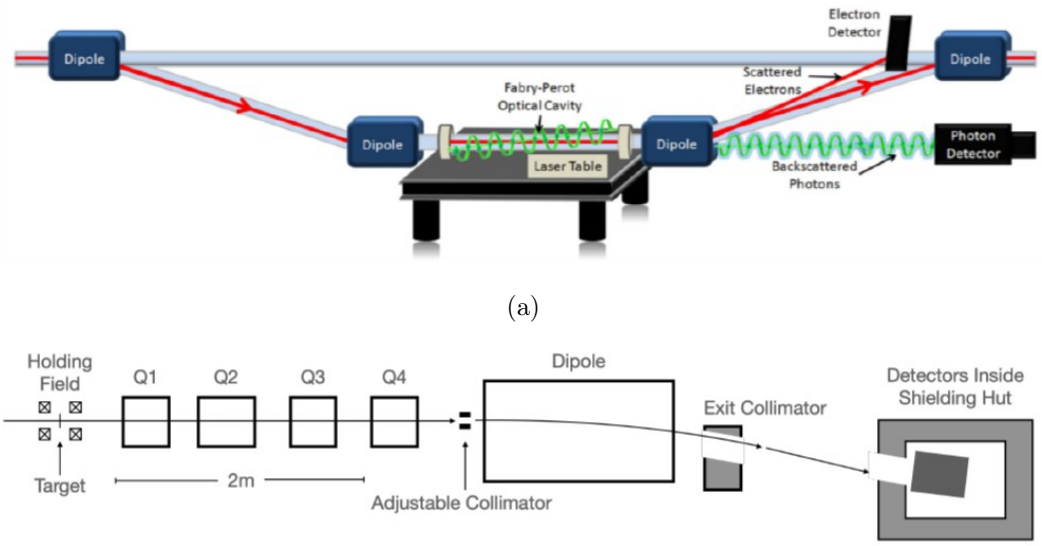

Figure 4.8: Top: A diagrom of the Hall A Compton Polarimeter reproduced from [118]. Bottom: A diagram of the Hall A Møller Polarimeter reproduced from [122].

4.2.2 Target

The SBS G_M^n and nTPE experiments used a target system consisting of both cryogenic and solid targets sealed in a scattering vacuum chamber. The cryogenic targets included

both liquid hydrogen (LH_2) and liquid deuterium (LD_2) loops. The LH_2 loop allowed scattering from only protons, which is used for a detector calibration necessary for evaluating a dominant systematic uncertainty. The LD_2 loop provided access to scattering from protons and neutrons simultaneously, and was necessary for the main physics result. The solid targets consisted of thin foil Carbon and Aluminum targets used for calibrating spectrometer optics and measuring contributions due to cryotarget cell walls. This section will describe the main properties of the scattering chamber, cryogenic targets, and solid targets.

Scattering Chamber

The target scattering vacuum chamber is a cylinder mounted vertically on a central pivot post. The main portion of the scattering chamber is composed of a stainless-steel base ring, an aluminum middle ring, and an upper ring. The ring segments have a diameter of 1037 mm, and the pivot support has a diameter of 607 mm. The base ring has ports for various functions including vacuum pumping, electrical feedback, and internal viewing. The middle ring is located at beam height and has vertical cutouts on the full angular range to serve as entry and exit ways for the electron beam and the scattered particles respectively. These vertical cutouts are covered with thin ($\approx$0.38 mm) aluminum foils. The upper ring houses the support for the target ladder, which holds both cryogenic and solid targets. [121]. The internal structure of the scattering chamber and the target ladder can be seen in Fig. 4.9a and 4.9b. The outside and scattering chamber as it was being assembled is shown in Fig. 4.10.

Cryogenic Targets

The standard Hall A cryogenic target system has three independent target loops: a LH_2 loop, a LD_2 loop, and a gaseous helium loop. In Fig. 4.9a the target ladder with cylindrical tube cryotargets are shown; in this diagram the electron beam would traverse from the entrance window on the right to the exit window on the left along the direction of a

single loop. The cryotarget cell is made of Al 7075 material. For the SBS G_M^n and nTPE experiments only the LH_2 and LD_2 loops were instrumented. The liquid cryogens circulate through each loop, driven by a fan. The liquid cryogen loops include aluminum cylindrical cells with rounded exit windows, mounted on the target ladder. The dimensions and specifications for the aluminum target cells are shown in Table 4.1. The target cell diameter is 63.5 mm. The operating temperatures for the LH_2 and LD_2 loops are 19 K and 22 K, respectively. The cyrogenic targets are cooled to the operating temperatures by a heat exchanger with helium coolant supplied at a temperature of 15 K from the End Station Refrigerator (ESR). The liquid cryogen flows through the target cell and interacts with the electron beam, which slightly heats up the cryogen. The helium coolant exchanges some of the power deposited from the electron beam and is returned to ESR at slightly more than 20 K. Overall, the maximum cooling power of the 15 K helium is 1 kW [121]. Each target loop uses small heaters to stabilize the cryogenic target at the operational temperature, accounting for both macroscopic differences and microscopic fluctuations. The coolant supply for each cryogenic target cell is controlled with a Joule-Thomson (JT) valve that is able to be adjusted both remotely and locally.

Target	Entrance Thickness (mm)	Exit Thickness (mm)	Wall Thickness (mm)	Length (mm)
LH_2 (top)	0.145 ± 0.004	0.158 ± 0.012	0.143 ± 0.009	150.00 ± 0.26
LH_2 (bot)	0.132 ± 0.004	0.152 ± 0.009	0.136 ± 0.009	150.00 ± 0.26
LD_2 (top)	0.125 ± 0.004	0.138 ± 0.007	0.136 ± 0.008	150.00 ± 0.26
LD_2 (bot)	0.119 ± 0.003	0.155 ± 0.008	0.137 ± 0.015	150.00 ± 0.26

Table 4.1: Cryogenic target cell specifications. Adapted from [123].

Solid Targets

The solid targets were instrumented for apparatus calibrations and systematic studies. Single foil carbon targets, one with a 2 mm diameter center hole and one with a 5 mm diameter center hole (carbon "hole" targets), were available for evaluating the electron

beam profile in the scattering region. Two multi-foil (5-foil and 4-foil) carbon targets were instrumented for spectrometer optics calibration. A single foil carbon target was included for detector checkouts. The dummy targets consisting of a pair of aluminum foils were included to evaluate the contributions of the entrance and exit windows of the cryogenic targets. The single foil carbon targets each had a foil at $z = 0$ cm. The two sets of multi-foil optics targets had foils at the locations:

- a 4-foil carbon target with foils at $z = \pm 2.5$ cm and $z = \pm 7.5$ cm,
- a 5-foil carbon target with foils at $z = 0$ cm, $z = \pm 5$ cm, and $z = \pm 10$ cm.

The aluminum foil dummy targets were located at the same z-position as the entrance and exit windows of the cryocells. The dummy targets had foils at $z = \pm 7.5$ cm. Detailed specifications about the material properties of all solid targets can be found in [123].

Target	Total Thickness (g/cm^2)	Material
Dummy Upstream	0.350 ± 0.0003	Al 7075
Dummy Downstream	0.349 ± 0.0003	Al 7075
Optics	0.044 ± 0.001	carbon (99.95%)
Carbon Hole	0.044 ± 0.001	carbon (99.95%)
Carbon 0.5%	0.1740 ± 0.00035	carbon (99.95%)

Table 4.2: Solid target foil specifications. Adapted from [123].

4.2.3 BigBite Spectrometer

The BigBite Spectrometer detects scattered electrons, specifically it measures the momentum and angle of the scattered electrons. The BigBite Spectrometer consists of a single dipole magnet and a detector system. The BigBite detector system for this experiment includes 5 layers of Gas Electron Multiplier (GEM) tracking detectors, a Gas Ring Imaging Cherenkov (GRINCH) detector, a Timing Hodoscope, and Preshower and Shower Calorimeters. A picture of the BigBite Spectrometer from the SBS G_M^n and nTPE experiments run period is displayed in Fig. 4.11. The remainder of this section will describe the specifications and details for each of the sub-systems of the BigBite Spectrometer.

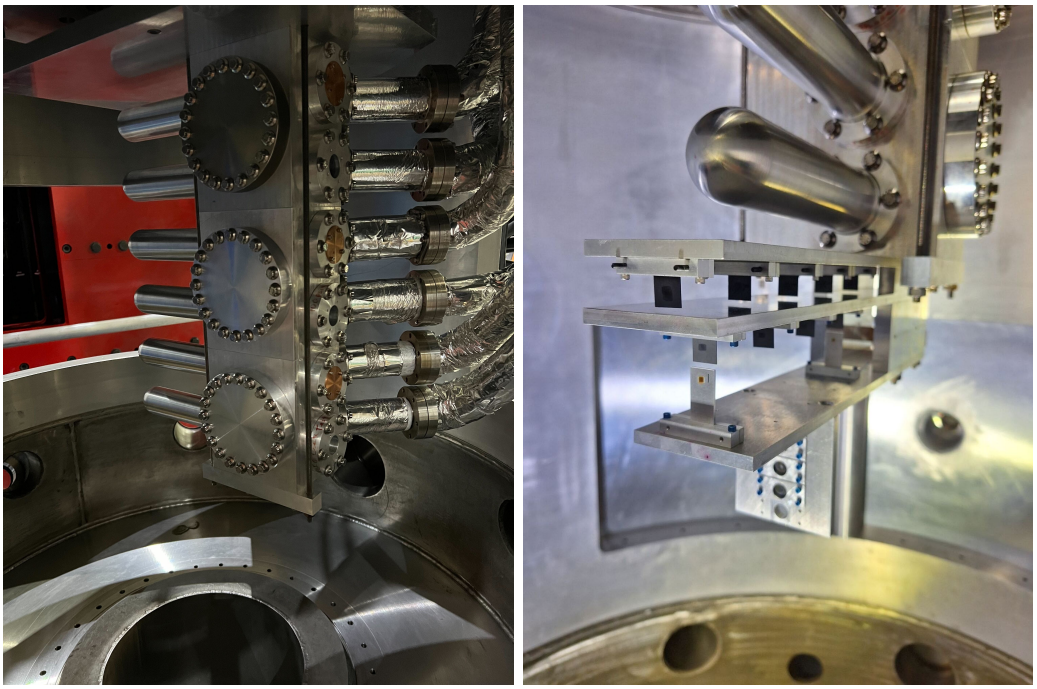

(a) (b)

Figure 4.9: Left: Inside of the target scattering chamber showing the standard Hall A target ladder, holding both cryogenic and solid targets. The Beam traverses from right (entrance window) to left (exit window) along the length of the cryocell. The target ladder is shown with 7 cryogenic cells, however, for this experiment only 2 cryogenic cells were used. The standard Hall A target ladder is typically instrumented for 3 different cryogens (hydrogen, helium, and deuterium), with 2 cells for each type of cryogen; one entrance window with a copper radiator and one without. There is also a spare cryocell available. Right: A close-up of the solid targets on the target ladder.

BigBite Magnet

The 20 ton BigBite dipole magnet [105, 124] constructed at the Budker Institute was originally used at NIKHEF and was later used in experiments during the 6 GeV era of CEBAF. A front facing picture of the BigBite magnet taken from the target region is shown in Fig. 4.12a and a side view is in Fig. 4.12b. Both are pictures of the BigBite magnet in Hall A. The horizontal and vertical openings of the magnet yoke are 25 cm and 148 cm respectively. The yoke and the polar pieces of BigBite magnet are composed of low-carbon steel. The BigBite magnet is water-cooled using a series of hollow copper pipes. The nominal magnetic field of the BigBite magnet is approximately 1.2 T. To reach a

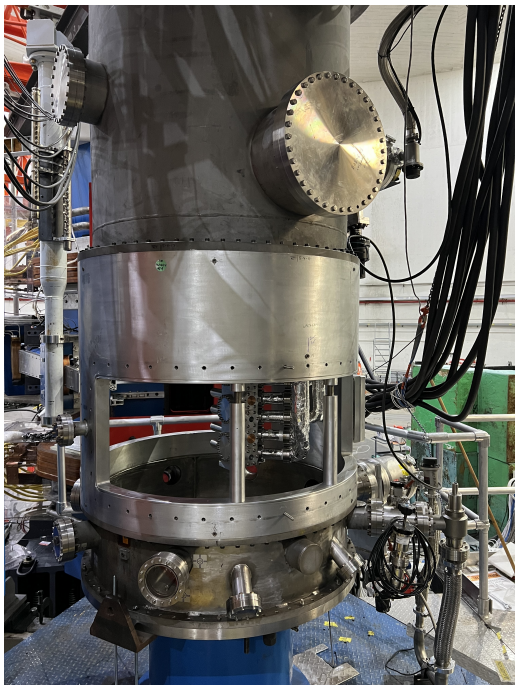

Figure 4.10: Outside of scattering chamber during assembly, as viewed from upstream.

magnetic field of 1.2 T requires a current of 750 A. The angular acceptance of the BigBite magnet is 53 msr, for a target 1.6 m upstream of the magnet placement. The BigBite magnet deflects charged particles of the correct sign, primarily scattered electrons, into the detector package of the BigBite Specrometer.

Gas Electron Multipliers (GEMs)

Gas Electron Multiplier (GEM) detectors were used in the BigBite Spectrometer for charged particle tracking. A general GEM detector description and details pertaining to the GEM detectors for the SBS program are the focus of Chapter 5. Further supplementary technical information pertaining to the GEM detectors for the SBS program is presented in Appendix A.

The BigBite Spectrometer is instrumented with five GEM layers total. Four GEM layers were front-tracker layers, each with an active area of 150 cm $\times$ 40 cm. The front-tracker GEM layers were located between the BigBite magnet and the GRINCH detector.

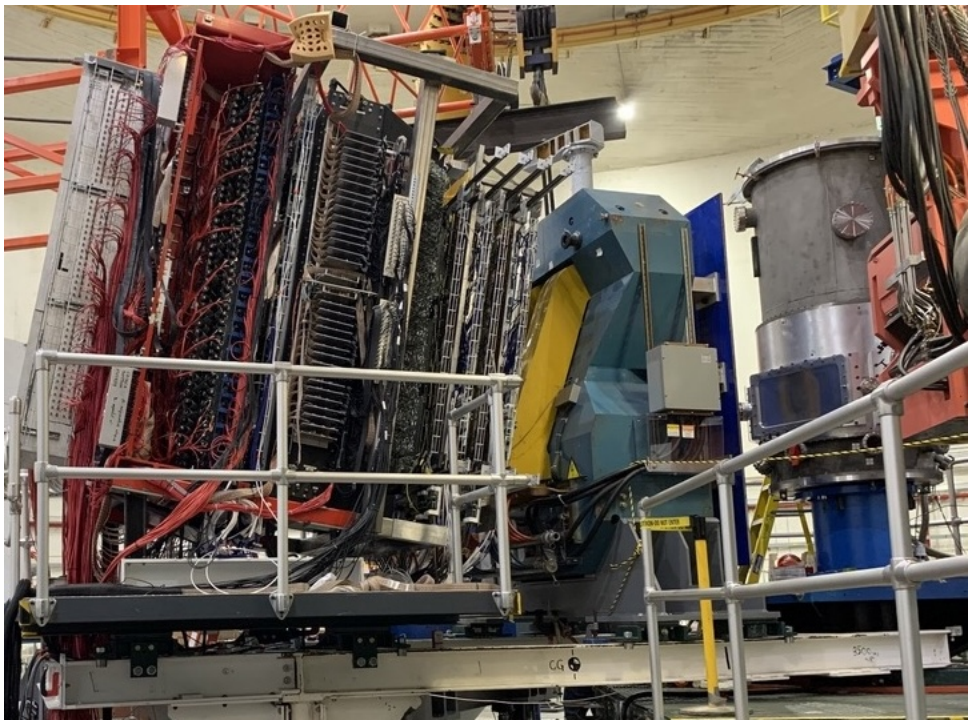

Figure 4.11: A picture of the BigBite Spectrometer in Hall A, with the target chamber on the right.

The fifth GEM layer serves as a back-tracker and was located between the GRINCH detector and the Preshower calorimeter. The back-tracker GEM layer had an active of 200 cm $\times$ 60 cm.

Gas Ring Imaging Cherenkov

The Gas RINg Imaging CHerenkov (GRINCH) detector was instrumented in the BigBite Spectrometer for the purpose of particle identification, primarily discriminating between electrons and pions. Further information and details about the GRINCH detector system is available from Ref. [125]. The GRINCH detector was located between the 4 front tracker GEM layers and the 1 back tracker GEM layer. Cherenkov radiation is electromagnetic radiation produced when a charged particle passes through a medium with a speed greater than the phase velocity of light in that medium. The concept of a Cherenkov particle identification detector is that charged particles with speed below the threshold will pro-

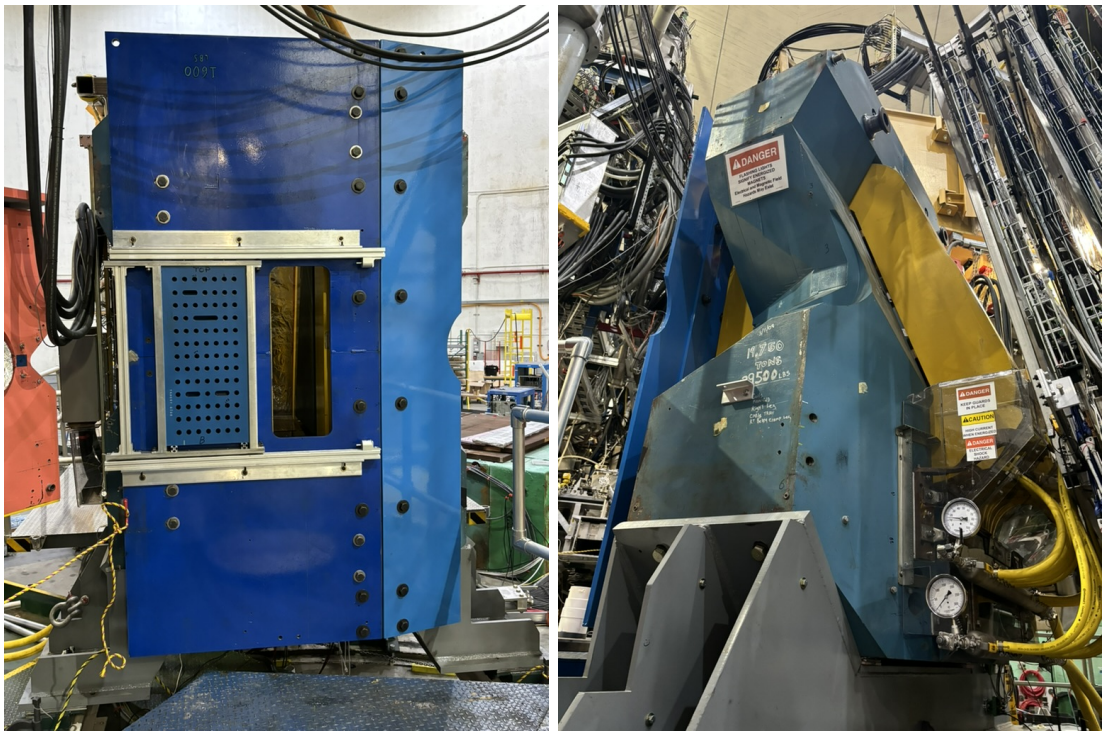

(a) (b)

Figure 4.12: Left: The BigBite magnet taken from the target region. Also displayed is the sieve collimator. Right: A side view of the BigBite magnet, showing the yoke, polar regions, and coolant system.

duce Cherenkov radiation and produce a signal, whereas particles above the threshold will not radiate and therefore not generate any signal. The pion threshold of GRINCH is 2.7 GeV/c, using the heavy gas C_4F_8. The GRINCH detector assembly [126] is composed of 510 28.2 mm diameter photomultiplier tubes (PMTs) in a honeycomb array, 4 highly reflective cylindrical mirrors, a gas distribution system, and a magnetically shielded box with dimensions 48.82 in $\times$ 35.00 in $\times$ 97.62 in. The GRINCH box assembly is composed of components with the following material properties: steel, stainless steel, aluminum, and G-10 fiberglass. The internal and exterior structure of GRINCH are shown in Figs. 4.13a and 4.13b respectively. The data acquisition electronics associated with the GRINCH include 32 ASIC NINO amplifier/discriminator cards [127] (16 channels per card), 4 VETROC TDC modules [128] (128 channels per module), 1 global trigger processor, 1 trigger in-

terface, and 2 fADC250 modules [129]. The low voltage for the GRINCH NINO cards is supplied by a KEYSIGHT N5744A DC supply. Each NINO cards requires 5 V and 1.5 A for normal operation. The GRINCH detector was commissioned during the earlier parts of the G_M^n and nTPE run period, and was not required for the completion of either experiment. During the earlier kinematics of the G_M^n and nTPE run period GRINCH was filled with CO_2 gas before kinematics SBS8 and SBS9. For both kinematics SBS8 and SBS9 the heavy gas C_4F_8 was present, and though GRINCH is not an essential detector for this analysis, properly calibrated data from GRINCH is available and could be used in related analysis for better constraining inelastic backgrounds.

(a) (b)

Figure 4.13: Left: The GRINCH from a side view showing the cylindrical mirrors. Right: A side view of the GRINCH installed in BigBite, taken from beam left, showing the PMT array and front-end NINO electronics.

Each GRINCH PMT was manufactured with the technical specification of ETL 9125B and originally instrumented for the BaBar DIRC detector [130]. The PMTs were immersed in deionized water for 10 years, which led to surface damage of the tube's photocathodes. Prior to instrumentation into the GRINCH detector, thin fused silica disks were glued onto the photocathode windows. Each GRINCH PMT was outfitted with a reflective cone around the perimeter of the photocathode made of thermoplastic. Both the thin fused silica disks and the thermoplastic reflective cones improved each PMT's light collection efficiency and thus the number of detected photons. The primary purpose of the PMTs is to collect any light within the GRINCH and then via a photocathode convert photons to electrons. These electrons are further amplified to generate a signal which can be read out via electronics. During regular data collection the GRINCH PMTs are kept at high-voltage which is provided by SHV cables connected to six 12 channel LeCroy 1421 P modules located in a LeCroy 1458 high volatage mainframe.

Other key components of the GRINCH assembly are 4 highly-reflective cylindrical mirrors. The mirrors have a radius of curvature of 130 cm. Each mirror is made of a metallic-coated Lexan sheet; the mirror coating is a composite of aluminum and magnesium fluoride [131]. All of the mirrors are located in a frame that holds the mirrors by the sides. This frame construction allows the frame to be adjusted in order to align the mirror system. Also, the frame structure applies a force on the sides of the mirror-coated Lexan sheets to reach the desired curvature. The primary function of the cylindrical mirrors is to focus Cherenkov radiation produced inside the GRINCH box onto the acceptance of the PMTs.

The GRINCH gas distribution system is composed of various pressure system elements, which directly connect to the Cherenkov pressure vessel to maintain an absolute pressure slightly above 1.0 atm. The GRINCH gas distribution system either provides CO_2 gas or C_4F_8 heavy gas. The CO_2 gas is relatively inexpensive and is used for initial testing of detector performance. The C_4F_8 heavy gas has an index of refraction n=1.00135 (at 1 atm) and is chosen to produce Cherenkov radiation for electrons and not pions, for the range of momenta accepted by BigBite.

The GRINCH primarily provides time-to-digital-converter (TDC) information from each PMT to the global experiment data acquisition system. A full schematic of the DAQ components for the GRINCH subsystem is shown in Fig. 4.14. The 32 front-end NINO cards near GRINCH are connected to 32 100 m ribbon cables which connect to an intermediate LVDS to ECL translator patch panel. Subsequently, 32 more 100 m ribbon cables are connected from this translator board to the 4 VETROC TDC modules located in the larger DAQ electronics bunker. Each NINO front-end card [127] includes an amplifier, discriminator, and an input charge measurement by time-over-threshold for slewing correction. The VETROC board [128] is a high-rate pipelining TDC module. The TDC words have a dynamic range of 32 bits, and each board has 128 channels for data input. The VETROC has a bandwidth of four gigabytes per second. For more complicated trigger systems the VETROC module is equipped with an FPGA. The GRINCH also has 4 NINO cards for analog-to-digital-convertor (ADC) information. The 4 NINOs for analog information are connected to 2 fADC250 modules [129] via 64 channels of flat BNC cables. The global trigger processor and trigger interface pertain to the overall experiment DAQ system which will be described in more detail in Secs. 4.2.5,4.2.6.

Timing Hodoscope

The Timing Hodoscope detector [132][133] was instrumented in the BigBite Spectrometer for the function of high precision timing reference, with high efficiency for minimum ionizing particles over the range of scattered electron momenta. In the middle of each part of Fig. 4.16a and 4.16b is shown the Timing Hodoscope in the BigBite Spectrometer. The Timing Hodoscope is a vertical array of 90 Eljen Technologies EJ200 plastic scintillator bars and was located between the Preshower and Shower Calorimeters. The two types of fully-assembled scintillator bars is shown in Fig. 4.15. The dimensions of each scintillator bar is $600 \times 25 \times 25$ mm^3. Each scintillator bar has dual-edge readout with an attached light guide and PMT on each side. Both ends of each scintillator bar are connected to a 24 mm diameter Eljen Technologies UVT acrylic rod light guide via Dymax 3094 light-

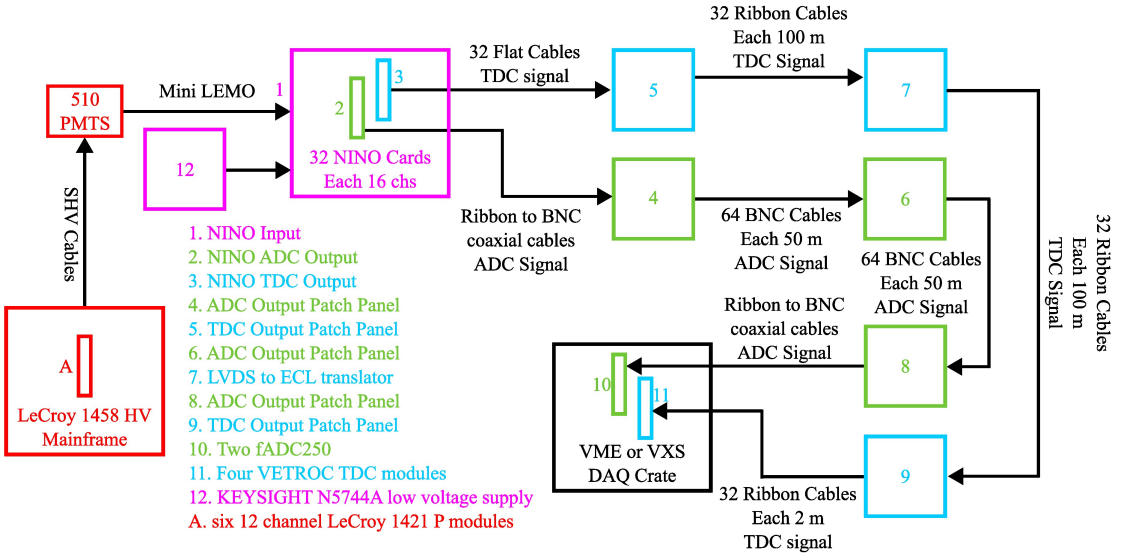

Figure 4.14: Schematic for GRINCH data acquisition and readout electronics. For the TDC signal, the GRINCH used 32 NINO cards, which reads out the all GRINCH PMTs. For the ADC signal, only a portion of the GRINCH PMTs were read out and this used 4 NINO cards.

curable plastic bonding adhesive. To fit a high density of light guides in the constrained space of the detector, the light guides alternate between straight and curved geometries over the vertical direction of the scintillator stack. Each light guide is connected to an Electron Tubes ET9124SB single channel PMT, for a total of 180 readout channels for the Timing Hodoscope. Each PMT base is housed within an assembly that incorporates MuMETAL for electromagnetic shielding. The high-voltage for the PMTs is supplied by a CAEN SY1527LC mainframe, equipped with 4 CAEN A1932A 48-channel HV distributor boards. A series of metal supports are implemented to hold the entire scintillator assembly so that it is aligned in the same focal plane as the other detector subsystems of the BigBite Spectrometer.

An overall flow diagram of the data acquisition components specific to the Timing Hodoscope subsystem is present in Fig. 4.17. The signals from the PMTs are read out to 12 front-end amplifier/discriminator NINO cards (16 channels per card) [127] by 180 coaxial signal cables, each with a length of 1.5 m. The low voltage for the NINO cards

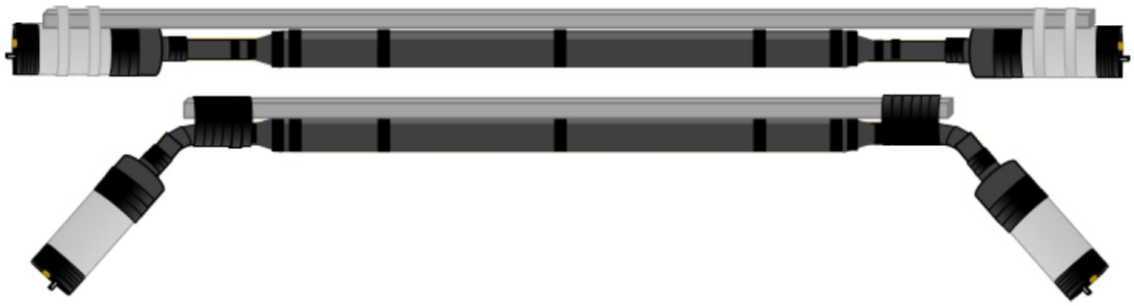

Figure 4.15: A diagram of the two types of scintillator bar assemblies, showing the light-tight scintillator bars, the light guides, the PMT housings, and support bars. Adapted from [132].

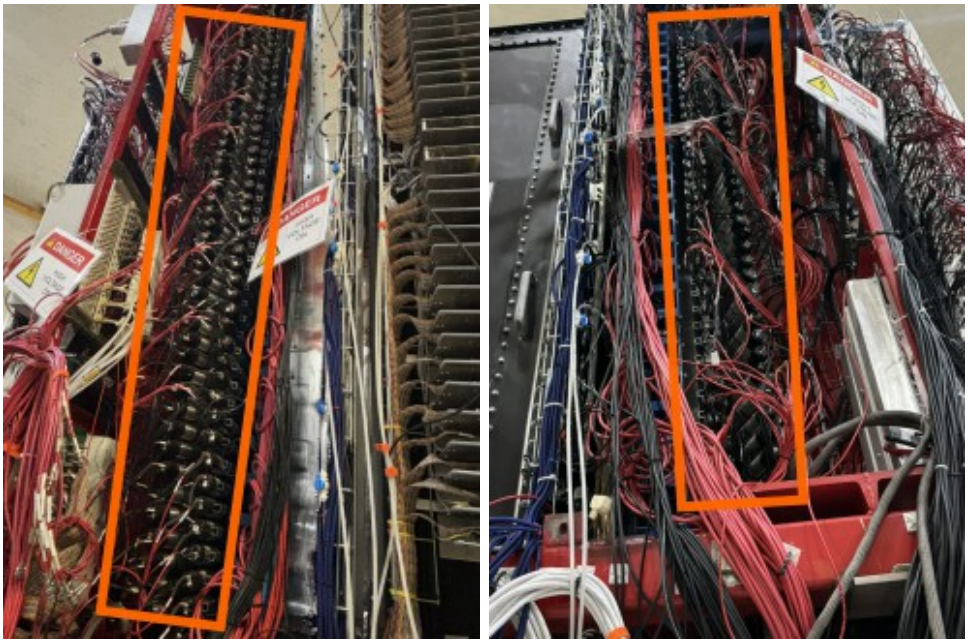

(a) (b)

Figure 4.16: Left: The Timing Hodoscope side view as seen from beam left. Right: The Timing Hodoscope side view as seen from beam right, with some electronics. In both orientations the Timing Hodoscope is outlined in orange.

is supplied by a KEYSIGHT N5744A DC supply. All 180 TDC channels are read out by the 12 NINO cards, both during commissioning and production data operation. First, a description of the path the TDC signals traverse. The TDC signals start in the NINO card

and travel through twelve 34-way twisted ribbon cables of length 2 m, and connect from the NINO cards to the TDC patch panel on the beam-left side of the BigBite Spectrometer support frame. From the TDC patch panel on the BigBite frame, the TDC signal goes to an LVDS-ECL level translator in a separate electronics rack by twelve 34-way twisted ribbon cables of length 40 m. Then, by twelve 34-way twisted ribbon cables of length 10 m, the TDC signal goes from the level translator to a TDC patch panel in the main electronics bunker. From the TDC patch panel in the electronics bunker to the input of the CAEN VME v1190 TDC, twelve 34-way twisted ribbon cables of length 1 m are used to transmit the TDC signal. A subset of 4 NINO cards were used to read out ADC channels; only 64 ADC channels were read out, which were primarily used as diagnostics during experiment commissioning. To now describe the path of the ADC signal cables. First the ADC signals traverse eight 34-way twisted ribbon cables of length 2 m, soldered to 16 way co-axial ribbon cable which connects the NINO cards to the ADC patch panel on the beam-left side of the BigBite Spectrometer support frame. To connect the ADC signal from the ADC patch panel on the BigBite frame to the ADC patch panel in the main electronics bunker, 64 coaxial cables with BNC connectors each of length 100 m are used to transmit the ADC signal. From the ADC patch panel in the electronics bunker to the 4 fADC250 modules [129], 64 individual coaxial cables of length 5 m with one side a BNC connector and the other a LEMO connector are used to transmit the ADC signal.

Preshower and Shower Calorimeters

The Preshower (PS) and Shower (SH) Calorimeters were instrumented in the BigBite Spectrometer; together they are called the BigBite Calorimeter [134], or BBCal. The primary functions of the BigBite Calorimeter is to measure the energy of scattered electrons. The energy deposition in the PS is used for pion rejection, to provide position information used to constrain the electron track search region, and to provide the experimental trigger for the data acquisition. The BigBite Calorimeter as part of the BigBite Spectrometer is shown in Fig. 4.18. The BigBite Calorimeter is constructed from lead-glass blocks which

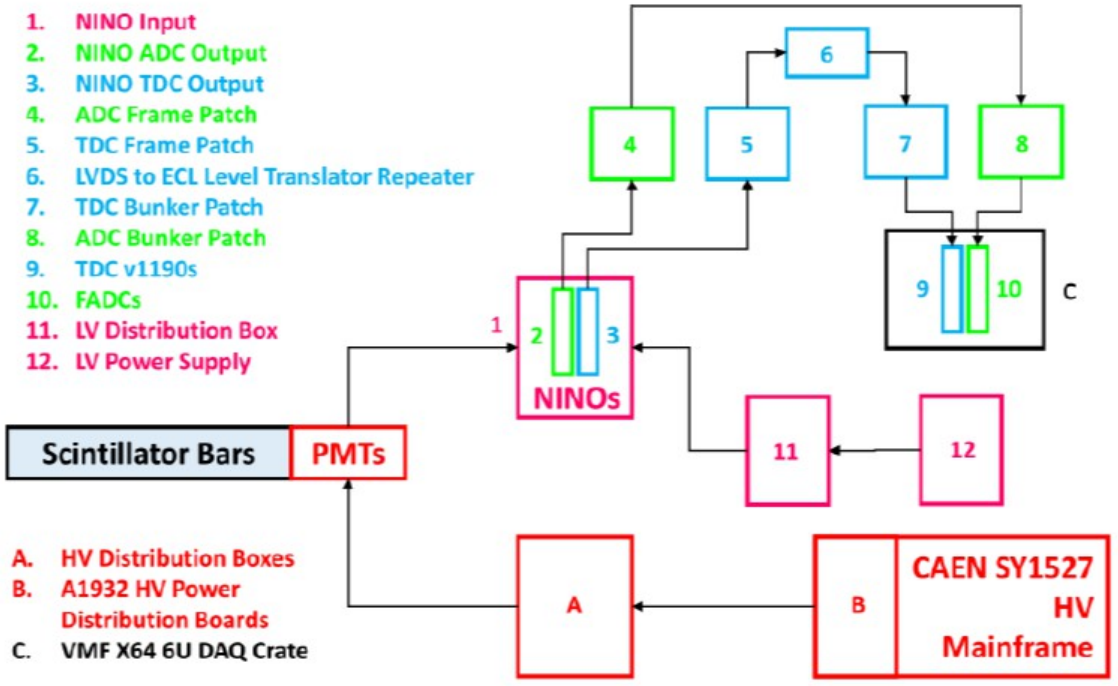

Figure 4.17: Schematic for Timing Hodoscope data acquisition and readout electronics, reproduced from [132].

operate by the formation of an electromagnetic shower as energy is deposited by energetic electrons. The PS Calorimeter is an array of 52 (26 rows $\times$ 2 columns) F101 lead-glass blocks contained in a metallic support structure. The organization of the PS blocks is shown on the left of Fig. 4.19. The dimensions of each PS lead-glass block is 9.0 $\times$ 9.0 $\times$ 29.5 cm^3. A diagram of an individual PS block is in the left of Fig. 4.20. Each PS lead-glass block has 2 layers of surface wrapping. The inner layer is made of aluminized Mylar foil and is oriented such that the Mylar side makes contact with the block and the aluminized side makes contact with the outer layer. The outer layer is made of Tedlar foil. The combined wrapping of aluminized Mylar foil and Tedlar foil serves to provide light isolation to the PS block. Each PS block is connected to a 7.5 cm Philips XP3461 PMT [135] via a light guide and epoxy. Each PS PMT is housed within an assembly of 0.05 inch thick MuMETAL, for magnetic field shielding. Each PS PMT high-voltage can be individually manipulated; the high-voltage is supplied by five 12-channel LeCroy 1461N

modules located in a LeCroy 1458 high-voltage mainframe.

The SH Calorimeter is an assembly of 189 (27 rows $\times$ 7 columns) TF1 lead-glass blocks sealed in a metallic light-tight box. The schematic of the SH blocks is shown on the right of Fig. 4.19. Each SH lead-glass block has dimensions of 8.5 $\times$ 8.5 $\times$ 34 cm^3. A diagram of an individual SH block is in the right of Fig. 4.20. Each SH lead-glass block has 1 layer of aluminized Mylar foil wrapping, the foil is oriented such that the Mylar side makes contact with the block and the aluminized side makes contact with any other blocks in the assembly. The aluminized Mylar foil is to provide another form of light isolation for the SH blocks. For the SH blocks, each is connected to either a 7.0 cm IHEP FEU-110 PMT [136, 137] or a 7.6 cm Photonis XP5312B PMT [119], each PMT is connected to the lead-glass block via epoxy and a light guide. The SH PMTs are encased either 0.04 inch or 0.05 inch thick MuMETAL, in alternating layers, for electromagnetic shielding. Each SH PMT high-voltage can be individually manipulated; the high-voltage is supplied by sixteen 12-channel LeCroy 1461N modules located in a LeCroy 1458 high-voltage mainframe.

A flow diagram of the data acquisition components specific to the BigBite Calorimeter subsystem is shown in Fig. 4.21. Since the BigBite Calorimeter is composed of both PS and SH calorimeters, a description of each detectors electronics will follow respectively. For each of the 52 PS PMTs, first a signal goes from the PMT to a Phillips Scientific NIM Model 776 2-output 10x gain amplifier via a 12.5 m coaxial signal cable with BNC connectors. One output of the PS signal goes from the amplifier to a channel on 4 fADC250 modules [129] via a 50 m coaxial signal cable with BNC connectors. The second output of the PS signal goes from the amplifier to a 2-output custom passive splitter module. The signal from the passive splitter goes to a pair of Phillips Scientific NIM Model 740 Quad Linear Fan-in/Fan-out module and LeCroy 428F Quad Linear Fan-in/Fan-out module. The Quad Linear Fan-in/Fan-out modules are used to combine the signals for one layer of the left and right PMTs in the PS calorimeter. The outputs of the first set of Quad Linear Fan-in/Fan-out modules goes to a second set of Phillips Scientific NIM Model 740 Quad Linear Fan-in/Fan-out modules. The second set of Quad Linear Fan-in/Fan-out

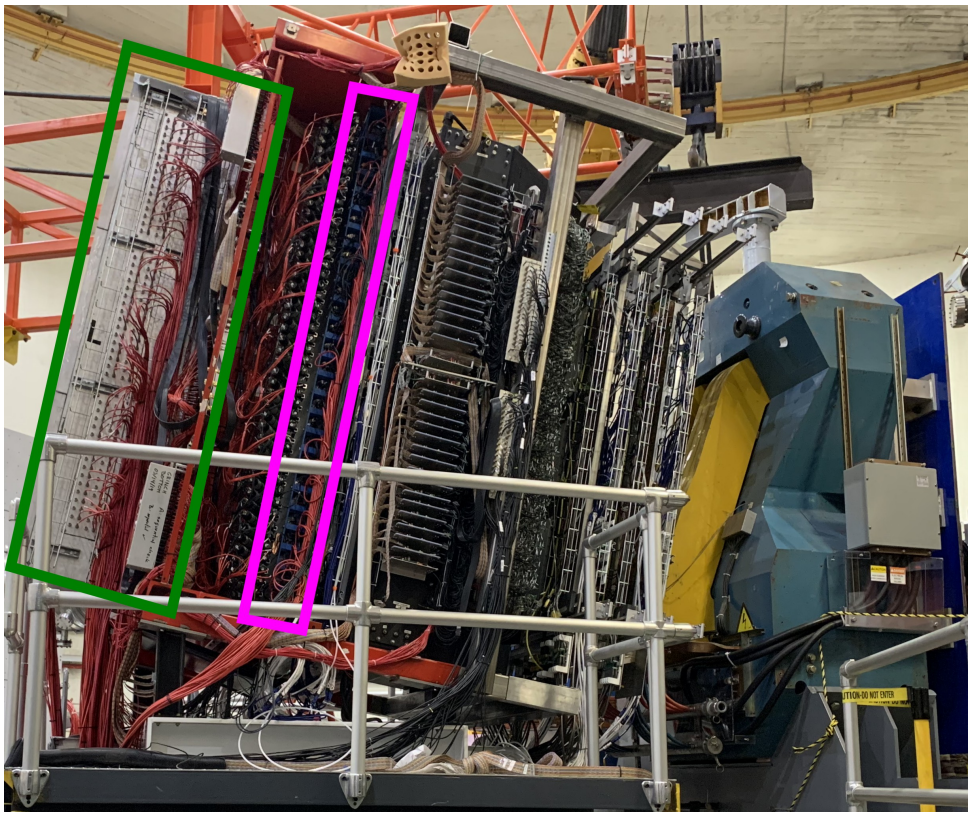

Figure 4.18: The BigBite Calorimeter as seen from beam left; the PS is outlined in magenta and SH is outlined in green.

modules are used to combine the signals for the overlapping row sum in each PS and SH layer. For each of the 189 SH PMTs, first a signal goes from the PMT to a channel of 14 custom 7-channel Amplifier/Summer module via a 12.5 m coaxial signal cable with BNC connectors. One output of the SH signal goes from the Amplifier/Summer module to a channel on 13 fADC250 modules [129] via a 50 m coaxial signal cable with BNC connectors. The second output of SH signal goes from the Amplifier/Summer module a set of Phillips Scientific NIM Model 740 Quad Linear Fan-in/Fan-out modules. This set of Quad Linear Fan-in/Fan-out modules are used to combine the signals for the overlapping row sum in each PS and SH layer. The overlapping row sums for the PS and SH and the association with the trigger and the DAQ will be described in more detail in Secs. 4.2.5,4.2.6.

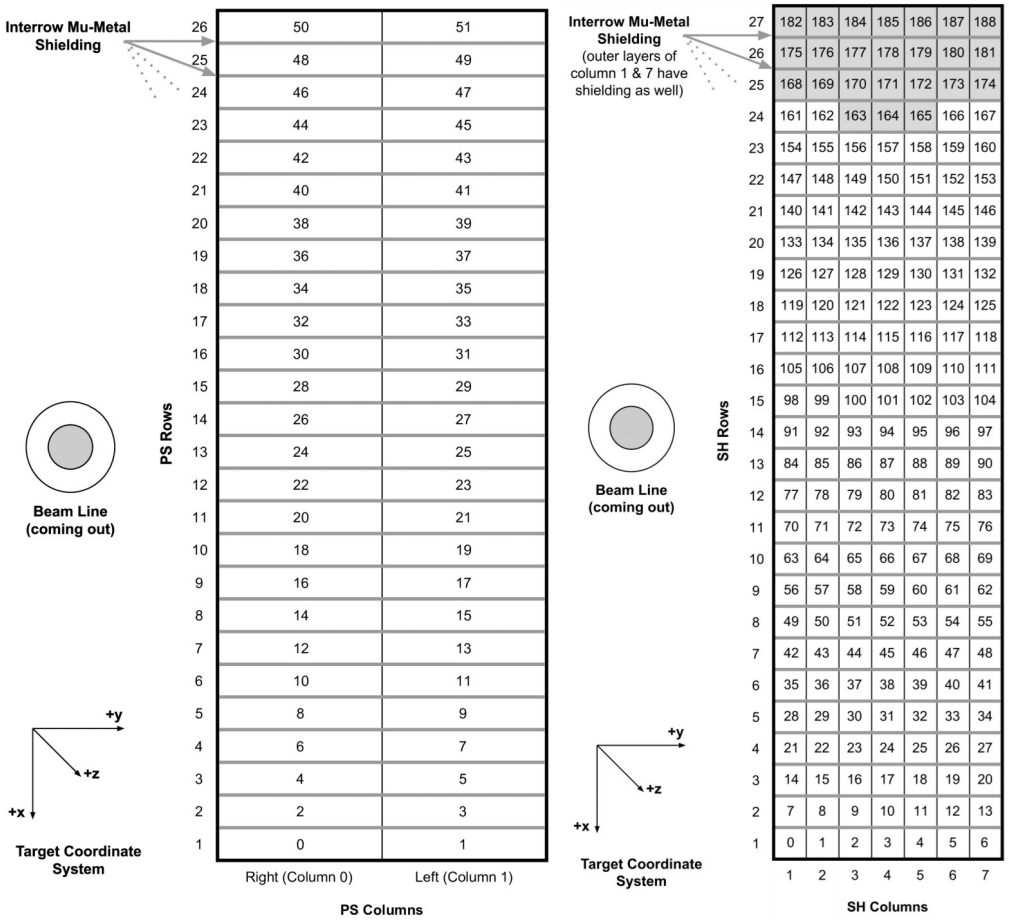

Figure 4.19: Block Mapping for the BigBite Calorimeter. Left is for PS blocks and right is for SH blocks. The diagram is from the down-stream perspective of the BigBite Spectrometer.

4.2.4 Super BigBite Spectrometer

The Super BigBite Spectrometer detects scattered nucleons, specifically it measures the particle's energy and position information. The Super BigBite Spectrometer, during the SBS G_M^n and nTPE experiments, consisted of a large dipole magnet called Super BigBite (SBS) and a Hadron Calorimeter (HCal). A picture of the SBS magnet is displayed in Fig. 4.22a. A picture of HCal is shown in Fig. 4.23a. The remainder of this section will describe the specifications and details for each of the sub-systems of the Super BigBite Spectrometer.

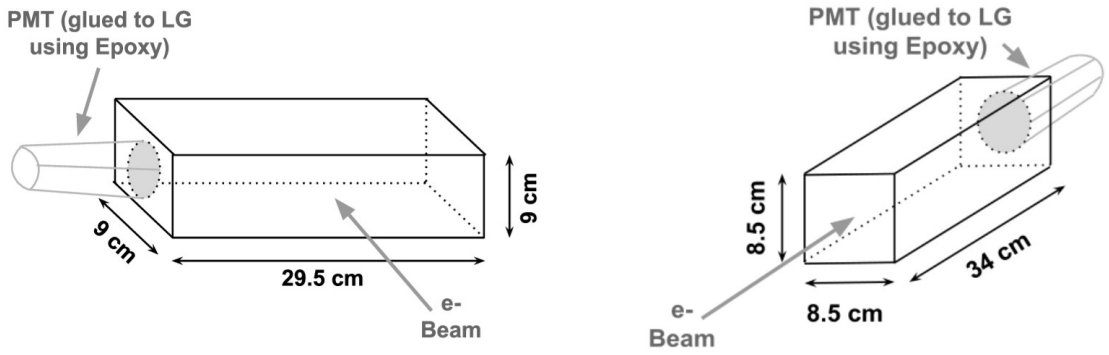

Figure 4.20: Individual BigBite Calorimeter lead-glass blocks. The left is a schematic of a typical block in the PS. The right is a schematic of a typical block in the SH. Reference to the direction of the scattered electron beam is provided.

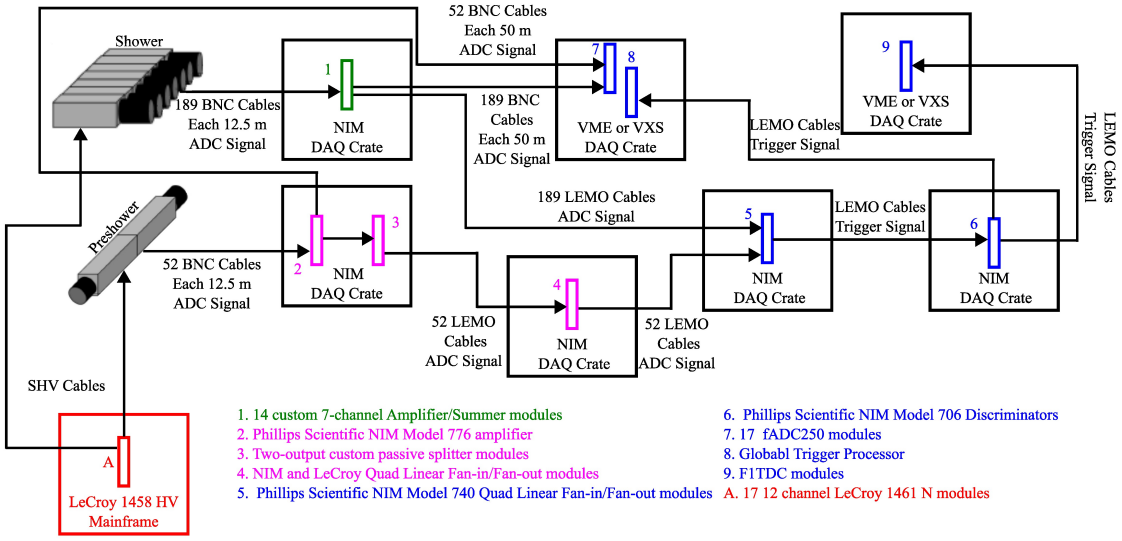

Figure 4.21: Schematic of BigBite Calorimeter data acquisition and readout electronics, adapted from [138].

Super BigBite Magnet

The 100 ton Super BigBite magnet [139] is a modified dipole[1] magnet from Brookhaven National Laboratory, where it was used for the fixed target program with the Alternating Gradient Synchrotron. The Super BigBite magnet has a large aperature with a vertical to horizontal aspect ratio of 2:1 and dimensions of 469 mm $\times$ 1219 mm $\times$ 1219 mm.

[1] At Brookhaven National Laboratory it was known as a 48D48 dipole.

The magnet yoke is composed of five SAE 1008 steel slabs. The magnet is water-cooled using a series of hollow metallic pipes. The magnet has 2 saddle-shaped copper coils, each with 120 turns; these coils generate the magnetic field. The original 48D48 dipole magnet was modified for use at small scattering angles, this modification required a deep cut in the right yoke and a repositioning of the right coils to allow for close proximity with the beamline path. The Super BigBite magnet is capable of producing a field integral of 3 T · m with a 4 kA excitation current. For the SBS G_M^n and nTPE experiments the maximum field integral necessary from the Super BigBite magnet is 1.7 T · m, which requires a 2.1 kA excitation current. The angular acceptance of the Super BigBite magnet is 35 msr. The Super BigBite magnet deflects positively-charged particles away from the Hall floor, which allows the differentiation between quasi-elastically scattered protons and neutrons in the Hadron Calorimeter.

Hadron Calorimeter

The Hadron Calorimeter[140] (HCal, or SBS HCal) is a segmented sampling calorimeter used to measure the energy of 1-10 GeV hadrons. The HCal is designed to have a time resolution of at least 0.5 ns, a position resolution of 3-4 cm for hadrons of energy $\approx$ 8 GeV, and an energy resolution of 30-50%. The design of HCal is based on the COMPASS HCAL1 calorimeter [141] which detects 10-100 GeV hadrons at CERN. The HCal is composed of 288 calorimeter modules, which are arranged into 4 cranable subassemblies. When fully assembled the HCal is an array of 12 columns and 24 rows of individual calorimeter modules, and has a total weight of approximately 40 tons. The HCal in Hall A and the calorimeter module mapping are displayed in Fig. 4.23a and Fig. 4.23b respectively. Each calorimeter module consists of 40 layers of 1 cm thick PPO (2,5 Diphenyloxazole) plastic scintillator alternating with 40 layers of 1.5 cm thick iron absorber, the structure of the module is shown in Fig. 4.24. The iron absorbers and scintillating layers are offset from each other to increase the light output by 20%. Each calorimeter module has dimensions of 15×15 cm^2 with a length of 1 m. Functionally for each calorimeter module, the hadron

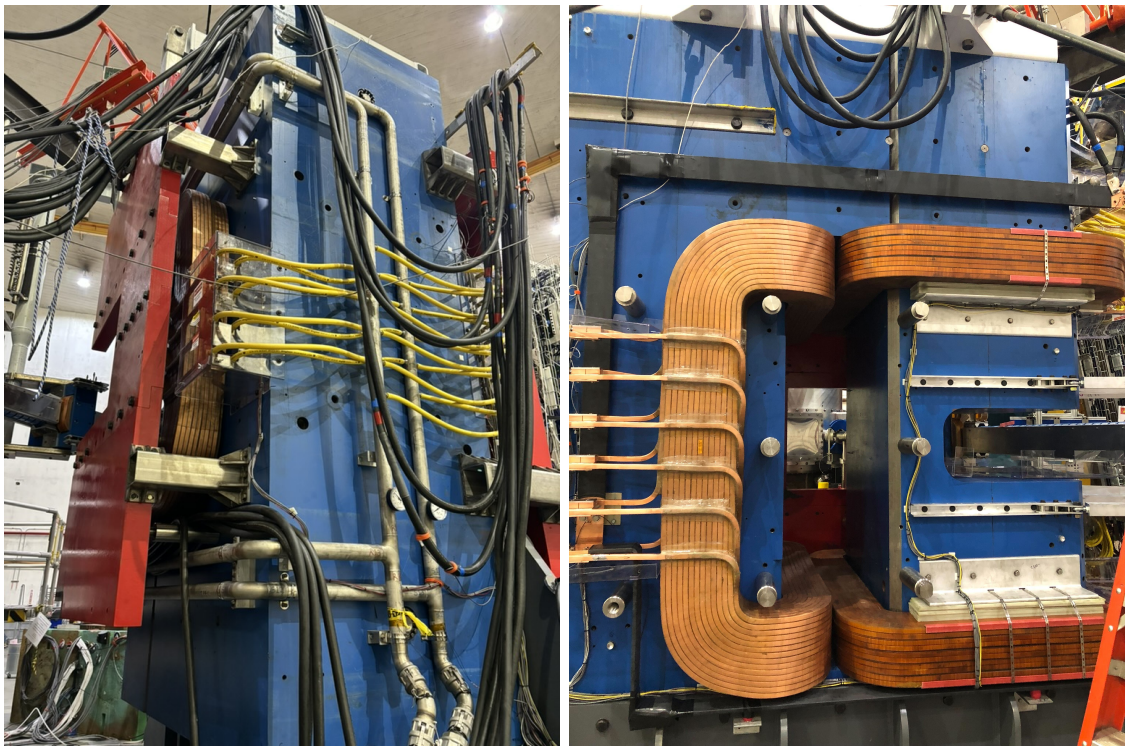

(a) (b)

Figure 4.22: Left: A side view of the SBS magnet. The copper coils are towards the upstream side of the magnet (left side). The yoke of the magnet consists of the blue components. The yellow and silver pipes make up the water-cooling system. The red metallic component attached to the upstream side of the magnet yoke is a field clamp, only an upstream field clamp was present during the G_M^n and nTPE experiments. Right: A downstream view of the SBS magnet.

strikes an iron absorber which may cause a shower and the scintillators produce optical photons from these particle showers. In the center of the layers of iron and scintillator, as shown in Fig. 4.24, is a St. Gobain BC-484 wavelength shifter which has a decay time of 3 ns and is implemented to improve light collection efficiency and uniformity [142]. The photons collected in the wavelength shifter are transported to PMTs on the downstream end of each calorimeter module via a custom-built light guide. For PMTs on the 288 HCal modules, 192 2 inch Photonis XP2262 12-stage and 96 2 inch Photonis XP2282 8-stage PMTs are instrumented throughout the HCal detector. Each HCal PMT high-voltage is instrumented for individual manipulation and is supplied by 24 LeCroy 1461N modules

located in 2 LeCroy 1458 high-voltage mainframes. The HCal high-voltage modules are connected to the PMTs via 75 m SHV cables and 12 high-voltage patch panel boxs, which distribute the SHV cables to the PMTs. HCal is also equipped with an LED pulser system, which is used to calibrate the PMTs.

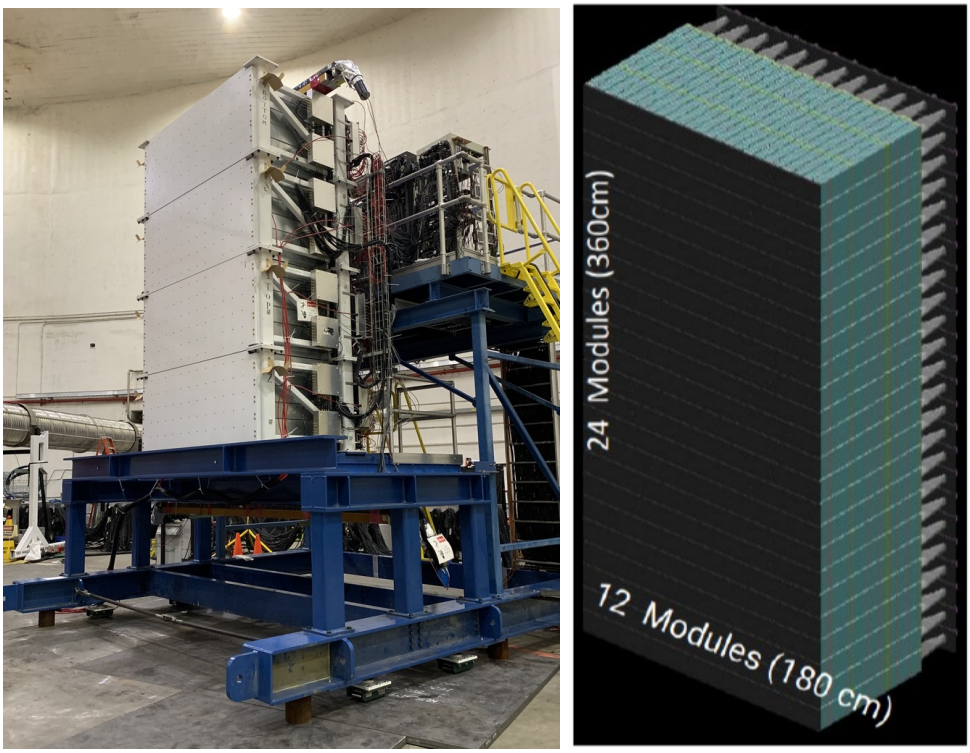

(a) (b)

Figure 4.23: Left: A side view of the Hadron Caloriemter in Hall A. Right: Block mapping for HCal.

The data acquisition components for the HCal are organized into three groups, based on whether the PMT signal flows to the fADC250 modules [129], the F1TDCs [143], or the UVA-120 summing modules.

First we describe the path the PMT signal flows to the fADC250 modules. The 288 PMT analog signals go first to 18 Phillips Scientific NIM Model 776 2-output 10x gain amplifiers via 5 m BNC-LEMO RG58 A/U cables. From the Phillips Scientific NIM Model 776 amplifiers, the PMT analog signal goes to 5 BNC-BNC patch panels near the HCal via

2 m BNC-LEMO RG58 A/U cables. The PMT analog signal then goes from the BNC-BNC patch panels near the HCal to 5 identical BNC-BNC patch panels near the main electronics bunker via two hundred eighty-eight 100 m BNC-BNC RG58 A/U cables. From the BNC-BNC patch panels in the main electronics bunker the PMT analog signal is transmitted to 18 fADC250 modules via 2m BNC-LEMO RG58 A/U cables. The fADC250 modules provide both energy and timing measurements from the PMT signals per triggered event.

Next we describe the path the PMT signal takes to the F1TDCs. The 288 PMT analog signals go first to 18 Phillips Scientific NIM Model 776 2-output 10x gain amplifiers via 5 m BNC-LEMO RG58 A/U cables. From the Phillips Scientific NIM Model 776 amplifiers the PMT analog signal goes to nine 50-50 dual output splitter panels via 2 m BNC-LEMO RG58 A/U cables. The halved PMT signal then exists the 50-50 dual output splitter and travels to 18 Phillips Scientific NIM Model 706 Discriminators via 2 m BNC-LEMO RG58 A/U cables. From the Phillips Scientific NIM Model 706 Discriminators the PMT analog signal goes to 5 BNC-BNC patch panels near the HCal via 2 m BNC-LEMO RG58 A/U cables. The PMT analog signal then goes from the BNC-BNC patch panels near the HCal to 5 identical BNC-BNC patch panels near the main electronics bunker via two hundred eighty-eight 100 m BNC-BNC RG58 A/U cables. From the BNC-BNC patch panels in the main electronics bunker the PMT analog signal is transmitted to 18 LeCroy 2313 CAMAC discriminators via 2 m BNC cables. The PMT signal is transmitted from the LeCroy 2313 CAMAC discriminators to 5 F1TDCs via eighteen 16 channel ribbon cables. The F1TDCs provide timing measurements from the PMT signals per triggered event.

The third set of signals to describe are those that go from the PMTs to the UVA-120 summing modules. The 288 PMT analog signals go first to 18 Phillips Scientific NIM Model 776 2-output 10x gain amplifiers via 5 m BNC-LEMO RG58 A/U cables. From the Phillips Scientific NIM Model 776 amplifiers the PMT analog signal goes to nine 50-50 dual output splitter panels via 2 m BNC-LEMO RG58 A/U cables. The halved PMT signal then exits the 50-50 dual output splitter and travels to 18 UVA-120 summing modules. The UVA-120 summing modules add the analog signal of 16 PMTs together for triggering

and analysis purposes.

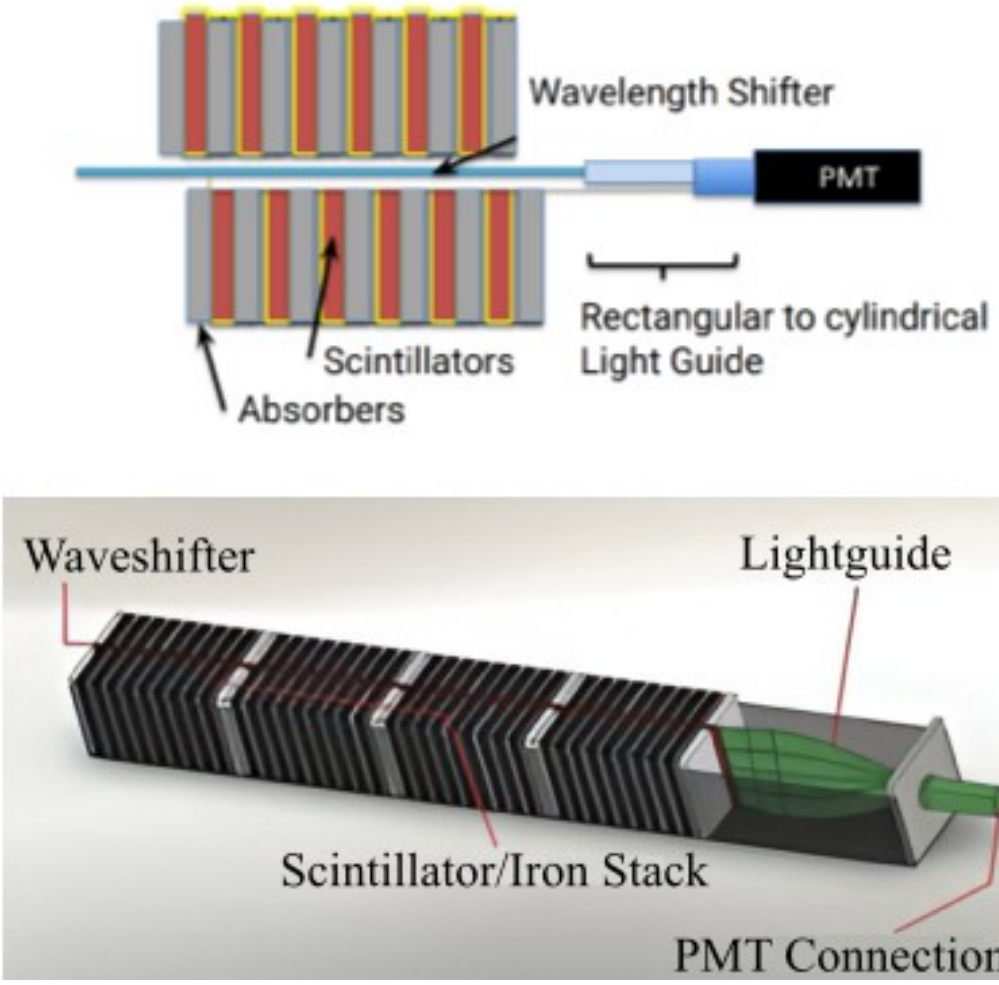

Figure 4.24: The interior of each HCal module consists of alternating layers of iron absorbers and scintillators. The hadrons shower in the iron and these showers create photons in the scintillator. The photons pass through a wavelength shifter before being transported into the PMT via light guides. Diagram adapted from [142].

4.2.5 Trigger System

The main experimental trigger for the the SBS G_M^n and nTPE experiments was a single-arm electron trigger, dependent only on the BigBite PS and SH Calorimeters. Other trigger logic was implemented for some detector systems, including GRINCH and HCal, during

the experiment running. However, these other implemented triggers did not constitute the main trigger for production data collection; they were primarily used for detector diagnostics and performance. As described in detail in Sec. 4.2.3, the PS is a lead-glass module array with 26 rows and 2 columns and the SH is a lead-glass module assembly composed of 27 rows and 7 columns. Based on the materials of the lead-glass blocks, the electromagnetic shower in the calorimeters will typically be contained in a 2×2 module sum for the SH, and a 2 row sum for the PS. From this information one can conclude that the shower of a quasi-elastically scattered electron should be contained in the sum of 2 rows of PS modules plus 2 rows of SH modules. The geometry of the PS and SH lead-glass blocks is not the same, as shown in Fig. 4.20, so there is not a one-to-one correspondence between the sum of 2 rows in the PS and 2 rows in the SH. However, accounting for the difference in the SH and PS lead-glass module geometries, an association between the two sets of modules can be made to have sums of overlapping row modules. That correspondences is displayed in Fig. 4.25a.

The remainder of this section will describe the trigger logic implementation with BigBite Calorimeter signals and how that is connected to the main components of the data acquisition, which are described in Sec. 4.2.6. The overall signal path from the BigBite Calorimeter PMTs through the NIM electronics to the Phillips Scientific NIM Model 740 Quad Linear Fan-in/Fan-out modules is described in detail in Sec. 4.2.3. The Quad Linear Fan-in/Fan-out modules generate a summed signal from the 2 rows in the PS and 2 rows in the SH and this is done for every combination of neighboring sets of 2 rows. A diagram of the all of the row sums overlayed with the lead-glass modules is shown in Fig. 4.25a and a diagram defining the summed signals based on PS and SH block numbers is displayed in Fig. 4.25b. The total sums of the analog signal in the PS and SH rows are then connected to Phillips Scientific NIM Model 706 16 Channel Discriminators. The Discriminator signals are then connected to form a logic "OR" gate, which is implemented using more Phillips Scientific NIM Model 740 Quad Linear Fan-in/Fan-out modules. A trigger signal is issued to the Global Trigger Processor [144] if at least one discriminator output generates a gate

signal. When the Global Trigger Processor receives a signal from the discriminator this causes the Global Trigger Processor to send the trigger signal to the Trigger Supervisor which sends an event readout signal through the distribution system. The event readout signal includes information about trigger, clock, and sync signals. The components of the distribution system include signal distributors [144], Trigger Distributors [145], and Trigger Interfaces [146]. The process of data collection and experimental event generation is described in Sec. 4.2.6.

4.2.6 Data Acquisition

At Jefferson Lab, all experimental data is usually collected through a common software and hardware framework known as CODA (CEBAF Online Data Acquisition) [147]. The overall CODA framework directly connects modular hardware, in the form of front-end electronics and Readout Controllers (ROCs), to an Agent Framework for Experiment Control Systems (AFECS) based user-oriented software package. The CODA software platform manages the acquisition of experimental data from ROCs for each subsystem of detector front-end electronics. CODA allows the starting and stopping of data (i.e. of triggered events) over time. CODA compartmentalizes a set of triggered events, typically called a run, and run configuration information into a single data file, which as of CODA v3 uses the Event IO (EVIO) file format. Data for a single detector subsystem will be digitized and pre-processed by front-end electronic components. CODA then manages the run control, the event building, the event recording, the event transfer, and compiles all of the data and information into individual EVIO files. Subsequently the EVIO files can be decoded and used for processing or analysis with another form of software (e.g. ROOT). A flow diagram of how data is managed and assembled in a simple CODA implementation is shown in Fig. 4.26. The primary versatility of the CODA framework is the modularity of the implementation. A straightforward instance of CODA is able to be created for a single detector test setup. Similarly the same CODA framework can be implemented to handle the entire data acquisition for one of the experimental halls, which may have greater than

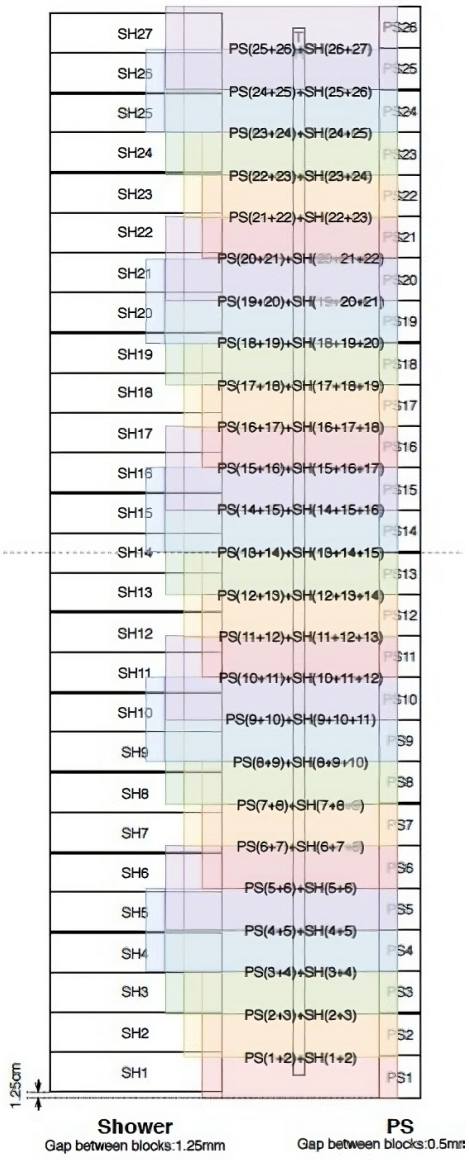

(a)

Trigger sums	Associated SH and PS Rows
SC 25-26	SH 26 + SH 27 + PS 25 + PS 26
SC 24-25	SH 25 + SH 26 + PS 24 + PS 25
SC 23-24	SH 24 + SH 25 + PS 23 + PS 24
SC 22-23	SH 23 + SH 24 + PS 22 + PS 23
SC 21-22	SH 22 + SH 23 + PS 21 + PS 22
SC 20-21	SH 21 + SH 22 + PS 20 + PS 21
SC 19-20	SH 20 + SH 21 + PS 19 + PS 20
SC 18-19	SH 18 + SH 19 + SH 20 + PS 18 + PS 19
SC 17-18	SH 17 + SH 18 + SH 19 + PS 17 + PS 18
SC 16-17	SH 16 + SH 17 + SH 18 + PS 16 + PS 17
SC 15-16	SH 15 + SH 16 + SH 17 + PS 15 + PS 16
SC 14-15	SH 14 + SH 15 + SH 16 + PS 14 + PS 15
SC 13-14	SH 13 + SH 14 + SH 15 + PS 13 + PS 14
SC 12-13	SH 12 + SH 13 + SH 14 + PS 12 + PS 13
SC 11-12	SH 11 + SH 12 + SH 13 + PS 11 + PS 12
SC 10-11	SH 10 + SH 11 + SH 12 + PS 10 + PS 11
SC 9-10	SH 9 + SH 10 + SH 11 + PS 9 + PS 10
SC 8-9	SH 8 + SH 9 + SH 10 + PS 8 + PS 9
SC 7-8	SH 7 + SH 8 + PS 7 + PS 8
SC 6-7	SH 6 + SH 7 + PS 6 + PS 7
SC 5-6	SH 5 + SH 6 + PS 5 + PS 6
SC 4-5	SH 4 + SH 5 + PS 4 + PS 5
SC 3-4	SH 3 + SH 4 + PS 3 + PS 4
SC 2-3	SH 2 + SH 3 + PS 2 + PS 3
SC 1-2	SH 1 + SH 2 + PS 1 + PS 2

(b)

Figure 4.25: Left: A diagram showing the main trigger logic for the SBS G_M^n and nTPE experiments. It shows a side view of the PS and SH Calorimeter blocks and the overlapping row trigger sums. Right: The same trigger sum information is alternatively presented in a table format.

6 different detector subsystem instrumented.

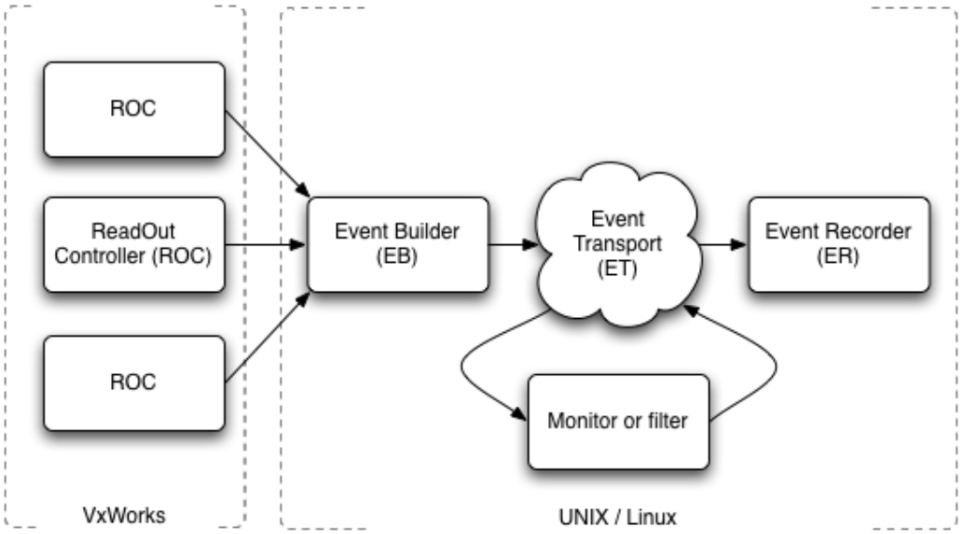

Figure 4.26: Flow diagram of the hardware and software components for a simple CODA implementation. Reproduced from [147]. VxWorks is a real-time operating system designed for use in embedded systems and ,in many cases, safety and security certification. VxWorks is proprietary software developed by Wind River Systems.

4.2.7 EPICS, Slow Controls, and Online Analysis

While running an experiment at Jefferson Lab it is necessary to have a real-time information monitoring system for the apparatus. During the SBS G_M^n and nTPE experiments, a system of "slow controls" and prompt data analysis were implemented. The system that collects experimental information and reports it in real-time to Shift Crew members is the Experimental Physics and Industrial Control System (EPICS) [148]. EPICS was developed at Argonne National Laboratory and is implemented at Jefferson Lab for most systems used in the accelerator and experimental halls. EPICS functions by collecting information from a series of servers called Input/Output Controllers (IOCs) for relevant signals from system components. The readback of these signals is updated system-wide and is available on all local Jefferson Lab computer systems and also remotely via Internet access. The readback polling is conducted on average once per second, however, due to the importance of the system the polling time can be faster or slower.

For the SBS G_M^n and nTPE experiments, EPICS was used to track relevant beam

quantities and spectrometer information. EPICS gave experimenters real-time information about critical beamline parameters including beam position and energy, raster currents, and beamline vacuum strength. EPICS provide experimenters with prompt information about crucial apparatus quantities including spectrometer magnet currents, detector high-voltage, detector gas properties, data acquisition components, and target temperatures. EPICS enables experimenters to control apparatus hardware remotely. EPICS also provides the ability to interlock critical systems together which allows automatic shutdowns of experimental equipment, in the event of hazardous apparatus behavior. The combined functions of remote hardware control and automatic safeguards were constantly employed during the experiment running. The complete list of critical systems which operated within the EPICS framework is too numerous to individually list, so this section provides a selected description to encapsulate some of the more noteworthy systems.

Another component of conducting an experiment at Jefferson Lab is a method of addressing data quality and spectrometer performance in real-time In Hall A during the SBS G_M^n and nTPE experiments, such an online analysis was employed called Panguin [149]. Panguin is a primarily C++ based software that processes a subsection of a designated data run and makes critical system quality assurance plots available to experimenters. Panguin is a modular software which can be implemented for different experiments or apparatus configurations. During the SBS G_M^n and nTPE experiments, Panguin was primarily used to look at raw physics quantities and sets of plots associated with the operation and performance of each detector subsystem.

Chapter 5

Gas Electron Multiplier Detectors

5.1 Overview of GEM Detectors

Modern particle and nuclear physics experiments require instrumentation and techniques for reconstructing trajectories of electrically charged particles. The main purpose of a tracking detector system is twofold: to identify real tracks from charged particles (track-finding), and track fitting. The concept of track-finding is to resolve enough points along the particle's path so that the corresponding signal particle can be found among random background processes and thus a specific charged particle track can be identified. Track-fitting is the procedure of mathematically fitting a curve to the found points (hits) on a particle track and from this fit extracting such information as the momentum of a charged particle.

The Gas Electron Multiplier (GEM) is a type of gaseous ionization detector originally developed in 1997 by Fabio Sauli [150, 151]. Specifically GEM detectors are members of a class of detectors known as Micro-Pattern Gas Detectors (MPGDs) [152]. MPGDs were developed based on improvements from the predecessor technologies known as Multi-Wire Proportional Chambers (MWPCs) and Multi-Strip Gas Chambers (MSGCs). The inherent principle of MPGDs, and therefore GEMs, relies on the engineering (or etching) of micro-patterned structures of conductors and dielectric materials to amplify an ionization

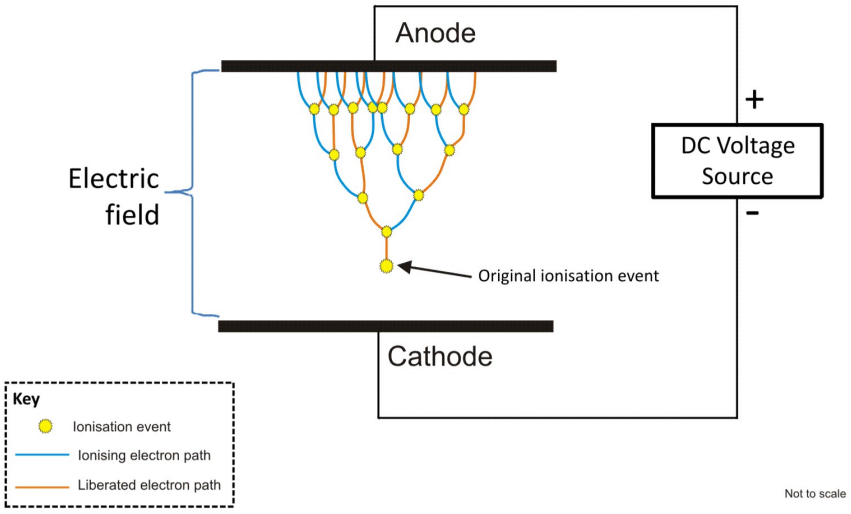

Figure 5.1: Electron Avalanche visualization. Image Credit: Dougsim via Wikimedia Commons.

event within a gasesous volume. The amplification of the ionization event occurs via a process known as Electron Avalanche (or Townsend Avalanche), as shown in Fig. 5.1. In an Electron Avalanche, a free electron generated by ionizing a gas molecule is accelerated by an intense electric field. The energetic electron can now collide with other gas molecules, thereby creating more free electrons (if the energy is greater than the ionization energy of the gas). These secondary free electrons will also be accelerated by the intense electric field, potentially yielding even more electrons. The ionizing process continues creating an avalanche multiplication and therefore a significant increase in electrical conduction through the gas. Ion are also produced and they drift towards the cathode, this is called ion backdrift.

GEM detectors are instrumented primarily for the purpose of tracking detector systems. However, since their original development, GEM detectors have been instrumented as drift chambers, time projection chambers, and imaging detectors, with many applications. GEM detectors are known for their ability to operate in high rate environments; dependent on the exact design, typical GEM detectors can function in environments with charged particle

rates on the order of hundreds of kHz/cm^2. The upper limit of the rate capabilities of GEM detectors has been demonstrated to be 2.5 MHz/cm^2 [153]. For a typical GEM detector, dependent on the strip pitch and readout electronics, the spatial resolution can reach sub-mm accuracy. One major advantage of the GEM detector technology is the relative inexpensive cost of detector manufacturing, compared to, for example, modern silicon tracking detectors. The remainder of this section will describe the structure of a single GEM foil, the anatomy of a GEM detector module, and both the structure and function of the GEM readout board.

5.1.1 Interactions of Charged and Neutral Particles With Matter

GEM detectors are sensitive to both charged and neutral particles. For charged particles this includes electrons and heavy charged particles (such as pions, muons, protons, ions, etc.). A GEM detector is sensitive to photons, which are neutral particles. To understand how GEM detectors respond to these types of particles, this section will summarize the ways in which charged particles and photons interact with matter in general. A charged particle has charge and interacts with the nuclei and orbital electrons of encountered atoms as it passes through matter. Charged particles are categorized as either heavy ($m_{\text{particle}} \gg m_e$) or light ($m_{\text{particle}} \approx m_e$) [10].

Heavy Charged Particles

The dominant energy loss mechanisms for heavy charged particles interacting with matter, in a single collision, are ionization and excitation. In this context, ionization is the process in which a charged particle interacts with an atom causing the atom to become positively charged (an ion) and thereby freeing electrons. Excitation is the process by which a charged particle transfers energy to an atom which causes the atom to be in a higher-energy state. The higher-energy state atom can de-excite back to the original ground state atom with the emission of a photon.

For a relativistic heavy charged particle, traveling with velocity $v = \beta c$, the mean rate of energy loss (called the mass stopping power) within a medium of atomic number Z, and mass number A is well described by the Bethe-Bloch equation [10],

$$\left\langle \frac{-dE}{dx} \right\rangle = K z^2 \frac{Z}{A} \frac{1}{\beta^2} \left[\frac{1}{2} \ln \left(\frac{2 m_e c^2 \beta^2 \gamma^2 W_{\max}}{I^2} \right) - \beta^2 - \frac{\delta(\beta\gamma)}{2} - \frac{C}{Z} \right] \tag{5.1}$$

In Eq. 5.1 the variables used are defined as the following. The Bethe-Bloch equation in

$$K = 4\pi N_A r_e^2 m_e c^2 \approx 0.307 \text{ MeV mol}^{-1} \text{ cm}^2$$

$N_A \approx 6.022 \times 10^{23}$ mol^{-1}	Avogadro's number
$m_e \approx 0.511$ MeV	electron mass
$r_e = \frac{e^2}{4\pi\epsilon_0 m_e c^2} \approx 2.8$ fm	classical electron radius
$\beta = v/c$	Particle velocity
$\gamma = 1/\sqrt{1-\beta^2}$	Lorentz factor
$W_{\max} = \frac{2 m_e c^2 \beta^2 \gamma^2}{1 + 2\gamma m_e/M + (m_e/M)^2}$	Maximum possible energy transfer in a single collision

c:	Speed of light
A:	Atomic mass of the medium
z:	Charge number of incident particle
Z:	Atomic number of the medium
M:	Incident particle mass
I:	Mean excitation energy
$\delta(\beta\gamma)$:	Density correction due to polarization at high-energy
C:	Atomc shell correction at low-energy

Eq. 5.1 [10] is valid in the region of $0.1 \lesssim \beta\gamma \lesssim 1000$ with a few percent accuracy. If we consider the implications of the valid region for Eq. 5.1, at $\beta\gamma \sim 0.1$ the incident particle speed is comparable to the "speed" of an atomic electron and at $\beta\gamma \sim 1000$ radiative effects begin to be important. Both limits on $\beta\gamma$ are Z dependent, with a minor dependence on M at higher energies. However, for practical considerations the mass stopping power in a given material is a function of β alone. The Bethe-Bloch equation does not account for energy loss at low energies, specifically this is the region where the incident particle's speed is small compared to that of the atomic electron (for $\beta\gamma \lesssim 0.1$). To extend the Bethe-Bloch equation to low energies the following corrections must be implemented: Shell correction,

the Barkas Bloch corrections; which consider corrections for higher-order powers of z. Additionally, one needs to account for the atomic electrons in the traversed medium not being stationary and this is known as the Shell correction. A complete description of these corrections is provided by information from the Particle Data Group [10]. The theoretical formulation of the Bethe equation is based on first-order Born approximation, and the energy loss is proportional to the square of the charge of the incident particle, z.

In the region of validity, the mass stopping power first falls as $1/\beta^{\alpha}$, where $\alpha \approx 1.7-1.5$ and with α decreasing with increasing value of Z. The mass stopping power then reaches a broad minimum at $\beta\gamma \sim 3$, dependent on the exact value of Z. Finally, for the valid region, the mass stopping power rises as the logarithmic term increases. As an example, Fig. 5.2 is a plot of the mass stopping power (Eq. 5.1) for positive muons in copper as a function of muon momentum. In Fig. 5.1 we can see the region of validity, which is represented as the second through third vertical gray bars. Furthermore, in Fig. 5.1 we can see the described behavior of Eq. 5.1 for this particular material. Also, Fig. 5.1 clearly shows the point for "Minimum ionization" (the minimum in the mass stopping power curve) at $\beta\gamma \sim 3$. Particles with $\beta\gamma \sim 3$ are referred to as "Minimum Ionizing Particles", or "MIPs." For practical considerations, most relativistic particles have mean energy loss rates close to the point of minimum ionization.

For gaseous detectors, including GEM detectors, ionization of gas molecules is the primary mechanism that enables gaseous detectors to measure position and time information of charged particles traversing the detector medium. When a charged particle interacts with elements of the gaseous detector, such as the gas volume, copper GEM electrodes, and drift cathode, an amount of energy is lost in the process of ionizing atoms in detector material. For a charged particle passing through a gaseous ionization detector, the formulation of the Bethe-Bloch equation is predicated on three major assumptions [154]. The first is that the energy transferred between the incident particle and the medium does not change the direction of the path of the ionizing particle. In a single collision, a relativistic heavy charged particle transfers a small fraction of its energy [10]. Therefore, as the relativistic

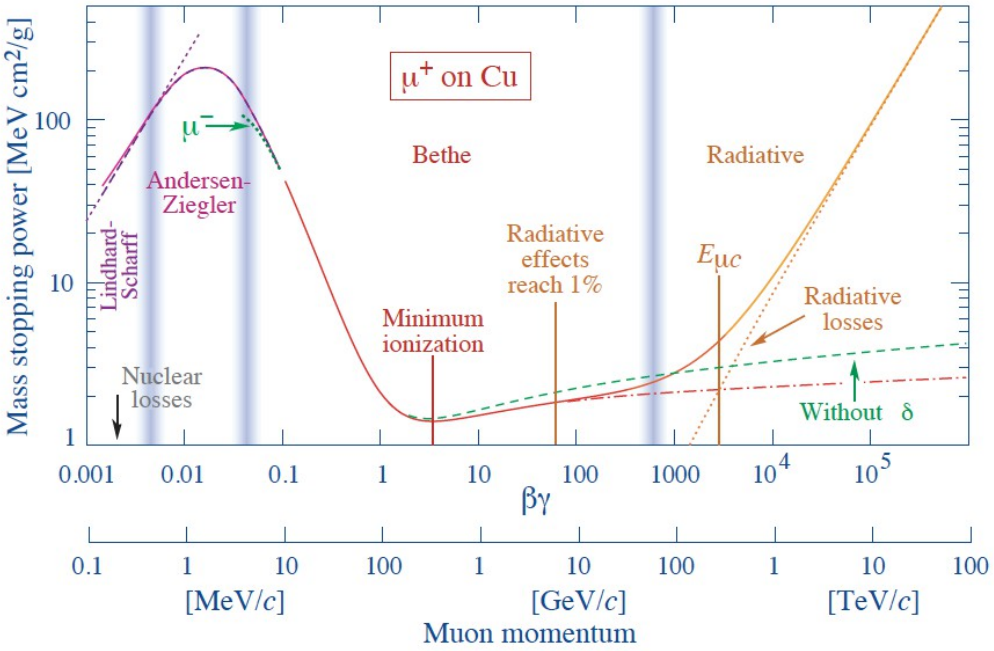

Figure 5.2: Mass Stopping Power (the Bethe-Bloch equation) for positive muons in copper as a function of muon momentum, represented here as $\beta\gamma$. Plot reproduced from [10].

heavy charged particle travels through a medium it interacts with atomic electrons through a large number of collisions and continuously loses energy in a straight path, essentially undeflected. Secondly, the gas molecules in the detector volume are considered to be at rest. The third assumption is that the ionizing particle is much heavier than electron, that is $m_{\text{particle}} \gg m_e$.

Light Charged Particles

For light charged particles ($m_{\text{particle}} \approx m_e$) there are two dominant energy loss mechanisms: collisions and radiation loss (bremsstrahlung) [10, 155]. As already described for heavy charged particles, collisional energy losses for light charged particles arise from interactions with orbital electrons or atoms in matter. These collisional interactions, similarly, lead to ionization or excitation of the atoms in the traversed medium. However, when considering energy losses for light charged particles, due to collisions, there are two modifications to

the Bethe-Bloch equation. For heavy charged particles, we assumed that the incident particle remains undeflected during the collision process. This assumption is not valid for light charged particles, due to the small mass of the particle. For this reason, the first modification arises, and the Bethe-Bloch equation must account for the small mass of the particle and the deflection in the collision. The path of the light charged particle will have multiple deflections or larger scattering angles and therefore the track will not be straight. The second reason is that for light charged particles, like electrons or positrons, the collision is between identical particles. So the Bethe-Bloch equation will also need to be modified to account for the indistinguishability of the light charged particle.

The second energy loss mechanism [155], because of the small mass of the charged particle, is the emission of electromagnetic radiation arising from the scattering in the electric field of a nucleus. This process is known as bremsstrahlung or "braking radiation." Broadly, bremsstrahlung is electromagnetic radiation arising from the acceleration of a light charged particle as it is deviated from its straight-line path by the electrical attraction of the atomic nucleus. The energy of the bremsstrahlung photon is directly related to the energy change of the light charged particle decelerating in the nuclear electric field. Bremsstrahlung can also arise from interactions with the field of the atomic electrons. That process is known as electron-electron bremsstrahlung, to distinguish from interactions between electron and nuclei. This effect is not particularly relevant to the interactions within GEM detectors, however, electron-electron bremsstrahlung is included for completeness.

The total energy loss of light charged particles is therefore composed of two parts: a contribution from collision loss, and a term for radiation loss.

$$\left(\frac{dE}{dx}\right)_{\text{tot}} = \left(\frac{dE}{dx}\right)_{\text{rad}} + \left(\frac{dE}{dx}\right)_{\text{coll}} \tag{5.2}$$

The collision loss contribution is essentially a modified version of the heavy charged particle Bethe-Bloch equation, which accounts for the two necessary modifications already described. The radiation loss term can be derived from the bremsstrahlung cross-section

and will be dependent on the material traversed by the incident light charged particle. Since the energy loss by radiation depends strongly on the absorbing material, we can define a critical energy, E_c, at which radiation loss equals the collision loss. Above the critical energy, radiation loss will dominate over collision losses and vice-verse for below E_c.

Photons

The behavior of photons in matter is different from the previous descriptions for charged particles. Unless otherwise stated in the context of this dissertation and GEM detectors "photons" refers to energetic photons such as X-rays and γ-rays, not other types of photons like optical photons or radio waves. Neutral particles, including photons, lack a surrounding electric field and therefore cannot interact with the nuclei and orbital electrons of matter in the same manner as charged particles. Though photons are electrically neutral particles, they can couple to charged particles via electromagnetic interactions and can transfer energy to charged particles. The three main interactions of photons in matter are: the photoelectric effect, Compton scattering, and pair production [155]. For the purposes of photon interaction, there are two notable qualitative features of photons interacting with matter. The first is that photons are many times more penetrating in matter than charged particles. The second is that a beam of photons is not primarily degraded in energy as it passes through a thickness of matter, rather the intensity of the beam of photons is attenuated.

The photoelectric effect involves the absorption of a photon by an atomic electron with the subsequent emission of an electron from the atom (known as a photoelectron) [155]. The energy of the outgoing electron is described by $E_e = E_\gamma - E_{\text{Binding}}$, where E_{Binding} is the binding energy of the electron. A free electron cannot absorb a photon and also conserve energy and momentum, so the photoelectric effect will only occur on bound electrons with the atomic nucleus absorbing the recoil momentum.

Compton scattering is the process when a photon elastically scatters from a free electron

[155]. In this case, elastic scattering arises from the consideration that the internal state of the electron remains unchanged, such that energy and momentum conservation is applied to the interaction between the photon and electron. However, when a photon passes through matter the electrons are bound to atoms. If the photon energy is high with respect to the electron binding energy, that is $E_\gamma \gg E_{\text{Binding}}$, the electron binding energy can be ignored and the electrons are considered as essentially free (or quasi-free). When Compton scattering occurs, the incident photon only transfers some, not all, of its energy to the electron and thus a lower-energy scattered photon also emerges from the interaction.

Generically, pair production is the process where a neutral boson is transformed into a particle and its corresponding antiparticle. For the consideration of photons, pair production usually involves the transformation of a photon into an electron-positron pair [155]. The principle constraints on pair production are both energy and momentum conservation. For energy conservation to be preserved, the photon much have at least twice the electron rest mass energy, that is $E_\gamma \geq 2m_e \approx 1.022$ MeV. In order to conserve momentum, the photon must be near a nucleus for pair production to occur. During pair production, the nucleus will receive some recoil. The production of an electron-positron pair in free space would violate either momentum or energy conservation. A result of the combined effect of pair production by high energy photons and bremsstrahlung emission by electrons is the formation of electron-photon showers. A high energy photon in matter transforms into an electron-positron pair which then can emit energetic bremsstrahlung photons, which can, inturn pair produce. The result is a cascade or shower of photons, electrons, and positrons. This process continues until the energy of the pair-produced electrons and positrons drops below the critical energy, and so their energy loss is no longer dominated by bremsstrahlung emission.

5.1.2 Interactions in Gas Mixtures

The gas that fills the GEM module volume is a critical component for the stable operation and performance of the detector. The interaction of high energy electrons with the gas

mixture provides the mechanism for primary ionization. An ideal candidate gas mixture should have optimal signal production, sufficient gain capabilities, and safe long-term operation. Noble gases have high specific ionization (low ionization energy) and are chemically inert, and thus are the ideal ionizer for the gas mixture [156]. Of the noble gases, argon is the preferred choice of ionizer for GEM detectors [151]. Argon (Ar) possesses the desired positive features, and is also a low-cost option compared to other commercially available noble gases.

Operation of GEMs with pure argon was thought to be the ideal choice, however, there are some major drawbacks to using a pure noble gas in a GEM [156]. As described in Sec. 5.1.1, energy loss mechanisms for charged particles include ionization and excitation, which arise from atomic collisions between gas molecules and electrons. In the case of GEMs this interaction occurs between argon ions and electrons. The ions in the gas, from primary ionization, can absorb additional energy and elevate to an excited state. This excited atom may emit photons as the atom returns to the ground state. These emitted photons may propagate through the gas mixture and detector causing additional ionization processes. The ionization from the emitted photon will release electrons, which will initiate avalanches not correlated to the location of the primary ionization event. To suppress this unwanted phenomenon involving emitted photons, a so-called "quencher gas" is mixed with the argon in certain percentages [157]. Ideal candidates for quencher gases consist of polyatomic molecules that have a large number of rotational and vibrational degrees of freedom, which allow the absorption of photons over a wide energy range. The quencher gas should absorb photons before they reach any electrodes, and therefore avoid undesired additional avalanches which may lead to permanent discharges. For the GEMs considered by this dissertation, the quencher gas chosen is carbon dioxide (CO_2).

The gas mixture volume ratios of argon and CO_2 have varied for different experiments and operational applications of GEM detectors. The most common ratio is 70% argon and 30% CO_2 by volume. This 70/30 Ar/CO_2 ratio provides sufficient protection from discharges associated with undesired avalanches, however, the amplification gain is not

diminished to an unusable threshold [158]. For the GEMs associated with the SBS G_M^n and nTPE experiments, which will be described in Sec. 5.2, the gas mixture ratio was 75/25 Ar/CO_2. The energy loss of a heavy charged-particle in a gas mixture can be found by averaging dE/dx over each element in the mixture weighted, w_i by the fraction of electrons belonging to each element, known as Bragg additivity or Bragg's Rule [10, 155]. The relation for the energy loss in the mixture is thus

$$\left\langle \frac{dE}{dx} \right\rangle = \sum w_i \left\langle \frac{-dE}{dx} \right\rangle_i . \tag{5.3}$$

5.1.3 Single GEM Foil

A typical GEM foil (or GEM electrode) [151, 154] is a 50 μm thick polymer foil with a 5 μm copper coating on both sides with a high-density of holes etched into both sides of the surface, as shown in Fig. 5.3. The GEM foil is manufactured so the density of holes is high, typically 50-100 per mm^2. For most GEM foils, and for the GEMs associated with the SBS program, each hole has an outer diameter of 70 μm, an inner diameter of 50 μm, and a spacing between the perforations ("pitch") of 140 μm. The GEM foil hole structure in the form of a diagram and as an image from an electron microscope are shown in Figs. 5.3a and 5.3b, respectively. Polymer foil is used as the substrate of the GEM foil, as it has a low outgassing rate and is a good insulator. A material that is often used for the GEM polymer foil is Kapton. Maintaining low outgassing ensures detector operational stability, which affects the overall detector performance. Additionally, the polymer foil should be robust under high temperature. During operation of the GEM foil, a few hundred volts are applied across the two outer copper surfaces creating a potential difference and generating a strong electric field within the GEM holes, as depicted in Fig. 5.3c. The strong electric field has two main advantages, the first, the electron field guides free electrons generated by ionization caused by radiation on one side of the GEM foil. The second, the electric field causes any entering electrons to accelerate causing more ionizing collisions and generating more free electrons, which contributes to an avalanche multiplication and amplifies the

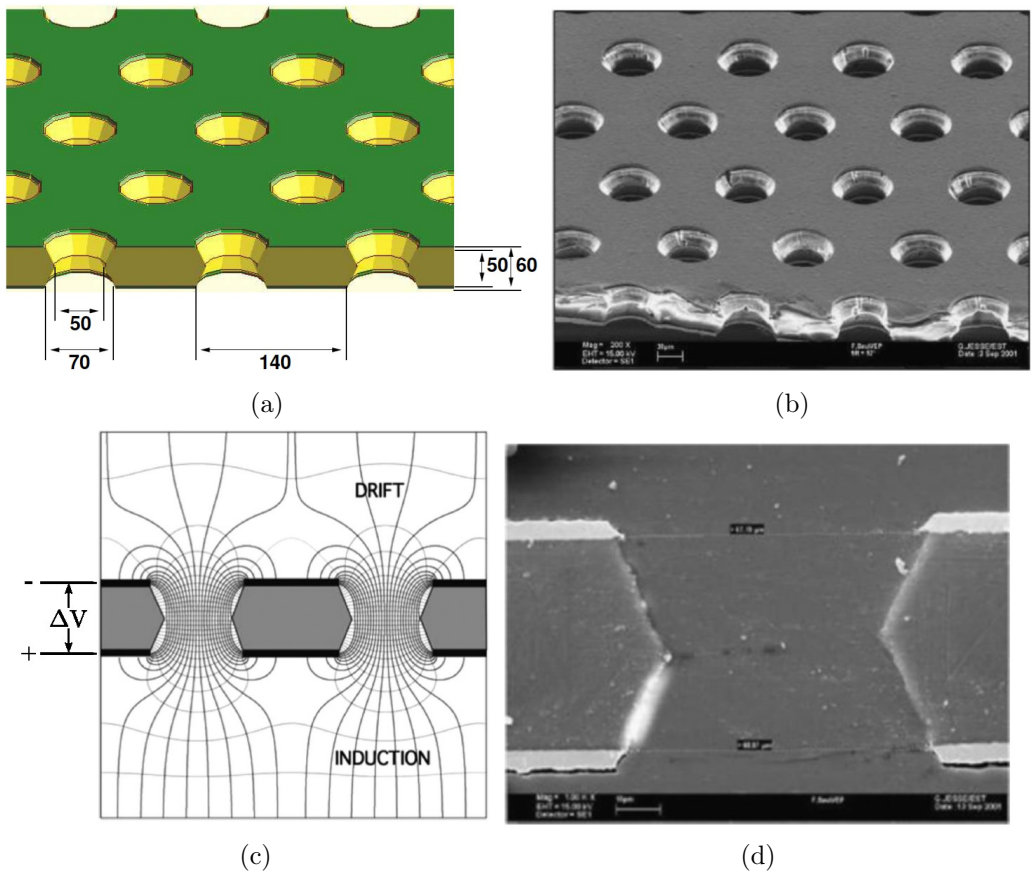

Figure 5.3: Top Left: A computer-generated diagram showing typical dimensions of a single GEM foil. Reproduced from [154] Top Right: Electron microscope image of a section of a GEM foil, reproduced from [151]. Bottom Left: Diagram of the electric field and equipotentials in the region of the holes of a GEM foil, adapted from [151]. Bottom Right: GEM hole cross-section, reproduced from [151].

signal of the original particle.

A GEM foil is manufactured via a photo-lithographic technique known as double-mask high-quality wet etching. This manufacturing method starts with a high-quality polymer foil that is metal coated on both sides. Then a photosensitive resin and masks are applied to the metal-coated polymer foil. The foil with the photosensitive resin and masks is then exposed to ultra-violet light. The exposure to ultra-violet light chemically removes the metal coating in the location of the masks; everywhere else on the polymer foil is preserved by the photosensitive resin. At this stage in the manufacturing process the

pattern corresponding to the masks is the same pattern at which the holes will be located on the GEM foil. Once the metal has been removed, the foil is immersed in a solvent which removes the polymer from both sides in the same location as the hole pattern. The manufacturing process results in the characteristic double-conical shape of the holes, as shown in Fig. 5.3d. All of the GEM foils which were used to manufacture the GEM detectors for the SBS program have been produced at CERN.

5.1.4 GEM Modules

This section will include a description of single-foil and triple-foil GEM detectors, focusing on the detector properties and function. Part of the section will compare and contrast the two types of GEM detectors, and how the triple-foil GEM detector design has become a standard for particle tracking detectors.

Single-Foil GEM Detector

In its simplest form, a GEM detector (also called a GEM module or chamber) is comprised of a drift cathode, a GEM foil, and an electronics Printed Circuit Board (PCB) readout board as shown in Fig. 5.4 [151]. In this configuration with only one GEM foil, the detector is often referred to as a "single foil GEM detector" or "single GEM." The entire detector volume of the GEM detector should be filled with a gas, or a gas mixture, capable of generating free electrons from stable ionization. The gas is a critical component of the GEM detector, responsible for the avalanche and gain mechanisms that occur during operation. The drift cathode is located at the entry plane of the detector and acts as a negatively charged electrode which collects positive ions when charged particles pass through the GEM. Essentially, the drift cathode initiates the detection process by creating the primary ionization event. The GEM foil is described in detail in the previous section, and is responsible for avalanche multiplication which causes signal amplification. The GEM foil is located between the drift cathode and readout board. The PCB readout board anode is located at the exit plane of the detector and collects electrons, after amplification. The

two-dimensional readout strips of the PCB readout board allow the reconstruction of the 2D-position information associated with the original ionizing event. During operation of the GEM detector, voltage is applied to both the drift cathode and the GEM foil, with the readout board held as ground.

As shown in Fig. 5.4, a single foil GEM detector is characterized into two regions: the drift region and the induction region. The drift region is the volume between the drift cathode and the top of the GEM foil. The induction region is characterized as the volume between the bottom of the GEM foil and the readout board. Each of these regions has a specific purpose and understanding the regions provides insight into the function of the whole detector and the interactions that occur during operation. When a charged particle enters the GEM detector it will interact with the gas molecules in the drift region generating ionization events, both ions and electrons. Due to the electric field between the cathode and the GEM foil, the electrons liberated during ionization will drift towards the holes of the GEM foil. While passing through the holes of the GEM foil the electrons will gain large amounts of energy, causing further ionization of the gas molecules and freeing more electrons. After passing through the holes of the GEM foil, into the induction region, the electric field carries the electrons produced from the multiplication to the readout strips of the PCB board, and charge is collected on these readout strips to generate a detector signal.

The gain [154, 157] of a GEM detector is the ratio of detected charge collected on the readout strips to the charge generated by initial ionization in the drift region. However, a fraction of the electrons generated during the avalanche multiplication are absorbed by the GEM foil. Therefore it is better to define the gain as an "effective gain." The effective gain of a GEM detector is dependent on multiple parameters: the properties of the gas, the GEM foil geometry, and the strengths of the electric fields in the detector regions. For single foil GEM detectors, dependent on these parameters, the gain has been characterized to reach a value between 10^2 and 10^3 [151]. For large-acceptance geometry GEM foils, produced under standard conditions by CERN such as those operated for the SBS program, it is

expected that a single GEM foil will provide a gain of approximately 20 [157]. It has been observed that the maximum attainable gain of a single GEM detector is limited [150]. This limitation in gain is due to damage by discharges initiated by heavily-ionizing tracks; this effect is enhanced by high rate environments. Since there are limitations in gain with single-foil GEM detectors, this naturally motivates the introduction of multi-foil GEM detectors which will be described in the next section.

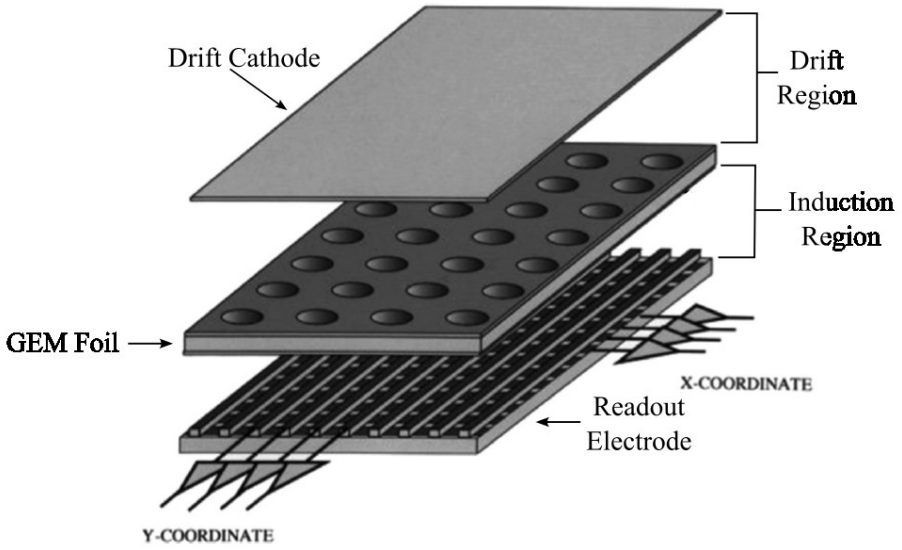

Figure 5.4: Schematic of a Single-Foil GEM Detector. Adapted from [151].

Triple-Foil GEM Detector

Triple-Foil or Triple GEM detectors differ from the concept of a single GEM detector, as described in Sec. 5.1.4, by including two more GEM foils between the drift cathode and the PCB readout board. By introducing two more GEM foils the structure of the GEM detector can be characterized as a drift region, two transfer regions, and an induction region. Functionally, the transfer region guides a fraction of the amplified electrons, after a GEM foil, to another GEM foil where they can be injected and further amplified. By organizing multiple GEM foils into a single detector many properties are improved, compared to the single GEM detector case. It has been demonstrated that for multi-GEM detectors

(with at most 5 GEM foils), much higher gains are attainable and each additional stage of amplification increases the effective GEM detector gain by about an order of magnitude [151]. Another advantage of the multi-foil GEM design is that a given (or "desired") overall gain of the detector can be attained with lower operational voltage for each GEM foil, and therefore being significantly less prone to damaging discharges. For Triple GEM detectors, dependent on the detector properties, effective gains on the order of 10^4 have been observed [151]. For large-acceptance triple GEM detectors used in the SBS program it is expected that the total effective gain is approximately 8000. The total effective gain is the multiplicative product of the gains for all foils, with each foil having a gain of about 20.

As a result of the successful operation of the COMPASS triple GEM detectors [153, 157], triple GEM detectors have become a standard instrumentation for minimum-ionizing particle tracking under high rate environments. In particular, the SBS program adopted the COMPASS triple GEM design for their tracking detectors. A cross-section schematic of a triple GEM detector, overlaid with a graphical representation of a single ionizing event is shown in Fig. 5.5. Any further reference or discussion throughout this dissertation, unless explicitly stated, involving a GEM module, detector, etc. will assume a triple-foil GEM design.

5.1.5 GEM Readout Board

The readout board or readout plane is the final internal layer of a GEM detector; the location of the readout board for a triple GEM detector is shown in Fig. 5.5. The readout board is where the charge from the final-stage electron avalanche gets deposited and read out. The purpose of the readout plane is to reconstruct a two-dimensional spatial position from the collected charged of the incident particles on the GEM detector.

For large-active area GEM detectors the readout board is typically a strip-based 2D coordinate system. For applications of GEM detectors with small active areas, a silicon pixel readout is available as an alternative. The pixel readout is the ideal case for high

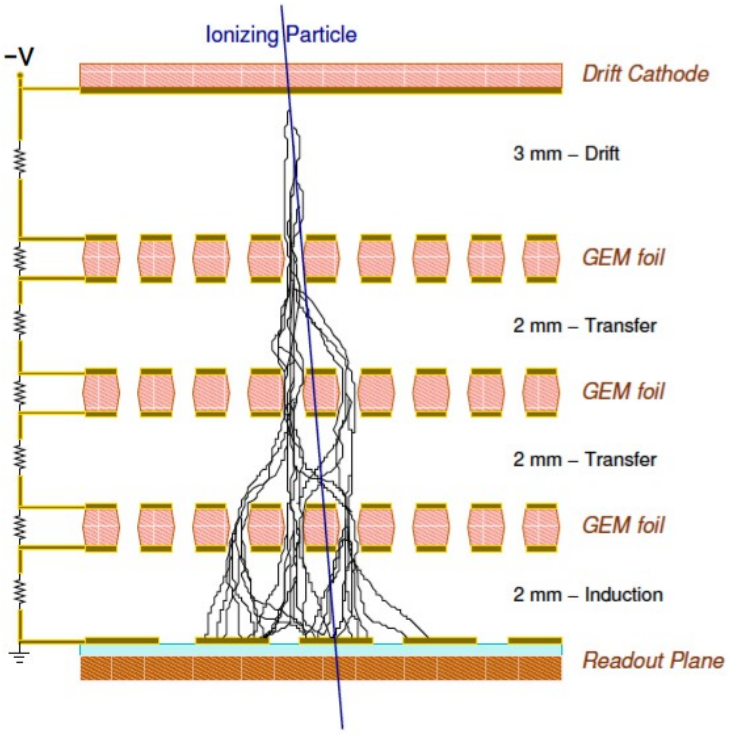

Figure 5.5: Schematic of a Triple-Foil GEM Detector. The schematic is overlaid with a single ionizing particle causing a shower cascading through the GEM foils and ending on the readout board. Reproduced from [139]. This Triple-Foil GEM detector design was adopted for the SBS program.

background environments, as it eliminates the effect of multiple combinatorics, which is an inherent feature of a strip-based readout. However, the pixel readout scheme requires orders of magnitude more channels compared to the strip-based readout. Therefore, instrumenting a pixel readout for large acceptance GEM detectors, like those for the SBS program, is cost-prohibitive.

The strip-based readout board consists of two sets of thin parallel copper strips, separated by a thin layer of insulating material. This readout plane design creates a top layer of strips that sit slightly higher than a bottom layer of strips, which are connected to a support structure. When charge is deposited on the readout strips, this generates a small voltage which is read out by front-end electronics connected to the copper strips. An important feature to consider when designing a readout board is that there is a linear

relationship between the capacitance of the readout channels and the noise in the front-end electronics. Therefore, to limit the capacitance and thus the noise fluctuations, it is preferable to limit the length of the readout strips.

In a traditional "XY" Cartesian layout, the top layer of strips are arranged orthogonal to the bottom layer of strips. For the XY GEMs in the SBS program, as shown in Figs. 5.6 and 5.7a, the top readout strips have a width of 80 μm and the bottom readout strips have a width of 340 μm. For both the top and bottom layer of strips the pitch between the readout strips is 400 μm. The insulating layer between the two set of strips is made from Kapton and has a thickness of 50 μm.

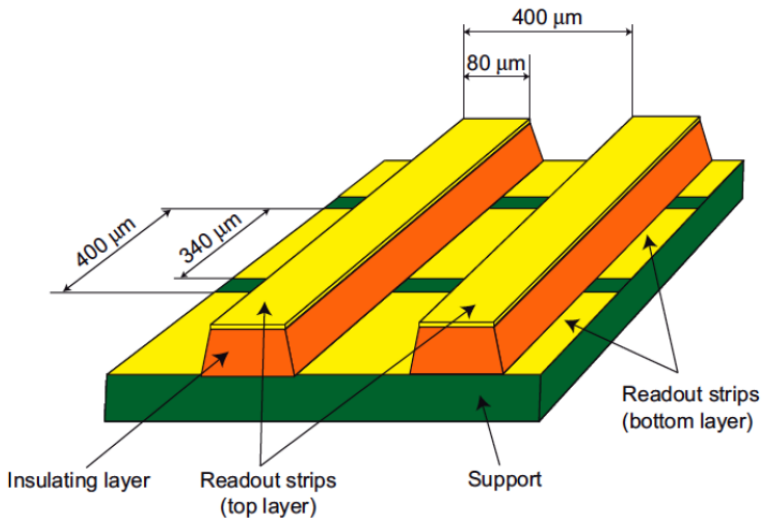

Figure 5.6: Schematic of a 2D GEM readout plane. In this case, the two sets of orthogonal readout strips are shown mounted on the support structure.

Depending on the desired detector properties, there are other ways to organize the readout strips of a GEM detector. One such arrangement, relevant to the SBS program, is a planar non-orthogonal or "UV" angle construction. For the GEMs with the UV configuration, in the SBS program, a stereo angle of 60° between the two sets of strips is instrumented. The copper strips for the UV GEM configuration are shown in Fig. 5.7b. The strip widths and pitches of the UV readout are identical to those of the XY readout, only the angle between the strip layers has been altered.

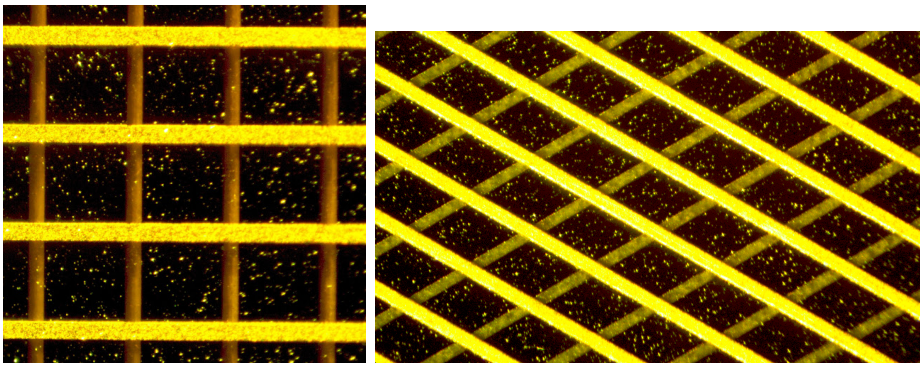

(a) (b)

Figure 5.7: Microscopic images of different GEM readout plane configurations. Left: XY Cartesian, the readout strips are orthogonal to each other. Right: UV Stereo, the two sets of strip planes are separated by a stereo angle of 60°.

5.2 GEM Detectors for the SBS Program

The SBS program requires two main configurations of GEM, which are categorized as either front-trackers or back-trackers. GEMs for the front of the spectrometer are called "front-trackers" and cover an active area of 150 cm × 40 cm. GEMs instrumented throughout the rest of spectrometer are called "back-trackers" and cover an active area of 200 cm × 60 cm. The detectors for the SBS program were developed and manufactured by two groups from the University of Virginia (UVA) and the Istituto Nazionale di Fisica Nucleare (INFN). During the G_M^n and nTPE experiments three types of GEM layers were instrumented: UVA XY, UVA UV, and INFN XY GEMs. The naming scheme for the SBS GEM layers references both the manufacturing group and the readout strip orientation. The remainder of this section will describe the key features of each type of SBS GEM detector. Information pertaining to instrumentation of GEM detectors in Hall A during the SBS G_M^n and nTPE experiments will be described further in Sec. 5.6. Topics pertaining to the instrumentation in Hall A include gas distribution systems, DAQ readout, high voltage, low voltage, etc.

5.2.1 UVA XY GEMs

The readout strips of the UVA XY GEM are oriented in a Cartesian coordinate system. An individual UVA XY GEM module has an active area of 50 $\times$ 60 cm^2. For a more complete description of the UVA XY GEM design and construction see Refs. [159, 160]. A single UVA XY GEM module is outfitted with a total of 22 APV readout cards (these readout cards are described in Sec. 5.3.1): 10 APVs along the shorter (horizontal strip) length and 12 APVs along the longer (vertical strip) length. The UVA XY GEM modules are segmented into sectors (for high voltage) on the top of each of the GEM foils within the detector. On the top of each of the GEM foils in a UVA XY module there are 30 electrically-isolated sectors. Thus the the UVA XY GEM modules contain singly-sectored GEM foils. To meet the acceptance requirements of the SBS program and to minimize potential dead active area, UVA XY GEM modules are arranged into a composite layer. A UVA XY GEM layer consists of 4 GEM modules as shown in Fig. 5.8, for a total active area of 200 $\times$ 60 cm^2. For the SBS G_M^n and nTPE experiments one GEM layer of this type was instrumented in the BigBite Spectrometer.

5.2.2 UVA UV GEMs

A UVA UV GEM layer is a single module GEM detector with an active area of 150 $\times$ 40 cm^2. The readout strips of the UVA UV GEM are oriented at an angle of 60° between the two sets of strips. A UVA UV GEM layer is shown in Fig. 5.9. Further information about the design and construction of the UVA UV GEM layers is available in Refs. [159, 161]. A UVA UV GEM layer has a total of 60 APV readout cards: 30 APVs associated with U-direction strips and 30 APVs associated with the V-direction strips. The APV readout cards are distributed over 3 sides of the GEM layer. The UVA UV GEM modules have a sectorization on both the top and the bottom foils of each GEM foil. That is, the GEM foils in this type of GEM detector are doubly-sectored. Instrumenting doubly-sectored GEM foils is beneficial in the event of a short across the GEM foil. For GEM detectors with

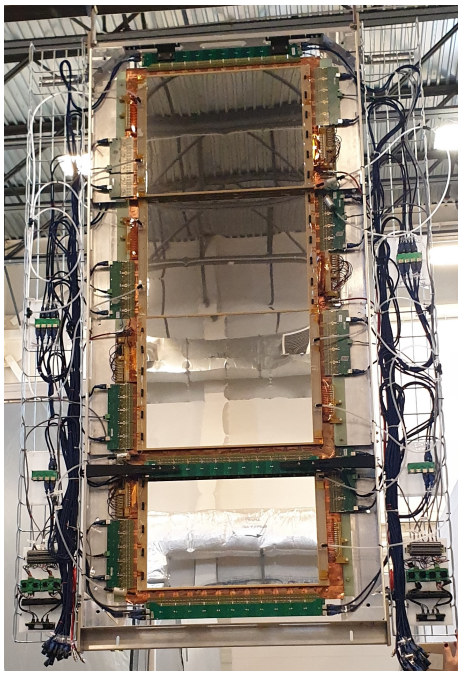

Figure 5.8: A UVA XY GEM layer. This layer is composed of four 50×60 cm^2 UVA XY GEM modules. The lowest module (vertically) is considered "module 0" and the highest module is "module 3". This UVA XY GEM layer does not have any RF shielding instrumented. However, the UVA XY GEM in BigBite during the G_M^n and nTPE experiments did have RF shielding.

resistive divider high voltage distribution systems, in the singly-sectored case the entire module active area would inoperable. For the doubly-sectored case, only the active area the size of one sector is affected, assuming the sector was electrically isolated from the other sectors. For the UVA UV GEM modules there are a total of 60 electrically isolated sectors. During the G_M^n and nTPE experiments four UVA UV GEM layers were installed in the BigBite Spectrometer.

5.2.3 INFN XY GEMs

A single INFN XY GEM module has an active area of 50×40 cm^2. The readout strips of the INFN XY GEM module are oriented such that the two sets of strips are orthogonal. More information about the design and construction of INFN XY GEM modules is available in Ref. [162]. One INFN XY GEM module is instrumented with a total of 18 APV readout

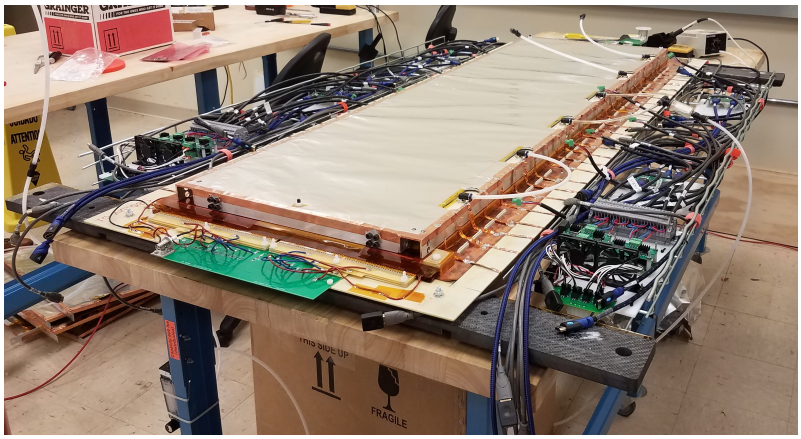

Figure 5.9: A UVA UV GEM layer. The layer is one single module with a 150 × 40 cm^2 active area. This layer has RF shielding instrumented, which is identical to how the GEMs of this type would have been installed in the BigBite Spectrometer.

cards: 8 APVs along the shorter (vertical strip) length and 10 APVs along the longer (horizontal strip) length. The INFN XY modules are sectorized on the top of each of the GEM foils within the detector. Each GEM foil is divided into 2 rows of 10 sectors, for a total of 20 sectors. The INFN XY GEM layers consist of 3 GEM modules so the total layer active area is 150 × 40 cm^2. A fully assembled INFN XY GEM layer is show in Fig. 5.10. For the SBS G_M^n and nTPE experiments two INFN XY GEM layers were instrumented in the BigBite Spectrometer.

5.3 GEM DAQ Electronics

The purpose of the GEM DAQ system is to convert physical charge collected (analog signal) into a digital signal. A diagram showing the GEM DAQ electronics essential for operation is presented in Fig. 5.11. The APV25 (or just APV) front-end readout cards are directly connected to the readout strips of a GEM detector, and these are the first DAQ components to receive the analog signals. The APV cards are triggered to collect raw signals by input information from trigger supervisor modules, which are part of the broader experimental trigger, as described in Secs. 4.2.5 and 4.2.6. The analog signal

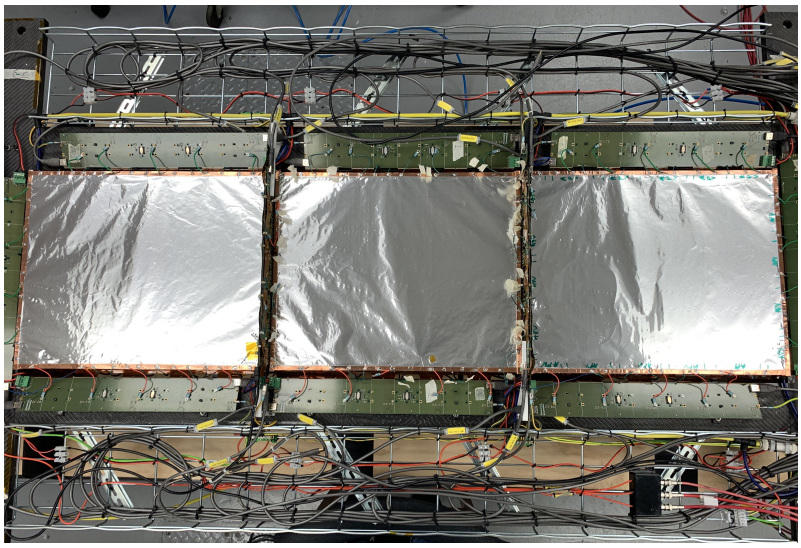

Figure 5.10: An INFN XY GEM Layer. This layer consists of three 50 $\times$ 40 cm^2 INFN XY GEM modules. The lowest module (left-most horizontally in photo) is considered "module 0" and the highest module (right-most) is "module 2." This INFN XY GEM layer has RF shielding installed on each module, which is identical to how the GEMs of this type would have been installed in the BigBite Spectrometer.

from the APV25 cards is transmitted to a Multi-Purpose Digitizer (MPD) module, which converts analog information to a digital signal. The digitized signal from the MPD is then transmitted over fiber optic cables to the VXS Trigger Processor (VTP) module. The VTP module is a switch card which handles the central trigger processing for the GEM DAQ system and interfaces with other components (e.g. ROCs) of the DAQ system for the entire experimental apparatus. For the G_M^n and nTPE experiments a UVA XY GEM layer had 10,240 strips/channels, a UVA UV GEM had 7,680 strips/channels, and an INFN XY GEM had 6,912 strips/channels. The primary components of the GEM DAQ system will be described in more detail in the remainder of this section.

5.3.1 Analog Pipeline Voltage 25 (APV25) Card

The purpose of the APV25 is to serve as a front-end device to shape, sample, identify, amplify, and store analog (charge) signals. The APV25[163] is an analog pipeline chip with 128 channels based on a Very Large Scale Integration (VLSI) circuit. Originally, the

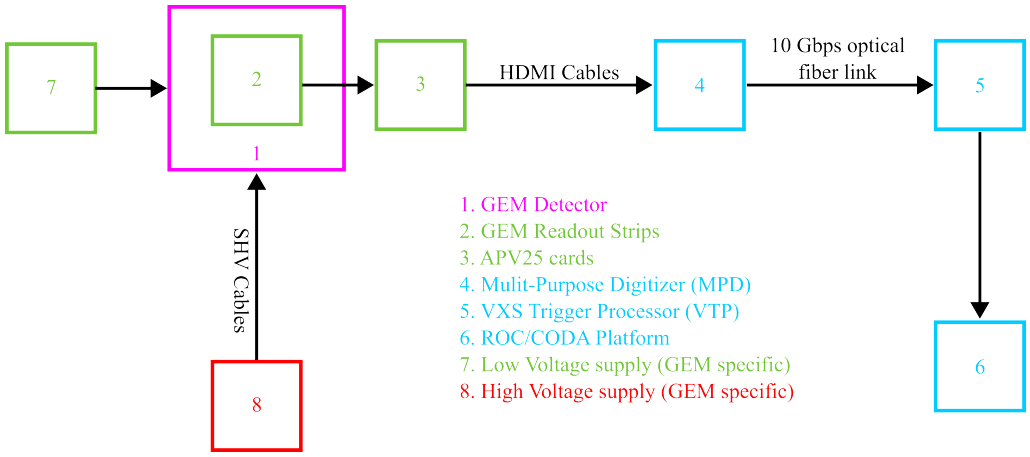

Figure 5.11: A flow diagram showing the essential components of a GEM DAQ system.

APV25 was for the readout of silicon microstrip detectors in the Compact Muon Solenoid (CMS) tracker at the Large Hadron Collider (LHC). The chip is fabricated in a standard 0.25 μm complementary metal-oxide-semiconductor (CMOS) process to take advantage of the radiation tolerance, lower noise, and high circuit density of CMOS technology. Experimental characterization of the circuit shows full functionality, both in pre- and post-irradiation conditions after, up to 20 Mrad of irradiation. The output data format of the APV25 consists of 12 bits of digital header, 3 start bits followed by an 8-bit pipeline column address and 1 error bit, and the 128 analog data samples. In order to keep synchronization with the data acquisition if no data is present, a tick mark is output every 1.75 μs. The APV25 can accommodate data readout speeds of both 40 MHz and 20 MHz frequencies.

The GEM detectors for the SBS program have adapted the APV25 chips into preamplifier and multiplex cards as front-end electronics. The APV25 cards connect directly to the two-dimensional readout strips of the GEM detectors in groups of 128 strips/channels, as shown in Figure 5.12a for INFN APV cards with ZIF connectors and Figure 5.12b for UVA APV cards with Panasonic connectors. Depending on the organization of front-end electronics for each particular type of SBS GEM detector, the APV25 cards are connected together in groups of 3,4,5, or 12 on electronics boards called Backplanes. The Backplanes distribute low voltage to the APV25 cards. The Backplanes also control the transmission

of analog and digital signals between the APV25 cards and MPDs. The connection between the APV Backplanes and the MPDs is done via shielded copper based cables known as HDMI cables. HDMI cable lengths of 10 to 20 meters or less are used to minimize noise directly arising from the cables.

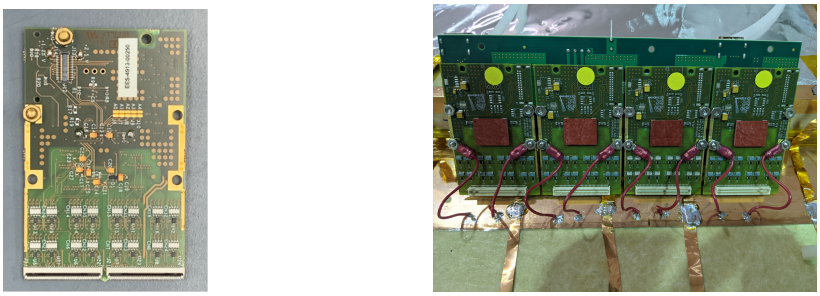

(a) (b)

Figure 5.12: Left: INFN APV card with ZIF connector, Right: Multiple UVA APV cards with Panasonic connectors.

5.3.2 Multi Purpose Digitizer (MPD)

The Multi Purpose Digitizer (MPD) [164] is an electronics board that is able to manage 16 APV25 front-end cards by reading out the respective analog data streams and also transmitting control and configuration signals. An example of a version 4.0 MPD board is shown in Figure 5.13. The MPD board was designed by INFN for the SBS program. The MPD can be used in VME based environments, such as VME32 VME64x, and VXS. The core of the MPD is an Altera ARRIA GX Field Programmable Gate Array (FPGA). The MPD, because of the FPGA, is able to handle sixteen 12 bit analog/digital converters operating at 40 MHz, I2C protocols for configuring the APV25 cards, coaxial front panel I/O for external control signals, Ethernet 10-100 capability, high speed optical protocol via a Small Form-Factor Pluggable (SFP) transceiver, and large SDRAM for data buffering.

The MPD is able to support multiple real-time tasks including common-mode (see Appendix A.2.3) and pedestal subtraction (see Appendix A.2.4), sparse readout, multi sample trigger uncorrelated hit suppression, and event building. The MPD has trigger rate and

data readout bandwidth limitations, so the MPDs were coupled with extension electronics boards to reach data readout rates necessary for the SBS program. The extension electronics board known as the VTP module, is a specialized Jefferson Lab board and was instrumented for the SBS program.

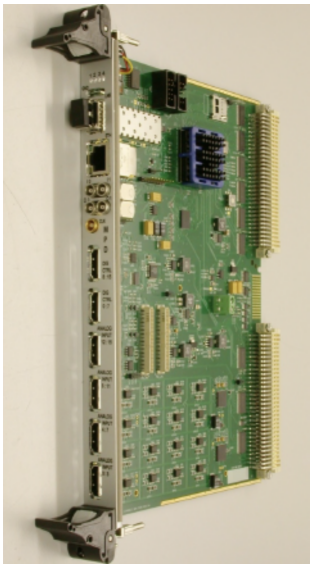

Figure 5.13: A release 4.0 MPD board, reproduced from [164].

5.3.3 VXS Trigger Processor (VTP) Modules

The VXS Trigger Processor (VTP) module [165] is a switch card that participates in the Level 1 trigger in both capacities, in the front-end VXS slot as a central trigger process or in the global trigger VXS slot as a global trigger processor. A picture of a VTP module is shown in Fig. 5.14. The VTP was developed to handle fast and large data processing. The VTP module has the ability to prepocess data; for the SBS program this involves applying data reduction techniques before sending the data to be recorded. The data reduction technique is known as online zero suppression which involves removing channels that do not contain signal above a predetermined pedestal threshold. The VTP contains a dual-core 1 GHz ARM processor that runs a CODA ROC on a Linux OS capable of event building trigger diagnostic information from an FPGA. The available processors on the

VTP board can handle 34 Gbps of input data. The VTP is also able to transmit 40 Gbps of data output to ROCs or other DAQ components.

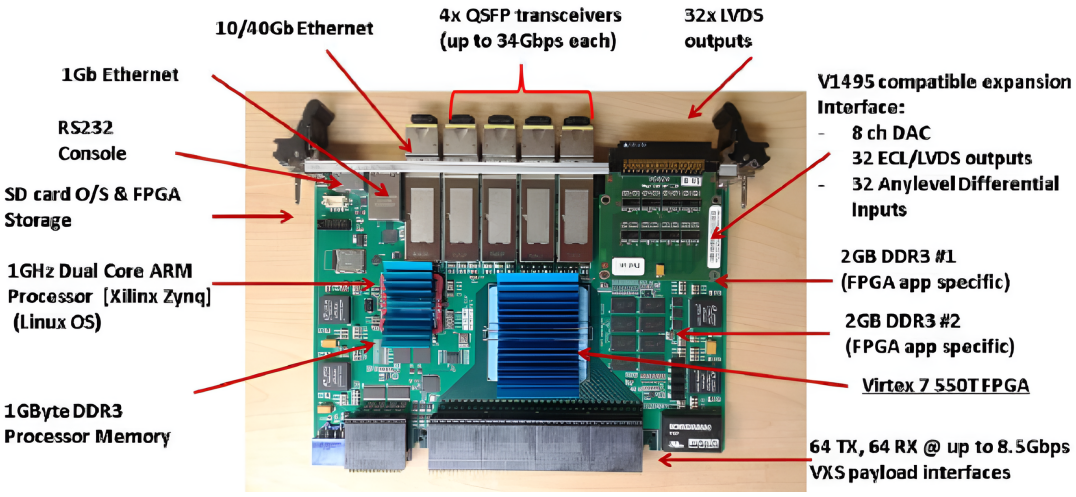

Figure 5.14: A VTP module with descriptions of board components. Reproduced from [165].

5.4 GEM Auxilliary Systems in Hall A

To properly operate the SBS GEMs either in a test setup for commissioning, or in Hall A, certain auxiliary systems are necessary. Low-voltage power supplies are needed to power the front-end APV25 readout cards. During any type of data taking the GEM detectors (foils) must be energized to amplify ionization from incident charged particles and generate a signal; this is accomplished with high-voltage power supplies. In order to safely and properly operate a GEM detector, gas must flow through the detector volume and thus a gas distribution system is required. This section will describe the support systems associated with the GEMs in the BigBite Spectrometer during the SBS G_M^n and nTPE experiments. Also throughout this description, if applicable, systems specific to UVA vs. INFN GEMs will be differentiated.

5.4.1 Front-End Electronics Low-Voltage Power Supply Systems

As described in Sec. 5.3.1, the front-end electronics for the GEM detector are APV cards. These APVs are organized in various quantities on backplanes. For successful operation of the GEM detector both the APVs and backplanes require a source of electrical power via low-voltage power supplies. For GEMs manufactured by both the UVA and INFN groups the low-voltage requirements are identical, rather the implementation of low-voltage power supplies differs. This section will first generically address the voltage and power consumption requirements of an APV25 card/chip. Specific information about low-voltage power supply implementations for the UVA and INFN GEMs is described in Appendix A.1.

The APV25 User Guide [166] states that under nominal conditions each readout channel of the APV25 chip consumes approximately 2.31 mW of power. When all 128 channels of the APV25 chip are considered the power consumption per APV25 chip is approximately 296 mW. When considering nominal conditions, the APV25 requires three voltages: positive supply voltage VDD = +1.25 V (+90 mA), negative supply voltage VSS = -1.25 V (-155 mA), and ground GND = 0 V (65 mA). To apply these voltage levels properly to the APV cards a radiation-hard low-voltage regulator chip is instrumented near the GEM detectors (for UVA) and as part of the backplanes (for INFN). This particular regulator chip was originally designed by CERN and is known as LHC4913 [167]. The regulator chip serves the purpose of stepping down voltage from 5 V DC to +2.5 V and +1.25 V against a common ground. The chip was originally designed to sustain rugged conditions in nuclear and particle physics with the main feature that it is resistant to radiation damage, along with applications in space.

5.4.2 High-Voltage Power Supply Systems

For standard operation of any GEM detector a source of electrical potential across each GEM foil is necessary. During the SBS G_M^n and nTPE experiments the GEMs made by both the UVA and INFN groups implemented a resistive divider chain on each GEM

module. The resistive divider distributed the electric potential levels across each of the component foils within the detector. The choice of implementing a resistive divider chain for high-voltage distribution was also cost-effective. The remainder of this section will detail the high-voltage power supplies and specifications used during the SBS G_M^n and nTPE experiments for both UVA and INFN GEM detectors.

UVA GEMs

The high-voltage power supplies used for the UVA GEMs in the BigBite Spectrometer were WIENER MPOD EHS 8060n HV modules installed in a WIENER MPOD computer-controllable crate [159, 160]. Each channel of the EHS 8060n high-voltage module is rated for a negative voltage of up to 6 kV and a current draw of up to 1 mA. Each EHS 8060n supply has eight channels meeting these specifications. For a single UVA GEM module the resistive divider needs to be provided with an approximate voltage of 3.65 kV and current of 745 μA, in optimal operation conditions.

INFN GEMs

The INFN GEMs installed in the BigBite Spectrometer used CAEN V6521N VME HV power supply modules installed in a VME or VMEx64 computer-controllable crate. The CAEN V6521N HV module contains 6 channels. Each HV channel on the CAEN V6521N supply is rated for a negative voltage of up to 6 kV and current draw of up to 300 μA. During the G_M^n and nTPE experiments a resistive divider for a single INFN GEM module needed to provide, during nominal operation, an approximate voltage of 4 kV and current of 102.5 μA.

5.4.3 Gas Distribution System

For the safety, lifespan, and performance of a GEM detector the detector gas volume must be replenished with a mixture of argon and carbon dioxide. During in-beam operations or cosmic-ray testing, a gas mixture of Ar/CO_2 with the gas volume ratio of 75/25 is

used for the GEM detectors in the SBS program. A custom gas mixing and distribution system was specifically developed in Hall A for the GEM detectors of the SBS program. The critical components of the Hall A GEM gas system include individual gas sources (cylinders/bottles of argon and carbon dioxide), mass-flow controllers, a mixing controller, mixing tank, buffer tank, Stanford Research Systems Binary Gas Analyzer (BGA) Model BGA244, gas-flow meter manifold, and online monitoring system. A schematic of the key components of the Hall A GEM gas system is presented in Fig. 5.15.

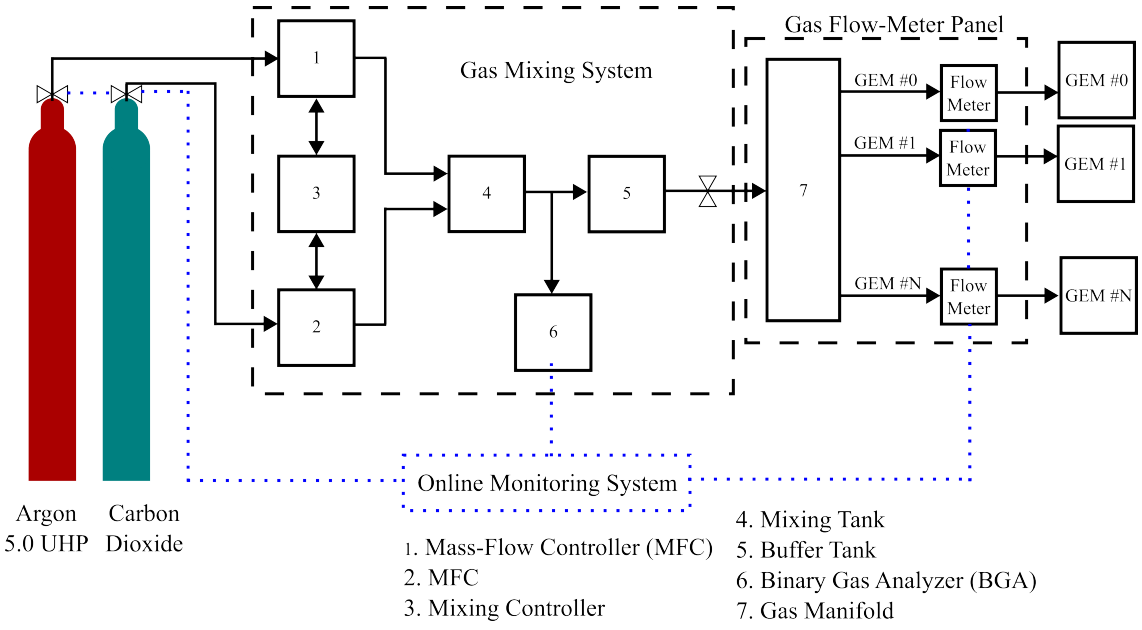

Figure 5.15: A schematic of the key components of the GEM gas distribution system for Hall A as during the G_M^n and nTPE experiments.

To allow access to the GEM gas-mixing system and the regular change-out argon and carbon dioxide cylinders during in-beam operations, a Hall A gas shed exists and these components were located there. The gas flow-meter panel that provides gas lines to each module are located within Hall A. Separate cylinders of pure argon and carbon dioxide are connected via gas lines to individual mass flow controllers (MFCs). Individual cylinders of pure gas are used as a cost reduction measure, since cylinders of pre-mixed Ar/CO_2 are relatively more expensive. The MFCs are responsible for regulating the relative flow

of argon and carbon dioxide into the Mixing Tank, and the MFCs are controlled by the Mixing Controller module. The MFCs and the Mixing Controller ensure that the desired mixture ratio of 75/25 (within less than a 1% range of uncertainty) Ar/CO_2 is produced. In between the Mixing and Buffer tanks a Binary Gas Analyzer (BGA) is connected. The BGA is one of the most critical components of the entire gas mixing system as it is constantly provides gas mixture concentration monitoring. The BGA is able to determine an accuracy on the gas or vapor mixture ratio on the order of 0.01%. The principle of operation of the BGA relies on precisely measuring the speed of sound and temperature within a gas mixture. By knowing the thermodynamic properties and molar masses of the gas mixture, the BGA is able to determine the composition of the gas mixture. During the commissioning phases of the G_M^n and nTPE experiments the BGA was calibrated to multiple cylinders from different batches of pre-mixed Ar/CO_2 cylinders from the same gas manufacturer. Directly downstream of the Mixing tank is a large-volume Buffer tank, which holds the produced gas mixture. The Buffer tank connects directly to the Gas Manifold panel in Hall A, which contains all of the gas flow-meters. The gas flow-meters are instrumented so that each individual GEM module (gas volume) is connected to just one flow-meter. Along each individual gas line, between the flow-meter and the GEM detector volume, is a high-quality gas filter, which removes most remaining undesired impurities from the gas mixture before entering the GEM modules.

A major component of the Hall A GEM gas system is the Online Monitoring System, as shown in Fig. 5.15. As mentioned previously in this section, the most key component of said Online Monitoring System is the BGA. However, the BGA is not the only component in this monitoring system. Without describing the location of every monitoring component, one can broadly describe where most of the feedback modules are located. Each individual cylinder, valve, or critical component has a feedback monitoring unit associated with the component. This allows monitoring of almost the entire system, which can be done remotely without entering Hall A. A notable feature of the Online Monitoring System is that the entire system is interlocked with the high-voltage system of the GEM detectors.

Therefore if the gas mixture ratio is not within the desired range of safe operations, the high-voltage system is programmed to turn off and alert members of the shift crew with different types of alarms.

5.5 Overview of GEM Analysis

The major function of the GEM detector system is to identify and fit good charged particle tracks. In order to identify tracks through the GEM detectors the raw data collected from the readout electronics must be decoded and processed with software for higher-order analysis. The initial stage of data analysis includes online analysis and digitization of raw analog signals from the GEM detectors, which occur in real-time during data collection. The main components of the online GEM analysis include: pedestal subtraction, common mode subtraction, and online zero suppression. The purpose of the online analysis is to record into the GEM data stream only hits which were above a certain noise threshold and which most likely correspond to parts of a charged particle track. This online data analysis provides a significant reduction in overall data file size, while still preserving events which correspond to electron track candidates. After the data were collected, the next stage of data processing is the offline analysis, which comprises defining the calorimeter search region, 1-dimensional cluster formation, 2-dimensional hit association, and the track-finding algorithm. For each given charged particle track candidate, a calorimeter search region is defined, based on where the BigBite calorimeter detected a cluster for a given event. During 1-dimensional cluster formation and 2-dimensional hit association, the calorimeter search region is projected to each GEM layer to ensure any strips associated with clusters or hits are within the calorimeter search region. The implementation of the calorimeter search is critical to offline analysis as it significantly reduces the number of hit combinatorics during higher-order offline analysis. Next in the analysis is 1-dimensional cluster formation, which involves determining sets of contiguous strips, for each GEM strip axis, which have an ADC sum above a certain noise threshold, on an event-by-event basis. Once

the 1D clusters are formed on both strip axes, 2D hit associations are determined from the 1D clusters by evaluating specific ADC and timing correlations. Tracks are determined through a chi-squared minimization process by evaluating 2D hit associations and combinations of hits that are projected to all the GEM layers, the target, and the calorimeter. A detailed description of the raw signals from the GEM readout electronics, the low-level diagnostic software useful for operational testing, the pedestal information, online GEM analysis, and the offline GEM analysis is provided in Appendix A.2.

5.6 GEM Installation and Operation in Hall A

This section will describe the installation and operation of the GEMs in the BigBite Spectrometer during the G_M^n and nTPE experiments. The section will also describe electromagnetic shielding which was instrumented on the GEM detector during the installation phase of these experiments. GEM performance parameters including detector resolution, track-based efficiency, and 2D hit maps will be presented. The section will conclude by discussing GEM gain studies (also called high-voltage studies) in high rate environments, which were conducted in this first experimental run period of the SBS program. Lessons learned and further improvements on the GEM detector instrumentation will be briefly summarized.

5.6.1 GEM Setup in Hall A for G_M^n and nTPE Experiments

For the G_M^n and nTPE experiments, GEM detector layers were only instrumented in the BigBite Spectrometer; these GEM layers are collectively referred to as the BigBite GEMs. At any given time during the experimental run period, five GEM layers were instrumented in the BigBite Spectrometer as tracking detectors. The purpose of the BigBite GEMs is to reconstruct charged particle tracks (primarily electrons) and reconstruct the momentum of the corresponding charged particle. The BigBite GEM layers can be considered in two separate stacks the front-tracker GEM layers and a single back-tracker GEM layer, as de-

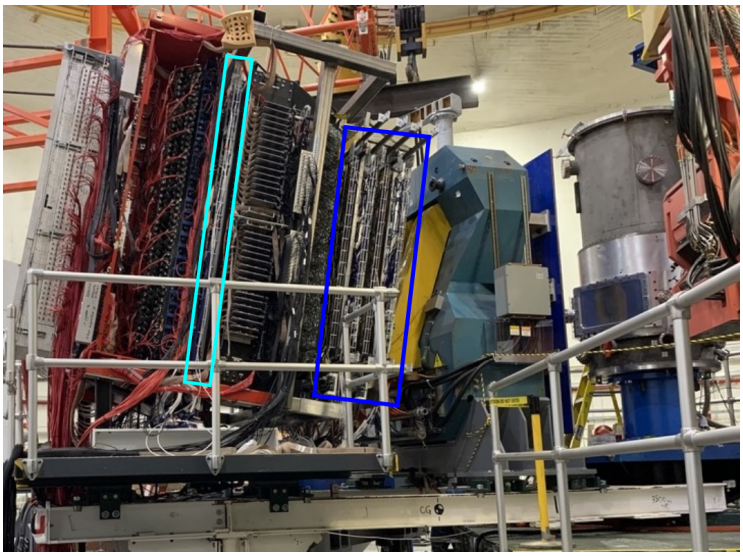

(a)

(b)

Figure 5.16: Pictures displaying the GEM layers in the BigBite Spectrometer during the G_M^n and nTPE experiments. Top: A side view of the BigBite Spectrometer. The front-tracker GEM layers, composed of both UVA UV and INFN XY GEM layers, are outlined in blue. The back-tracker GEM layer is a UVA XY layer and is outlined in cyan. Bottom: A close-up of the front-tracker GEM layers, outlined in blue. The picture contains 4 UVA UV layers and corresponds to the GEM configuration presented in Fig. 5.17c.

picted in Fig. 5.16a. Throughout the G_M^n and nTPE experiments, multiple configurations of UVA UV and INFN XY GEM layers were installed as the front-tracker GEMs. De-

scriptions of these different types of GEM layers is provided in Sec. 5.2. The front-tracker GEMs were located directly in front of the GRINCH and were attached to the BigBite Spectrometer frame. The single BigBite back-tracker GEM layer was always a UVA XY GEM layer. The back-tracker GEM was located between the GRINCH and the Preshower Calorimeter. A picture of the entire BigBite Spectrometer is presented in Fig. 5.16a; the front-tracker GEM layers are outlined in blue and the back-tracker GEM layer is outlined in cyan. A close-up picture of the BigBite front-tracker GEMs is shown in 5.16b.

Due to hardware failures and limitations during in-beam operations of the INFN XY GEM layers, multiple different BigBite GEM configurations were instrumented during the G_M^n and nTPE run period. Only the front-tracker GEMs were manipulated during experimental running, the back-tracker GEM remained unaltered. In chronological order throughout the experiment: two INFN XY and two UVA UV layers, one INFN XY and three UVA UV layers, and four UVA UV layers. A graphical representation of the multiple GEM configurations and the manner in which the BigBite GEMs were order is presented in Fig. 5.17. Having GEM detectors with different strip configurations allows a reduction in combinatorics when reconstructing particle tracks. If a single readout coordinate configuration is used in a tracking detector system some ambiguity in the track position exists. Introducing a second coordinate system provides an independent set of position variables, which can then be used to better identify hits along tracks within search regions of the GEM active area. Understanding when different GEM layers were instrumented in the BigBite Spectrometer has impacts on the GEM software calibrations, track reconstruction, and the overall ability of the BigBite spectrometer to successfully detect electrons.

5.6.2 Electromagnetic Shielding and Studies

During the initial cosmic-ray commissioning of the GEM detectors in test facilities at Jefferson Lab, significant common mode (presented in Appendix A.2.3) fluctuations of the raw signals were observed while the APV25 cards were connected to the GEM modules. The common mode, for the 128 channels of a single APV25 card, is the constant shared

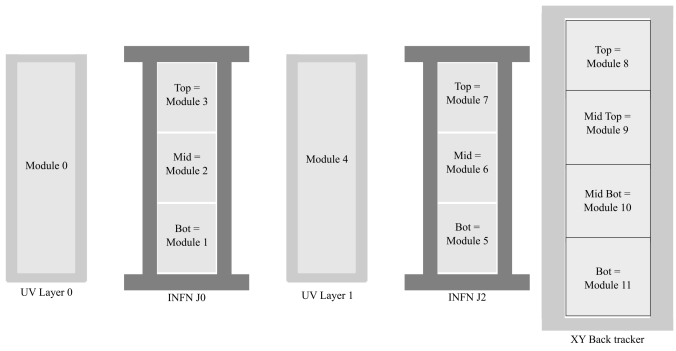

(a)

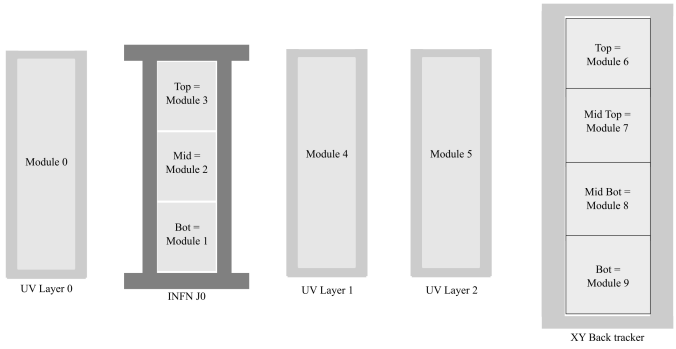

(b)

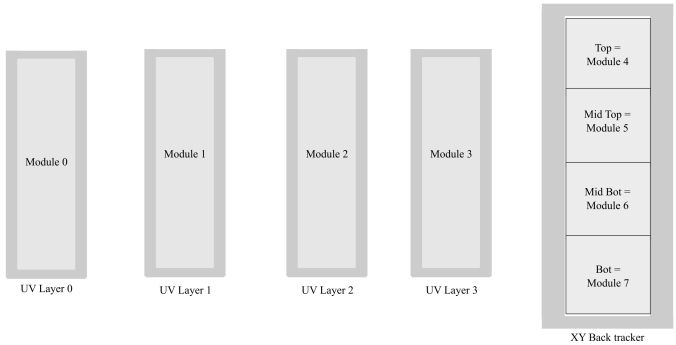

(c)

Figure 5.17: The three configurations of GEM tracking layers are presented vertically on the page in an order which is consistent with the chronological order in which the detector instrumentation was replaced. In a single sub figure, the GEM layers in BigBite from front (closest to the target) to back are graphically represented as left to right. The first, third, and fifth GEM layers in the BigBite Spectrometer did not require any re-instrumentation and as such, throughout the experimental run, remain unchanged. Only the GEM layers in the second and fourth positions were replaced. This diagram shows the progression of using multiple different types of SBS GEM detectors (UVA UV, INFN XY, and UVA XY) to only having UVA manufactured GEM detectors instrumented.

channel offset which the channels fluctuate around on a time sample-by-time sample and event-by event-basis. Similar observations and investigations were conducted on APV25 cards connected to GEM modules located in Hall A, to determine the most optimal operation of these detectors. For INFN XY GEMs these common mode fluctuations typically were within the range of 40-60 ADC units. The UVA-manufactured GEMs had common mode fluctuations between 60-80 ADC units, on average. When considering both INFN and UVA made GEMs there were some instances where the common mode fluctuation was 100 ADC units or a slightly greater. A signal caused by a minimum ionizing particle in a GEM module would have a value no larger than a couple hundred ADC units and the typical pedestal RMS noise values have a mean of 10 ADC units. Clearly, common mode fluctuations with the values as described would have a substantial effect. This substantial common mode fluctuation was considered unsatisfactory for operations during the experiment, particularly causing significant challenges for the then-available online common mode subtraction algorithms. Efforts were made to identify the source of this phenomena and reduce the common mode fluctuation; a solution was found and the remainder of this section will describe it.

Potential sources for this common mode fluctuation were investigated during the testing and commissioning phases of the GEM apparatus. These potential sources included: power supplies connected to GEM readout electronics, ground loops, and interference from RF electromagnetic waves in the surrounding environment. After investigation, it was ultimately determined that the most likely source for the common mode fluctuation was RF interference. To shield an object from electromagnetic waves, one can encase it in a continuous conductive material known as a "Faraday Cage." Simultaneously, prototype GEM Faraday Cages (henceforth shields or shielding) were constructed for both INFN XY and UVA XY GEM modules. From early evaluations of the detector noise, comparing the effects of the prototype shielding it was evident that the common mode fluctuation was significantly reduced.

Fig. 5.19a depicts the effect of shielding on a single APV25 card's common mode

fluctuation, for a single event, across all six time samples. It is evident from Fig. 5.19a that the variation of the common mode is more uniform after the shielding is installed. 5.19b shows the effect of the shielding on a typical common mode distribution, considering thousands of events. The common mode distribution plots are generated by taking the difference in the average ADC value for all 128 channels in one APV25 card between the first time sample and the next five time samples. The key factor for comparison is the standard deviation of these distributions. By comparing these common mode distributions and the corresponding standard distributions for many APV25 cards before and after shielding, a factor of 3-4 improvement was observed.

As a result of this significant reduction in the common mode fluctuation across all GEM modules, it was decided that every GEM module used during experimental operation should be equipped with shielding. As shown previously, Figs. 5.9 and 5.10 show UVA UV and INFN XY GEM modules, respectively, that have electromagnetic shielding installed. Fig. 5.18 shows a single UVA XY GEM module which has been equipped with shielding; when installed for experimental operation each module on the UVA XY GEM layer was equipped with shielding. Each different type of SBS GEM detector has unique specifications for the final mechanical design of the electromagnetic shielding. However, components and features which are common for all shielding equipped to the SBS GEM layers, for production conditions, will be described. The support structure of the shielding was made of U channel aluminum bars; four bars were machined to be fastened together in a rectangular shape to mimic the perimeter of the GEM module frames. The primary component of the electromagnetic shield was a 50 μm thick aluminum foil, which is stretched across the aluminum support and connected to the support by a conductive copper tape. Depending on the type of GEM module, a space between one to three cm is left between the aluminum foil and the gas window of the GEM module, so there is no significant electrostatic interaction. Kapton tape and Kapton foil, both 3 mil and 5 mil thick, are included as needed for electrical isolation on the side of the shield which is closest to the GEM module. Since each GEM module has two sides (or faces), two shield frames must

be installed on a given GEM module to account for a full set of electromagnetic shielding; this type of design necessitates that the two shield frames must be electrically connected for it to be a sufficient Faraday Cage. Standard gauge electrical wire in the range of 10 to 20 AWG was soldered onto the copper tape and thereby connected to both frames. The number of wires connected the two shield frames was at least the same as the total number of APV25 cards connected to the corresponding GEM module. Similar electrical wires were soldered to the copper tape and connected to the ground of the APV25 cards via fasteners; the number of wires used was consistent with the total number of APV25 cards connected to the GEM module. Every electromagnetic shield installed on GEM modules during the experiment had these common features.

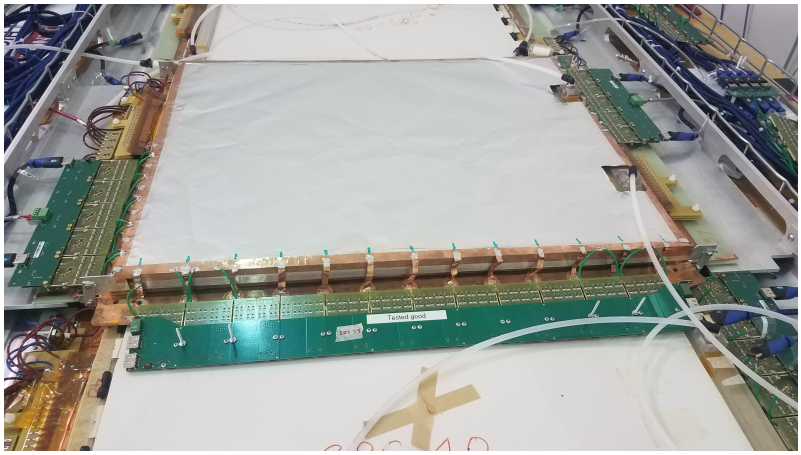

Figure 5.18: One single UVA XY GEM module with RF shielding installed. All modules on the back-tracker layer in the BigBite Spectrometer had shielding identical to this design installed for G_M^n and nTPE.

5.6.3 GEM Performance

This was the first time large-area GEM detectors in high rate environments were instrumented at Jefferson Lab. This section will present some key performance parameters: spatial resolution, 2D hit maps, track-based efficiency, and GEM gain studies. As part of this description of GEM performance some challenges and lessons for operating GEM detectors in such environments will be discussed.

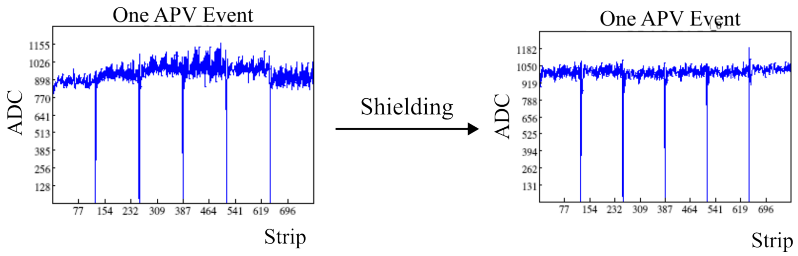

(a)

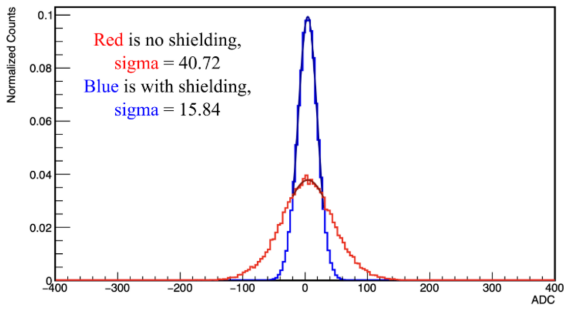

(b)

Figure 5.19: Top: An example of the effect of shielding on a single event GEM raw data frame. The key improvement is that the variation in the common mode is significantly less after the installation of RF shielding. Bottom: An example of a typical common mode distribution comparison for a single APV25 card with and without RF shielding.

Spatial Resolution

The spatial resolution for a given axis is determined from the tracking residual distribution. For a given track and GEM detector layer there are x and y positions where the track intersects with the GEM plane, called track positions. Similarly, there is a 2D hit on a GEM layer, which was used to form a track, which has x and y positions, called hit positions. For a given event with a track, a tracking residual can be formed which is the difference between the hit position and the track position. If one considers many events with corresponding tracks, a distribution for the tracking residual can be generated for a given GEM module. The standard deviation of this tracking residual distribution is then taken as the spatial resolution for a particular GEM module, along that position axis.

The spatial resolution of the BigBite Spectrometer when it contained some INFN XY GEMs is shown in Fig. 5.20a, using the GEM configuration as shown in Fig. 5.17a.

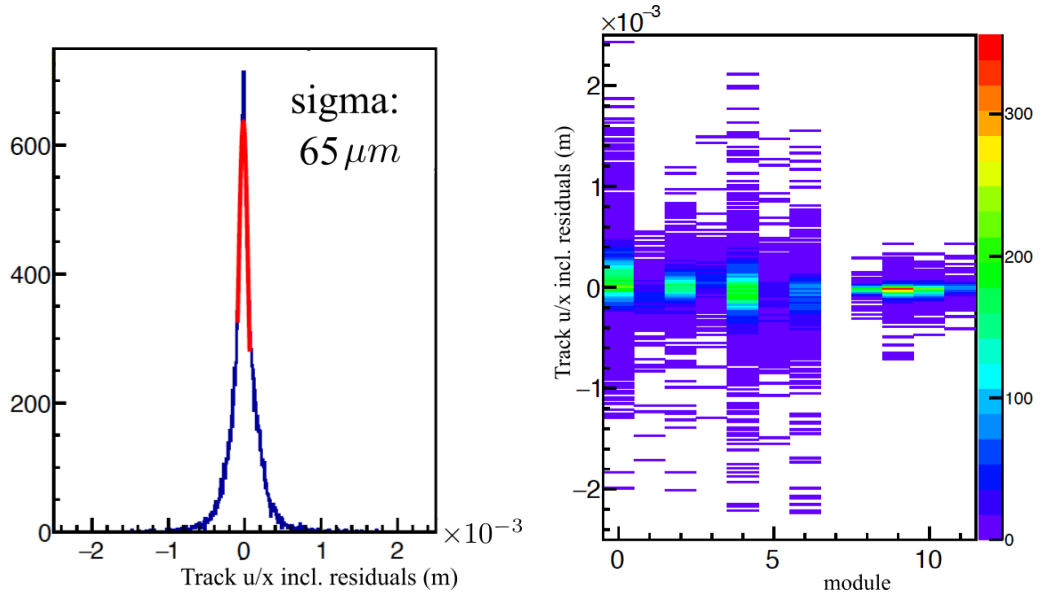

(a) (b)

Figure 5.20: Tracking residual information corresponding to the GEM configuration in Fig. 5.17a. Left: Tracking residuals along the x coordinate direction for all the hits on GEM modules in the BigBite Spectrometer. Right: A plot of tracking residuals for each GEM module in the BigBite spectrometer. In this case, GEM module 7 was turned off. These plots correspond to data taken on the LH2 target with a beam current of 1 μA, during the SBS7 kinematic.

The tracking residual in Fig. 5.20a considers all hits of all the GEM detectors and is therefore representative of the entire BigBite Spectrometer tracking system; the spatial resolution is 65 μm. The tracking residual distributions for each GEM module, in this GEM configuration, are presented in Fig. 5.20b. It should be noted that GEM module 7 (INFN layer J2, top module) was turned off during this time. The data which correspond to the plots in Fig. 5.20 were taken on the LH2 target with a beam current of 1 μA, during the SBS7 kinematic.

The spatial resolution of the BigBite Spectrometer when it contained mostly UVA UV GEMs is shown in Fig. 5.21a, the GEM configuration as shown in Fig. 5.17c. The tracking residual in Fig. 5.21a considers all hits of all the GEM detectors and is therefore representative of the entire BigBite Spectrometer tracking system, the spatial resolution is 67 μm. The tracking residual distributions for each GEM module, in this GEM configuration, are

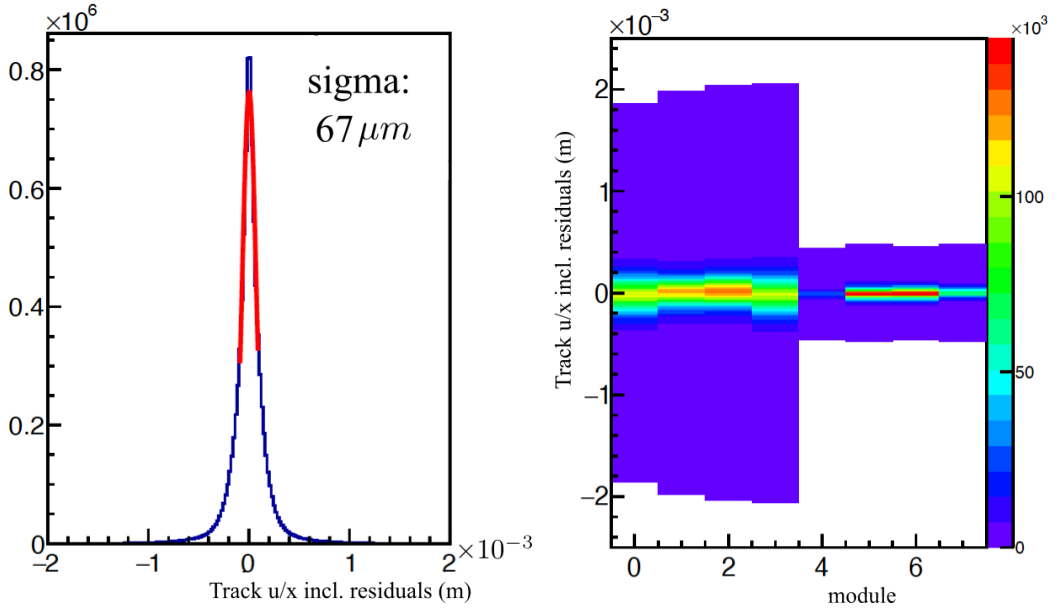

(a) (b)

Figure 5.21: Tracking residual information corresponding to the GEM configuration in Fig. 5.17c. Left: Tracking residuals along the x coordinate direction for all the hits on GEM modules in the BigBite Spectrometer. Right: A plot of tracking residuals for each GEM module in the BigBite spectrometer. These plots correspond to data taken on the LH2 target with a beam current of 5 μA, during the SBS8 kinematic.

presented in Fig. 5.21b. The data which correspond to the plots in Fig. 5.21 were taken on the LH2 target with a beam current of 5 μA, during the SBS8 kinematic.

2D Hit Maps

Another form for viewing GEM detector performance is the 2D hit maps, where the hits are defined as described in Appendix A.2.6. The plots presented in Fig. 5.22 show the 2D hit maps for the two INFN XY GEM layers, which were used in earlier parts of the G_M^n and nTPE experiments. The plots presented in Fig. 5.23 show the 2D hit maps 4 UVA UV layers and one UVA XY layer as the backtracker. We will first describe the INFN XY layer 2D hit maps, then those for the UVA layers.

From Fig. 5.22 it is evident that INFN layer J0 has good acceptance coverage during its operation, other than two narrow regions around the middle module. Every INFN

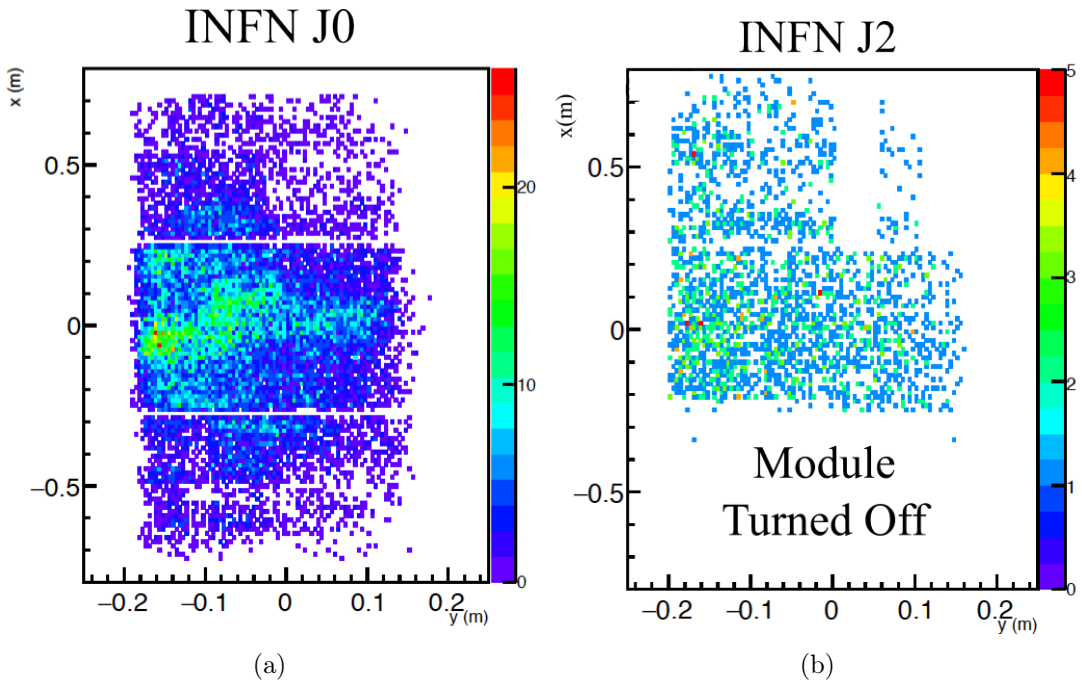

(a) (b)

Figure 5.22: 2D maps of hits on tracks. These plots correspond to the INFN GEM layers J0 and J2. For these plots the negative x-direction corresponds to the physical top of the GEM layers. In this case, the top module of layer J2 is turned off. For the 2D hit map for layer J0, the plot corresponds to data taken on the LD2 target with a beam current of 8 μA, during the SBS11 kinematic. For the 2D hit map for layer J2, plot corresponds to data taken on the LH2 target with a beam current of 1 μA, during the SBS7 kinematic.

GEM layer is designed such that the module acceptance does not overlap and therefore a narrow gap between two INFN GEM modules is present in the hit map. However, when considering INFN layer J2 the performance is less than desirable. The top module of INFN layer J2 (bottom of plot) was turned off in early stages of commissioning due to hardware issues associated with the high voltage. This clearly leaves a gap in the layer acceptance. The middle module of INFN layer J2 demonstrates a reasonable 2D hit map, with no missing acceptance. The bottom module INFN layer J2 (top of plot) has some missing acceptance along the x-direction of the module, these gaps in the acceptance were associated with APV25 readout cards which were not stable during normal data collection, and so were removed from the data stream.

Fig. 5.23 shows the 2D hit maps for the UVA GEM layers in the BigBite Spectrometer;

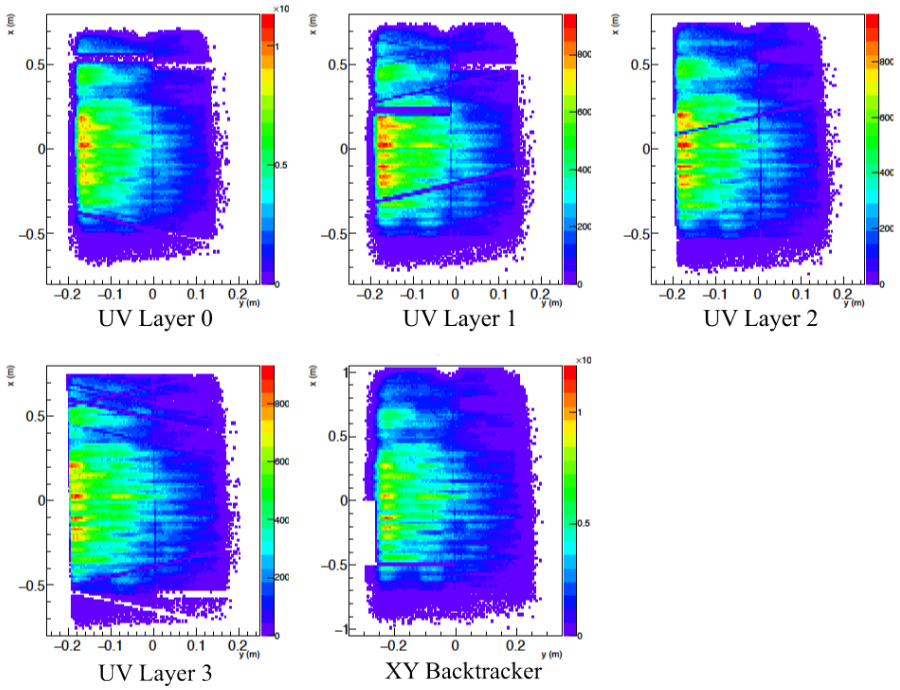

Figure 5.23: 2D maps of hits on tracks. These plots correspond to the GEM configuration in Fig. 5.17c. For these plots the negative x-direction corresponds to the physical top of the GEM layers. These plots correspond to data taken on the LH2 target with a beam current of 5 μA, during the SBS8 kinematic.

four are UVA UV layers in the front tracker and the fifth is the UVA XY backtracker GEM layer. From Fig. 5.23 it is clear that the acceptance coverage of these GEM layers is reasonable. However, we will note regions of poor performance in these GEM layers, which either developed during operation in the experiment or were known issues prior to installing the GEM layers in the BigBite Spectrometer. Five dead high-voltage sectors are present on some of the front tracker layers, as indicated by horizontal bands of reduced 2D hits. UVA UV layer 0 has two dead high-voltage sectors at an approximate x value of 0.5 m. UVA UV layer 1, similarly, has two dead high-voltage sectors at approximate x values of 0.2 m and 0.5 m, respectively. UVA UV layer 3 has one dead high-voltage sector at an approximate x value of -0.6 m. The are also bad readout channels visible, which are evident as diagonal lines of lower intensity. UVA UV layer 1 and layer 2 each

have one area of bad readout channels. UVA UV layer 3 has two areas of bad readout channels, one near the bottom and one near the top of the plot. The source of these bad readout channels is most likely a poor connection between the APV25 card connector on the readout board and the readout strips. The UVA XY backtracker does not have any issues with dead high-voltage sectors or bad readout channels, rather there is a single malfunctioning APV25 card at an approximate y value of -0.3 m and an x value between 0.0 m and -0.5 m. This malfunctioning APV25 card was located in such a manner that it could not be manipulated while the backtracker was in the spectrometer and so was not replaced during the experimental run.

Track-Based Efficiency

The GEM module efficiencies for the SBS experiments were determined from data with a large set of tracks. When a charged particle passes through a GEM module it may or may not cause a signal to be generated in the GEM module. The number of tracks that pass through a given GEM module is denoted, $N_{\text{should hit}}$. The number of tracks that pass through a given GEM module and the module has a hit associated is denoted, $N_{\text{did hit}}$. The track based efficiency is just $\epsilon = N_{\text{did hit}}/N_{\text{should hit}}$. It should be noted that if at least 3 GEM layers do not report a found hit, the track is not recorded. This condition artificially increases the track-based efficiency because $N_{\text{should hit}}$ is decreased. In an ideal detector system, the value $N_{\text{should hit}}$ should be determined independently of the GEM detectors. However, the GEMs are the only tracking detectors available during the SBS experiments and thus are used to determine their own efficiencies.

The track-based efficiency of the GEM modules in the BigBite Spectrometer when it contained some INFN XY GEMs is shown in Fig. 5.24, the GEM configuration as shown in Fig. 5.17a. It should be noted that GEM module 7 (INFN layer J2, top module) was turned off during this. The data which correspond to the plots in Fig. 5.24 were taken on the LH2 target with a beam current of 1 μA, during the SBS7 kinematic. The track-based efficiency of the GEM modules in the BigBite Spectrometer of the BigBite Spectrometer

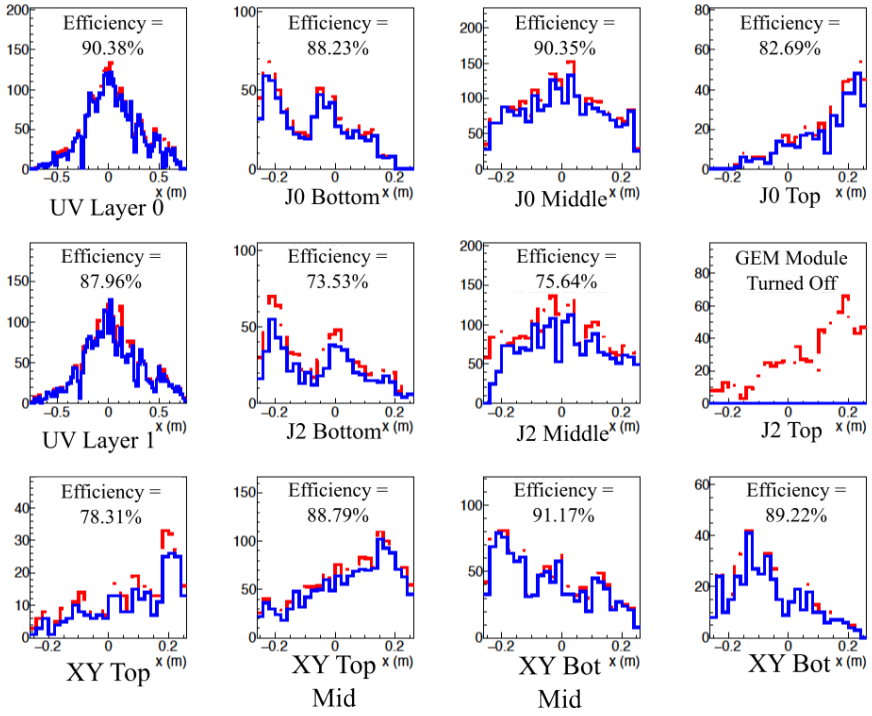

Figure 5.24: GEM module average track-based efficiency values overlayed on plots of hits on tracks as function of x-direction position. Blue represents hits that were detected on tracks, whereas, red is for hits that should have been on tracks. These data correspond to the GEM configuration in Fig. 5.17a. These plots correspond to data taken on the LH2 target with a beam current of 1 μA, during the SBS7 kinematic.

when it contained mostly UVA UV GEMs is shown in Fig. 5.25 (the GEM configuration as shown in Fig. 5.17c).The data which correspond to the plots in Fig. 5.21 were taken on the LH2 target with a beam current of 5 μA, during the SBS8 kinematic.

5.6.4 GEM Gain Studies in High Rate Environment

During the G_M^n and nTPE experiments it was discovered that the background rates in the GEM detectors were significantly higher than originally expected. To study the GEM detector gain as a function of the background, a reasonable observable to study is the current through the resistive high-voltage divider. When the GEM is operated under conditions in which there are no significant background rates (e.g. when beam is not delivered to the experimental Hall) then the high-voltage divider exhibits stable behavior consistent with

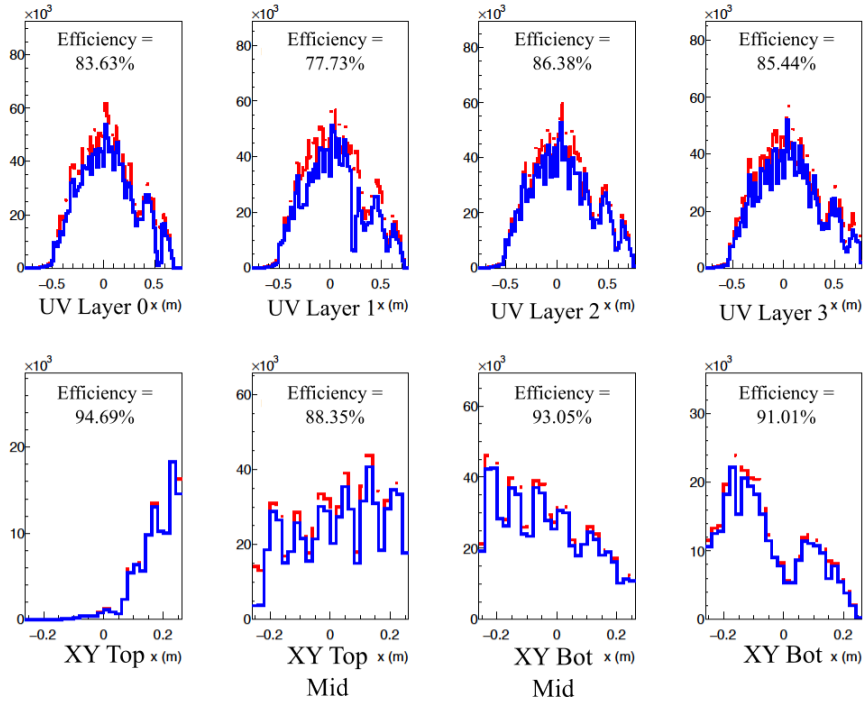

Figure 5.25: GEM module average track-based efficiency values overlayed on plots of hits on tracks as function of x-direction position. Blue represents hits that were detected on tracks, whereas, red is for hits that should have been on tracks. These data correspond to the GEM configuration in Fig. 5.17c. These plots correspond to data taken on the LH2 target with a beam current of 5 μA, during the SBS8 kinematic.

Ohm's Law. However, when significant background rates are present, the divider current increases above the nominal value, and this reduces the effective voltage provided by the resistive divider. This reduction in divider voltage is caused by ions and electrons depositing charge on the GEM electrodes and then traveling into the resistive divider chain. The high-voltage power supply then responds by increasing the applied current to meet the proper voltage settings. This leads to a gain reduction. For GEM detectors operating with resistive high-voltage dividers, this means that as the beam particle rate increases, the gain and thus the tracking efficiencies are significantly reduced.

This reduction in GEM gain can be observed at the hardware level by studying a quantity known as the "excess divider current." The excess divider current is defined to be the GEM current draw during in-beam conditions minus the GEM current with no beam (a

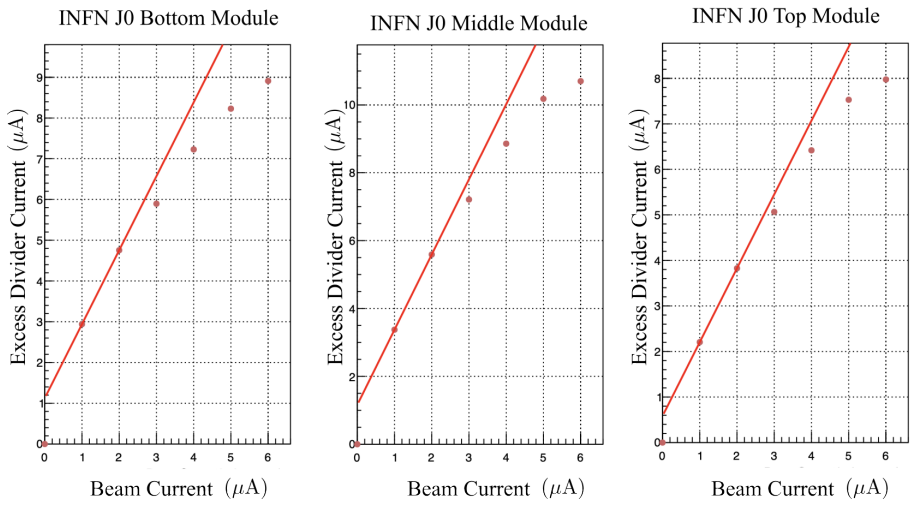

Figure 5.26: Plots of excess divider current vs. beam current for each module of INFN layer J0. A linear fit to low beam current data is applied to demonstrate that some data points demonstrate a non-linear behavior. These plots are typical of INFN GEM modules in the G_M^n and nTPE experiments.

significantly less background environment). From this definition, the excess divider current is zero when beam current is zero. It is known that during beam operations, the GEM foils' current is proportional to flux of ionizing particles and the detector gain factor. If the GEM detector gain remains constant, one would expect a linear relationship between the GEM current draw and the particle flux (during beam operations on a given target). Fig. 5.26 shows a plot of Excess Divider Current vs. Beam Current for each of the GEM modules for INFN layer J0. A similar plot is presented in Fig. 5.27 for UVA UV layer 0. These plots are typical of the behavior for the types of GEM detectors instrumented in the BigBite Spectrometer during the G_M^n and nTPE experiments. When these GEM gain and high-voltage studies were performed the operational conditions remained the same, while only the beam current was increased. From both Figs. 5.26 and 5.27 it is evident that the excess divider current becomes inconsistent with a linear relationship and begins to plateau at higher beam current. This plateauing behavior is consistent with a reduction in the GEM detector gain.

As a result of studying the gain drop effect in the GEMs, the GEM group from UVA

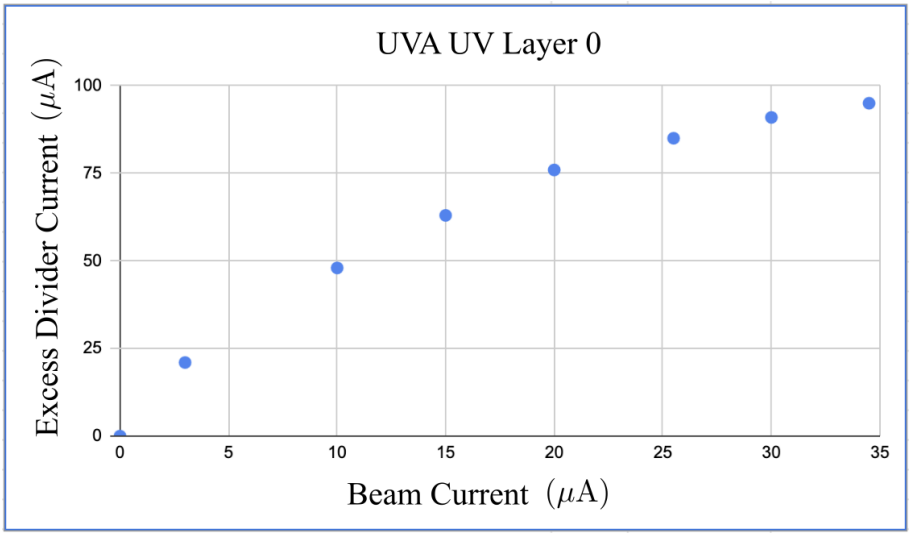

Figure 5.27: Plots of excess divider current vs. beam current for each module of UVA UV layer 0. The non-linear behavior is evident as the data points at higher beam current tend to plateau. These plots are typical of UVA GEM modules in the G_M^n and nTPE experiments. Plot credit: [160]

.

tested and implemented two solutions for future SBS experiments. For more complete descriptions of both solutions see Refs. [160, 161]. One implemented solution is known as the "Two-Path" resistive high-voltage divider. The overall effect of this method is reducing the resistance of the divider effectively by one half. This allows double the amount of current to flow through the high-voltage divider and therefore forces this gain drop effect to be less pronounced and have more stable GEM operation. The second solution is known as the "Individual Channel Power Supply." For this particular method the GEM high-voltage distribution is designed to deliver the high-voltage of a given GEM module as 7 individual channels, corresponding to the GEM electrodes, anode, and cathode. The seven high-voltage channels are then individually managed by a CAEN A1515BTG power supply.

Chapter 6

Experiment Data Analysis

6.1 Analysis Framework

As described in Sec. 3.2, to obtain a calculation for the neutron Rosenbluth slope, S^n, it is necessary to extract the ratio of neutron to proton cross-sections, R, as described in Eq. 3.2. To obtain the physics observable, R, an analysis of the raw data must be conducted. The reactions observed in this experiment were D(e,e'n) and D(e,e'p) for quasi-elastic electron-deuteron scattering. When extracting the physics observable, R, from electron-deuteron scattering processes, known effects including the nuclear binding energy, nucleon Fermi momentum, and final state interactions will inherently be part of the observed cross-sections.

As outlined in Fig. 6.1, the major steps of the data analysis include apparatus calibration, event reconstruction, event selection, realistic Monte Carlo (MC) simulation, and data/MC comparison. Event decoding is the process of parsing, event-by-event, collected raw data to determine signals in the form of integrated charge (ADC) or time information (TDC) from individual detector channels. Event reconstruction is a process that involves combining the detector information from the event decoding to determine cluster and hit formation in detectors, electron track reconstruction, and physics kinematic parameters, thus reconstructing necessary information corresponding to an electron scattering event. A

more detailed description of event decoding and event reconstruction software algorithms for the G_M^n and nTPE experiments is provided in Ref. [134]. Multiple iterations of apparatus calibrations are performed to achieve the optimal detector resolutions. Event selection cuts based on detector geometries and kinematic information are applied to the data sets to determine candidate quasi-elastic scattering events. A simulation machinery is used to generate simulated data which realistically reproduces experimental data. The Monte Carlo simulation incorporates relevant physics and detector effects. The Monte Carlo simulated data are also subjected to an identical analysis procedure as the experimental data. Ultimately, by comparing the experimental data and the simulated data, the ratio R is extracted. The focus of this chapter will be a description and methodology of the data analysis used to extract the physics observables.

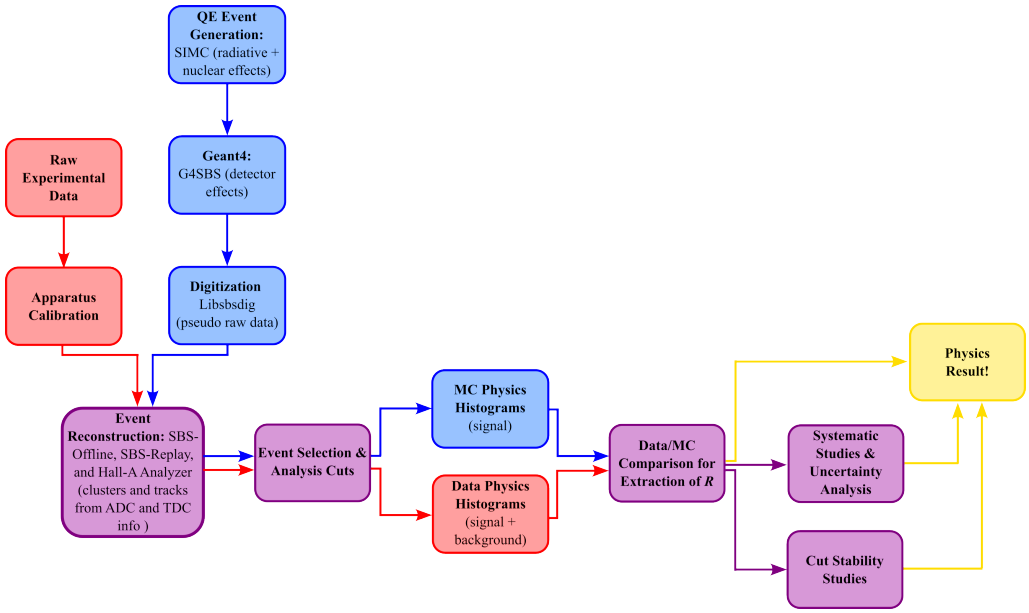

Figure 6.1: A flow diagram of the G_M^n and nTPE analysis. Blocks in red correspond to analysis on only real data. Blue blocks are associated with analysis on only Monte Carlo simulated files. Any analysis which is identically applied to both real data and Monte Carlo simulated files is presented in purple.

6.1.1 Experimental Data Analysis Software

The experimental data is primarily processed with three software packages: the Hall-A Analyzer, SBS-Offline, and SBS-Replay. The remainder of this section will summarize each of these software packages with some detail.

Hall-A Analyzer

Hall-A has a standard data analysis software known as the "Hall-A Analyzer [168]." The Hall-A analyzer is developed in the programming language C++ and utilizes the data analysis libraries and framework of ROOT, which is developed by CERN. The Hall-A analyzer is an object-oriented modular framework that manages raw data decoding, event reconstruction, and physics quantity determination. The Hall-A analyzer is able to take both raw data files (CODA EVIO files) or simulated data as primary input and decode the raw information into ROOT files for further physics analysis. Historically, the Hall-A analyzer was developed for the physics program involving the High Resolution Spectrometers, which have since been decommissioned. The extensible construction of the Hall-A Analyzer allows its core libraries to be implemented for other software packages, including those specific to the SBS program, and the Hall-C Analyzer (known as "hcana"). A description of the essential software for the SBS program and how it connects to the the G_M^n and nTPE experiments will be provided in the following sections.

SBS-Offline & SBS-Replay

The SBS program required the installation of entirely new apparatus to Hall A, and a corresponding requirement for data collection from this new apparatus was analysis software to decode raw signals and reconstruct physics events. The SBS-Offline software package [169], developed by the SBS Software Group, inherits libraries and extends the analysis framework from the Hall-A Analyzer to manage the event reconstruction for experiments using the SBS apparatus. SBS-Offline includes class structures representing each detector

subsystem which have specialized algorithms to support the operational demands of the SBS physics program.

The SBS-Replay software package [170] is a collection of apparatus database files, raw data analysis scripts (called replay scripts), physics analysis scripts, and detector calibration scripts. SBS-Replay is primarily responsible for interfacing with the Hall-A Analyzer and SBS-Offline to process raw CODA event files (EVIO files) into ROOT files via the replay scripts. These output ROOT files contain detector and basic physics kinematic information which can be used for further physics analysis. The database files embedded in SBS-Replay contain information for spectrometer and detector specific configurations and parameters which are essential to properly processing the raw data. The database files have a feature which allows time-stamping of detector parameters and calibration coefficients to reflect any changes in the condition of the apparatus throughout experimental run periods. When data processing occurs, the Hall-A analyzer manages these time-stamps and matches the corresponding database information to the proper EVIO files. The calibration scripts are iteratively used on the output ROOT files to determine essential parameters for defining and replicating spectrometer and detector conditions in software.

To reduce unnecessary use of limited computing resources and to ensure that analyses have a common set of detector calibrations, multiple mass software replays of the entire physics data set were produced. Each of these mass data replays will be referred to as an individual data processing "pass" (or passes). So far there have been three passes of mass data replays for the G_M^n and nTPE experiments. The status of the detector calibrations and software for each pass is available as a software version of SBS-Replay and SBS-Offline. The first set of mass replayed data files is known as Pass 0 and was produced during the running period. Most of the detector calibrations for Pass 0 were based on the commissioning phase of the experiment. Some detector calibrations were iteratively developed as throughout the experimental running, and these also contributed to the calibrations used during the Pass 0 mass replay. The Pass 1 mass data replay was complete in Fall 2022. The calibrations associated with Pass 1 are based on improved iterations of calibrations

performed for the Pass 0 mass replay. The calibrations for the Pass 1 mass replay also are based on the understandings of detector performance from the entire experimental run period. Significant calibrations were performed for all detector subsystems in-preparation of the Pass 2 mass replay; descriptions for most of these calibrations are documented in Refs. [134] and [140]. The data used for this data analysis were from the Pass 2 data mass replay. Further improvements to detector calibrations could be introduced to the software which would necessitate additional mass replay iterations, and ideally produce better quality processed data files.

6.1.2 Monte Carlo Simulation Software

The processing of the Monte Carlo simulated data is mainly completed with four different software packages: SIMC, G4SBS, LIBSBSDIG, and SBS-Replay. The generation of simulated events is handled by SIMC. The propagation of these simulated events through the detector geometries and modeling detector responses is managed by G4SBS. After propagating the simulated events through the detectors, LIBSBSDIG formats the simulated responses in a psuedo-raw data format which mimics the organization of the raw experimental data. SBS-Replay then applies identical event reconstruction to the simulated data which is now in a pseudo-raw data format, so that the simulated data is then prepared to undergo higher-order levels of physics analysis.

SIMC

SIMC [171] is a Monte Carlo simulation package written in FORTRAN, primarily for coincidence reaction experiments conducted in Hall C at Jefferson Lab. SIMC provides realistic physics models for elastic and quasi-elastic scattering event generation, which include both radiative corrections and nuclear-effect models. The capabilities of SIMC were adapted for the simulation requirements of the G_M^n and nTPE experiments to incorporate modeling the acceptances of the BigBite and SuperBigBite Spectrometers, realistic target geometry, and implementation of a model for quasi-elastic electron-neutron scattering from

deuterium. At the time this analysis was conducted, simulated events of quasi-elastic electron-neutron and electron-proton scattering were used where radiative corrections were implemented for only the incoming and outgoing electron. Final state interactions of the scattered nucleon are not modeled by SIMC. The elastic and quasi-elastic event generators rely on cross-section information from the Kelly parameterization (as described in Sec. 2.5.1) for G_E^p, G_M^p, and G_M^n, and the Hall A G_E^n Collaboration fit for G_E^n [72]. A detailed description of the event generation process for SIMC, in the context of the G_M^n and nTPE experiments, is provided in Ref. [134].

G4SBS

G4SBS [172] is a Monte Carlo simulation package used to realistically model the detector geometries and responses for the experiments in the SBS program. G4SBS is written by the SBS Software Group and is an extension of the Geant4 simulation toolkit by CERN. Detailed properties, geometries, and particle-interactions for all detector and spectrometer components of each experiment in the SBS program are modeled in G4SBS. G4SBS has many configurable parameters including the given experiment, the target, beam energy and current, spectrometer angles, magnet fields and maps, and the number of generated events. The output format of G4SBS is a ROOT file which contains charge and energy deposition information for relevant detector channels.

G4SBS is constructed with many useful built-in event generators including elastic and quasi-elastic electron-nucleon scattering, inclusive inelastic electron-proton or electron-deuteron scattering, and other event generators which are necessary for other experiments in the SBS program. The inelastic event generator are determined using Christy-Bosted parameterizations [173, 174] of inclusive $p(e, e')$ and $d(e, e')$ reactions to compute inelastic cross-sections for protons and neutrons. However, radiative corrections are not implemented in the event generators of G4SBS. Therefore more realistic event generation is handled by SIMC, as described in Sec. 6.1.2, and given as input to G4SBS to properly manage the propagation of the generated events through the relevant SBS experimental

spectrometer and detector geometries. It is important to note that the MC files used for this analysis have known deficiencies for two particular apparatus components. The first issue pertains to the size of the Preshower blocks modeled in G4SBS. Originally, the experiment was going to use larger lead-glass blocks for the Preshower calorimeter. A smaller lead-glass block size was used in the apparatus, as such the size of the block was properly altered in the G4SBS simulation. However, the spacing between the Preshower blocks, as modeled within the simulation, was not properly adjusted and thus produces a pattern spacing artifact in Preshower calorimeter distributions. The second deficiency corresponds to the target scattering chamber geometry. The geometry of the downstream window of the target scattering chamber was modeled in G4SBS as being smaller than what was presented in the experimental apparatus. Both deficiencies have been resolved within the G4SBS software, but are present within the MC files used for this analysis.

LIBSBSDIG

LIBSBSDIG [175] is a C++ software library used for digitizing the output detector information in the files from G4SBS. Ultimately, after G4SBS output files are processed by LIBSBSDIG the detector information is organized in a pseudo-raw data format. These resultant digitized Monte Carlo event-generated files from LIBSBSDIG can then be analyzed by the SBS-Replay and SBS-Offline software frameworks, which were described in Sec. 6.1.1.

6.1.3 Physics Analysis Software

The C++ based software package, developed by the author, used to extract physics results and generate analysis plots used in this dissertation is named "nTPE Analysis" [176]. The key features of this standalone repository are parser programs that generate plots and information for detectors and physics extraction parameters which are stored in a ROOT tree for further analysis. There are two versions of the parser programs which manage data processing for input from replayed data or MC simulated files, respectively.

The parsed data and MC files are then used for higher-order levels of analysis involving quasi-elastic event selection, data/MC comparison, detector studies, systematic studies and uncertainties. The comparison of data and MC distributions are used primarily for the extraction of physics ratio R.

6.1.4 Elastic Electron-Nucleon Kinematics and HCal Δx and Δy

The variables Δx and Δy, called delta variables, are essential to the data analysis and extraction of physics observables for the G_M^n and nTPE experiments. The delta variables encapsulate position information from both quasi-elastic scattered nucleons detected by the hadron arm and projections of quasi-elastic scattered electrons as reconstructed by the electron arm. The delta variable position distributions allow the identification and separation of distinct distributions corresponding to protons or neutrons.

A prerequisite to defining the delta variables is calculating the expected neutron position $\left(x_{\mathrm{HCal}}^{\mathrm{exp}}, y_{\mathrm{HCal}}^{\mathrm{exp}}\right)$ at the plane on the face of HCal. The calculation of the expected neutron position, $\left(x_{\mathrm{HCal}}^{\mathrm{exp}}, y_{\mathrm{HCal}}^{\mathrm{exp}}\right)$, is based on quasi-elastic electron-nucleon scattering kinematics for each primary track reconstructed in the BigBite Spectrometer.

6.1.4.1 Elastic Electron-Nucleon Kinematics

The Hall spatial coordinate system is defined such that the origin is at the center of the cryotarget cell, the $+z$ axis points (downstream) in the direction of the incoming electron beam, the $+y$ axis points vertically toward the ceiling of the experimental Hall, the $+x$ axis points horizontally to beam left, thereby forming a right-handed coordinate system. The Hall Coordinate system is depicted in Fig. 6.2. The momentum four-vector of the incoming electron can be defined as

$$p_e^\mu = (E_{\mathrm{beam}}, 0, 0, p_{z,e}) \simeq (E_{\mathrm{beam}}, 0, 0, E_{\mathrm{beam}})\,, \tag{6.1}$$

where E_{beam} is the electron beam energy, and $p_{z,e}$ is the electron momentum in the z-direction. In this analysis, the electron beam energy, E_{beam}, includes corrections for energy losses within the target and due to the target chamber aluminum windows. At the GeV

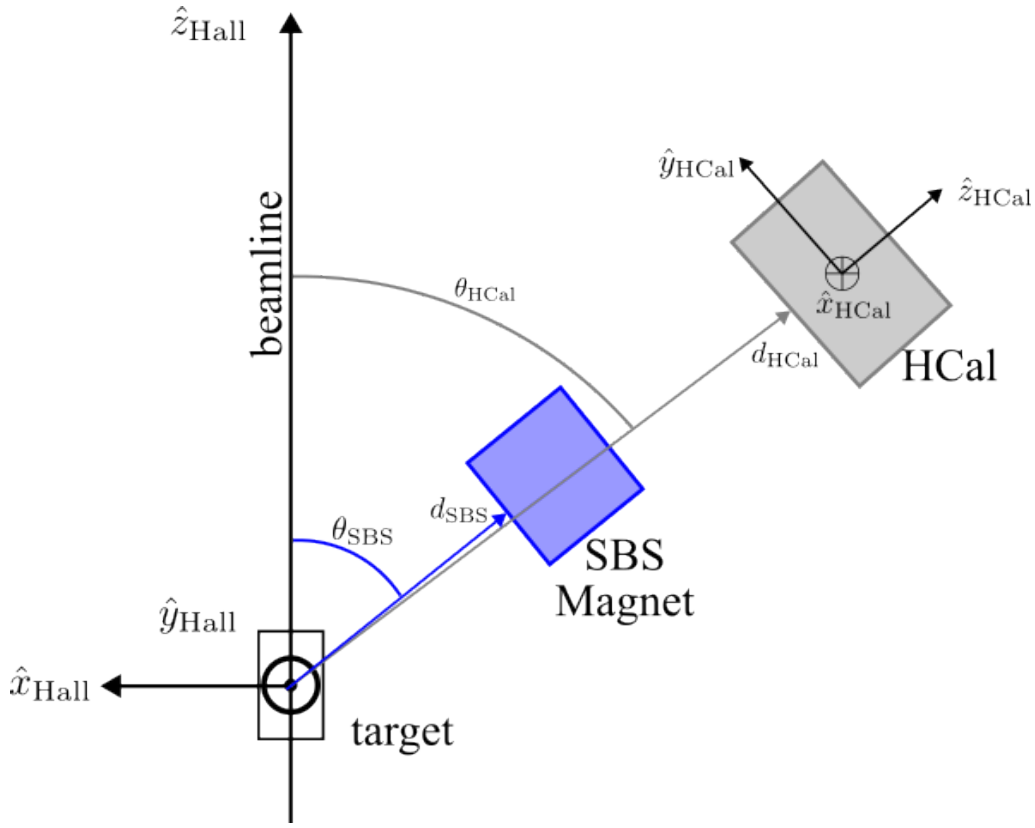

Figure 6.2: A conceptual diagram, not to scale, showing the HCal Coordinate system $(\hat{x}_{\text{HCal}}, \hat{y}_{\text{HCal}}, \hat{z}_{\text{HCal}})$ relative to the Hall Coordinate system $(\hat{x}_{\text{Hall}}, \hat{y}_{\text{Hall}}, \hat{z}_{\text{Hall}})$. The SBS magnet and HCal central angles (θ_{SBS} and θ_{HCal}, respectively) as well as the distances from the Hall Coordinate system origin to the SBS Magnet, d_{SBS}, and HCal, d_{HCal}, are independently configurable parameters.

energy scale being considered, the rest mass of the electron is negligible and therefore $p_{z,e} \simeq E_{\text{beam}}$ is a reasonable approximation. The nucleons in the target are assumed to be at rest and the momentum four-vector of the initial nucleon is

$$p_N^\mu = (M_N, 0, 0, 0)\,, \tag{6.2}$$

where M_N is the mass of the corresponding nucleon. The BigBite Spectrometer provides the necessary information to reconstruct the momentum of the scattered electron which is represented by the four-vector

$$p^{\mu}_{e'} = \left(E', p_{x,e'}, p_{y,e'}, p_{z,e'}\right). \tag{6.3}$$

Since the scattered electron will be at the GeV energy scale, the scattered electron energy is given by

$$E' = p_{e'} = \sqrt{p^2_{x,e'} + p^2_{y,e'} + p^2_{z,e'}}. \tag{6.4}$$

Equivalently one can consider the scattered electron momentum from the polar and azimuthal angles of the reconstructed track

$$p^{\mu}_{e'} = (p_{\text{elas}}, p_{\text{elas}} \sin(\theta_{e'}) \cos(\phi_{e'}), p_{\text{elas}} \sin(\theta_{e'}) \sin(\phi_{e'}), p_{\text{elas}} \cos(\theta_{e'})), \tag{6.5}$$

where the momentum of the quasi-elastically scattered electron, p_{elas}, is calculated using

$$p_{\text{elas}} = \frac{E_{\text{beam}}}{1 + \left(\frac{E_{\text{beam}}}{M_N}\right)(1 - \cos(\theta_{e'}))}. \tag{6.6}$$

The reconstructed polar and azimuthal electron scattering angles can be determined from components of the scattered electron momentum

$$\theta_{e'} = \arccos\left(\frac{p_{z,e'}}{E'}\right), \tag{6.7}$$

$$\phi_{e'} = \arctan\left(\frac{p_{y,e'}}{p_{x,e'}}\right). \tag{6.8}$$

The four-momentum transferred to the nucleon, or the four-momentum of the virtual photon, is defined as

$$q^{\mu} = p^{\mu}_{e} - p^{\mu}_{e'} = p^{\mu}_{N'} - p^{\mu}_{N} = (\nu, \vec{q}), \tag{6.9}$$

where the quantities $\nu = E_{\text{beam}} - E'$ and $\vec{q}$ are the energy and momentum transfer, respectively, in the scattering process and we have assumed energy-momentum conservation of the incoming and outgoing momenta. The four-momentum of the expected quasi-elastic nucleon, $p^{\mu}_{N'}$, can be extracted from the four-momentum transfer, q^{μ}, as follows

$$p^{\mu}_{N'} = q^{\mu} + p^{\mu}_{N} = p^{\mu}_{e} - p^{\mu}_{e'} + p^{\mu}_{N}. \tag{6.10}$$

By taking the invariant dot product of $p^{\mu}_{N'}$ with itself, one can determine the invariant mass squared

$$\begin{aligned} W^2 &= \left(q^{\mu} + p^{\mu}_{N}\right)^2 = \left(p^{\mu}_{e} - p^{\mu}_{e'} + p^{\mu}_{N}\right)^2, \\ &= q^2 + M_N^2 + 2q \cdot p_N. \end{aligned} \tag{6.11}$$

We define Q^2 with the condition that q is spacelike as follows

$$\begin{aligned} Q^2 = -q^2 &= -\left(p^{\mu}_{e} \cdot p_{e,\mu} + p^{\mu}_{e'} \cdot p_{e',\mu} - 2p^{\mu}_{e} \cdot p_{e',\mu}\right), \\ &\simeq 2p^{\mu}_{e} \cdot p_{e',\mu} = 2\left(E_{\text{beam}}E' - E_{beam}p_{z,e'}\right), \\ &= 2\left(E_{\text{beam}}E' - E_{beam}E'\cos(\theta_{e'})\right), \\ &= 2E_{\text{beam}}E'\left(1 - \cos(\theta_{e'})\right). \end{aligned} \tag{6.12}$$

This allows for a simplified version of the invariant mass squared

$$W^2 = -Q^2 + M_N^2 + 2M_N\nu. \tag{6.13}$$

From the four-momentum transfer one can determine the magnitude of the quasi-elastic nucleon momentum

$$|\vec{p}_{N'}| = \sqrt{\nu^2 + 2M_N\nu}. \tag{6.14}$$

By requiring coplanarity in the scattering process, the polar angle of the scattered nucleon is

$$\phi_{N'} = \phi_{e'} + \pi. \tag{6.15}$$

From conservation of momentum in the z-direction and from information from the scattered electron, the azimuthal angle of the scattered nucleon is

$$\theta_{N'} = \arccos\left(\frac{E_{\text{beam}} p_{\text{elas}} \cos(\theta_{e'})}{|\vec{p}_{N'}|}\right). \tag{6.16}$$

The unit vector in the direction of the quasi-elastically scattered nucleon is defined as

$$\hat{p}_{N'} = (\sin\theta_{N'}\cos\phi_{N'}, \sin\theta_{N'}\sin\phi_{N'}, cos\theta_{N'})\,. \tag{6.17}$$

The four-momentum of the scattered nucleon in the Hall coordinate system, based on the projection of information of the scattered electron track is

$$p^{\mu}_{N'} = (\nu + M_N, |\vec{p}_{N'x}|\hat{p}_{N'x}, |\vec{p}_{N'y}|\hat{p}_{N'y}, |\vec{p}_{N'z}|\hat{p}_{N'z}). \tag{6.18}$$

On an event-by-event basis the four-momentum of the scattered nucleon is used to define the expected position of the nucleon on the face of HCal, based on the primary track information of the scattered electron, as discussed next.

6.1.4.2 Calculation of Expected Positions on HCal

The description for the provided kinematic information is presented within the Hall Coordinate System. The HCal cluster position, as determined by the SBS analysis software, is provided in the HCal Coordinate system. This HCal Coordinate system is different than the Hall Coordinate system. The HCal Coordinate system can be defined relative to the Hall Coordinate System by considering the HCal central angle, θ_{HCal}, with respect to the downstream beamline. A diagram of the HCal Coordinate system relative to the Hall Coordinate system is presented in Fig. 6.2. The HCal Coordinate system axes are represented by the following equations:

$$\hat{z}_{\text{HCal}} = (\sin(-\theta_{\text{HCal}}), 0, \cos(-\theta_{\text{HCal}}))\,, \tag{6.19}$$

$$\hat{x}_{\mathrm{HCal}} = (0, -1, 0)\,, \tag{6.20}$$

$$\hat{y}_{\mathrm{HCal}} = \frac{\hat{z}_{\mathrm{HCal}} \times \hat{x}_{\mathrm{HCal}}}{||\hat{z}_{\mathrm{HCal}} \times \hat{x}_{\mathrm{HCal}}||}. \tag{6.21}$$

The HCal origin in the HCal Coordinate system is defined as

$$\vec{O}_{\mathrm{HCal}} = d_{\mathrm{HCal}}\hat{z}_{\mathrm{HCal}} \tag{6.22}$$

where d_{HCal} is the distance from the target to the face of HCal. With the HCal Coordinate system defined, the expected nucleon positions on HCal can be determined by projecting a straight line from the interaction vertex to the HCal plane along the nucleon's trajectory. The distance between the interaction vertex and the position on HCal is denoted $s_{\mathrm{intersect}}$ and is defined by

$$s_{\mathrm{intersect}} = \frac{\left(\vec{O}_{\mathrm{HCal}} - \vec{v}\right) \cdot \hat{z}_{\mathrm{HCal}}}{\hat{p}_{N'} \cdot \hat{z}_{\mathrm{HCal}}} \tag{6.23}$$

where $\vec{O}_{\mathrm{HCal}}$ is the HCal origin, $\vec{v}$ is the interacting vertex, $\hat{z}_{\mathrm{HCal}}$ is the HCal z-axis, and $\hat{p}_{N'}$ is the unit vector for the scattered nucleon. The vector projecting from the interacting vertex, in the Hall Coordinate system, to the expected nucleon position, $\vec{h}_{\mathrm{intersect}}$, is calculated by

$$\vec{h}_{\mathrm{intersect}} = \vec{v} + s_{\mathrm{intersect}}\hat{p}_{N'}. \tag{6.24}$$

The x (dispersive direction) and y (transverse direction) coordinates of the expected nucleon position at HCal, denoted $x^{\mathrm{exp}}_{\mathrm{HCal}}$ and $y^{\mathrm{exp}}_{\mathrm{HCal}}$ respectively, are calculated by

$$x^{\mathrm{exp}}_{\mathrm{HCal}} = \left(\vec{h}_{\mathrm{intersect}} - \vec{O}_{\mathrm{HCal}}\right) \cdot \hat{x}_{\mathrm{HCal}}, \tag{6.25}$$

and

$$y^{\mathrm{exp}}_{\mathrm{HCal}} = \left(\vec{h}_{\mathrm{intersect}} - \vec{O}_{\mathrm{HCal}}\right) \cdot \hat{y}_{\mathrm{HCal}}, \tag{6.26}$$

where $\hat{x}_{\mathrm{HCal}}$ and $\hat{y}_{\mathrm{HCal}}$ are the x and y HCal coordinate system axes, respectively.

In this determination of the expected nucleon positions, $x^{\mathrm{exp}}_{\mathrm{HCal}}$ and $y^{\mathrm{exp}}_{\mathrm{HCal}}$, only a straight-line projection is considered and as such it is only an exact calculation for neu-

tral particles, i.e. neutrons, and is called "the neutron hypothesis". This calculation of the expected nucleon positions does not account for the deflection of charged particle, i.e. proton, tracks by the SBS dipole magnet. The calculation of the proton expected positions on HCal is not necessary for the observable extraction of deuterium data for the G_M^n and nTPE experiments. Further information on the Δx and Δy distributions will be described in the following section, including the motivation for omitting proton expected positions on HCal in the construction of these analysis variables.

Though the proton expected positions on HCal are not necessary for physics analysis of deuterium data, there is practical use for these quantities in the analysis of systematic uncertainties and certain detector studies. We will continue by providing a description of how to account for the deflection, introduced by the SBS dipole magnet, of charged particle tracks in the calculation of the expected nucleon positions on HCal. The angular deflection, θ_{deflect}, of a proton is calculated by

$$\theta_{\text{deflect}} = \frac{0.3 \cdot BdL}{|\vec{p}_{N'}|}, \tag{6.27}$$

where BdL is the field integral of the SBS magnet in T·m and $|\vec{p}_{N'}|$ is the magnitude of the proton's four-momentum. The deflection distance, d_{deflect}, for scattered protons on the face of HCal caused by the SBS magnet is

$$d_{\text{deflect}} \approx \tan\left(\theta_{\text{deflect}}\right)\left(d_{\text{HCal}} - \left(d_{\text{SBS}} + \frac{d_{\text{SBSgap}}}{2}\right)\right) \tag{6.28}$$

where d_{HCal} is the distance from the target to the HCal, d_{SBS} is the distance from the target to the SBS magnet, and d_{SBSgap} is the width of the gap of the SBS magnet. Since the SBS magnet is a dipole, the deflection of charged particles should only occur in the dispersive direction, so within the HCal coordinate system charged particles (protons) will be swept towards the top of HCal, in the negative x-direction in the HCal Coordinate system. Thus one can account for the expected proton position on the face of HCal by subtracting the

deflection distance, Eq. 6.28, from the x-coordinate of the expected nucleon position, Eq. 6.25. The application of the deflection due the SBS magnetic field is only relevant for certain analyses and studies and as such when part of the described analysis it will be explicitly noted in the remainder of this chapter.

6.1.4.3 Δx and Δy Distributions

Two quantities necessary for this data analysis and physics extraction are the Δx and Δy distributions. The delta variables quantify the correlation between the observed and expected nucleon positions at HCal in both the dispersive (Δx) and transverse (Δy) directions. Each delta variable, respectively, is defined as the difference between the observed position as detected by the HCal and the expected nucleon position projected to HCal as described in Sec. 6.1.4.2. The delta variables are

$$\Delta x = x_{\mathrm{HCal}}^{\mathrm{obs}} - x_{\mathrm{HCal}}^{\mathrm{exp}}, \tag{6.29}$$

and

$$\Delta y = y_{\mathrm{HCal}}^{\mathrm{obs}} - y_{\mathrm{HCal}}^{\mathrm{exp}}, \tag{6.30}$$

where $x_{\mathrm{HCal}}^{\mathrm{obs}}$ and $y_{\mathrm{HCal}}^{\mathrm{obs}}$ are the position information as measured and reconstructed by HCal, and $x_{\mathrm{HCal}}^{\mathrm{exp}}$ and $y_{\mathrm{HCal}}^{\mathrm{exp}}$ are expected nucleon positions determined from Eqs. 6.25 and 6.26.

From Eqs. 6.29 and 6.30, one can construct both one-dimensional (1D) and two-dimensional (2D) distributions of the delta variables for a particular kinematic and SBS magnetic field setting, from a particular target. For the 2D distribution Δx vs. Δy when scattering from a deuterium target, the "spots" corresponding to quasi-elastically scattered neutrons and protons are identifiable and distinct. The individual 1D Δx and Δy distributions are essentially projections of the 2D distribution. Similarly for the Δx distribution, one can clearly determine the two different proton and neutron "peaks." Fig. 6.3 shows typical plots for both 1D and 2D delta variable distributions. Generally for

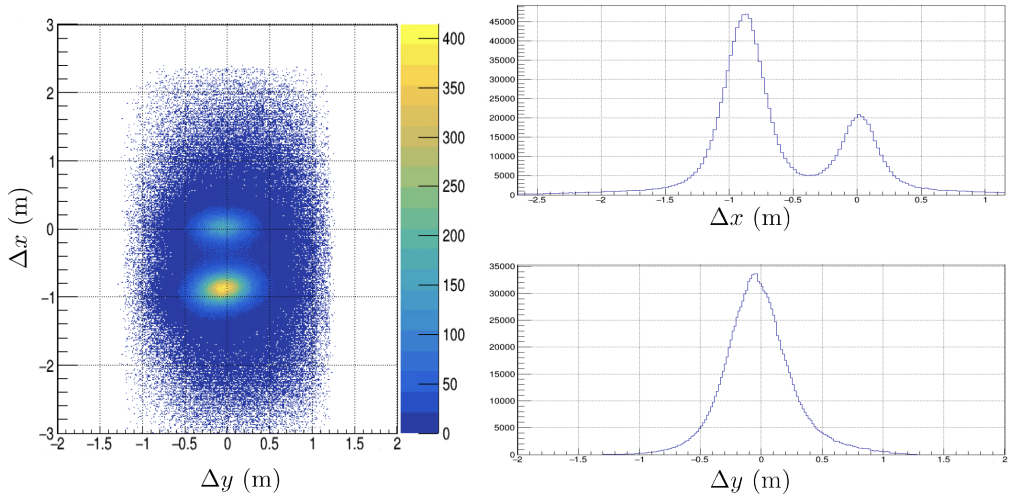

Figure 6.3: Example Δx and Δy distributions generated from all deuterium data from the SBS-8 kinematic 70% SBS magnetic field setting. Event selection cuts have been applied to the data to generate these distributions; descriptions of these cuts will be presented in Secs. 6.2 and 6.4.2. The "neutron spot" in the Δx and Δy distribution, or "neutron peak" in the Δx distribution, is centered at $(\Delta y, \Delta x) = (0\,\text{m}, 0\,\text{m})$. For this particular kinematic and SBS magnetic field setting, the "proton spot" manifests at a value approximately centered at $(\Delta y, \Delta x) = (0\,\text{m}, -0.9\,\text{m})$.

Δx vs. Δy distributions one spot, or peak in the 1D Δx plot, will emerge at approximately $(\Delta y, \Delta x) = (0\,\text{m}, 0\,\text{m})$, respectively $\Delta x = 0\,\text{m}$ for the Δx plot, for events where the observed position on HCal is very close to the expected positions under the neutron hypothesis and thus corresponds to quasi-elastically scattered neutrons. The second spot in Δx vs. Δy (for the 1D Δx plot it is a peak) is centered around a non-zero value in the $-\hat{x}_{\text{HCal}}$ direction (towards the physical top of the HCal face). This second spot, or peak, corresponds to quasi-elastically scattered protons whose observed positions see a position offset due to a trajectory deflection introduced by the SBS magnet. As described in Sec. 6.1.4.2, the determination of $x^{\text{exp}}_{\text{HCal}}$ only considers straight-line projections and does not account for the deflection of charged particles. However, for the case of proton trajectories, $x^{\text{obs}}_{\text{HCal}}$ will be shifted by the position offset due to the SBS magnet and this position offset manifests as a shifted to the left ($-\hat{x}_{\text{HCal}}$ direction) in the Δx distributions. This position offset in the Δx distributions, due to the SBS magnet, allows for the clear

separation of quasi-elastically scattered neutrons and protons. In Fig. 6.3, the proton spot is approximately at $(\Delta y, \Delta x) = (0\,\text{m}, -0.9\,\text{m})$.

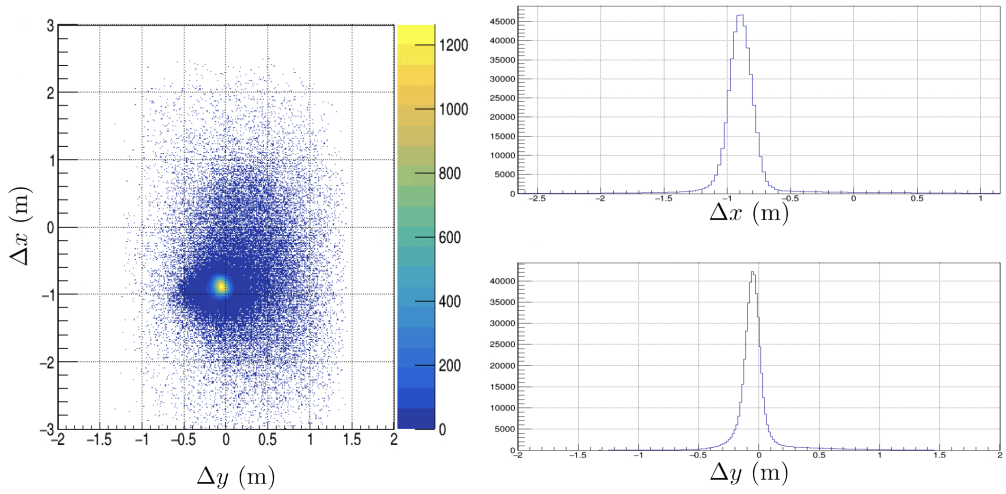

Figure 6.4: Example Δx and Δy Distributions generated from all hydrogen data from the SBS-8 kinematic 70% SBS magnetic field setting. Event selection cuts have been applied to the data to generate these distributions; descriptions of these cuts will be presented in Secs. 6.2 and 6.4.2. Only the proton spot, or proton peak, is present in the delta variable distributions. For this particular kinematic and SBS magnetic field setting, the proton spot is at a value approximately centered at $(\Delta y, \Delta x) = (0\,\text{m}, -0.9\,\text{m})$.

For this data analysis and extraction, the most important type of plot of the delta variable distributions is the 1D Δx plot. The 1D Δx distributions are used to extract neutron to proton reduced cross-section ratios, which is determined from relative scaling of the proton and neutron peaks within the Δx distribution. More details on the methodology for extracting information from Δx distributions will be the focus of Sec. 6.4.1.

So far in the discussion of the delta variable distributions the focus has primarily been on the 2D Δx vs. Δy and 1D Δx distributions. The Δy distribution is unable to distinguish between the two types of quasi-elastically scattered nucleons. However, Δy is useful as an event selection criteria for isolating quasi-elastically scattered nucleons, without bias towards protons or neutrons. Events which are located in the peak of the Δy distribution are more likely to correspond to quasi-elastically scattered nucleons, whereas events located in the tails of the distribution come from some source of background process.

Similarly, delta variable distributions can be constructed for data which was taken by scattering from hydrogen. Evaluating delta variables for hydrogen data is useful for multiple detector calibrations and studies. A typical set of delta variable plots is shown in Fig. 6.4. If one compares the two sets of distributions from hydrogen data (Fig. 6.4) and deuterium data (Fig. 6.3) the distributions from hydrogen data are significantly narrower. The distributions from deuterium data are significantly broader when compared to equivalent distributions from hydrogen data due to nuclear effects within the deuteron, which includes the Fermi motion of the proton and neutron.

A useful analysis tool, for specific aspects of detector and systematic studies, is the selection of 2D regions in Δx vs. Δy corresponding to a particular quasi-elastically scattered nucleon, and as such are called proton (neutron) spot cuts. The spot cuts improve the selection of a quasi-elastic proton or neutron, by removing events with a detection location in HCal that differs greatly from the expected quasi-elastic kinematics. The nucleon spot cuts are centered around the respective proton or neutron distribution and are informed by the mean values of Δx and Δy. These nucleon spot cuts are formed from elliptical regions in Δx vs. Δy, where the major and minor axes of the ellipse are regulated by a number of sigma, defined by the widths of the Δx and Δy distributions.

6.2 Event Selection

The fully processed data files include all reconstructed events in which a scattered particle (predominantly an electron) triggered the BigBite Spectrometer. Extracting the physics observables for the G_M^n and nTPE experiments is dependent on isolating quasi-elastic electron-nucleon scattering events coming from deuterium. The events corresponding to quasi-elastic electron-nucleon scattering are considered the "signal" for this analysis. A significantly large proportion of the reconstructed events present in data files will be from other processes that are not quasi-elastic electron-nucleon scattering and as such are considered "background" processes. The goal of event selection in this physics analysis is

simultaneously to reject events corresponding to background processes and keep events associated with signal. The main sources contributing to background events include inelastic scattering, scattering from the target end-windows, and two-arm spectrometer accidentals. Events associated with inelastic scattering contribute the most to background processes for this analysis. These inelastic scattering processes may include pion production mechanisms (pion electroproduction or resonant pion production), photoproduction, and deep inelastic scattering. Another type of event which should be rejected are events appearing similar to quasi-elastic nucleons, but are poorly defined events due to either detector resolution or multiple scattering effects. The remainder of this section will be to describe parameters used for the good electron and the exclusive quasi-elastic event selection.

6.2.1 Good Electron Event Selection

Prior to applying any selection criteria corresponding exclusively for quasi-elastic nucleons, we can implement cuts for identifying candidate scattered electrons. These so called "good electron cuts" include track quality, vertex z position, optics validity, and particle identification (PID) cuts. Each of these individual event selection criteria will be described in some detail in this section. By leveraging all of these cuts one can limit the data set to events which likely correspond to scattered electrons. This is typically the first major step in the event selection procedure as there are significant design considerations from the BigBite Spectrometer which motivate rejections of certain events, even before considerations of hadron arm information.

6.2.1.1 Track Quality Cuts

The accuracy of the momentum reconstruction for tracks from the GEM detectors is dependent on the quality of determined tracks. To ensure the quality of tracks from the GEM detectors, two parameters can be manipulated; they are the number of GEM layers with hits (N_{GEMhits}) and the track χ^2 per number of degrees of freedom (χ^2/ndf).

Number of GEM Layers with Hits

As described in Chapter 5, five GEM layers were instrumented in the BigBite Spectrometer during the G_M^n and nTPE experiments. As part of the track-finding algorithm (Appendix A.2), the algorithm requires a minimum of three 2D GEM hits on a given reconstructed track. Due to the high background rate environment in which the GEMs were operated, the probability of tracks generated with some false hits was significant. Additionally from the high background rate environment, it's possible for completely spurious "tracks" (false tracks) to be formed from random combinations of false hits. Typically, tracks with more 2D GEM hits correspond to an event which is a more reliable good electron candidate. Enforcing a cut on the number of GEM layers with hits for a given track helps to eliminate events corresponding to tracks with false hits in the data analysis. For all of the analysis presented in this dissertation a cut requiring that the number of GEM layers with hits is greater than or equal to 3.

Track χ^2/ndf

A separate step in the track-finding algorithm is the determination of tracks by generating three dimensional straight line fits through the combination of GEM layer 2D hits. Associated with each one of these straight line fits is a χ^2 per number of degrees of freedom (track χ^2/ndf). The track χ^2/ndf reflects the quality of the track reconstruction. Improvements to some GEM detector calibrations could have an impact on the overall value of the track χ^2/ndf. For the analysis presented in this dissertation a track χ^2/ndf of less than or equal to 15 is implemented. A typical track χ^2/ndf distribution, with the cut location, is shown in Fig. 6.5.

6.2.1.2 Vertex z Position (v_z)

The length of the deuterium and hydrogen targets used during the G_M^n and nTPE experiments was 15 cm. The reconstructed vertex z position, as determined by the electron track,

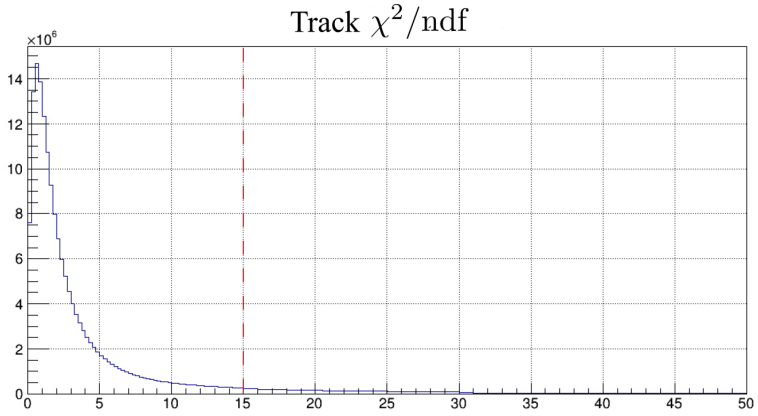

Figure 6.5: A typical track χ^2/ndf distribution, without any selection cuts applied. The histogram corresponds to all deuterium data of the SBS-8 kinematic setting at the SBS magnetic field setting of 70%. The dashed red line indicates the location of the cut applied χ^2/ndf parameter. All events less than or equal to the cut value are accepted.

provides access to the point of interaction for a given scattering event. A more in-depth description of the scattered electron angle and vertex position reconstruction procedure used during the G_M^n and nTPE experiments is documented in Ref. [134]. From this vertex z position reconstruction, the finite resolution was determined to be approximately 6 mm. Therefore, any scattering events that are originating from outside of the target length and beyond the resolution of the vertex reconstruction must be removed from the final physics data set. As part of the physical instrumentation of the cryogenic targets, there are aluminum entrance- and end-windows located at vertex z positions at $\pm$ 0.075 m (where -0.075 m corresponds to the upstream entrance window). As consequence of the finite resolution effects of the vertex reconstruction, some scattering events from the entrance- and end-windows are expected to contaminate the final physics data set. For the analysis presented in this dissertation a vertex z position region of $|v_z| \leq 0.07$ m is selected.

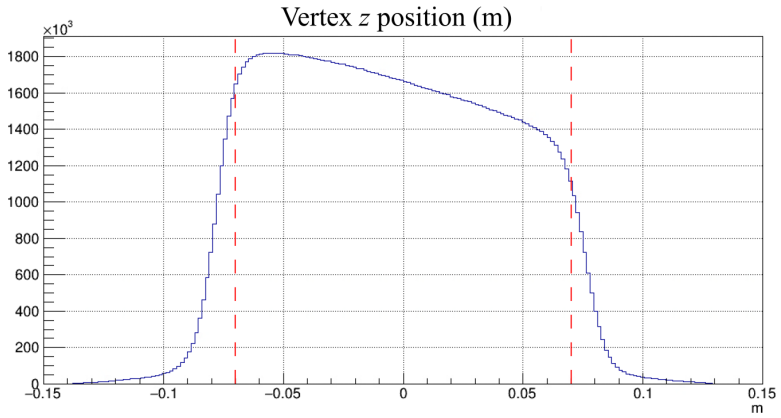

Figure 6.6: An example of the reconstructed vertex z position, without any selection cuts applied. The histogram corresponds to all deuterium data of the SBS-8 kinematic setting at the SBS magnetic field setting of 70%. The dashed red lines indicate the boundaries of the cut region for the vertex z position parameter.

6.2.1.3 Optics Validity Cuts

The reconstructed track coordinates projected to the mid-plane of the BigBite magnet (x_{BB},y_{BB}) can be calculated as

$$x_{BB} = x_{fp} - 0.9\theta_{fp}, \tag{6.31}$$

$$y_{BB} = y_{fp} - 0.9\phi_{fp}, \tag{6.32}$$

where (x_{fp}, y_{fp}, θ_{fp}, ϕ_{fp}) are the focal plane coordinates of the track, and -0.9 m is the z-position of the BigBite magnet mid-plane relative to the focal plane coordinate system. The cut variables (x_{BB}, y_{BB}) are the so called optics validity parameters. Enforcing cuts on optics validity parameters ensures that the reconstructed track in the BigBite Spectrometer passed through the magnet mid-plane and, dependent on the cut selection, the track passed through a uniform field region of the BigBite magnet.

Fig. 6.7 shows the a typical correlation between the optics validity parameters and W^2; also included in Fig. 6.7 are regions of uniform field in both the dispersive (x_{BB}) and transverse (y_{BB}) directions. Plots included in Fig. 6.7 are used to guide the choice of cut

ranges for the optics validity parameters. The acceptance of the BigBite magnet varies between kinematics, so the optimized cut ranges for the optics validity parameters must be determined for each kinematic configuration.

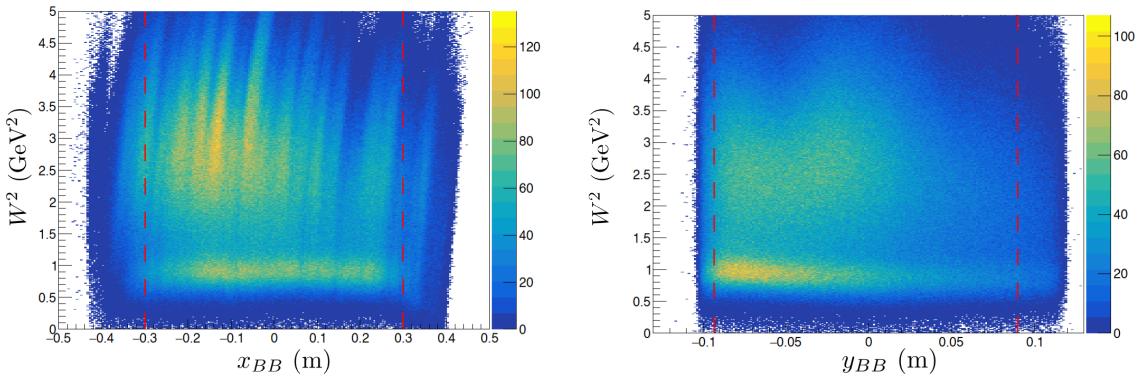

Figure 6.7: Example distributions of W^2 as correlated to optics validity parameters x_{BB} and y_{BB}, respectively, with all other event selection cuts applied. The histograms correspond to all deuterium data of the SBS-8 kinematic setting at the SBS magnetic field setting of 70%. The dashed red lines indicate the regions where the boundaries are between uniform and non-uniform BigBite magnetic field.

6.2.1.4 PID Cuts

The detectors in the BigBite Spectrometer provide parameters useful for particle ID (PID) of detected scattering events. One is the energy deposited in the Preshower calorimeter. A second is the ratio of the energy deposited in the Shower calorimeter over the magnitude of the reconstructed track momentum. For completeness, the GRINCH detector is also capable of providing PID information, but was not sufficiently calibrated to be used in this analysis. A more detailed motivation for implementing each of these selection criteria is described in this section.

Preshower Energy (E_{PS}) Cut

As described in Sec. 4.2.3, the primary function of the Preshower Calorimeter is to identify hadrons (predominantly pions) and can be used to reject pions in the BigBite Spectrometer.

Due to the design and shorter length of the PS calorimeter blocks, pions will behave as minimum ionizing particles and high-energy scattered electrons will create electromagnetic showers. Pions will not travel enough distance, within a given PS block, to deposit a sufficient amount of energy. For high-energy scattered electrons, the length of a PS block is ideal for it to deposit a sufficient amount of energy. However, the high-energy scattered electrons will only deposit a fraction of their energy in the PS blocks via electromagnetic showers. Fig. 6.8 presents an example of the Preshower cluster energy; it is evident that there are two types of distributions. A narrower peak centered around 0.1 GeV corresponds to mainly pions and is a background which must be removed. There is also a wider distribution which constitutes the majority of Fig. 6.8, which corresponds to scattered electrons. Requiring a Preshower cluster energy greater than 0.2 GeV suppresses the majority of the pion background detected by the BigBite Spectrometer.

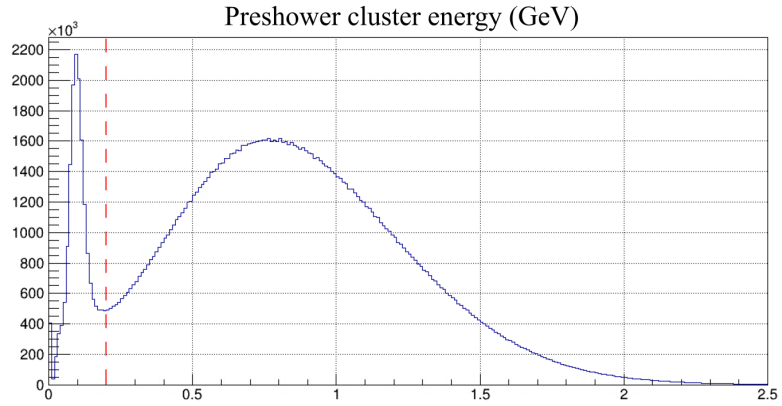

Figure 6.8: An example of the Preshower energy cluster energy distribution, without any selection cuts applied. All deuterium data of the SBS-8 kinematic setting at the SBS magnetic field setting of 70% are presented in the histogram. The dashed red line indicates the boundary of the cut region at 0.2 GeV.

E_{BBCal}/p Cut

At the GeV energy scale the rest mass of the electron is negligible, and therefore it is expected that the scattered electron energy, as measured by BBCal, and the magnitude

of the reconstructed track momentum should be equal. Or, rather, that E_{BBCal}/p should form a distribution with a peak at approximately one. Applying a cut on E_{BBCal}/p allows further rejection of pions and fake track candidates. Fig. 6.9 presents an example of E_{BBCal}/p without any event selection cuts applied. This cut is dependent on adequate calibrations of BigBite magnet optics and momentum and of BBCal energy calibrations.

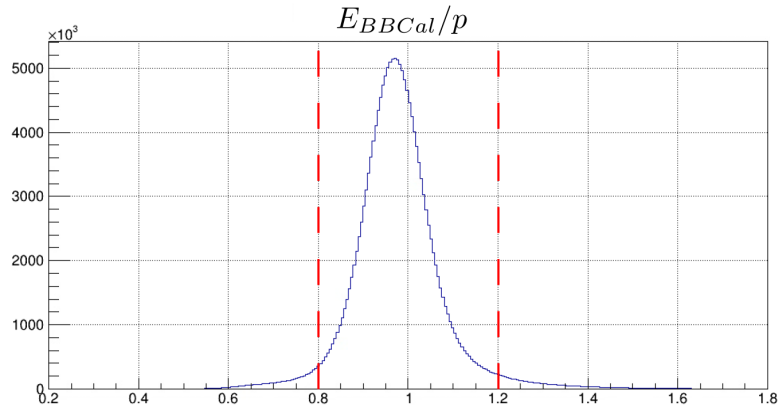

Figure 6.9: An example of the E_{BBCal}/p distribution, without any selection cuts applied. All deuterium data of the SBS-8 kinematic setting at the SBS magnetic field setting of 70% are presented. The dashed red line indicates the boundary of the cut region.

6.2.2 HCal Cluster Energy Selection

Applying event selection criteria on HCal cluster energy is compartmentalized into two tasks. The first occurs during early stages of physics analysis, after the event reconstruction framework of SBS-Replay and SBS-offline and is a re-implementation of the HCal cluster selection algorithm. The second component is selecting events based by defining an acceptable region in the HCal cluster energy cut parameter. This section will describe both stages of event selection for HCal cluster energy.

HCal Cluster Selection Algorithm

The cluster formation algorithm for HCal as implemented in SBS-Offline will be summarized based on Refs. [140] and [160]. For each event, all blocks which are above an energy

threshold are added to a list and sorted in descending order by block energy. Considering the first (highest-energy) block on the list, cluster formation begins by attempting to associate other neighboring blocks, over the energy threshold, with the primary block. The criteria for adding blocks to an HCal cluster is an iterative process which evaluates the potential additional block based on two parameters. A limit is placed on the physical distance between the potential additional block and the nearest block already in the cluster. A selection on the ADC time difference between the potential additional block and the nearest block already in the cluster is also enforced. If both criteria are met the potential block is added to the current cluster and removed from the original block list. This process repeats until no further blocks can be added to the current cluster consideration, and a new cluster is formed based on the highest-energy block still available on the block list. For a given cluster the total energy deposited by the hadron is interpreted as the sum of all block energies in the cluster. The cluster position is determined via an energy-weighted centroid algorithm.

If one uses the clusters formed from this algorithm according to SBS-offline, the default primary cluster is the cluster that had the highest-energy primary block. The primary cluster is the cluster that is most likely to correspond to an elastically or quasi-elastically scattered nucleon detected in HCal. However, it has been found [140] that the cluster selection algorithm based on the highest-energy primary block leads to a non-negligible amount of quasi-elastic yields lost. An alternative cluster selection algorithm, known as the "in-time algorithm" and developed by the authors of Refs [140] and [160] was implemented, after event reconstruction, for all of the analysis presented in this dissertation and improves on the default primary cluster of SBS-Offline. The in-time algorithm loops over all available clusters for a given event and proceeds in two steps. The first step applies a wide cut on the ADC coincidence time difference between the highest-energy block in the HCal cluster and the SH calorimeter. The second step proceeds by selecting the HCal cluster with the highest-energy block sum, from those clusters that pass this cut. This cluster is identified as the new primary cluster and is saved for use in further physics analysis. It should be

noted that the majority of events determined by the in-time cluster algorithm will also be selected by the default primary clustering algorithm of SBS-Offline. Furthermore the in-time cluster algorithm is considered better motivated than the default SBS-Offline cluster formation because the total cluster energy is more physically meaningful than the highest-energy block and it is expected that the scattered electron and nucleon should have a very tight time-of-flight correlation.

HCal Cluster Energy Cut

A cut on the HCal cluster energy, E_{HCal}, rejects events with very low HCal cluster energy. Events with very low HCal cluster energy tend to be associated with background processes, mainly inelastic scattering. Fig. 6.10 depicts a typical HCal cluster energy distribution, with all other event selection cuts applied; it is clear that there are low-energy events present which most likely do not correspond to quasi-elastically scattered nucleons. However, the HCal is known to have poor energy resolution (from detector studies conducted during the G_M^n and nTPE experiments [140]) which makes assignment of HCal cluster energy cuts nontrivial. Systematic cut stability study is necessary to make decisions about HCal cluster energy selection criteria and will be described in Sec. 6.4.2.

6.2.3 Electron-Nucleon Coincidence Time Cut

For an electron and nucleon involved in the same scattering event one would expect the scattered particles to reach their respective detectors at a correlated time. By constructing and applying event selection criteria on a coincidence time parameter one can reduce background events which are associated with accidental hits in detectors.

One can construct a coincidence time parameter from timing information available from the BigBite Spectrometer and the HCal. Ideally, timing information pertaining to scattered electrons should be available from TDC information provided by the BigBite Timing Hodoscope. However, for the data sets used in this analysis the Timing Hodoscope detector calibrations were not fully-developed (see Ref. [134] for more details) and therefore

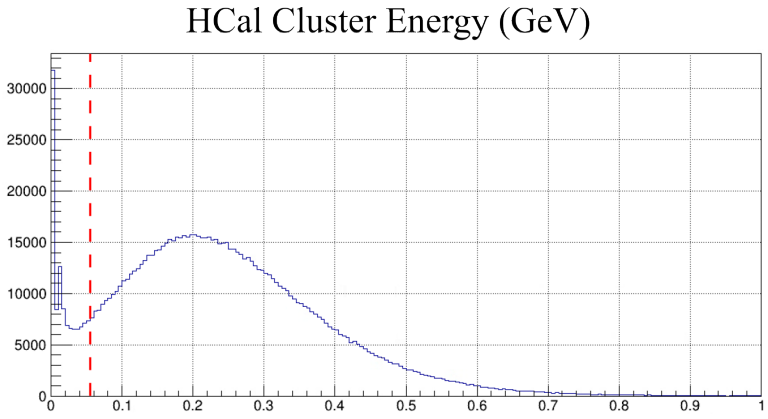

Figure 6.10: An example of the HCal cluster energy distribution; all other event selection cuts are applied. This plot is generated using all deuterium data from the SBS-8 kinematic and the 70% SBS magnetic field setting. The dashed red line indicates the cut boundary for this particular kinematic setting; all events with lower cluster energy of this boundary are rejected.

using the Timing Hodoscope TDC information as part of the coincidence time was not possible. Instead, sufficient timing calibrations were performed for the BigBite Calorimeter ADCs, and this produces reasonable timing information for detected scattered electrons. For HCal and the case of scattered nucleons, measurements made by TDCs are expected to inherently have a better timing resolution and therefore would be a first choice as a source of timing information. However, for significant portions of the G_M^n and nTPE data collection period HCal TDC, signals are missing for corresponding events with good ADC information [140]. For the data set used in this analysis, sufficient calibrations were performed for HCal ADC time, and timing information for the scattered nucleons is used from the HCal ADC time. Therefore, the coincidence time parameter, Δt, presented in this dissertation is constructed from the HCal ADC time subtracted by the BBCal SH ADC time. Fig. 6.11 shows the HCal - SH ADC coincidence time with two different stages of selection criteria applied. Fig. 6.11a shows an ADC coincidence time with no selection cuts applied, though an in-time HCal cluster energy requirment is present. Figure 6.11b presents an ADC coincidence time with all other selection cuts applied. Due to all the apparatus and calibration complications associated with the coincidence time, a systematic

study of the cut stability is necessary to properly assign cut boundaries; this topic will be described in Sec. 6.4.2.

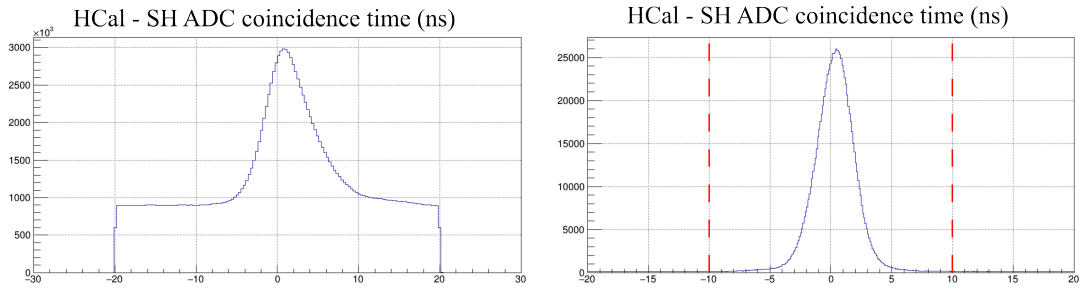

(a) (b)

Figure 6.11: Typical distributions of the HCal - SH ADC coincidence time. The plots are generated using all deuterium data from the SBS-8 kinematic and the 70% SBS magnetic field setting. Left: This plot has no event selection cuts applied to the data. However, the data are processed with an in-time HCal cluster energy algorithm, described in Sec. 6.2.2. Right: This plot shows the ADC coincidence time, where all other event selection cuts have been applied. The dashed red line indicates the cut boundary for this particular kinematic setting. Events which are further from the mean of the distribution and outside the boundary are rejected.

6.2.4 Invariant Mass Squared (W^2) Cut

The invariant mass squared, denoted W^2, of the virtual photon-nucleon system is an important kinematic parameter which functions to definitively isolate events associated with quasi-elastic electron-nucleon scattering. The invariant mass squared under the conditions of quasi-elastic electron-nucleon kinematics was described in Sec. 6.1.4.1. For the cases of quasi-elastic D(e,e'n) and D(e,e'p) scattering, the peak of the W^2 distribution should be centered around a value of $\approx$0.88 GeV^2. For these kinematic conditions the central value of the W^2 distribution corresponds to the square of the rest mass value for either the proton or neutron, and can be represented by $W^2 = M_N^2$ where $M_N = M_p$ for scattering from hydrogen and $M_N = \frac{M_p + M_n}{2}$ for scattering from deuterium.

Fig. 6.12 demonstrates the strength and importance of the W^2 selection criteria. Specifically, Fig. 6.12a shows the W^2 distribution where no event selection criteria has

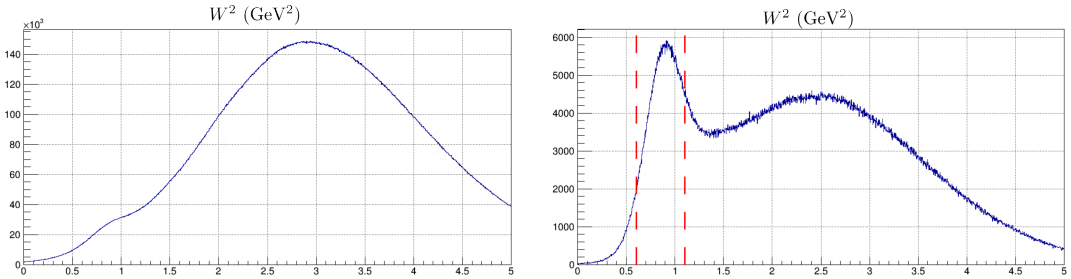

(a) (b)

Figure 6.12: Example W^2 distributions generated from all deuterium data for the SBS-8 kinematic and the 70% SBS magnetic field setting. Left: This plot shows W^2 with no event selection criteria applied. The quasi-elastic nucleon peak is difficult to distinguish. Right: The plot shows W^2 with all other event selection cuts applied. One can clearly identify the quasi-elastic nucleon peak. However, events corresponding to other background processes are still present at higher values of the W^2 distribution. The dashed red line indicates the cut boundary for this particular kinematic setting. Events which are further from the quasi-elastic nucleon peak and outside the boundary are rejected.

been applied. The quasi-elastic nucleon peak is almost entirely indistinguishable and the entire W^2 distribution is dominated by inelastic scattering processes, which correspond to background events for this analysis. This effect where the W^2 distribution, without any event selection criteria, is predominantly events from inelastic scattering processes becomes even more present with higher values of Q^2. Fig. 6.12b shows the W^2 distribution where all other event selection cuts have been applied. Under these conditions the quasi-elastic nucleon peak is distinct and identifiable in the distribution. However, events corresponding to inelastic scattering processes are still clearly present and need to be effectively minimized or rejected if possible. Also one would expect that even with a defined W^2 cut region, some fraction of that region is going to include tails of the distribution corresponding to inelastic scattering processes, based on the respective shapes of the two distributions. For the determination of the W^2 cut region, ideally, the central value would be 0.88 GeV^2, and the boundaries of the region would be optimized such that the inelastic contamination is maximally rejected and the quasi-elastic events are maximally accepted. The determination of the W^2 cut region will be determined based off of careful cut systematic studies and will be described in Sec. 6.4.2.

6.2.5 Δy Cut

The Δy parameter was introduced in Sec. 6.1.4.3 and it provides access to information in the non-dispersive direction of the scattered nucleon momentum. Since the Δx distribution is used to extract ratios of neutron to proton reduced cross-sections, we cannot inherently apply selection criteria to the 1D Δx or 2D Δx and Δy distributions. However, since we do not extract physics observables from Δy, cut selections are permitted. Implementing a cut on the Δy parameter is used to select events that correspond to a quasi-elastically scattered nucleon, while rejecting events that likely are either associated with a background scattering process or where there is a significant discrepancy between the observed and expected non-dispersive positions. Fig. 6.13 shows a typical cut region for the Δy parameter. To reduce the impact Δy has on the overall physics result and to properly address the cut regions systematic cut studies are performed and will be described in Sec. 6.4.2. Moreover, the Δy parameter is known to be correlated to other event selection parameters and this further necessitates cut stability and systematic studies.

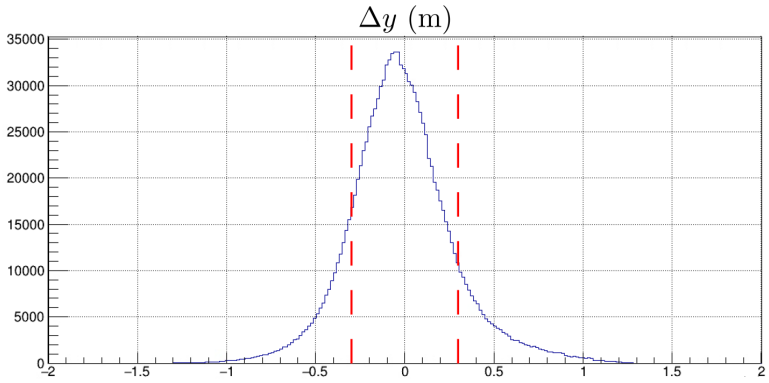

Figure 6.13: A typical Δy distribution generated from all deuterium data for the SBS-8 kinematic and the 70% SBS magnetic field setting. The dashed red line indicates the cut boundary. Events which are further from the central value and outside the boundary are rejected.

6.2.6 Fiducial Cut

For extractions of cross-section ratios from D(e,e'n) and D(e,e'p) scattering, it is important to control or minimize effects due to relative acceptance losses and efficiency differences. These effects can lead to systematic effects on physics observables, mainly R, if not properly considered. A fiducial region can be applied to the trajectories of scattered nucleons, as predicted by the electron kinematics described in Sec. 6.1.4.2, thereby matching the acceptances of the two scattered nucleons and limiting the phase space of the scattered electron. Conceptually, the fiducial region should be defined such that for a particular set of electron kinematics (expected nucleon positions) for each neutron (proton) detected in the HCal active area a corresponding proton (neutron) would need to be able to be detected in the HCal active area. This definition of the fiducial region needs to account for the dispersive deflection applied to protons by the SBS magnet. Any Fermi-smearing affects from the quasi-elastic scattering present in the observed HCal positions also should be considered. Introducing "safety margins" into the fiducial region typically mitigates effects introduced by Fermi-smearing.

The HCal active area is defined to be the full physical detector area, with the exclusion of the column and row of blocks at the outermost edge of the HCal. To determine the average deflection of the protons and the safety margins for both the dispersive and non-dispersive directions empirical methods were used. One should consider Δx and Δy 1D distributions in which all other event selection criteria have been applied; this produces distributions similar distributions to those presented in Fig. 6.3. If one fits Gaussian distributions to the individual proton and neutron peaks of the Δx distribution, the respective mean values and standard deviations can be extracted. The difference between the mean value of the proton peak and the neutron peak is considered the average proton deflection introduced by the SBS magnet, for the particular kinematic settings. The standard deviations of the proton and neutron peaks will be used to quantify the safety margins in the dispersive direction of the fiducial cut. By fitting a Gaussian to the Δy distribution

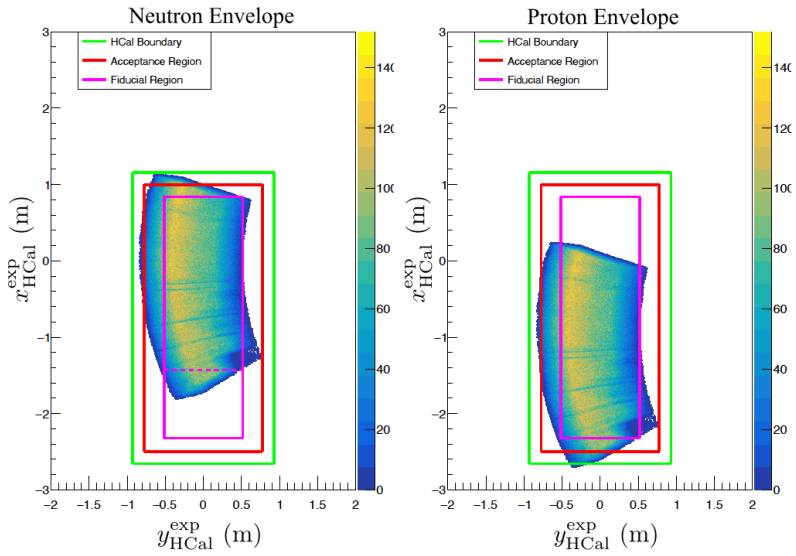

Figure 6.14: Typical 2D correlations of x^{exp}_{HCal} and y^{exp}_{HCal} from all deuterium data for the SBS-8 kinematic and the 70% SBS magnetic field setting. These plots have good electron and W^2 cuts applied to the distributions to cleanly visualize the respective nucleon envelopes. No fiducial cut is present. See the text for descriptions of the three different boundaries. Left: The plot corresponds to the expected positions envelope for neutrons. Right: The plot includes the average deflection as determined by empirical methods, and shows the expected position envelope for protons, including this deflection.

one can use the standard deviation to quantify the safety margin in the non-dispersive direction of the fiducial cut. In both Figs. 6.14 and 6.15 the physical boundary of HCal is identified by a green rectangle, the HCal active area is identified by a red, and the fiducial region is formed by the solid magenta rectangle.

As described in Secs. 6.1.4.1 and 6.1.4.2, the expected nucleon positions x^{exp}_{HCal} and y^{exp}_{HCal} can be determined and one can consider 2D correlations between these two parameters. These 2D correlations form an "envelope" of the expected nucleon positions at HCal, and these distributions can have a fiducial region criteria applied to them. As a consequence of the deflection of the SBS magnet, the proton and neutron expected position envelopes will be different at HCal. Fig. 6.14 shows the neutron and proton envelopes with only good electron and W^2 cuts applied; a fiducial region is not enforced in these plots. Figure 6.15 visualizes the respective nucleon envelopes and enforces all event selection criteria,

particularly the fiducial cut is enforced. By comparing Figs. 6.14 and 6.15, one can directly see the effect of the fiducial cut on the neutron and proton envelopes. It is important to note that the fiducial region sufficiently accounts for the HCal active area, the average proton deflection, and the safety margins to select events within a region of HCal that matches the acceptances of the quasi-elastic nucleons. Even after all these considerations, the ratio of neutron to proton cross-section is sensitive to the choice of boundary for the fiducial region, and as such the expected nucleon positions will undergo cut stability analysis which will be described further in Sec. 6.4.2.

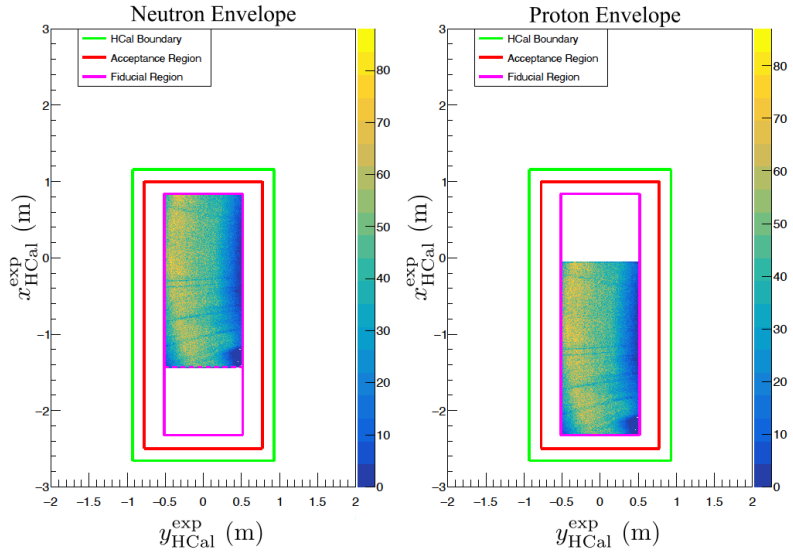

Figure 6.15: Typical 2D correlations of $x^{\mathrm{exp}}_{\mathrm{HCal}}$ and $y^{\mathrm{exp}}_{\mathrm{HCal}}$ from all deuterium data for the SBS-8 kinematic and the 70% SBS magnetic field setting. These plots include all event selection criteria to visualize the respective nucleon envelopes within the fiducial region. See the text for descriptions of the three different boundaries. Left: The plot corresponds to the expected positions envelope for neutrons. Right: The plot includes the average deflection as determined by empirical methods, and shows the expected position envelope for protons, including this deflection.

6.3 HCal Nucleon Detection Efficiency

The extraction of the ratio of neutron to proton quasi-elastic cross-sections, R, is dependent on the ratio of neutron to proton detection efficiencies. Neutron and proton detection efficiencies are studied from the behavior of the HCal detector, HCal is described in Sec. 4.2.4. HCal was designed with the ability to detect protons and neutrons to high-valued and similar efficiencies. However, the HCal detection efficiency is anticipated to slightly differ between the two scattered nucleons, due to how protons and neutrons interact with matter as they traverse the HCal module structure. Though it is expected that the scattered nucleons will have similar efficiencies in HCal, it is important to experimentally verify these nucleon detection efficiencies. Sources of systematic uncertainties on R, associated with HCal nucleon detection efficiency (NDE), can arise through two phenomena. The first is if there are any deviations between absolute neutron and proton detection efficiencies in HCal, i.e. if the neutron to proton detection efficiency ratio significantly deviates from unity. The second effect, which is a source of systematic uncertainty, involves any non-uniform regions of the HCal active area which could lead to position-dependent efficiency variation in HCal. This section will describe methods for studying the HCal nucleon detection efficiency for both MC and experimental data.

6.3.1 Nucleon Detection Efficiency from Monte Carlo

The HCal nucleon detection efficiency is extracted from the MC simulation (using the G4SBS package) by examining the energy deposition in HCal as a function of nucleon momentum. The MC events produced for this study were simulated from generators which separately generate proton and neutron events. These individual particle generators are capable of simulating events with user-configurable energy and angular parameters. These user-configurable parameters are chosen so the entire HCal active area is uniformly populated for the relevant nucleon momentum range of the G_M^n and nTPE experiments (1-9 GeV/c). The MC events for this study will be thrown with the SBS magnet field off,

flat in position and nucleon momentum to span the acceptances of both nucleon types. The number of MC events generated for each nucleon type should meet the condition that each channel in HCal is populated with a minimum of 1000 events. These simulated events were digitized and reconstructed through the respective software packages to account for known detector effects.

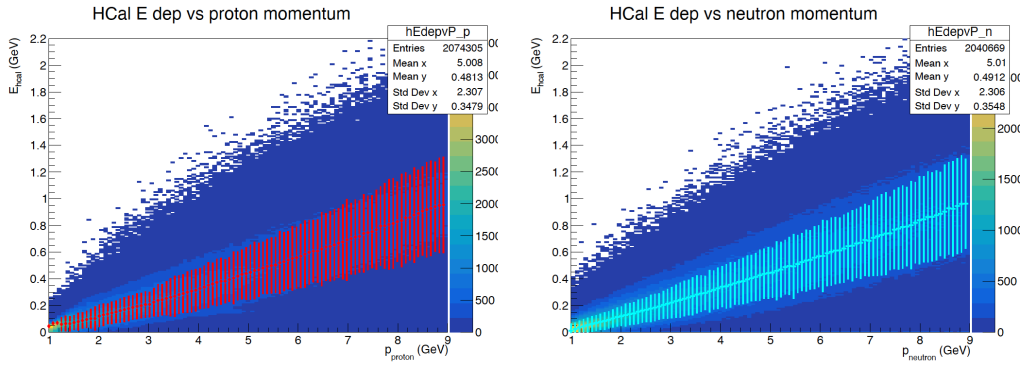

Figure 6.16: Simulated HCal Energy Deposition versus nucleon momentum. Left: The energy spectrum for proton simulated events. The Gaussian fit mean and standard deviation is overlayed in red. Right: The energy spectrum for neutron simulated events. The Gaussian fit mean and standard deviation is overlayed in cyan.

For each of the two sets of nucleon simulated events, a spectrum of energy deposited in HCal with respect to nucleon momentum will be created. Figure 6.16 depicts the energy deposition as function of nucleon momentum for both proton and neutron simulated events. The procedure for extracting nucleon detection efficiency from a given energy spectrum in Fig. 6.16 is as follows

1. Segment the entire momentum range of the energy spectrum into many narrow momentum bins. The number of momentum bins can be visualized from the total number of red (or cyan) points in Fig. 6.16.

2. For every momentum bin, fit a Gaussian to the energy distribution and extract the mean, $\overline{E}$, and the standard deviation.

3. For every momentum bin, form an energy distribution of events passing an energy threshold of $E_{Th} = \overline{E}/4$. The integral of this energy distribution, corresponding to

the number of events passing E_{Th}, will form the efficiency numerator and be denoted N_{pass}.

4. For every momentum bin, form an energy distribution without any threshold criteria. The integral of this energy distribution will correspond to the total number of events and be denoted N_{Total}.

5. Over the entire momentum range, for each bin, calculate the MC nucleon detection efficiency as

$$\xi^{p(n)}_{\text{MC,HCal}} = \frac{N^{p(n)}_{\text{pass}}}{N^{p(n)}_{\text{Total}}}. \tag{6.33}$$

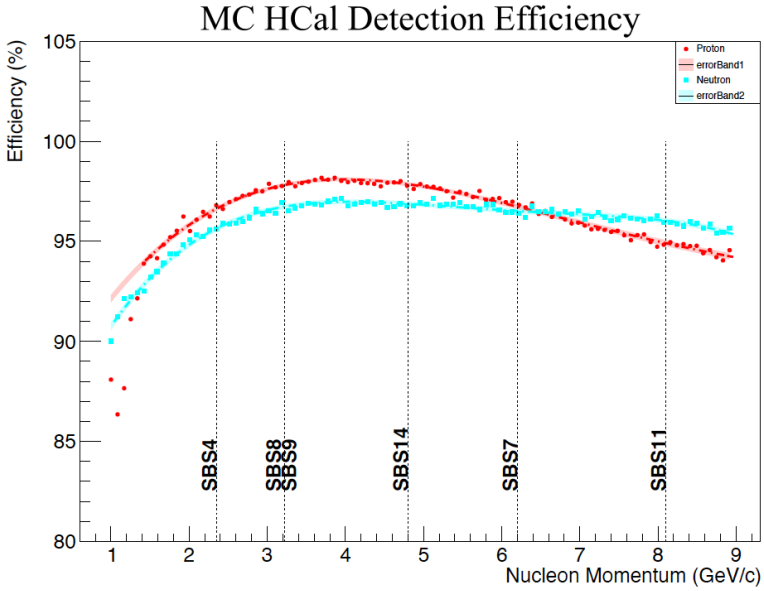

Figure 6.17: HCal detection efficiency as a function nucleon momentum from MC simulation. The proton detection efficiency is plotted as red points, while the neutron detection efficiency is plotted as cyan points. The respective nucleon detection efficiencies are fit with a polynomial of the same color.

The resulting proton and neutron detection efficiencies as functions of nucleon momentum are presented in Fig. 6.17. Each set of nucleon detection efficiency points are fit with a

fourth-order polynomial, and the error band is determined from a binomial expression as

$$\sigma^{p(n)}_{\mathrm{MC,HCal}} = \sqrt{\frac{\xi^{p(n)}_{\mathrm{MC,HCal}}(1-\xi^{p(n)}_{\mathrm{MC,HCal}})}{N^{p(n)}_{\mathrm{Total}}}}. \tag{6.34}$$

The values for the respective MC proton and neutron HCal detection efficiencies for each particular kinematic setting are presented in Tab. 6.1. The HCal nucleon detection efficiencies from MC simulation exhibit behavior of high- and similar- efficiency values, which is consistent with HCal design expectations.

Kinematic	MC HCal Efficiency	
	Proton	Neutron
SBS-4	96.6%	95.6%
SBS-8 & SBS-9	97.8%	96.7%
SBS-14	97.9%	96.9%
SBS-7	96.7%	96.5%
SBS-11	94.9%	96.0%

Table 6.1: The values of the respective proton and neutron detection efficiencies in HCal from MC simulation, for each kinematic of the G^n_M and nTPE experiments.

6.3.2 Proton Detection Efficiency

The description of HCal NDE, thus far, has relied on idealized models and conditions of HCal to obtain nucleon detection efficiencies from MC simulation. Since the NDE is anticipated to be a dominant systematic effect for both the G^n_M and nTPE experiments, it is crucial that methods are developed for evaluating NDE from experimental data. This section will focus on studies addressing proton detection efficiency, as significant data were collected by scattering from liquid hydrogen, which allows us to directly distinguish elastically scattered protons. Evaluating neutron detection efficiency in the context of this experimental data analysis is more complicated and will be separately addressed in Sec. 6.3.5.

One method for evaluating the relative proton detection efficiency (relative-rate) from experimental data was developed by members of the G^n_M and nTPE analysis working

group and employs a position-dependent "cut-based" methodology (see Refs. [134, 140] and a presentation by A. Puckett from Ref. [177]). This position-dependent "cut-based" methodology for evaluating proton relative-rate has been adapted for the analysis presented in this dissertation and has been used for study of proton relative-rate beyond the original development. As such this methodology will be directly summarized with some detail. This position-dependent "cut-based" methodology for evaluating proton relative-rate can also be applied to MC simulated events which are generated under identical conditions as the experimental data. A basic assumption of this position-dependent "cut-based" methodology is that within the region defined by the fiducial cuts the data should be distributed uniformly over the HCal face.

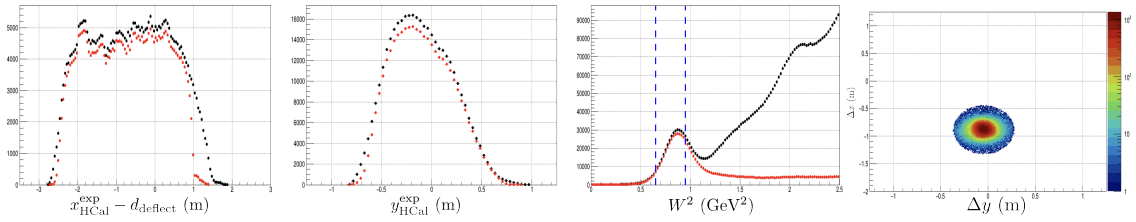

(a) Data

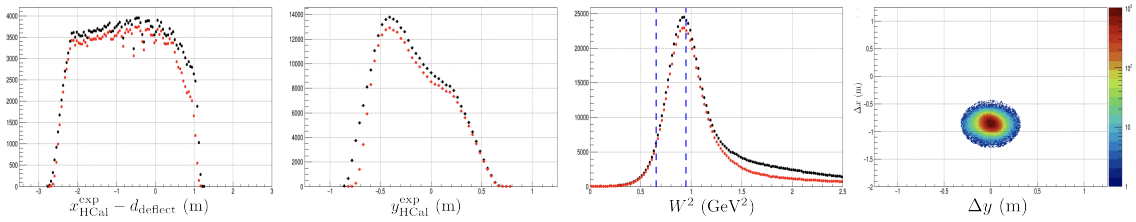

(b) MC

Figure 6.18: Plots relevant to the proton relative-rate analysis procedure described in this section. The plots are produced, respectively, from both experimental data and SIMC MC simulation corresponding to the SBS-8 ($Q^2 = 4.5$ (GeV/c)^2) kinematic and SBS magnet 70% field setting. Plots presented with black points correspond to the denominator distributions for the proton relative efficiency ratio. Similarly, plots presented with red points correspond to the numerator distributions for the proton relative efficiency ratio. See the text for details on applied cut selections which distinguish between the numerator and denominator conditions. The W^2 distributions are overlayed with dashed blue lines indicating the strict cut region. The right-most column presents 2D Δx vs. Δy distributions, which visualize the proton spot cuts implemented as part of the numerator condition.

In this approach for evaluating proton relative-rate, elastic H(e,e'p) events are selected,

respectively, from either experimental data collected from the LH_2 target or from simulated events produced using the SIMC MC elastic proton generator. Two quantities central to the procedure of this proton detection efficiency study are the proton expected positions at HCal in the dispersive- and transverse-directions, denoted $\left(x^{\text{exp}}_{\text{HCal}}\right)_p$ and $y^{\text{exp}}_{\text{HCal}}$, respectively. The proton expected position in the dispersive-direction accounts, on an event-by-event basis, for the deflection introduced by the SBS magnet and is defined as

$$\left(x^{\text{exp}}_{\text{HCal}}\right)_p = x^{\text{exp}}_{\text{HCal}} - d_{\text{deflect}}, \tag{6.35}$$

where $x^{\text{exp}}_{\text{HCal}}$ is the expected position at HCal under the neutron hypothesis, defined by Eq. 6.25, and d_{deflect} is defined by Eq. 6.28. The proton expected position in the transverse-direction, $y^{\text{exp}}_{\text{HCal}}$, is determined by the same calculation as under the neutron hypothesis, by Eq. 6.26, since charged particle effects are only present in the dispersive-direction. Procedurally, the proton relative-rate analysis method is presented in the following steps:

1. Consider experimental data collected by scattering from the LH_2 target, for a given kinematic and SBS magnet field setting. Or, equivalently with sufficient statistics, consider MC simulated events produced using the SIMC elastic proton generator, under identical kinematic conditions. Throughout every stage of this analysis study, events from data and MC will be evaluated under consistent and identical conditions. Particularly, cut selection regions will be identically applied to events corresponding to data or MC. For the analysis presented in this dissertation the kinematics studied were SBS-4, SBS-8, and SBS-9 for both experimental data and MC simulated events.

2. Construct two versions of each proton expected position distribution. For a given proton expected position distribution, the two versions will be produced from two different sets of selection criteria. The two different sets of selection criteria represent the separate numerator and denominator conditions. The numerator is formed by the number of events detected by HCal. While the denominator is the total number

of events expected to hit HCal. The selection criteria for forming the denominator and numerator distributions will be described in the following steps.

3. For the corresponding $\left(x^{\text{exp}}_{\text{HCal}}\right)_p$, or $y^{\text{exp}}_{\text{HCal}}$, distribution, the denominator condition enforces a good electron selection criteria, described in Sec. 6.2, with cut regions that are identical or more strict than presented in Tab. 6.3, a strict W^2 cut of $[0.65, 0.95]$ GeV^2, and a fiducial cut in the corresponding $y^{\text{exp}}_{\text{HCal}}$, or $\left(x^{\text{exp}}_{\text{HCal}}\right)_p$, direction identical to values presented in Tab. 6.3. The $\left(x^{\text{exp}}_{\text{HCal}}\right)_p$ and $y^{\text{exp}}_{\text{HCal}}$ distributions forming the denominator conditions are shown, respectively, in Fig. 6.18 with the black points. On a position-dependent basis, the denominator condition represents the total number of events expected to hit HCal.

4. For the corresponding $\left(x^{\text{exp}}_{\text{HCal}}\right)_p$, or $y^{\text{exp}}_{\text{HCal}}$, distribution, the numerator condition enforces all of the selection criteria of the denominator condition, and in addition requires that the event has a cluster in HCal, $E_{\text{HCal}} > 0$, and the event passes a wide five-sigma elliptical proton spot cut. The $\left(x^{\text{exp}}_{\text{HCal}}\right)_p$ and $y^{\text{exp}}_{\text{HCal}}$ distributions forming the numerator conditions are shown, respectively, in Fig. 6.18 with the red points. On a position-dependent basis, the numerator condition represents the number of events detected by HCal.

5. The bin-by-bin position-dependent proton relative-rate is formed from the ratio of bin values corresponding to numerator condition divided by denominator condition, for a given $\left(x^{\text{exp}}_{\text{HCal}}\right)_p$ or $y^{\text{exp}}_{\text{HCal}}$ distribution.

6. For each $\left(x^{\text{exp}}_{\text{HCal}}\right)_p$ and $y^{\text{exp}}_{\text{HCal}}$ distribution, a weighted average of the proton relative-rate is determined by fitting a constant value to the distribution. Example resultant plots showing proton relative-rate with the fitted weighted averages are presented in Fig. 6.19. The acceptance-averaged proton detection efficiency is then the average-value, from both directions, of the proton relative-rate.

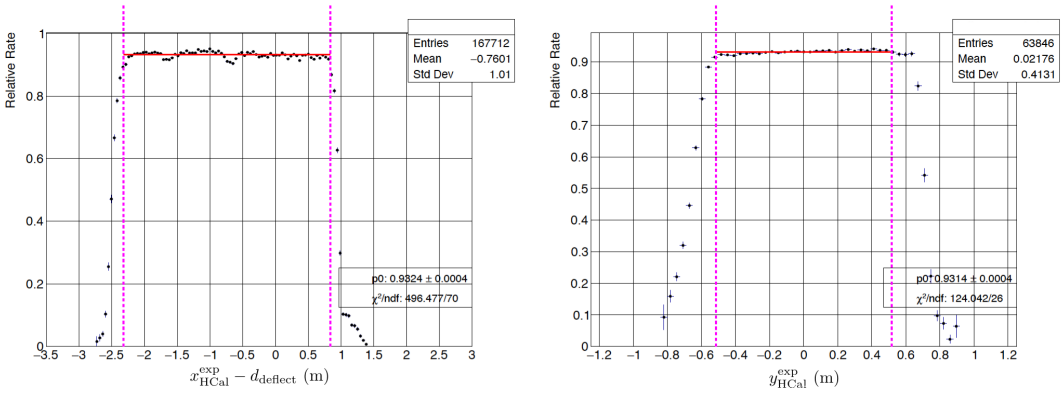

(a) Data

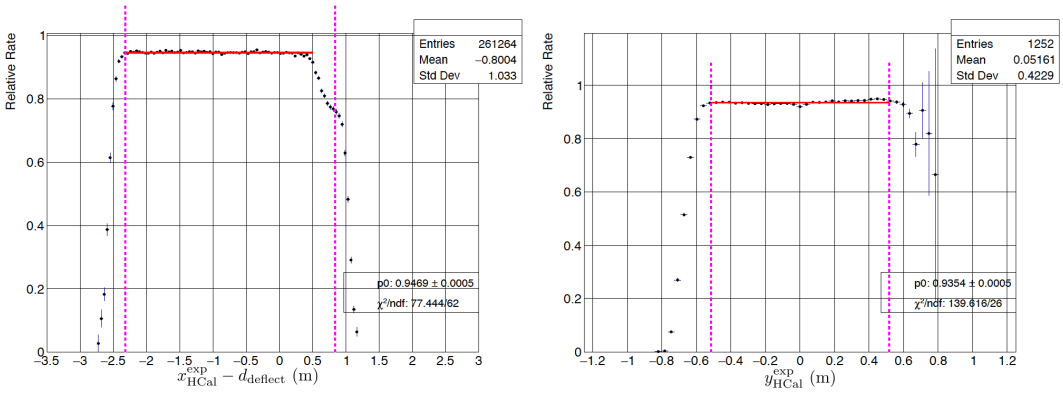

(b) MC

Figure 6.19: HCal proton relative-rate profiles for both experimental data and MC simulation for the SBS-8 ($Q^2 = 4.5$ (GeV/c)^2) kinematic and SBS magnet 70% field setting. The left column shows plots for expected proton position in the dispersive-direction. The right column shows plots for the transverse-direction expected proton position. The experimental data plot of proton relative-rate in $\left(x^{\rm exp}_{\rm HCal}\right)_p$ demonstrates regions of non-uniformity centered around -0.6 m and -1.7 m, respectively. The equivalent MC plot demonstrates a uniform proton relative-rate. The dashed magenta lines represent the boundary of the fiducial regions.

We will now describe features, and implications of results for this position-dependent "cut-based" method for evaluating relative proton detection efficiency. A strict W^2 cut region will be applied to minimize inelastic contamination. For lower-Q^2 kinematics: SBS-4, SBS-8, and SBS-9, it is a reasonable approximation to neglect a background subtraction component for this procedure, as events corresponding to inelastic contamination are not statistically significant. However, this assumption about the W^2 cut region and the inelas-

tic contamination becomes less valid for higher-Q^2 kinematics and therefore this method for estimating proton detection efficiency becomes less reliable for those kinematics.

The result of this analysis procedure is a mapping of the values for position-dependent proton relative-rate for both data and MC simulated events, and an example is presented in Fig. 6.19. For the SBS-8 (Q^2 = 4.5 (GeV/c)^2) kinematic and SBS magnet 70% field setting, the acceptance-averaged proton detection efficiency values between data and MC agree within 1.45%. This suggests that the MC simulation realistically and consistently reproduces the experimental data, but is not an exact reproduction. The profile of the proton relative-rate between the data and the MC is almost identical in the transverse-direction. For the experimental data, the dispersive-direction exhibits position-dependent non-uniform behaviors (dips) at approximate values of $\left(x^{\rm exp}_{\rm HCal}\right)_p = -0.6$ m and -1.7 m. Non-uniformities, towards the middle of the HCal active area, in proton relative-rate suggests there could be a larger-impact on HCal nucleon detection efficiency which is position-dependent. It is important to investigate the non-uniformities in HCal detection efficiency to determine if neutron to proton relative-rate profiles, in these regions, are similar or dissimilar. Overall position-dependent non-uniformities in HCal nucleon detection efficiency could introduce bias in the measurement of the experimental observable R. Therefore, addressing the non-uniformity and assessing any systematic effects is crucial. The detection efficiency non-uniformity will be described in the next section.

6.3.3 Detection Efficiency Non-Uniformity

By applying this position-dependent proton relative-rate "cut based" method to the various SBS magnet field settings for the SBS-4, SBS-8, and SBS-9 kinematics, see Ref. [177], it is evident there are non-uniform regions. Particularly, the SBS-8 kinematic has the broadest HCal acceptance coverage and clearly demonstrates non-uniform behaviors (dips) at approximate values of $\left(x^{\rm exp}_{\rm HCal}\right)_p = -0.6$ m and -1.7 m. Observed consistent proton relative-rate profiles for different SBS magnet field settings from the same kinematic setting strongly indicate these non-uniformities do not arise from electron-arm acceptance issues.

Rather, from studies of the HCal channel ADC spectra, it is known (from Ref. [140]) that some channels exhibit abnormal ADC distributions; examples are displayed in Fig. B.8. The position-dependent non-uniformities in proton relative-rate are highly-likely caused by HCal hardware issues.

6.3.3.1 Possible Approaches for Addressing Non-Uniformity

The source of the non-uniformity appears to be related to the HCal hardware. Manipulating HCal hardware to diagnose and resolve the non-uniformity was deemed not possible due to schedule constraints for completing the experiments in the SBS program. The SBS G_M^n and nTPE analysis working group has considered several approaches for addressing the HCal detection efficiency non-uniformity at the software level [177]. These possible approaches are to

- Improve HCal calibrations in software to minimize the non-uniformity effects in experimental data. This is the ideal solution, which directly targets the issue. However, such HCal calibrations were not ready at the time of this analysis.

- Model the efficiency loss mechanism in MC. This method would seek to reproduce non-uniformity effects by reducing the gains of affected HCal channels at the digitization level in the software. One challenge for this method is accurately mapping the problematic channels and their respective gain variations. Initial attempts of this method suggest susceptibility to over-correction or under-correction of detection efficiency, which makes realistic reproduction of non-uniformity difficult.

- Apply position-dependent efficiency corrections to MC events, before comparing to real data events. This method, comparatively, is the most straightforward to implement, benchmark, and compare with processed MC events. This method has been adopted for the analysis in this dissertation and will be described in more detail.

6.3.3.2 Formalism for Position-Dependent Efficiency Correction to MC Events

The goal of this method is to accurately reproduce the position-dependent HCal detection efficiency non-uniformities for MC simulated events, as observed in experimental data. Two key assumptions when implementing this method are that the detection efficiency variation depends only position and that protons and neutrons can be treated equally.

Procedurally, when processing MC event files for physics analysis, the detection efficiency non-uniformity can be artificially introduced by applying a multiplicative relative correction factor to the weights of the MC events. The relative efficiency correction factor, $c(x, y)$, [177] for a given position at HCal can be defined as

$$c(x, y) = \frac{\epsilon^{\text{data}}_{\text{HCal}}(x, y)}{\left\langle \epsilon^{\text{data}}_{\text{HCal}} \right\rangle}, \tag{6.36}$$

where $\epsilon^{\text{data}}_{\text{HCal}}(x, y)$ is the interpolated position-dependent HCal detection efficiency value, and $\left\langle \epsilon^{\text{data}}_{\text{HCal}} \right\rangle$ is the acceptance-averaged value; both as determined from "cut-based" analysis procedure described in Sec. 6.3.2. The position (x, y) for the correction factor should be based on the expected nucleon positions, and should be determined from MC truth information for relevant electron-arm parameters. Additionally from MC truth information, the position deflection introduced by the SBS magnet is accounted for in the position calculation based on the type of nucleon. Expected nucleon positions are determined from MC truth information to accurately account for nuclear and radiative effects, and to remove detector resolution effects. Conceptually the function of $c(x, y)$ is for a given MC nucleon event that hits a position at HCal where the experimental data efficiency is known to be reduced (enhanced) relative to the acceptance-averaged efficiency the relative efficiency correction factor adjusts the weight of the MC event to reduce (enhance) the detection probability.

A requirement when implementing this method for addressing HCal non-uniformity is a detailed efficiency map covering the entire HCal acceptance, as determined from experimental data. The SBS-8 kinematic data set is a viable candidate for generating such an

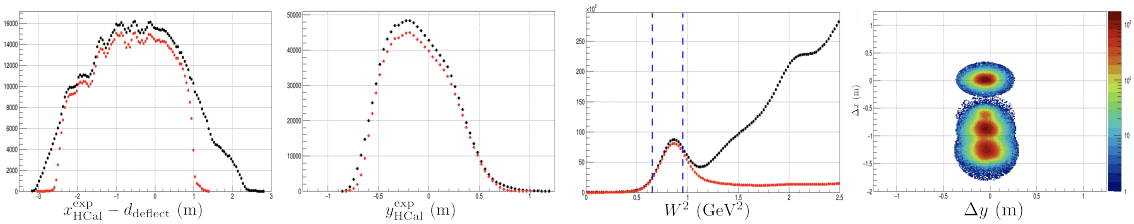

Figure 6.20: Plots relevant to the proton relative-rate analysis combining all SBS magnet settings (0%, 50%, 70%, and 100% settings) for the SBS-8 kinematic ($Q^2 = 4.5$ (GeV/c)^2) experimental data. The details and information pertaining to the present plots are identical to descriptions presented in Sec. 6.3.2 and Fig. 6.18.

efficiency map as the kinematic has multiple SBS magnet settings (0%, 50%, 70%, and 100% settings) which allows statistically significant estimations of the proton relative detection efficiency across the entire HCal acceptance. By consistently subjecting each data set, corresponding to a given SBS magnet setting, from the SBS-8 kinematic ($Q^2 = 4.5$ (GeV/c)^2) to the proton relative detection efficiency analysis procedure described in Sec. 6.3.2, a combined reference efficiency map can be determined for the entire SBS-8 kinematic. The relevant analysis procedure plots for combining the different SBS magnet data sets from the SBS-8 kinematic are presented in Fig. 6.20. Figure 6.21 shows the 1D and 2D proton relative-rate profiles for the combined analysis of the SBS magnet data sets for the SBS-8 kinematic. The 2D proton relative-rate profile will be treated as the reference efficiency map for the entire analysis presented in this dissertation. For a given position and event, the numerator of Eq. 6.36 will be determined from the 2D profile in Figure 6.21, whereas the denominator of Eq. 6.36 will be taken as the weighted-average of the fitted constant values determined from both 1D direction profiles presented in Fig. 6.21.

The relative efficiency correction factor, $c(x, y)$, was applied to all relevant MC simulated events presented in the physics analysis of this dissertation. Prior to this implementation, a study comparing and evaluating the proton expected positions after applying the correction factor to the relevant kinematics was conducted. Figure 6.22 shows the proton relative-rate profiles, after relative efficiency correction factor was applied, for the MC simulated events subjected to a similar combined analysis of the different SBS magnet

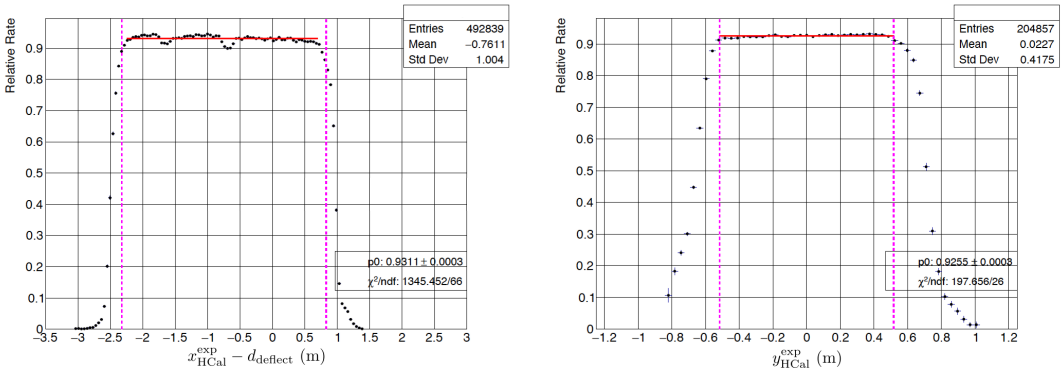

(a)

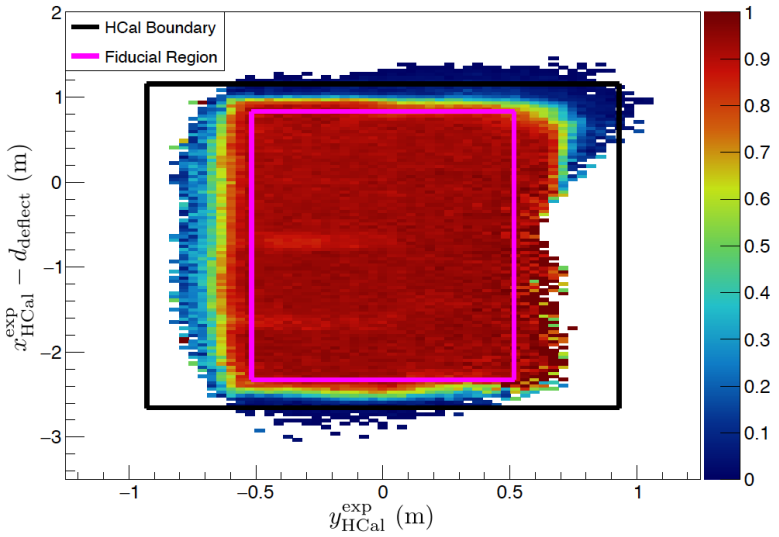

(b)

Figure 6.21: One-dimensional and two-dimensional dispersive and transverse proton expected position-dependent proton relative efficiency profiles are presented from the combined SBS magnet (0%, 50%, 70%, and 100% settings) experimental data sets for the SBS-8 kinematic ($Q^2 = 4.5$ (GeV/c)^2). The dashed magenta lines represent the boundary of the fiducial regions. For the dispersive-direction, in both the 1D and 2D plots, the non-uniformities are clearly present at values of $\left(x^{\rm exp}_{\rm HCal}\right)_p = -0.6$ m and -1.7 m. The SBS-8 combined 2D proton detection efficiency profile will be used at the detailed reference map for the MC relative efficiency correction factor.

settings for the SBS-8 kinematic. From Fig. 6.22 it is evident that this method realistically reproduced both the shape and locations of the non-uniformities in HCal detection efficiency. The material presented in the this section and Sec. 6.3.2 focuses on the study of

the SBS-8 kinematics; similar investigations were conducted on both the SBS-4 and SBS-9 kinematics. Information pertaining to the entire HCal proton detection efficiency and the non-uniformity is available in Ref. [177].

6.3.3.3 Non-Uniformity Systematic Effects

As previously noted, the extraction of the ratio of neutron to proton quasi-elastic cross-sections, R, is dependent on the ratio of neutron to proton detection efficiencies. The non-uniform regions described in earlier parts of this section could introduce bias to the ratio R and as such efforts were made to quantify potential systematic effects. To quantify the systematic effects we consider data/MC comparisons extracting the experimental observable $R_{sf}^{n/p}$, as described in Sec. 6.4.1, under two different conditions. The first extraction of the experimental observable is conducted with MC simulated events which do not correct for HCal detection efficiencies and therefore have proton expected position profiles consistent with Fig. 6.19b. The second extraction of $R_{sf}^{n/p}$ is conducted with MC simulated events where the MC simulated events are re-weighted with the relative efficiency correction factor from Eq. 6.36, as described in Sec. 6.3.3.2. By performing data/MC comparisons and extracting experimental observables under these two conditions, we directly study the systematic effect attributed to the non-uniform regions in HCal nucleon detection efficiency. Figure 6.23 shows data/MC comparison distributions under both conditions, the plots used in quantifying systematic effects attributed to HCal detection efficiency non-uniformities. Similar plots are considered for the other relevant kinematic and SBS magnet field settings and are available from Ref. [177]. Table 6.2 presents the extracted $R_{sf}^{n/p}$ values for every relevant kinematic and SBS-magnet setting for both described conditions of the MC simulated events. The absolute-value of the difference between each set of values is taken as the systematic effect on $R_{sf}^{n/p}$ attributed to HCal detection efficiency non-uniformities. It should be noted that this treatment of the systematic effect on $R_{sf}^{n/p}$ is an upper bound (i.e. quite conservative).

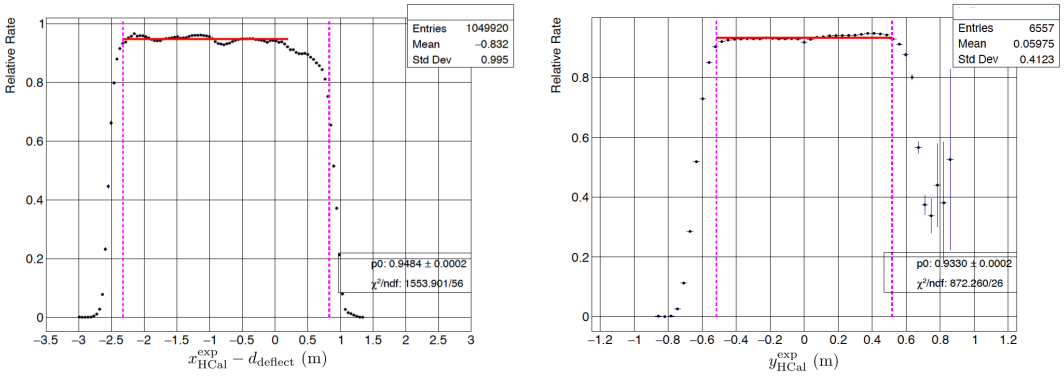

(a)

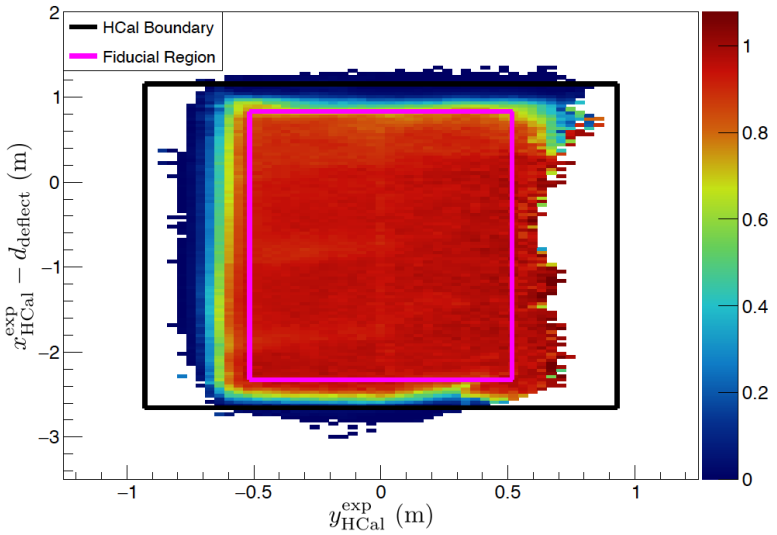

(b)

Figure 6.22: One-dimensional and two-dimensional dispersive and transverse proton expected position-dependent proton relative efficiency profiles are presented from the combined SBS magnet (0%, 50%, 70%, and 100% settings) MC simulated events for the SBS-8 kinematic (Q^2 = 4.5 (GeV/c)^2). The dashed magenta lines represent the boundary of the fiducial regions. From the dispersive-direction in both the 1D and 2D plots the non-uniformities are realistically reproduced at values $\left(x^{\rm exp}_{\rm HCal}\right)_p = -0.6$ m and -1.7 m. The relative efficiency drop in the region of $\left(x^{\rm exp}_{\rm HCal}\right)_p$ from approximately 0.2 m to 0.8 m is a known artifact from the MC simulation due to discrepancies in the geometry of the target scattering chamber.

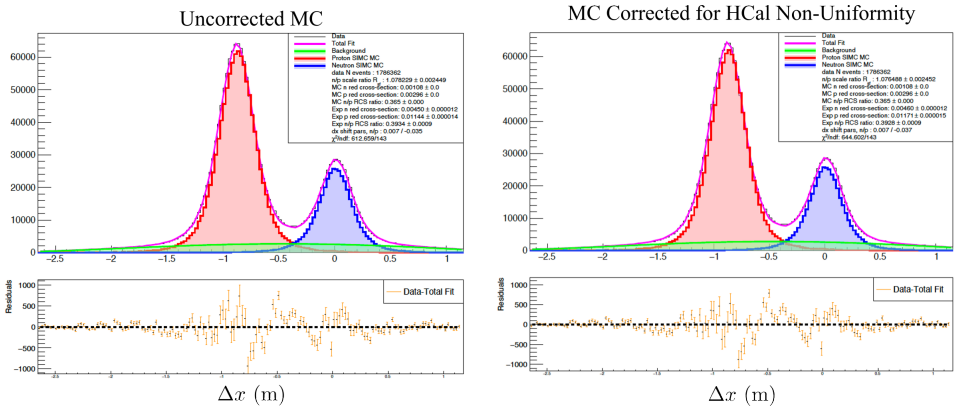

Figure 6.23: Example plots of Δx associated with the two conditions used for quantifying HCal detection efficiency non-uniformity systematic effect. Both plots are produced from the SBS-8 ($Q^2 = 4.5$ (GeV/c)^2) kinematic and SBS magnet 70% field setting. Left: A comparison including MC distributions which do not have any relative efficiency correction factor applied. Right: A comparison including MC distributions which are corrected on an event-by-event basis for any relative efficiency fluctuations.

Setting	$R_{sf}^{n/p}$ from Uncorrected MC	$R_{sf}^{n/p}$ from SBS-8 Map Corrected MC	Absolute Difference
SBS-8 50%	1.0842	1.0845	0.0003
SBS-8 70%	1.0782	1.0764	0.0018
SBS-8 100%	1.0678	1.0666	0.0012
SBS-9 70%	1.0876	1.0823	0.0053

Table 6.2: Extracted $R_{sf}^{n/p}$ values for both MC simulated events which remain uncorrected and MC simulated events which have been re-weighted according to the formalism for position-dependent efficiency correction (Sec. 6.3.3.2). For a single kinematic and SBS magnet field setting the absolute difference between the two extracted $R_{sf}^{n/p}$ values is presented in a third column. The absolute value of the difference is taken as the systematic effect on $R_{sf}^{n/p}$.

6.3.4 HCal NDE Profile Comparisons

For any given kinematic setting associated with the G_M^n and nTPE experiments, it is important to understand if there are variations in the HCal neutron and proton detection efficiencies. More importantly, for the extracted neutron Rosenbluth slope of the nTPE experiment it is important to understand detection efficiency profiles between the SBS-8 and SBS-9 kinematics. This section will present detection efficiency profiles selecting

protons from LH_2, detection efficiency profiles separately selecting proton and neutron events, and comparisons of detection efficiency profiles between SBS-8 and SBS-9. For context, the proton relative-rate profiles presenting 1D and 2D distributions generated from similar analysis as described in Sec. 6.3.2 are shown in Fig. 6.24.

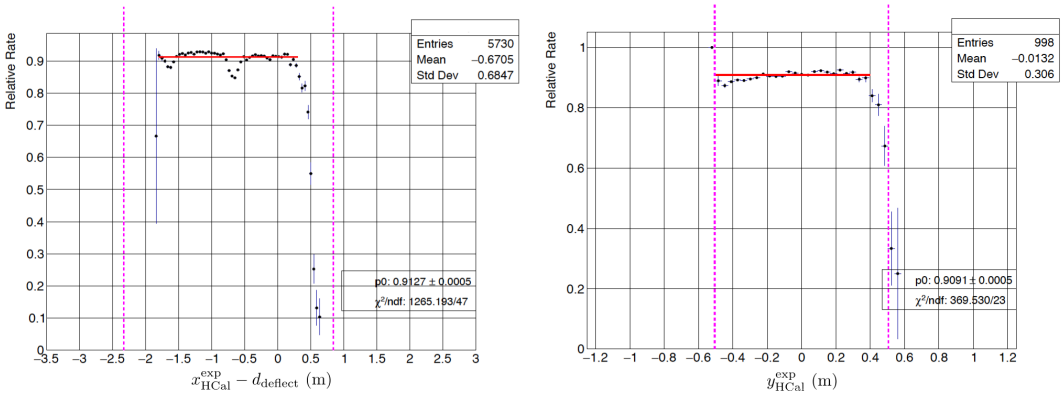

(a)

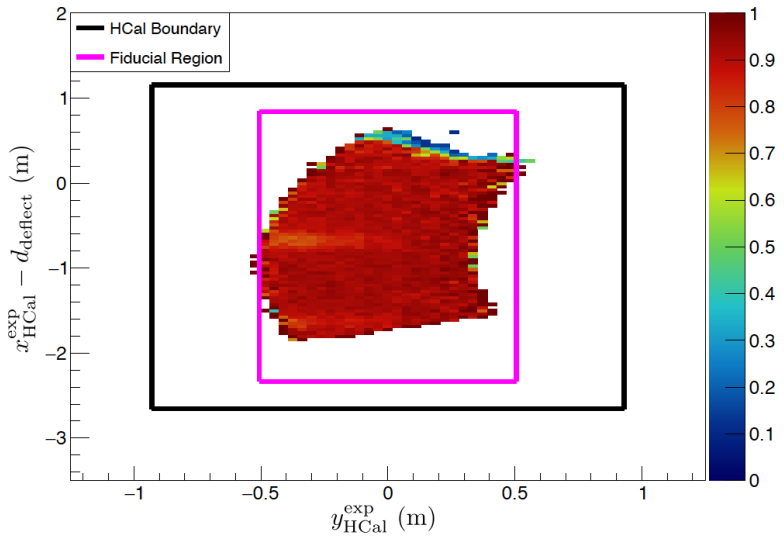

(b)

Figure 6.24: One-dimensional and two-dimensional dispersive and transverse proton expected position-dependent proton relative efficiency profiles are presented from the experimental data sets for the SBS-9 kinematic (Q^2 = 4.5 (GeV/c)^2) and 70% SBS magnet setting. The dashed magenta lines represent the boundary of the fiducial regions. From the dispersive-direction in both the 1D and 2D plots the detection inefficiencies are clearly present at values of $\left(x^{exp}_{HCal}\right)_p = -0.6$ m and -1.7 m.

An essential feature for easily comparing any two nucleon relative-rate profiles (relative detection efficiency) is a proper scaling of the two distributions for straightforward comparison. Suppose there are two relative-rate profiles (profile A and profile B). Procedurally, we will scale profile B to profile A with the following technique:

1. Consider a bin range in the relevant expected position quantity, either $\left(x_{\mathrm{HCal}}^{\mathrm{exp}}\right)_p$ for protons or $x_{\mathrm{HCal}}^{\mathrm{exp}}$ for neutrons, where data is not statistically limited for both compared distributions. Typically, for the dispersive-direction expected positions this is -1.5 m to 0.5 m. For the transverse-direction expected positions this is -0.4 m to 0.4 m. This range may slightly vary, dependent on the statistics and the kinematic and SBS-magnet setting considered.

2. For each relative-rate profile in the comparison analysis take the integral of the distribution in the defined bin range from the previous step.

3. Divide the integral of profile A by the integral of profile B. The resultant quantity is an estimated average scale factor to match the average value of profile B to the average value of profile A.

4. Apply the average scale factor defined in the previous step to profile B.

Throughout the comparison analysis presented in the remainder of this section, the profile A data points will be in black while the scaled profile B data points will be in red. For ease of clarity the scaled distribution will be denoted in the plots from the comparison analysis.

6.3.4.1 Proton Relative-Rate Comparisons from Hydrogen Data

As a first-order benchmark, to understand detection efficiencies between the SBS-8 and SBS-9 kinematics we can compare proton relative-rate profiles from LH_2, following the analysis procedure from Sec. 6.3.2, between the two relevant kinematics. Figure 6.25 displays the proton relative-rate profiles from experimental data sets for both the dispersive and transverse proton expected positions. The plots in the left column of Fig. 6.25, are

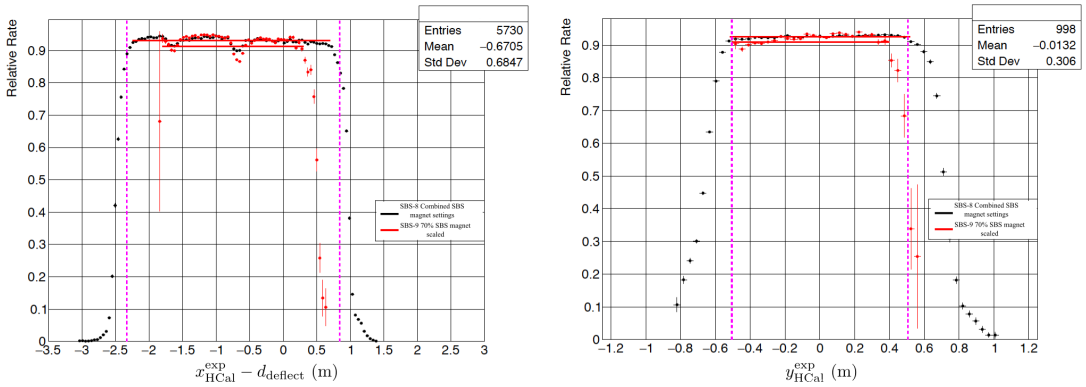

(a) Dispersive-Direction (b) Transverse-Direction

Figure 6.25: One-dimensional dispersive- and transverse-direction proton expected position relative efficiency profiles, from LH_2, are compared between the combined SBS magnet (0%, 50%, 70%, and 100% settings) data sets for the SBS-8 kinematic, and the SBS-9 kinematic and 70% SBS magnet setting ($Q^2 = 4.5$ (GeV/c)^2). The dashed magenta lines represent the boundary of the fiducial regions for relevant expected proton position direction. The plots shown have been scaled to match the average values of the two profiles as described in Sec. 6.3.4.

without any scaling, and we can see that the acceptance-averaged values for the SBS-8 and SBS-9 kinematic are very similar. From the plots in the right column of Fig. 6.25, which have scaled the SBS-9 relative-rate to the SBS-8 profile, we can clearly see that the detection efficiency non-uniformities are present in both the SBS-8 and SBS-9 proton relative-rate profiles. More importantly, the shapes of the profiles in the non-uniform regions are similar between the two kinematics. The plots presented in Fig. 6.25 are encouraging, as they suggest that the HCal proton relative efficiency does not drastically change between kinematics, particularly in the non-uniform regions. Similar analysis of proton relative detection efficiency were conducted for MC simulated events for both SBS-8 and SBS-9 [177].

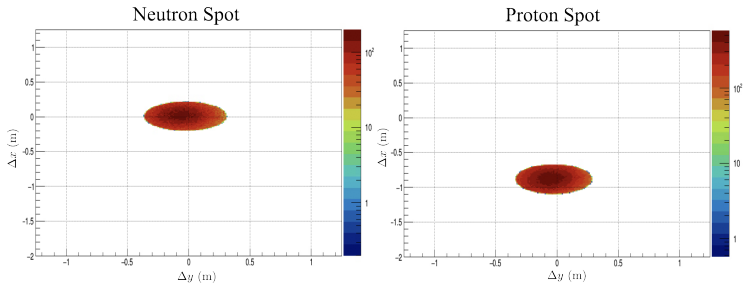

(a) SBS-8 ($Q^2 = 4.5$ (GeV/c)^2) kinematic and SBS magnet 70% field setting

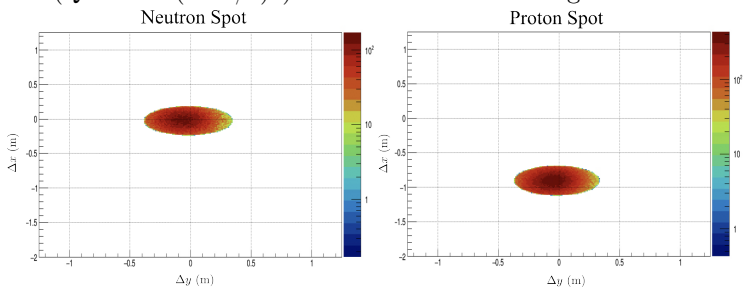

(b) SBS-9 ($Q^2 = 4.5$ (GeV/c)^2) kinematic and SBS magnet 70% field setting

Figure 6.26: Plots presenting the 2D Δx vs Δy distributions which visualize the neutron and proton spot cuts used to select individual nucleons from LD_2 data sets. For the SBS-8 kinematic and 70% SBS magnet field setting, 1.3 σ elliptical proton and neutron spots are used. For the SBS-9 kinematic and 70% SBS magnet field setting, a 1.3 σ elliptical proton spot and 1.35 σ elliptical neutron spot are used.

6.3.4.2 Proton and Neutron Selected Relative-Rate Comparisons from Deuterium Data

Qualitatively, we can extend the framework introduced in Sec. 6.3.2 to data sets taken with the LD_2 target to evaluate the nucleon relative-rate profiles for neutron and proton events which are separately selected with tight elliptical spot cuts. The description for implementing nucleon spot cuts is provided in Sec. 6.1.4.3. When determining a spot cut for this comparison analysis, for a particular nucleon type, it is important to ensure that the spot region is narrow enough to not overlap with events corresponding to the other nucleon type and to not include significant amounts of events corresponding to background. If events from either two conditions are included in this study, that clearly biases the attempt at isolating events for a particular nucleon type. The respective tight elliptical neutron and proton spot regions used for this comparison analysis are presented

in Fig. 6.26. Similar comparison analyses were conducted for the other SBS magnet field settings of the SBS-8 kinematic [177].

Figure 6.27 shows comparison plots between neutron and proton selected events from LD_2 for the SBS-8 kinematic ($Q^2 = 4.5$ (GeV/c)^2) and 70% SBS magnet setting. From the dispersive-direction plot, which has scaled the neutron relative-rate profile to the proton relative-rate profile, there is clear evidence that the shape of the relative-rate profiles is largely-consistent between neutrons and protons. Particularly, the non-uniform regions of the HCal detection efficiency show similar behaviors for both types of nucleons. This characterization of the different nucleon relative-rates is extremely encouraging as it suggests that the non-uniformities in HCal detection efficiency are similar for protons and neutrons.

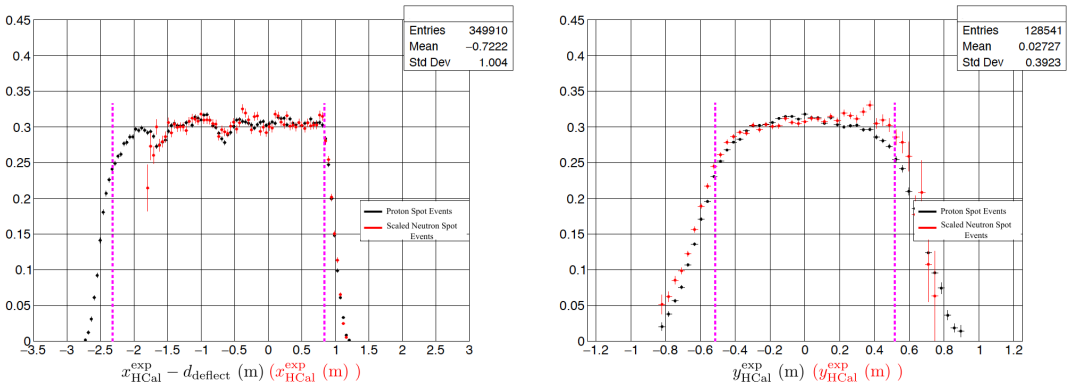

(a) (b)

Figure 6.27: One-dimensional dispersive- and transverse-direction expected position relative efficiency profiles are compared for proton and neutron selected events from LD_2 data sets for the SBS-8 kinematic ($Q^2 = 4.5$ (GeV/c)^2) and 70% SBS magnet setting. The dashed magenta lines represent the boundary of the fiducial regions for relevant expected position. The elliptical spot cuts used to select proton and neutron events are shown in Fig. 6.26. The plots shown have been scaled to match the average values of the two profiles as described in Sec. 6.3.4.

Figure 6.28 shows comparison plots between neutron and proton selected events from LD_2 for the SBS-9 kinematic ($Q^2 = 4.5$ (GeV/c)^2) and 70% SBS magnet setting. From the dispersive-direction plot which has scaled the neutron relative-rate profile to the proton

relative-rate profile, the non-uniformity at the corresponding nucleon expected position of -0.6 m is discernible and shows consistent behavior between the proton and neutron selected events. However, from limitations in the SBS-9 acceptance region and overall statistics from both nucleon profiles, the non-uniformity anticipated at the nucleon expected position of -1.7 m is not clearly observed. This comparison of the SBS-9 nucleon relative-rates is encouraging, as it shows agreement between the proton and neutron selected events for the assessable overlapping acceptance regions.

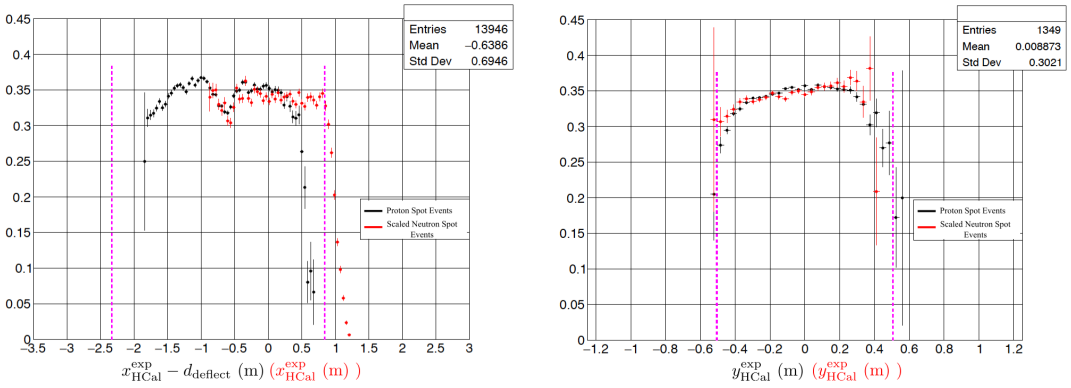

(a) (b)

Figure 6.28: One-dimensional dispersive- and transverse-direction expected position relative efficiency profiles are compared for proton and neutron selected events from LD_2 data sets for the SBS-9 kinematic ($Q^2 = 4.5$ (GeV/c)^2) and 70% SBS magnet setting. The dashed magenta lines represent the boundary of the fiducial regions for relevant expected position. The elliptical spot cuts used to select proton and neutron events are shown in Fig. 6.26. The plots shown have been scaled to match the average values of the two profiles as described in Sec. 6.3.4.

Thus far, for this comparison analysis, we have showed that qualitatively there is consistent behavior between proton and neutron selected events from deuterium data sets within both the SBS-8 and SBS-9 kinematics. For extraction of the neutron Rosenbluth slope, it is important to understand the respective proton and neutron detection efficiency profiles between the SBS-8 and SBS-9 kinematics. Figure 6.28 presents dispersive-direction nucleon expected position profiles separately comparing neutron selected and proton selected events between the SBS-8 kinematic and 70% SBS magnet setting, and the SBS-9

kinematic and 70% SBS magnet setting. The comparison of the scaled neutron relative-rate profiles shows consistency in the overlapping acceptance region, within the statistical uncertainties, between the settings. However, it is difficult to discern evidence for anticipated detection efficiency non-uniformities in either distribution, likely due to insufficient statistics after neutron selection. The comparison of the scaled proton relative-rate profile is more promising as both settings exhibited largely similar distributions, and both non-uniform regions are observed in the overlapping acceptance region. From Fig. 6.28 it is reasonable to suggest that for the SBS-8 and SBS-9 kinematic settings there is largely similar behavior in the detection of protons and neutrons on HCal in the experimental data.

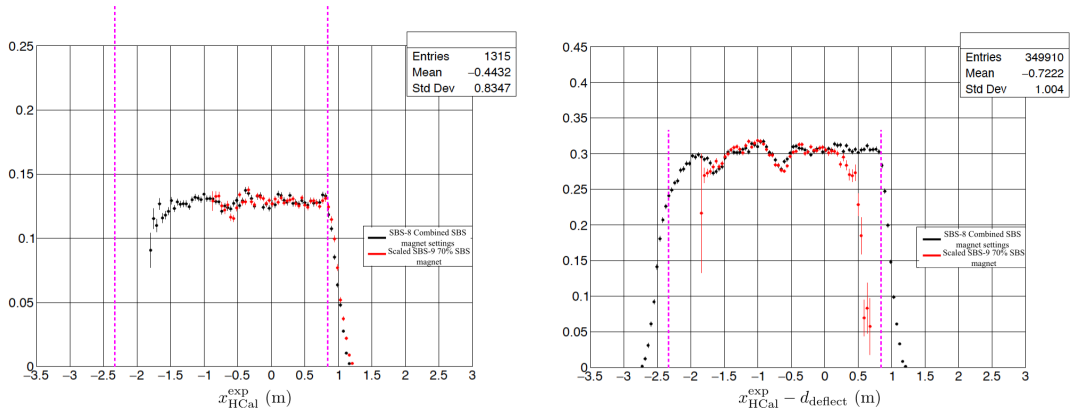

(a) Neutron Selected Events Comparison (b) Proton Selected Events Comparison

Figure 6.29: One-dimensional dispersive-direction expected position relative efficiency profiles are compared between SBS-8 and SBS-9 kinematic ($Q^2 = 4.5$ (GeV/c)^2) and 70% SBS magnet settings for proton and neutron selected events from LD_2 data sets. The dashed magenta lines represent the boundary of the fiducial regions for relevant expected position. The elliptical spot cuts used to select proton and neutron events are shown in Fig. 6.26. The plots shown have been scaled to match the average values of the two profiles as described in Sec. 6.3.4.

6.3.5 Remarks on Neutron Detection Efficiency

The direct evaluation of the neutron detection efficiency at HCal from the experimental data of the G_M^n and nTPE experiments is extremely challenging. This difficulty due to

the lack of stable free neutron targets, which would constitute an unambiguous source of neutrons that could functionally serve as the total number of expected neutron scattering events. From the collected experimental data and the apparatus, as it was during the G_M^n and nTPE experiments, there are two potential techniques for assessing the HCal neutron detection efficiency:

1. From LH_2 data: Tagged neutrons can be exclusively selected from the scattering process: $\gamma p \to \pi^+ n$. Originally, the apparatus for the G_M^n and nTPE experiments would have instrumented a copper radiator, to generate a beam of high-energy photons, and recommissioned the Left High Resolution Spectrometer (LHRS). The LHRS would have operated with the necessary momentum resolution to sufficiently detect positively charged pions. However, due to constraints on the operation schedule at JLab during the period of the G_M^n and nTPE experiments, neither the copper radiator nor the LHRS were instrumented. An alternative instrumentation for obtaining tagged neutrons from the same scattering process is possible using the BigBite Spectrometer. It would require the BigBite Spectrometer to detect π^+ pions, using a down-bending track analysis. Such an analysis of selecting π^+ events via a down-bending track analysis was explored with data from the SBS-9 kinematic, see Ref. [160]. This analysis selecting π^+ events demonstrated that only a limited portion of the HCal acceptance was populated with tagged neutrons and so was not sufficient for quantifying the HCal neutron detection efficiency. Additionally the momentum resolution of the BigBite Spectrometer is insufficient to suppress backgrounds from non-exclusive scattering processes, such as multi-pion production

2. From LD_2 data: Quasi-elastic electron-deuteron scattering serves as a potential source of neutrons. However, it is only possible to know, unambiguously, if the scattered nucleon corresponded to a proton or neutron if the spectator neutron or proton is also detected. The apparatus for the G_M^n and nTPE experiments was not instrumented for spectator nucleon detection.

6.3.6 Systematic Uncertainties Associated with HCal Nucleon Detection Efficiency

As described in Sec. 6.4.1, a quantity involved in the extraction of experimental observables is the individual ratio of detection efficiency for a given nucleon type as determined by the MC simulation divided by the value from the experimental data. As such, a systematic effect can be attributed to any discrepancies in HCal nucleon detection efficiency between the individual absolute neutron to proton detection efficiencies as modeled in the MC and as extracted from the experimental data. From limitations in proton detection efficiency at high-values of Q^2, described in Sec 6.3.2, and a lack of experimental data for tagged neutrons, described in Sec 6.3.5, it is beyond the scope of this dissertation to quantify systematic effects associated with discrepancies in *absolute* HCal nucleon detection efficiencies between MC and experimental data. Since there are significant limitations in quantifying systematic effects associated with absolute HCal nucleon detection efficiencies from experimental data, methods are being considered which involve the MC. Potential ways to estimate the variation in the MC ratio of neutron to proton absolute HCal detection efficiencies could include

- Varying HCal energy deposition parameterizations (or functional form) to model the development of hadronic showers differently and accurately for protons and neutrons,
- Varying the HCal gain parameters to study the response of the absolute HCal nucleon detection efficiency ratio.

From the methodologies presented in all of Sec. 6.3 for proton detection efficiency there is good agreement between the MC simulation and the experimental data. Furthermore studies have been presented which demonstrate qualitative agreement between proton and neutron selected events from deuterium for both the SBS-8 and SBS-9 kinematics. A study characterizing non-uniformities in HCal relative efficiencies have been presented in Sec. 6.3.3 and systematic effects have been quantified and presented in Sec. 6.3.3.3.

6.4 Experimental Observable Extraction

The primary experimental observable for this data analysis is a quantity known as $R_{sf}^{n/p}$; information about the extraction and interpretation of this observable will be provided in this section. Necessary studies of the systematic variations on $R_{sf}^{n/p}$ due to the functional form of the background and the choice of the cut regions will be described in this section. The final component of this section will present extracted values for $R_{sf}^{n/p}$ and their uncertainties for the relevant kinematics settings.

6.4.1 Methodology for Extracting R: Data & MC Fit to Δx

The comparison of Δx distributions from experimental data and SIMC simulated data is central to the methodology of extracting physics observables for this analysis. The first step is the generation of a Δx plot, as described in Sec. 6.1.4.3, from experimental data for a particular kinematic and magnetic field setting, with all event selection criteria applied as explained in Sec. 6.2. One then needs to independently produce two sets of simulated events using the quasi-elastic event generator from SIMC, separately corresponding to the D(e,e'n) and D(e,e'p) scattering reactions. SIMC, summarized in Sec. 6.1.2, provides realistic physics models for relevant scattering processes, and includes nuclear effects and radiative corrections in the event generation. The generated sets of quasi-elastic simulated events then need to be propagated through the remaining components of the SBS MC software machinery to account for detector and reconstruction effects in a manner identical to the processing of the experimental data. After full processing of the MC simulated files, one is able to produce separate Δx distributions corresponding to quasi-elastic neutrons or protons, respectively. These independent sets of D(e,e'n) and D(e,e'p) simulated events will be used to represent a realistic shape for the signals in the Δx distributions. In order to generate quasi-elastic events, SIMC considers n(e,e') and p(e,e') inclusive elastic scattering

cross-sections in a ratio, which we shall denote as

$$R'_{\text{sim}} = \frac{\left(\frac{d\sigma}{d\Omega}\right)_{\text{n(e,e')},\text{sim}}}{\left(\frac{d\sigma}{d\Omega}\right)_{\text{p(e,e')},\text{sim}}}. \tag{6.37}$$

To accurately compare the Δx distributions from experimental data and MC simulated D(e,e'n) and D(e,e'p) events, one should consider the ratio of quasi-elastic neutron to proton cross-sections, as determined by the simulation, which accounts for the known nuclear effects, radiative corrections, and detector properties built into the simulation framework. Such a quantity is represented by the following relation,

$$R_{\text{sim}} = \frac{\left(\frac{d\sigma}{d\Omega}\right)_{\text{D(e,e'n)},\text{sim}}}{\left(\frac{d\sigma}{d\Omega}\right)_{\text{D(e,e'p)},\text{sim}}} = R'_{\text{sim}} \frac{\eta_{\text{ne,n,sim}}\eta_{\text{rc,n,sim}}\xi_{\text{det,n,sim}}}{\eta_{\text{ne,p,sim}}\eta_{\text{rc,p,sim}}\xi_{\text{det,p,sim}}}, \tag{6.38}$$

where $\eta_{\text{ne,n(p),sim}}$, $\eta_{\text{rc,n(p),sim}}$, and $\xi_{\text{det,n(p),sim}}$ are the correction factors to the neutron (proton) elastic cross-sections, as modeled in the simulation, for nuclear effects, radiative corrections, and nucleon detection efficiency, respectively.

With Δx distributions, under conditions as identical as possible, from both experimental and MC data, the goal is to produce the best fit to the experimental Δx plot. We can represent the total fit to the data Δx distribution as a functional form that involves the individual neutron and proton MC Δx distributions, and a parameterized background. We can define the functional form of the total fit, f_{total}, to the experimental data Δx distribution at a particular bin center, x_i, as

$$f_{\text{total}}(x_i) = f_{sf}^{p}\left(R_{sf}^{n/p} h^n(x_i - \delta_n) + h^p(x_i - \delta_p)\right) + f_{\text{bkgd}}(x_i), \tag{6.39}$$

where h^n and h^p represent the MC neutron and proton Δx distributions, respectively, and f_{bkgd} represents the chosen functional form for the background. In Eq. 6.39, the parameter f_{sf}^{p} is the overall scale factor between the MC proton distribution and the data Δx distribution. As part of these MC neutron and proton Δx distributions, the

parameters, δ_n and δ_p, slightly shift the centroids to better match the experimental data distribution. The shift parameters, δ_n and δ_p, are allowed to vary during the fitting process. Shift parameter values for each kinematic setting relevant for this analysis are presented in Tab. B.1. Also for Eq. 6.39, the parameter $R_{sf}^{n/p}$ is the relative neutron to proton scale factor ratio. In Eq. 6.39, there are also a number of fit parameters associated with a particular choice for the background functional form. During the minimization processes used to determine the total fit to the experimental data Δx distribution, the parameters f_{sf}^{p}, $R_{sf}^{n/p}$, δ_n, δ_p, and the parameters associated with the background functional form are allowed to float freely. Typically the functional form of the background falls into two categories: a simple function or a scaled input histogram which approximates the shape of the background. For the case of a simple function, a reasonable candidate is a third-order polynomial and the background functional form would be described as

$$f_{\text{bkgd}}(x_i) = p_0 + p_1 x_i + p_2 x_i^2 + p_3 x_i^3, \tag{6.40}$$

where $p_0, \ldots, p_3$ are the parameters of the function. Alternatively, if the functional form of the background were represented by an input histogram it is the relation

$$f_{\text{bkgd}}(x_i) = B h^{\text{bkgd}}(x_i), \tag{6.41}$$

where B is an overall scaling factor of the input histogram representing the background.

By applying the form of the total fit, in Eq. 6.39 to the experimental Δx distribution we allow for the individual scaling of the simulated D(e,e'n), D(e,e'p), and background component distributions. By using this total fit functional form the fit parameter $R_{sf}^{n/p}$ is able to be directly extracted.

$R_{sf}^{n/p}$ is the primary experimental observable of this analysis. The SIMC generators use specific parameterizations to model the neutron and proton quasi-elastic scattering cross-sections. The experimental Δx distributions extract an empirically-motivated and more

realistic ratio of neutron to proton quasi-elastic scattering cross-sections. $R_{sf}^{n/p}$ quantifies the relative scaling of the neutron to proton quasi-elastic scattering cross-section ratio as modeled by simulation generator and as observed from the experimental data. If the measured cross-sections matched those parameterized in the simulation, then $R_{sf}^{n/p}$ will be exactly 1.00. With the ability to extract $R_{sf}^{n/p}$, for each relevant analysis kinematic setting, the formalism described in Sec 3.2 for relating nuclear cross-section ratios to nucleon cross-section ratios will be extended. Consider Eqs. 3.2 and 3.3, which represent the experimentally observed nuclear and nucleon cross-section ratios, respectively, and the quasi-elastic electron-nucleon scattering cross-section ratio encoded in the simulation. We define a relation between the experimentally measured and MC simulated nuclear quasi-elastic neutron to quasi-elastic proton scattering cross-section ratio as

$$\begin{aligned} R &= \frac{\left(\frac{d\sigma}{d\Omega}\right)_{\mathrm{D(e,e'n)}}}{\left(\frac{d\sigma}{d\Omega}\right)_{\mathrm{D(e,e'p)}}} = R_{sf}^{n/p} \cdot \frac{\left(\frac{d\sigma}{d\Omega}\right)_{\mathrm{D(e,e'n),sim}}}{\left(\frac{d\sigma}{d\Omega}\right)_{\mathrm{D(e,e'p),sim}}}, \\ &= \frac{\left(\frac{d\sigma}{d\Omega}\right)_{\mathrm{n(e,e')}}}{\left(\frac{d\sigma}{d\Omega}\right)_{\mathrm{p(e,e')}}} \frac{\eta_{\mathrm{ne,n}}\eta_{\mathrm{rc,n}}\xi_{\mathrm{det,n}}}{\eta_{\mathrm{ne,p}}\eta_{\mathrm{rc,p}}\xi_{\mathrm{det,p}}} = R_{sf}^{n/p} \cdot \frac{\left(\frac{d\sigma}{d\Omega}\right)_{\mathrm{n(e,e'),sim}}}{\left(\frac{d\sigma}{d\Omega}\right)_{\mathrm{p(e,e'),sim}}} \frac{\eta_{\mathrm{ne,n,sim}}\eta_{\mathrm{rc,n,sim}}\xi_{\mathrm{det,n,sim}}}{\eta_{\mathrm{ne,p,sim}}\eta_{\mathrm{rc,p,sim}}\xi_{\mathrm{det,p,sim}}}, \\ &= R' \frac{\eta_{\mathrm{ne,n}}\eta_{\mathrm{rc,n}}\xi_{\mathrm{det,n}}}{\eta_{\mathrm{ne,p}}\eta_{\mathrm{rc,p}}\xi_{\mathrm{det,p}}} = R_{sf}^{n/p} \cdot R'_{\mathrm{sim}} \frac{\eta_{\mathrm{ne,n,sim}}\eta_{\mathrm{rc,n,sim}}\xi_{\mathrm{det,n,sim}}}{\eta_{\mathrm{ne,p,sim}}\eta_{\mathrm{rc,p,sim}}\xi_{\mathrm{det,p,sim}}}. \end{aligned} \tag{6.42}$$

As originally described in Sec. 3.2, to extract nucleon electromagnetic form factors we are interested in the ratio of neutron to proton elastic cross-sections, represented by R'. As such, when considering Eq. 6.42, we want to isolate R' in terms of either extracted experimental observables or known quantities from simulation as

$$R' = R_{sf}^{n/p} \cdot R'_{\mathrm{sim}} \frac{\eta_{\mathrm{ne,n,sim}}}{\eta_{\mathrm{ne,n}}} \frac{\eta_{\mathrm{rc,n,sim}}}{\eta_{\mathrm{rc,n}}} \frac{\xi_{\mathrm{det,n,sim}}}{\xi_{\mathrm{det,n}}} \frac{\eta_{\mathrm{ne,p}}}{\eta_{\mathrm{ne,p,sim}}} \frac{\eta_{\mathrm{rc,p}}}{\eta_{\mathrm{rc,p,sim}}} \frac{\xi_{\mathrm{det,p}}}{\xi_{\mathrm{det,p,sim}}}. \tag{6.43}$$

For Eq. 6.43 to be used for extracting nucleon form factors, we should validate any discrepancies or assign uncertainties between the experimental data and the simulated events accounting for nuclear effects, radiative corrections, and nucleon detection efficiencies. Which are represented by the ratio terms in Eq. 6.43. We will claim that the SIMC event

generators realistically model the individual neutron and proton nuclear effects and radiative corrections which are present within the experimental data. SIMC, however, does not include models for a phenomenon known as final-state interactions. In the context of quasi-elastic electron-deuteron scattering, final-state interactions involve the struck nucleon interacting with the spectator nucleon in a manner that significantly modifies the momentum and angular distributions of the outgoing nucleon. To properly account for final-state interactions, theoretical models for the nucleon-nucleon interactions over the relevant momentum range need to be employed and studies quantifying systematic effects on experimental observables are needed. Such implementation of theoretical models and study of systematic effects is beyond the scope of this dissertation. For quasi-elastic electron-nucleon scattering, it is known that radiative corrections largely effect the electron component of the scattering cross-section and so modifications to the respective neutron or proton components should largely be similar. Thus, for the terms representing nuclear effects and radiative corrections, we will claim the conditions $\eta_{\mathrm{ne,n(p),sim}} = \eta_{\mathrm{ne,n(p)}}$ and $\eta_{\mathrm{rc,n(p),sim}} = \eta_{\mathrm{rc,n(p)}}$ are sufficiently motivated and this leads to simplification of Eq. 6.43. Sec. 6.3 presents studies demonstrating strong agreement between HCal proton detection efficiency as observed in the experimental data and as implemented in the simulation. Moreover, position-dependent non-uniformities in HCal detection efficiency are studied from the experimental data, for both nucleon types, and such non-uniform regions are accurately reproduced for simulated events. Extracting direct measurements of HCal neutron detection efficiency from experimental data are not possible, and so validating neutron detection efficiency in MC is extremely challenging. For this dissertation, we will assume that the respective HCal neutron and proton detection efficiencies as implemented in the simulation and as present in the experimental data are consistent within a reasonable systematic uncertainty. For reasons described Secs. 6.3.5 and 6.3.6, assigning a value for the systematic uncertainty attributed to absolute HCal nucleon detection efficiencies is beyond the scope of this dissertation. As such, for terms representing the individual nucleon detection efficiencies, we will claim the conditions $\xi_{\mathrm{det,n(p),sim}} = \xi_{\mathrm{det,n(p)}}$ is suffi-

ciently motivated and this leads to simplification of Eq. 6.43. Therefore, we assume that the simulated events consistently replicate, within assignable uncertainties, the dominant physics and detector effects that are present (or observed) in the experimental data. For the purposes of extracting preliminary physics results for this dissertation, the simplified version of Eq. 6.43, accounting for the relevant effects, is the relation

$$R' = R_{sf}^{n/p} R'_{\text{sim}}. \tag{6.44}$$

Fig. 6.30 presents an example comparison between the data Δx distribution, the scaled signal distributions from the MC, and a second-order polynomial representing the background shape. The black experimental histogram represents the Δx distribution, after all event selection criteria are applied. The shaded red and blue curves correspond to the scaled MC proton and neutron Δx distributions, respectively, which are individually generated using the SIMC quasi-elastic generator. The background functional form is represented by the shaded green curve. The total fit to the data Δx as described by Eq. 6.39, is represented by an overlaid magenta curve. By overlaying the data and MC Δx distributions, and the respective total and background fits we obtain Fig. 6.30, which serves to visualize the data/MC comparison technique. The total fit and the experimental histogram are in reasonable agreement.

6.4.2 Cut Stability Studies

Understanding the stability of the experimental observable $R_{sf}^{n/p}$ when considering choices pertaining to cut regions is a critical component of data analysis. Broadly, cut stability studies can be considered in two main stages. The first stage is defining optimal regions and thresholds of cut variables to minimize sensitivity to extracted experimental observables. The second stage of cut stability evaluation is quantifying systematic uncertainties associated with the chosen cut regions. Ultimately, the systematic uncertainties associated with the cut regions are quantified by independently varying each cut variable boundary.

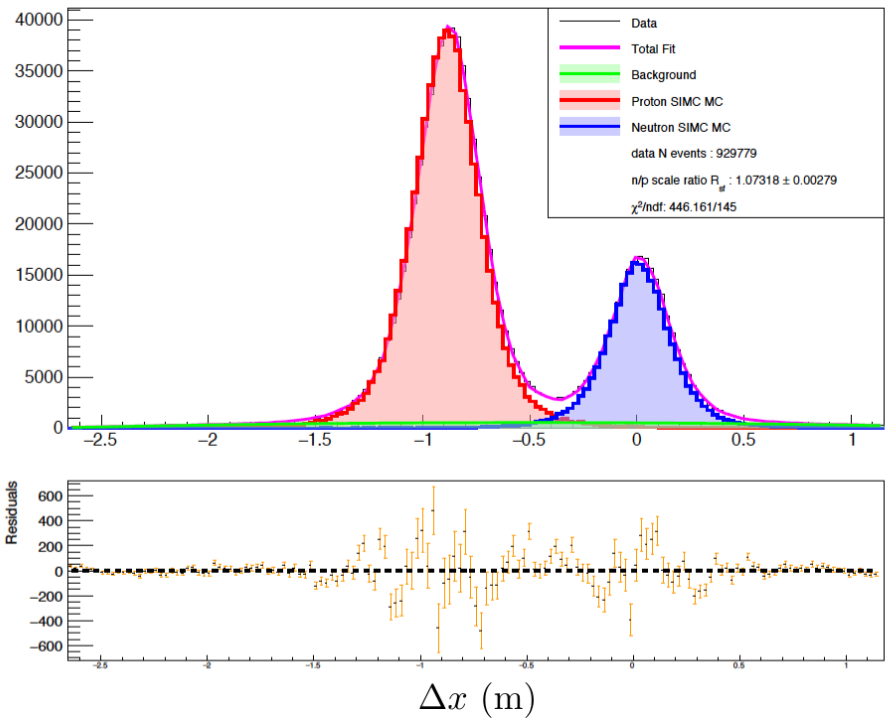

Figure 6.30: An example of a data/MC comparison for the Δx distribution produced from experimental data and simulated events (SBS-8 $Q^2 = 4.5$ (GeV/c)^2 kinematic and SBS magnet 70% field setting). A residual plot between the experimental data Δx distribution and the magenta total fit is also presented (lower panel). Event selection criteria (Sec. 6.2) have been identically applied to the data and MC distributions. The legend of every data/MC comparison presented in this dissertation will include the number of events in the data Δx distribution, the extracted $R_{sf}^{n/p}$ value with a statistical uncertainty, and the χ^2/ndf of the total fit. The statistical uncertainty on $R_{sf}^{n/p}$ only represents the statistical fluctuations in the experimental data.

Detailed descriptions of the analysis procedures associated with both cut optimization and systematic evaluation of cut regions in the remainder of this section.

An important consideration associated with cut stability studies is understanding effects due to known correlated cut variables, or minimally, being able to identify which cut variables are correlated. Figure 6.31 presents the correlation between dispersive and non-dispersive expected HCal positions, $x_{\mathrm{HCal}}^{\mathrm{exp}}$ and $y_{\mathrm{HCal}}^{\mathrm{exp}}$, and between optics validity parameters, x_{BB} and y_{BB}, respectively. Figure 6.32 shows the correlation between the W^2

and Δy quantities. By identifying these correlations we can make better informed decisions when optimizing certain cut regions and properly consider cut variables to not double-count (or overestimate) certain systematic effects.

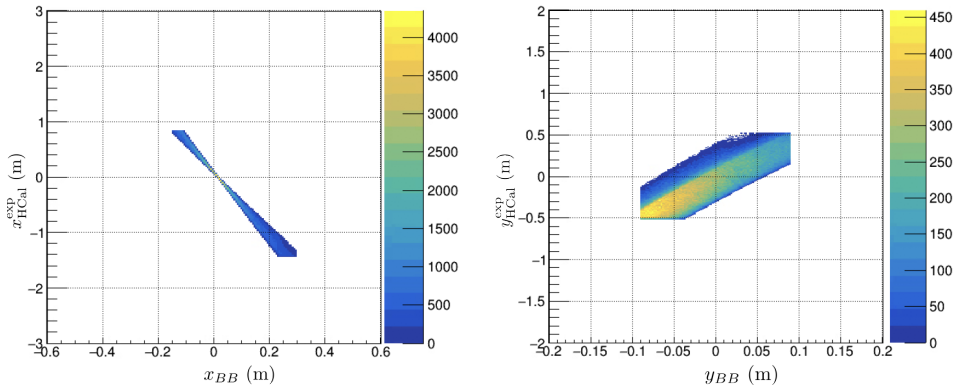

Figure 6.31: Example plots demonstrating the strong correlations, respectively, between the expected positions on HCal, $x^{\rm exp}_{\rm HCal}$ and $y^{\rm exp}_{\rm HCal}$, and the BigBite optics validity parameters, x_{BB} and y_{BB}. These plots are produced from data for the SBS-8 ($Q^2 = 4.5$ (GeV/c)^2) kinematic and SBS magnet 70% field setting. All event selection criteria has been applied to the plots. Plots from other kinematic and SBS magnet field settings show strongly similar behaviors.

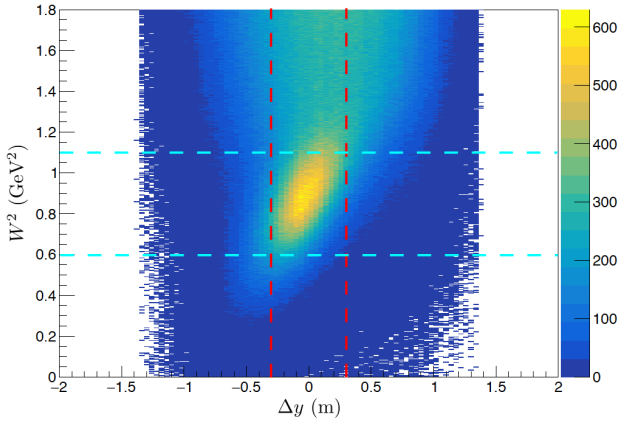

Figure 6.32: Correlation between W^2 and Δy. The plot is produced from data for the SBS-8 ($Q^2 = 4.5$ (GeV/c)^2) kinematic and SBS magnet 70% field setting. Event selection criteria, except for the two plotted quantities, has been applied to the plots. The dashed cyan lines represent the W^2 cut region and the dashed red lines represent the Δy cut region, respectively. Within the overlapping optimized cut regions, it is evident that there is a strong correlation W^2 and the Δy.

Cut Region Optimization

Optimizing the analysis cut regions is essential for a proper extraction of the experimental observable $R_{sf}^{n/p}$. Conceptually, a cut variable is an analysis tool which simultaneously selects event likely to correspond to signal, and rejects regions where background contamination are probable. For a given cut variable, if the cut region is too wide then there is a possibility for background contamination to be present in Δx distributions. Alternatively, if the cut region is too strict, there is potential for reductions in statistics or there could be effects which differently impact the quasi-elastic proton verses quasi-elastic neutron events.

For the experimental and simulated MC data sets corresponding to a given kinematic and SBS magnet field setting, each cut parameter, described in Sec. 6.2, undergoes an individual stability evaluation to determine the optimal region for that cut parameter. This cut optimization process involves assessing the stability of the experimental observable $R_{sf}^{n/p}$ as many small regions of the cut parameter are sampled, over the entire range of the cut parameter. The procedure, used in this analysis, for evaluating cut stability and determining the optimal cut region is as follows:

1. Construct a two-dimensional distribution of Δx as a function of an individual cut variable. Apply all event selection cuts on this 2D distribution, except for the examined cut variable. For any cut parameters which are known to be correlated, the additional correlated cut parameter is also excluded in the applied event selection criteria.

2. For the 2D distribution of Δx vs. the examined cut variable, segment the range of the examined cut variable so that the individual segmented regions are narrow. Ideally, these regions should not be statistically limited. The narrow segmented regions should sample across the entire range of the cut variable. Fig. 6.33 shows a visualization for the Preshower energy cut variable of the 2D distribution of Δx vs. Preshower energy and the 1D distribution of the examined cut variable. Overlayed is a single segmented region, represented by the double red solid lines, at the start of

the sampling range of this Preshower energy parameter. In practice, when this study is conducted there are many segments across the entire range of the cut parameter of equal size, as visualized, until the cyan solid line is reached. The exact size of each segment for a given cut variable can be interpreted from the horizontal uncertainties present in plots similar to Fig. 6.34.

3. From the events in a single segmented region of the 2D distribution, form a 1D projection of the Δx parameter.

4. For each 1D Δx projection, corresponding to an individual segmented region of the cut variable, iteratively process a Δx data/MC comparison for each segmented region, following a similar process as described in Sec. 6.4.1. This will extract a value for $R_{sf}^{n/p}$ from the events in each narrow segmented region.

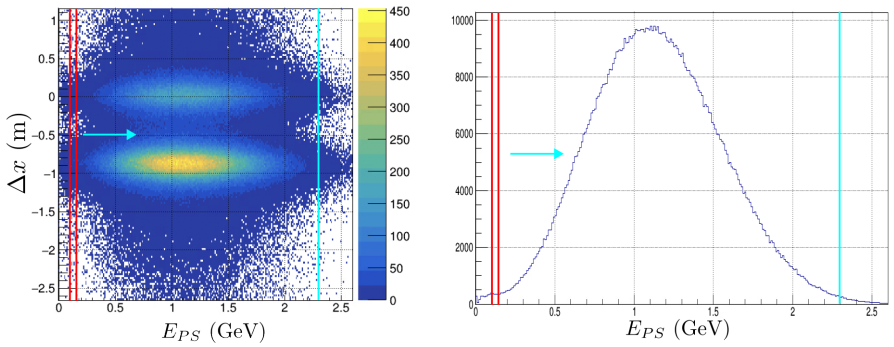

Figure 6.33: Example cut sensitivity plots. In both plots the red lines represent an example segmented region of the cut variable. In practice multiple segmented regions are considered as entire range of the cut variable is scanned. The individual segmented region would traverse the range of the cut variable until it reaches the cyan line. These plots are produced from data for the SBS-8 ($Q^2 = 4.5$ (GeV/c)^2) kinematic and SBS magnet 70% field setting. Left: An example of a two dimensional plot used in the cut optimization procedure; in this case the examined cut variable is the Preshower energy. Right: The Preshower energy distribution with all other cuts applied.

The entire cut optimization process is iterative. Initially, when there are no cut variables with optimal regions determined, reasonable and loose event selection criteria are applied for each cut variable. The procedure attempts to optimize less sensitive cut vari-

ables first, typically those corresponding to good electron cuts. Once those cut parameters have optimal cut regions then the optimization procedure is applied to cut parameters which are more sensitive to quasi-elastic event selection.

The primary result of this analysis procedure will be a graph which provides values of $R_{sf}^{n/p}$ as function of different small samples of the cut variable, for the entire variable range. Figure 6.34 shows an example of such a graph for the Preshower energy cut variable. Additional example graphs for every type of cut variable used in this analysis are shown in Figs. B.1 and B.2; these correspond to only a single kinematic and SBS magnet field setting. For any form of a graph of $R_{sf}^{n/p}$ as function of a cut variable (e.g. Fig. 6.34) the horizontal error bar represents the segment size, for a given cut variable. The vertical error bars of this graph represent the uncertainty on the fit parameter $R_{sf}^{n/p}$ as determined from the data/MC comparison, and it reflects the amount of statistics available for a given segment's Δx projection. The dashed magenta line is a constant value which is fit to each set of $R_{sf}^{n/p}$ values to approximate a central value. The process for determining stable regions of a given cut variable takes into account regions where the values of $R_{sf}^{n/p}$ are within reasonable statistical uncertainty of the approximate central value. Optimal cut regions are informed by known physics motivations for any particular cut variable. Alternatively, if a given cut variable exhibits significant fluctuations in values of $R_{sf}^{n/p}$, optimal cut regions are defined loosely as to not improperly introduce bias on the experimental observable. Tab. 6.3 shows all of the final cut regions used for this analysis. All cut regions, except the Δt cut, are equally applied to experimental data and MC simulated events used in this data analysis. Further information and plots used in the determination of optimal cut regions for each relevant kinematic and SBS magnet field setting are available in Ref. [178].

Systematic Uncertainty Due to Cut Regions

The experimental observable $R_{sf}^{n/p}$, and thus the ratio R', is sensitive to the values for cut regions and thresholds determined from the cut optimization process. To account for

Cut Variable	Optimized Cut Regions			
	SBS-8 50%	SBS-8 70%	SBS-8 100%	SBS-9 70%
N_{GEMhits}	≥ 3	≥ 3	≥ 3	≥ 3
Track χ^2/ndf	≤ 15	≤ 15	≤ 15	≤ 15
v_z (m)	$[-0.07, 0.07]$	$[-0.07, 0.07]$	$[-0.07, 0.07]$	$[-0.07, 0.07]$
x_{BB} (m)	$(-0.15, 0.30)$	$(-0.15, 0.30)$	$(-0.15, 0.20)$	$(-0.15, 0.30)$
y_{BB} (m)	$(-0.09, 0.09)$	$(-0.09, 0.09)$	$(-0.08, 0.08)$	$(-0.09, 0.09)$
E_{PS} (GeV)	> 0.2	> 0.2	> 0.2	> 0.2
E_{BBCal}/p	$(0.8, 1.2)$	$(0.8, 1.2)$	$(0.8, 1.2)$	$(0.8, 1.2)$
E_{HCal} (GeV)	≥ 0.055	≥ 0.055	≥ 0.055	≥ 0.05
Δt (ns)	$[-10, 10]$	$[-10, 10]$	$[-10, 10]$	$[-10, 10]$
W^2 (GeV^2)	$[0.6, 1.1]$	$[0.6, 1.1]$	$[0.6, 1.1]$	$[0.65, 1.1]$
Δy (m)	$[-0.3, 0.3]$	$[-0.3, 0.3]$	$[-0.3, 0.3]$	$[-0.3, 0.3]$
$x^{\text{exp}}_{\text{HCal}}$ (m)	$(-2.32, 0.83)$	$(-2.32, 0.83)$	$(-2.32, 0.83)$	$(-2.32, 0.84)$
$y^{\text{exp}}_{\text{HCal}}$ (m)	$(-0.51, 0.51)$	$(-0.51, 0.51)$	$(-0.51, 0.51)$	$(-0.5, 0.5)$

Table 6.3: Final optimized cut values. The cut values are compartmentalized by data sets associated with a particular kinematic and SBS magnet field setting. The values in this table were determined by the cut optimization process described in this section.

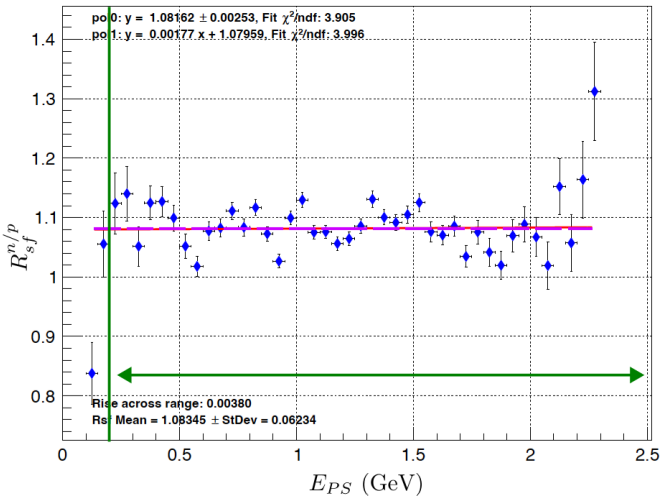

Figure 6.34: Example plot used for determining optimal cut regions. The cut variable presented in this plot corresponds to Preshower energy. This plot is produced from data and MC information from the SBS-8 ($Q^2 = 4.5$ (GeV/c)^2) kinematic and SBS magnet 70% field setting. General details about the information presented in a given plot will be described in the text.

effects arising from the determination of optimized cut regions and thresholds a dedicated systematic study was performed. This study was performed on experimental data and

MC simulated events by varying the boundary of an optimized cut region, for a single cut variable while keeping all other cut regions unchanged, and then extracting values for $R_{sf}^{n/p}$. All cut variables described in Sec. 6.2, and their corresponding optimized cut regions in Sec 6.4.2, were evaluated for any systematic effects on the experimental observable $R_{sf}^{n/p}$. Broadly, the cut variables can be separated into three different categories, dependent on the type of cut boundaries and properties of a given cut variable distribution. The three categories for the cut variables are a single boundary (or threshold), a two boundary cut region where each boundary is considered individually, and a two boundary cut region around a central value. For cut regions defined by a single boundary, this boundary value was slightly manipulated to evaluate any systematic change. For the case of a two boundary cut region where each boundary is separately considered, one boundary was held fixed at the optimal value and the other allowed to vary slightly around the optimal value. The cut variable distributions for this consideration typically are not symmetric and as such both boundaries will undergo evaluation and systematic effects will be quantified for each boundary. For the third case of a two boundary cut region around a central value, both cut boundaries were simultaneously varied around the central value of the cut variable. In this case the cut variable distribution are typically symmetric, and therefore the systematic effect was quantified by varying both boundaries. The procedure for quantifying systematic uncertainties associated with the choice of cut regions is as follows:

1. Construct a two-dimensional distribution of Δx as a function of an individual cut variable. Apply all event selection cuts on this 2D distribution, except for the examined cut variable. For any cut parameters which are known to be correlated, the additional correlated cut parameter is also excluded in the applied event selection criteria.

2. For the 2D distribution of Δx vs. the examined cut variable, segment the range of the cut variable so that the segmented regions are wide. The wide segmented regions are defined in a manner that is dependent on the type of category each cut

variable is considered. For the single boundary (or threshold) case, each wide segment is formed by allowing the single boundary value to systematically vary around the optimized value and correspondingly accept or rejects events. An example of the wide segments for the single boundary case is shown in Fig. 6.35 via the track χ^2/ndf cut variable. For the case of Fig. 6.35, each wide segment is individually formed from the solid cyan line to each of the solid red lines. For the case where both boundaries are considered separately, wide segments will be formed by holding one boundary fixed at the optimized value and the other boundary will be permitted to slightly vary around its optimal value. For this particular consideration, both boundaries are evaluated as described and are referred to as the "left" and "right" boundary evaluations. Fig. 6.36, shows the left boundary evaluation for the W^2 cut variable, where the wide segments are formed by regions going from each of the solid red lines to the fixed solid cyan line. The right boundary evaluation is similarly completed, but the right boundary is permitted to vary and the left boundary is fixed. For the category where both boundaries are simultaneously varied, the variation will occur symmetrically about the optimal value on both sides of the 2D distribution and this will be used to determine the wide segments. The vertex cut variable is treated with this symmetric prescription and is shown in Fig. 6.37. A given wide segment will be defined as the region between the solid cyan lines, where each wide segment corresponds to a pair of left and right symmetric solid red lines.

3. From the events in a single segmented region of the 2D distribution, form a 1D projection of the Δx parameter.

4. For each 1D Δx projection, corresponding to an individual segmented region of the cut variable, iteratively process a Δx data/MC comparison for each segmented region, following a similar process as described in Sec. 6.4.1. This will extract a value for $R_{sf}^{n/p}$ from the events in each wide segmented region.

5. Construct a graph of $R_{sf}^{n/p}$ as a function of the wide segmented regions, represented

by the values of the varied boundary of a given cut variable. Figures 6.35, 6.36, and 6.37 show examples of this type of plot for each of the three different boundary categories. Each graph is fitted with a constant value, shown as a dashed magenta line. Additionally a linear fit is applied to each graph and this is represented as a red sloped line. As a caveat, the vertical error bars are relatively large compared to the values of $R_{sf}^{n/p}$; this is due to wide segmented regions often encompassing largely similar sets of events within the 2D distribution. Therefore the vertical error bars are correlated.

6. From the linear fit we can extract the absolute value of the rise across the range, for a given graph of $R_{sf}^{n/p}$ as a function of cut variable. Since this systematic study for a given cut variable is varied around the optimal cut value, half of the rise across the range represents the sensitivity of $R_{sf}^{n/p}$ due to the variation of the cut variable boundary. As such, half of the absolute value of the rise across the range is taken as the systematic effect associated with the particular cut variable boundary.

The individual cut variable contributions to the total systematic uncertainty associated with the cut regions are presented in Tab. 6.4. The values in Tab. 6.4, for every cut variable boundary, are determined by the procedure described in this section. It has been demonstrated, from Fig. 6.31, that expected HCal positions and the optics validity parameters are highly correlated. Due to this known correlation, systematic effects are quantified for both sets of cut variables. However, only one cut variable in the dispersive and non-dispersive-directios, whichever produces the larger effect, is included in the determination of the total systematic uncertainty. It has also been demonstrated in Fig. 6.32 that W^2 and Δy are highly-correlated in the optimized cut regions. Similarly, in the determination of the total systematic uncertainty due to cut regions, of these two correlated cut variables only the one producing the large effect is included. In Tab. 6.4, correlated cut variables which are excluded from the total systematic uncertainty are denoted with an "$*$". From the uncertainty contributions presented in Tab. 6.4, the cut variables W^2 or Δy, Δt, and

the optics validity parameters typically are the dominant sources. The majority of good electron cut variables produce lower systematic uncertainty contributions. Example $R_{sf}^{n/p}$ graphs used for quantifying systematic effects for every other cut variable are presented in Sec B.2. Further information and plots relevant to quantifying systematic effects due to cut regions for every relevant kinematic and SBS magnet field setting are available in Ref. [178].

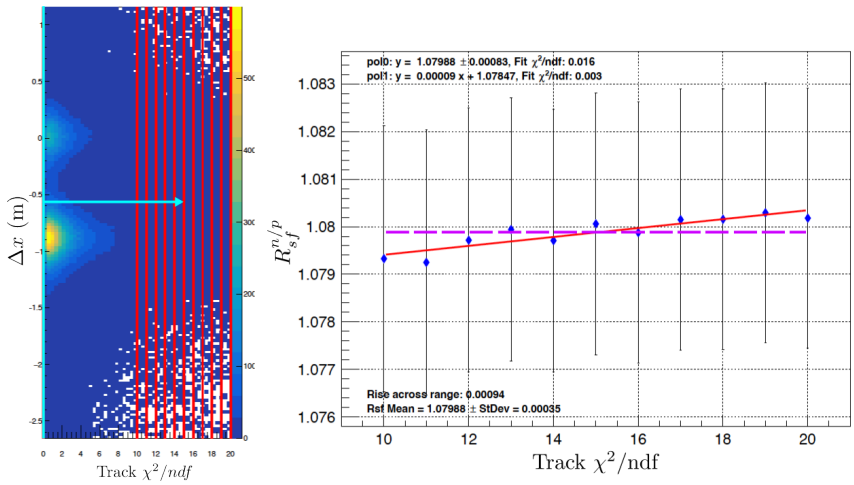

Figure 6.35: Example plots for the single boundary (or threshold) category for systematic quantification. The track χ^2/ndf cut variable is used to visualize this particular category. These plots are produced from data for the SBS-8 ($Q^2 = 4.5$ (GeV/c)^2) kinematic and SBS magnet 70% field setting. Left: A 2D plot of Δx vs. track χ^2/ndf. This plot visualizes the different wide segment regions. The details of the overlayed solid colored lines are described in the text. Right: The graph of $R_{sf}^{n/p}$ as a function of wide segments in the track χ^2/ndf cut variable. This graph is used to quantify systematic effects for the track χ^2/ndf cut variable.

6.4.3 Background Shape Estimation

The event selection criteria described in Sec. 6.2 significantly reduces the number of entries in the experimental Δx distributions which do not correspond to quasi-elastically scattered neutrons or protons. However, some amount of events persist which correspond to background processes, predominantly inelastic scattering, and this manifests as part of the experimental Δx distributions. To properly extract physics observable for this

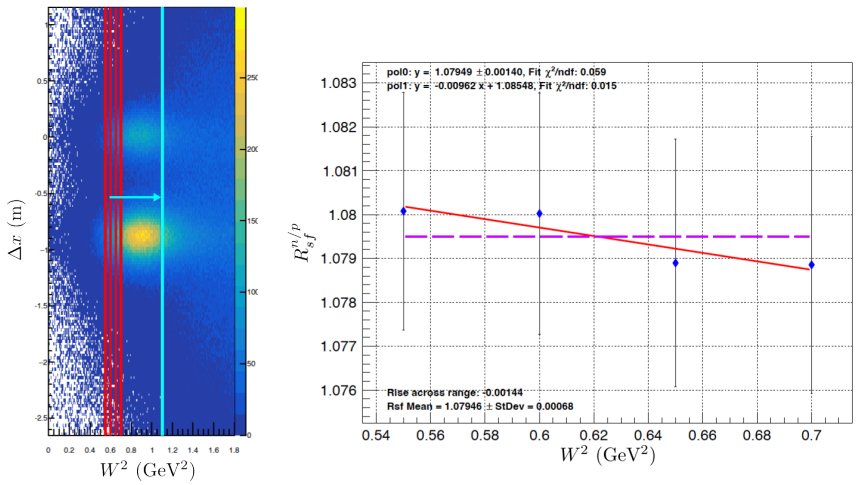

Figure 6.36: Example plots for the separate double boundary category used for systematic quantification. The W^2 cut variable is used to visualize this particular category. These plots are produced from data for the SBS-8 (Q^2 = 4.5 (GeV/c)^2) kinematic and SBS magnet 70% field setting. Left: A 2D plot of Δx vs. W^2. This plot visualizes the different wide segment regions for the left boundary evaluation. The details of the overlayed solid colored lines are described in the text. Right: The graph of $R_{sf}^{n/p}$ as a function of wide segments in the W^2 cut variable for the left boundary. This graph is used to quantify systematic effects for the left boundary of the W^2. A similar plot is considered and used to quantify the right boundary.

analysis, the background shape must be accurately estimated and systematic effects should be quantified.

As previously mentioned in Sec. 6.4.1, we choose to model the background functional form with two main categories. The first are smooth functional parameterizations. The second method involves extracting the shape of the background from data anti-cut distributions. These anti-cut distributions are formed from parameters which can be used to isolate events that are from regions not likely to correspond to quasi-elastic neutrons or protons, and therefore be a proxy for processes that could contribute to the overall background. To study the variation on the experimental observable $R_{sf}^{n/p}$ due the background, we will model the functional form of the background with five different techniques. The techniques for modeling the background employed in this analysis are as follows:

1. Gaussian: The amplitude, mean, and width of the Gaussian distribution are allowed

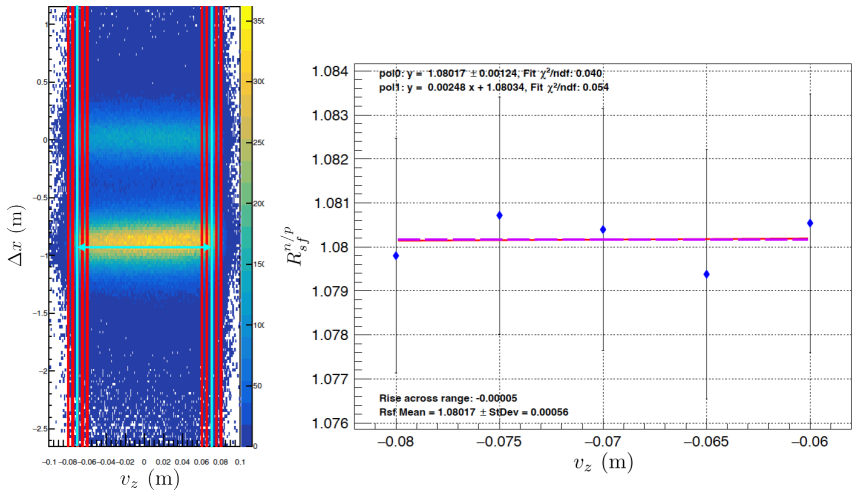

Figure 6.37: Example plots for the symmetric double boundary category used for systematic quantification. The v_z cut variable is used to visualize this particular category. These plots are produced from data for the SBS-8 ($Q^2 = 4.5$ (GeV/c)^2) kinematic and SBS magnet 70% field setting. Left: A 2D plot of Δx vs. v_z. This plot visualizes the different wide segment regions. The details of the overlayed solid colored lines are described in the text. Right: The graph of $R_{sf}^{n/p}$ as a function of wide segments in the v_z cut variable. This graph is used to quantify systematic effects for v_z cut variable.

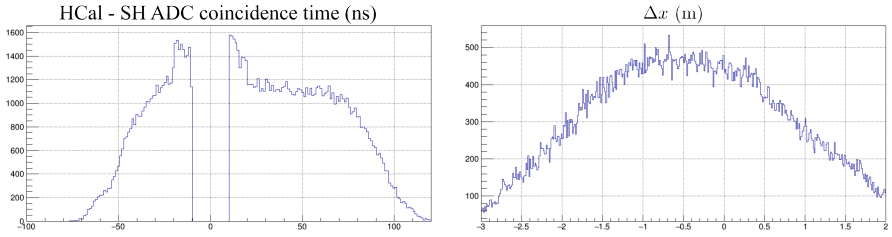

Figure 6.38: Example plots showing how the coincidence time anti-cut is determined. These plots are produced from data for the SBS-8 ($Q^2 = 4.5$ (GeV/c)^2) kinematic and SBS magnet 70% field setting. Left: The coincidence time distribution which is generated from events outside the signal region, constituting the anti-cut. Right: The background Δx distribution generated from events in the coincidence time anti-cut.

to vary, along with the scaling parameters, when the total fit functional form is applied to the data Δx histogram.

2. Polynomial Order-2: The three coefficients associated with the order-2 polynomial are permitted to vary, along with the scaling parameters, when the total fit functional form is applied to the data Δx histogram.

Cut Variable	Systematic Uncertainty Contribution			
	SBS-8 50%	SBS-8 70%	SBS-8 100%	SBS-9 70%
N_{GEMhits}	0.0025	0.0061	0.0029	0.00007
Track χ^2/ndf	0.0005	0.0005	0.0002	0.0014
v_z (m)	0.0017	0.00003	0.0003	0.0009
x_{BB} (m)	0.0012	0.0044	0.0021	0.0019
y_{BB} (m)	0.0014	0.0013	0.0023	0.0007∗
E_{PS} (GeV)	0.0002	0.0002	0.0006	0.0005
E_{BBCal}/p	0.0002	0.0007	0.0013	0.0003
E_{HCal} (GeV)	0.0006	0.0002	0.0003	0.0002
Δt (ns)	0.0027	0.0023	0.0022	0.0030
W^2 (GeV^2)	0.0063	0.0007∗	0.0012	0.0035
Δy (m)	0.0041∗	0.0019	0.0012∗	0.0010∗
$x^{\text{exp}}_{\text{HCal}}$ (m)	0.0006∗	0.0002∗	0.0006∗	0.0008∗
$y^{\text{exp}}_{\text{HCal}}$ (m)	0.0007∗	0.0007∗	0.0013∗	0.0011
$\Delta\left(R^{n/p}_{sf}\right)_{\text{cuts}}$	0.0078	0.0083	0.0052	0.0054

Table 6.4: The table presents contributions to the systematic uncertainties associated with cut variable regions for every relevant kinematic and SBS magnet field setting. The total cut systematic uncertainties are also presented. Any cut variables which are marked with an "∗" are excluded from the total cut systematic uncertainty, for that particular setting. For details about the exact procedure for determining the total systematic uncertainty due to cut regions, see the text.

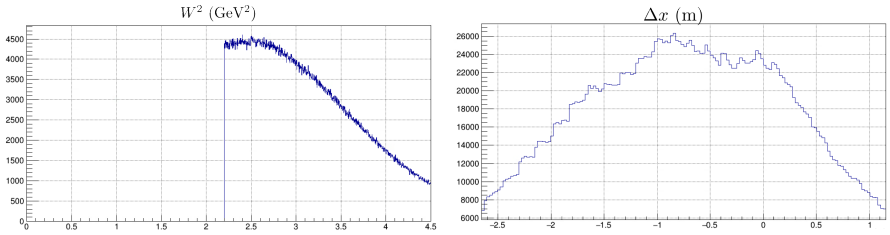

Figure 6.39: Example plots showing how the W^2 anti-cut is determined. These plots are produced from data for the SBS-8 ($Q^2 = 4.5$ (GeV/c)^2) kinematic and SBS magnet 70% field setting. Left: The W^2 distribution which is generated from events outside the signal region, constituting the anti-cut. Right: The background Δx distribution generated from events in the W^2 anti-cut.

3. Polynomial Order-3: The four coefficients associated with the order-3 polynomial are permitted to vary, along with the scaling parameters, when the total fit functional form is applied to the data Δx histogram.

4. Coincidence time anti-cut: A Δx distribution is generated, from the same data set as

the experimental data histogram, which passes all other selection criteria and ensures that events which populate the histogram are sourced outside the signal region of the coincidence time cut. During the fitting process, the Δx distribution representing the background shape is scaled as in Eq. 6.41. Fig. 6.38 depicts examples of the coincidence time anti-cut distribution and the Δx background shape that corresponds to these events.

5. W^2 anti-cut: A Δx distribution is generated, from the same data set as the experimental data histogram, which passes all other selection criteria and ensures that events which populate the histogram are sourced far into the inelastic region of the W^2 distribution, to attempt to minimize any presence of quasi-elastic nucleon tails. During the fitting process, the Δx distribution representing the background shape is scaled as in Eq. 6.41. Fig. 6.39 depicts examples of the W^2 anti-cut distribution and the Δx background shape that corresponds to these events.

The three smooth parameterizations for the background are the least physically motivated, however, they provide reasonable forms for the background shape without overfitting. The two anti-cut techniques are better motivated, as they try to isolate parameter regions which are less likely to include quasi-elastic nucleon events and therefore capture events which could correspond to background processes. Each of the two anti-cut techniques likely have their own limitations. The coincidence time anti-cut largely captures out-of-time events which can include both accidental and inelastic events. The W^2 anti-cut is sensitive to different types of processes included within the inelastic region of the W^2 distribution. As such processes contributing to higher-values of W^2, within the inelastic region, will not inherently contribute to the background near the quasi-elastic peak.

An even more justifiable representation of the background functional form could be estimated from Δx distributions formed from MC simulated events obtained using the inelastic generator of G4SBS. The inelastic generator characterizes physical processes which are likely to be the dominant background scattering processes, though it is not

all-encompassing. One could then verify that the W^2 distribution of the MC simulated events from the inelastic generator matches the inelastic region of the data W^2 distribution. A similar study of the background shape of events from the MC inelastic generator was conducted by Refs. [134] and [160], and the physics observables determined from this particular functional form were consistent with the technique employed in this analysis. For the analysis in this dissertation, though more physically motivated, the background shape associated with events simulated from the MC inelastic generator was not studied. Additionally, the χ^2/ndf of the total fit, from the studies conducted by Refs. [134] and [160], suggested the least compatible fit was with a background shape from events produced using the inelastic generator of G4SBS. This is likely due to a need for more MC statistics, passing physics event selection, for simulated files produced using the inelastic generator.

For a particular kinematic and SBS magnetic field setting, $R_{sf}^{n/p}$ is extracted by conducting a data/MC comparison of the Δx distribution for each of the different background techniques. The systematic uncertainty associated with the inelastic contamination of the experimental observable $R_{sf}^{n/p}$ is the standard deviation of the five $R_{sf}^{n/p}$ values. Fig. 6.40 shows five typical data/MC comparisons, demonstrating each background type, of the Δx distributions which are used to extract $R_{sf}^{n/p}$. The corresponding $R_{sf}^{n/p}$ values for the SBS-8 and SBS-9 kinematic and SBS magnet field settings relevant for this analysis are summarized in Tab. 6.5. The graph in Fig. 6.41 reorganizes the values presented in Tab. 6.5 as a plot of $R_{sf}^{n/p}$ versus the background functional form, for each relevant kinematic and SBS magnet field setting. For the different data sets for the SBS-8 kinematic there is an evident correlation between values of $R_{sf}^{n/p}$ and a given model technique for the background shape. During uncertainty analysis and propagation to determine experimental results, the systematic associated with the background model will be treated as a correlated uncertainty, when combining results for the different SBS magnet field settings for SBS-8. From the graph in Fig. 6.41, the data set does not exhibit the same behavior for SBS-9, and there does not seem to be a strong correlation between the $R_{sf}^{n/p}$ values of SBS-9 and SBS-8.

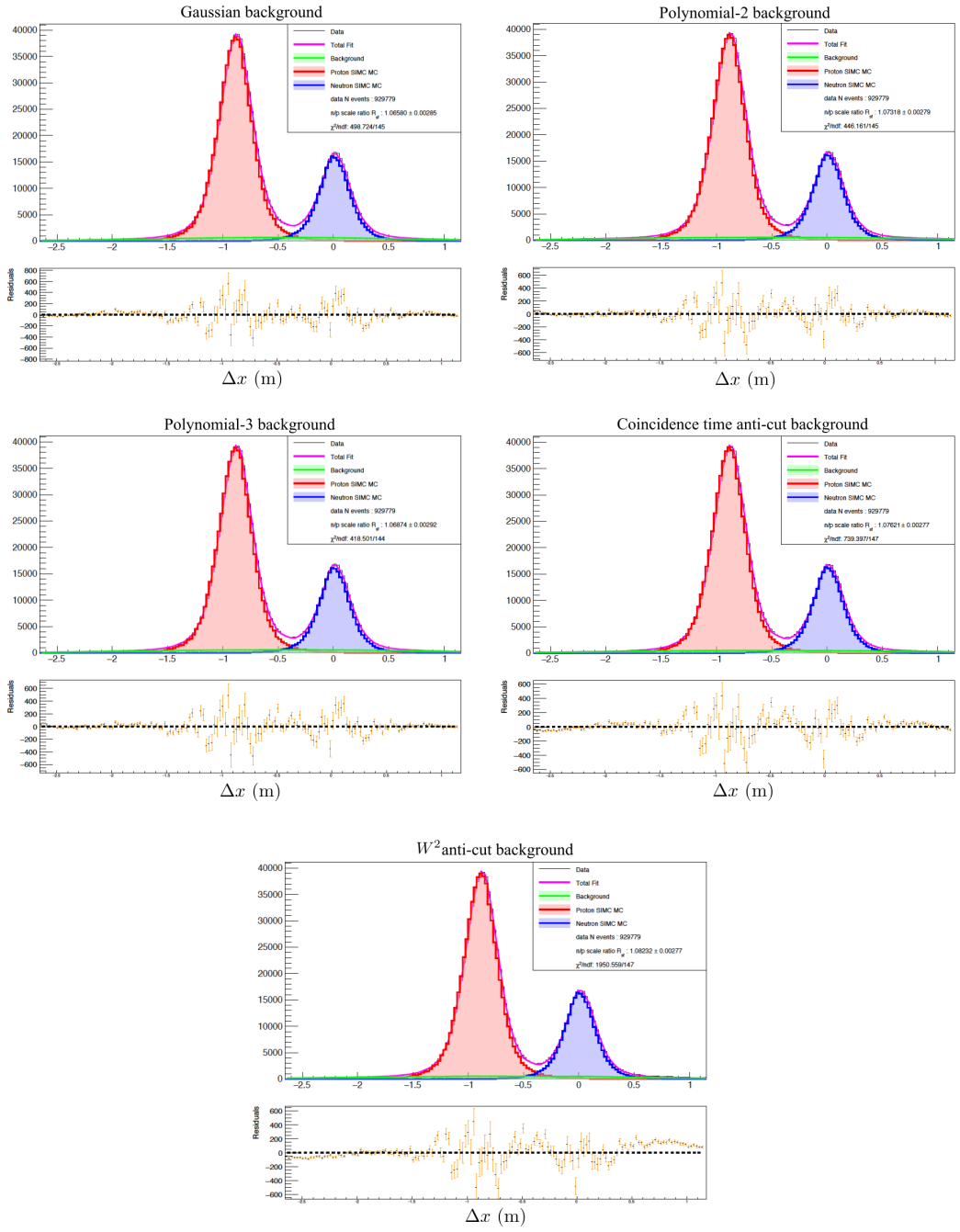

Figure 6.40: Example data/MC comparisons from the SBS-8 ($Q^2 = 4.5$ (GeV/c)^2) kinematic and SBS magnet 70% field setting. Each plot is generated with a different model for the background shape. Plots similar to these are generated for each kinematic and magnetic field setting to be used to quantify the systematic uncertainty due to the inelastic contamination.

For supplementary information and plots pertaining to the study of the inelastic contamination see Ref. [179]. The systematic uncertainty due to inelastic contamination will be treated as uncorrelated between SBS-8 and SBS-9 for this analysis. If one calculated the standard deviations, for a particular setting, of the values listed in Tab. 6.5, these would be the systematic uncertainty of $R_{sf}^{n/p}$ associated with the inelastic contamination. The systematic uncertainties of $R_{sf}^{n/p}$ will be described and presented in Sec. 6.4.4.

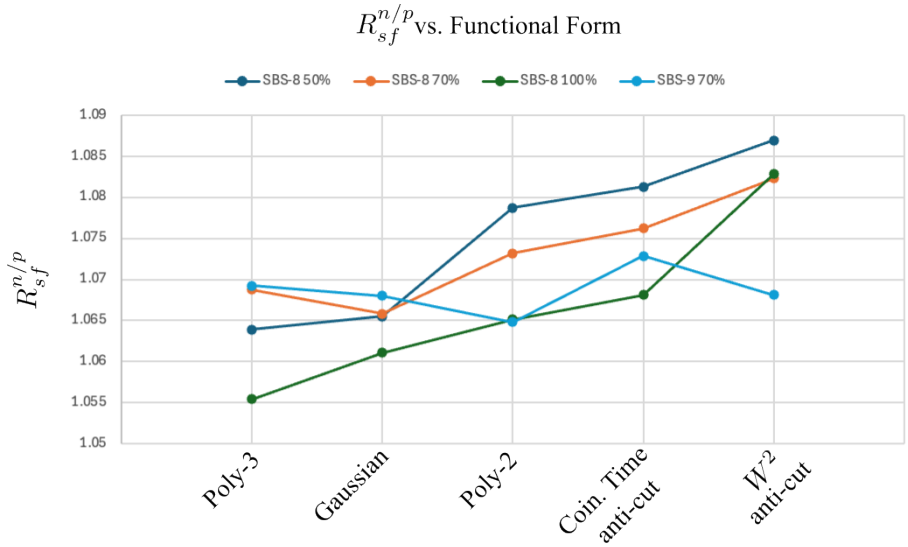

Figure 6.41: A plot of $R_{sf}^{n/p}$ values for a given kinematic, only considering SBS-8 and SBS-9, and SBS magnet field settings for each technique for modeling the background shape.

Bkgd Model	$R_{sf}^{n/p}$ value			
	SBS-8 50%	SBS-8 70%	SBS-8 100%	SBS-9 70%
Gaussian	1.066	1.066	1.061	1.068
Polynomial-2	1.079	1.073	1.065	1.065
Polynomial-3	1.064	1.069	1.055	1.069
Δt Anti-Cut	1.081	1.076	1.068	1.073
W^2 Anti-Cut	1.087	1.082	1.083	1.068

Table 6.5: A table showing the extracted $R_{sf}^{n/p}$ values corresponding to the different background functional forms, for the SBS-8 and SBS-9 kinematic and SBS magnet field settings relevant for this analysis.

6.4.4 Final $R_{sf}^{n/p}$ Values and Uncertainties

The $R_{sf}^{n/p}$ values for each SBS-8 or SBS-9 kinematic and SBS magnet setting are extracted using the Δx data/MC comparison technique, described in Sec. 6.4.1. The visualizations for each Δx data/MC comparison are presented in Fig. 6.42 and the corresponding extracted $R_{sf}^{n/p}$ values are summarized in Tab. 6.6. Table 6.6 also presents the respective total, statistical, and systematic uncertainties addressed in this dissertation. The value of the total uncertainty on $R_{sf}^{n/p}$ is taken as the quadrature sum of the respective statistical and systematic uncertainties. The optimized cut regions used in extracting these $R_{sf}^{n/p}$ values are summarized in Tab. 6.3. For each Δx data/MC comparison used to extract $R_{sf}^{n/p}$ a Polynomial-2 background functional form is used for final extraction.

The statistical uncertainty on $R_{sf}^{n/p}$, $\Delta\left(R_{sf}^{n/p}\right)_{\text{stat}}$, is directly determined from the fit parameter uncertainty as calculate by the ROOT software. Histograms in ROOT, by default, are fit with a particular functional form using a statistical minimum χ^2 estimation and generate a covariance matrix representing correlations between fit parameters. The standard error on a given fit parameter is calculated as the square-root of the corresponding diagonal element of the covariance matrix. The statistical uncertainty on $R_{sf}^{n/p}$ only reflects statistical fluctuations with the experimental data. For this analysis, no methods are adopted to estimate effects from MC statistics. For all data/MC comparisons conducted in this analysis, the χ^2/ndf of the total fit is not perfectly one; if MC statistics were included in the estimation of the total statistical uncertainty on $R_{sf}^{n/p}$ this would likely improve the overall χ^2/ndf. Studies were conducted by the author of Ref. [125] to estimate contributions to the overall statistical uncertainty from statistical fluctuations from simulated events; these contributions were found to have relatively small values. In principle, and likely for future extractions, sets of MC simulated events will be generated with high-enough statistics so contributions from the MC to the statistical uncertainty on $R_{sf}^{n/p}$ are negligible.

The systematic uncertainty budget for the analysis presented in this dissertation is

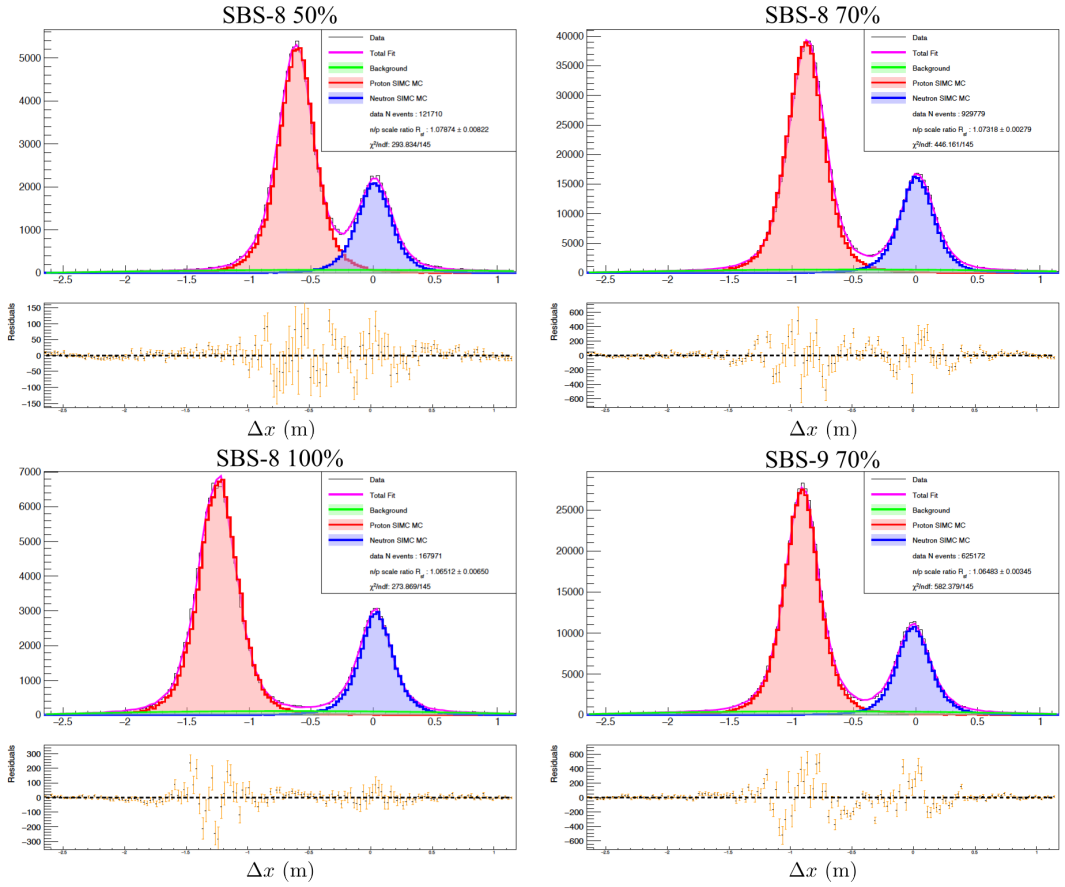

Figure 6.42: Δx Data/MC comparisons used for extracting $R_{sf}^{n/p}$ from all relevant kinematic and SBS magnet settings for this analysis.

Setting	$R_{sf}^{n/p}$	$\Delta\left(R_{sf}^{n/p}\right)_{\text{total}}$	$\Delta\left(R_{sf}^{n/p}\right)_{\text{stat}}$	$\Delta\left(R_{sf}^{n/p}\right)_{\text{sys}}$
SBS-8 50%	1.079	0.015	0.008	0.013
SBS-8 70%	1.073	0.011	0.003	0.011
SBS-8 100%	1.065	0.013	0.007	0.012
SBS-9 70%	1.065	0.009	0.003	0.008

Table 6.6: Extracted $R_{sf}^{n/p}$ values and uncertainties for each relevant SBS-8 and SBS-9 kinematic and SBS magnet setting.

summarized in Tab. 6.7. The sources contributing to the systematic uncertainty include HCal detection efficiency non-uniformity, cut stability, and inelastic contamination from background processes. The method for addressing systematic uncertainties due to HCal detection efficiency non-uniformity is described in Sec. 6.3. The systematic uncertainty

contributions for each cut variable are summarized in Tab. 6.4. The systematic uncertainty on $R_{sf}^{n/p}$ due to the inelastic contamination, for a given kinematic and SBS magnet setting, is taken as the standard deviation of the corresponding values presented in Tab. 6.5. This systematic uncertainty budget is not exhaustive and further study quantifying uncertainties on $R_{sf}^{n/p}$ from nuclear effects (final-state-interactions), radiative corrections, effects associated with absolute HCal nucleon detection efficiencies is necessary to provide the most complete evaluation. A proper assessment of any discrepancies in absolute HCal nucleon detection efficiencies between data and MC is essential, and is anticipated to contribute as an important systematic effect. It is anticipated that absolute HCal nucleon detection efficiency effects will largely cancel in the neutron Rosenbluth slope extraction.

	Uncertainty Source	Setting			
		SBS-8 50%	SBS-8 70%	SBS-8 100%	SBS-9 70%
$\Delta\left(R_{sf}^{n/p}\right)_{\text{sys}}$	HDENU	0.0003	0.0018	0.0012	0.0053
	Cut S.	0.0078	0.0083	0.0052	0.0054
	Ine. Con.	0.0101	0.0065	0.0103	0.0029
	Total	0.0128	0.0106	0.0116	0.0081

Table 6.7: Systematic Uncertainty Budget for for each relevant SBS-8 and SBS-9 kinematic and SBS magnet setting. The sources of systematic uncertainties consider in this dissertation include: HCal detection efficiency non-uniformity ("HDENU"), cut stability ("Cut S."), and inelastic contamination from background processes ("Ine. Con.").

6.4.5 Weighted Mean Analysis for SBS-8 $R_{sf}^{n/p}$ Values and Uncertainties

A weighted mean analysis was performed on the extracted experimental observables for the SBS-8 kinematic data sets. It is important, when considering the uncertainty propagation during a weighted mean analysis, to separate uncertainties into two categories as either uncorrelated or correlated uncertainties. For this analysis the uncertainties on $R_{sf}^{n/p}$ due to statistics, HCal detection efficiency non-uniformity, and cut stability are treated as uncorrelated among the respective SBS magnet settings within the SBS-8 kinematic. The statistical uncertainty on $R_{sf}^{n/p}$ is clearly uncorrelated as each SBS magnet setting for the SBS-8 kinematic are analyzed from different sets of experimental data and simulated events.

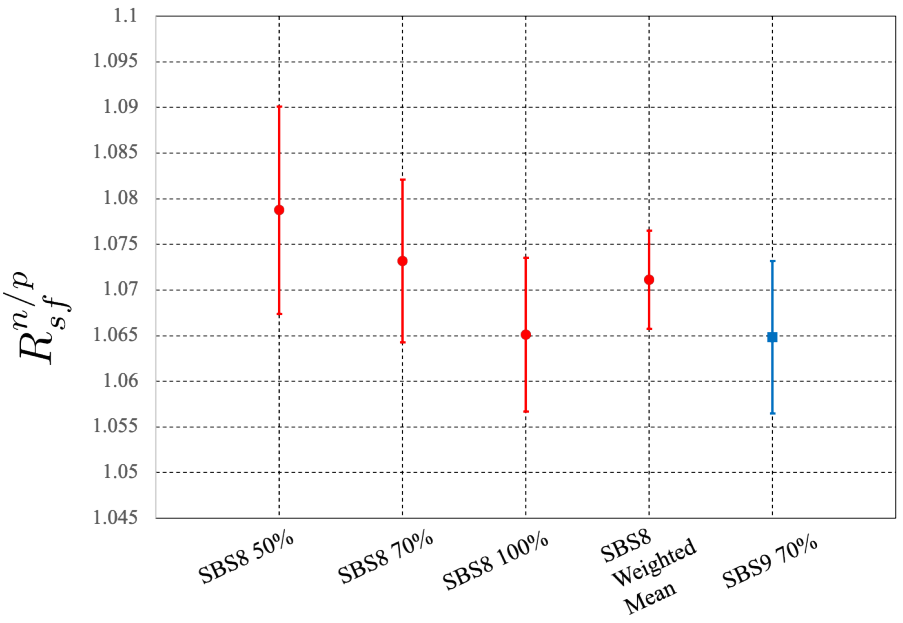

Figure 6.43: $R_{sf}^{n/p}$ for each relevant analysis setting. The SBS-8 kinematic and SBS magnet setting and the weighted mean values are presented as red circles. The SBS-9 70% setting is presented as a blue square. In this graph the error bars represent only uncorrelated uncertainties. It is evident from this graph that the SBS-8 and SBS-9 $R_{sf}^{n/p}$ agree within 1 standard deviation of the respective uncorrelated uncertainties.

The extracted values of $R_{sf}^{n/p}$ used for evaluating effects of HCal detection efficiency non-uniformity demonstrate no definitive trends and are treated as uncorrelated. Since the cut stability regions and the associated systematic effects are evaluated independently for each SBS magnet setting of the SBS-8 kinematic, the systematic uncertainty due to cut stability is treated as uncorrelated. The systematic uncertainty due to inelastic contamination from background processes is treated as a correlated uncertainty, as suggested by Fig. 6.41.

The weighted mean of $R_{sf}^{n/p}$ for the SBS-8 kinematic is calculated by the relation

$$\overline{R}_{sf}^{n/p} = \frac{\sum_{i=1}^{3} R_{sf,i}^{n/p} w_i}{\sum_{i=1}^{3} w_i}, \tag{6.45}$$

where $R_{sf,i}^{n/p}$ represents the extracted experimental observable, and w_i is the weight defined

by

$$w_i = \frac{1}{\sigma^2_{\text{uncorr,i}}}, \tag{6.46}$$

respectively, for a particular SBS magnet setting of the SBS-8 kinematic. In Eq. 6.46, $\sigma^2_{\text{uncorr,i}}$ represents the quadrature sum of the uncorrelated uncertainties for a given SBS magnet setting of the SBS-8 kinematic, as described in this section. The uncertainty on the weighted mean due to uncorrelated uncertainties is calculated by

$$\left(\Delta\left(\overline{R}^{n/p}_{sf}\right)_{\text{uncorr}}\right)^2 = \frac{1}{\sum_{i=1}^{3} w_i}. \tag{6.47}$$

Estimating the uncertainty on the weighted mean due to correlated uncertainties is non-trivial, and as such the following procedure is used:

1. For each data set corresponding to a particular SBS magnet setting of the SBS-8 kinematic, add the value of the correlated uncertainty to the extracted observable as follows

$$\left(R^{n/p}_{sf}\right)^{+1}_{i} = R^{n/p}_{sf,i} + \sigma_{\text{corr,i}}. \tag{6.48}$$

2. Calculate a new weighted mean using Eq. 6.45, from the $\left(R^{n/p}_{sf}\right)^{+1}_{i}$ values in the previous step. Denote this new weighted mean as $\left(\overline{R}^{n/p}_{sf}\right)^{+1}$.

3. The correlated uncertainty on the weighted mean is calculated as the absolute value of the difference between $\left(\overline{R}^{n/p}_{sf}\right)^{+1}$ and $\overline{R}^{n/p}_{sf}$:

$$\Delta\left(\overline{R}^{n/p}_{sf}\right)_{\text{corr}} = \left|\left(\overline{R}^{n/p}_{sf}\right)^{+1} - \overline{R}^{n/p}_{sf}\right|. \tag{6.49}$$

4. Steps 1. through 3. are repeated to instead evaluate the condition of subtracting the correlated uncertainty:

$$\left(R^{n/p}_{sf}\right)^{-1}_{i} = R^{n/p}_{sf,i} - \sigma_{\text{corr,i}}. \tag{6.50}$$

Similarly, this obtains a separate new weighted mean, $\left(\overline{R}^{n/p}_{sf}\right)^{-1}$, which when compared to $\overline{R}^{n/p}_{sf}$, obtains an identical value for $\Delta\left(\overline{R}^{n/p}_{sf}\right)_{\text{corr}}$.

The total uncertainty on the weighted mean is taken as the quadrature sum of the uncorrelated and correlated uncertainties of the weighted mean, Eqs. 6.47 and 6.49 respectively, represented by the relation

$$\Delta\left(\overline{R}_{sf}^{n/p}\right)_{\text{total}} = \sqrt{\left(\Delta\left(\overline{R}_{sf}^{n/p}\right)_{\text{uncorr}}\right)^2 + \left(\Delta\left(\overline{R}_{sf}^{n/p}\right)_{\text{corr}}\right)^2}. \tag{6.51}$$

The values for the SBS-8 kinematic $R_{sf}^{n/p}$ weighted mean, and total, uncorrelated, and correlated uncertainties, respectively, are summarized in Tab. 6.8. The $R_{sf}^{n/p}$ values for the relevant analysis settings, as well as the $R_{sf}^{n/p}$ weighted mean are presented in Fig. 6.43; the error bars represent only the uncorrelated uncertainties. From Tab. 6.8 it is clear that the majority of the total uncertainty is attributed to the correlated uncertainty. The total uncertainty on the SBS-8 kinematic $R_{sf}^{n/p}$ weighted mean is smaller than that for the highest-statistics data set (SBS-8 70%) for the SBS-8 kinematic. Since the weighted mean analysis results in a smaller total uncertainty, the SBS-8 kinematic $R_{sf}^{n/p}$ weighted mean and total uncertainty will be used for determining physics results, which are presented in Chapter 7.

	$\overline{R}_{sf}^{n/p}$	$\Delta\left(\overline{R}_{sf}^{n/p}\right)_{\text{total}}$	$\Delta\left(\overline{R}_{sf}^{n/p}\right)_{\text{uncorr}}$	$\Delta\left(\overline{R}_{sf}^{n/p}\right)_{\text{corr}}$
Value for SBS-8	1.0711	0.0104	0.0054	0.0089

Table 6.8: Weighted mean of $R_{sf}^{n/p}$ values and uncertainties for the SBS-8 kinematic setting.

Chapter 7

Results & Conclusions

7.1 Extraction of R' Values from $R_{sf}^{n/p}$

Setting	R'	$\Delta(R')_{\text{total}}$	$\Delta(R')_{\text{stat}}$	$\Delta(R')_{\text{sys}}$
SBS-8 50%	0.3936	0.0055	0.0030	0.0047
SBS-8 70%	0.3916	0.0040	0.0010	0.0039
SBS-8 100%	0.3886	0.0049	0.0024	0.0042
SBS-9 70%	0.3875	0.0032	0.0013	0.0030

Table 7.1: Extracted R' values and uncertainties for each relevant SBS-8 and SBS-9 kinematic and SBS magnet setting.

The physics observables for this dissertation include the neutron magnetic form factor, G_M^n, and the neutron Rosenbluth slope S^n. The respective extractions of each physics observable requires a determination of the elastic electron-neutron to electron-proton scattering cross-section ratio, denoted R'. As described in Sec 6.4.1, within the specified conditions, the experimental values for R' are determined from Eq. 6.44, for a given kinematic and SBS magnet setting. The $R_{sf}^{n/p}$ values and uncertainties are presented in Sec. 6.4.4 and summarized in Tab. 6.6. For given values of Q^2 and ϵ, the ratio of neutron to proton elastic cross-sections, as implemented by the MC event generators, denoted R'_{sim}, is determined from the parameterizations of the nucleon electromagnetic form factors used by the simulation. The value of G_E^n is parameterized using the Hall A G_E^n Collaboration fit

[72]. The remaining nucleon electromagnetic form factors: G_E^p, G_M^p, and G_M^n are parameterized from the Kelly Fit, as described in Sec. 2.5.1. By recreating R'_{sim} values identical to the MC generators and scaling these values with the respective $R_{sf}^{n/p}$, we can determine experimental R' values. Table 7.1 summarizes the experimental elastic electron-neutron to electron-proton scattering cross-section ratio values and uncertainties, for each relevant analysis setting. Each uncertainty associated with R' is propagated from the corresponding uncertainty on $R_{sf}^{n/p}$ by

$$\Delta\left(R'\right) = R'_{\text{sim}} \cdot \Delta\left(R_{sf}^{n/p}\right). \tag{7.1}$$

Similarly, from Eq. 6.44, the SBS-8 kinematic $R_{sf}^{n/p}$ weighted mean will be used to extract an R' value. The R' value, total, uncorrelated, and correlated uncertainties are presented in Tab. 7.2.

	$\overline{R}'$	$\Delta\left(\overline{R}'\right)_{\text{total}}$	$\Delta\left(\overline{R}'\right)_{\text{uncorr}}$	$\Delta\left(\overline{R}'\right)_{\text{corr}}$
Value for SBS-8	0.3908	0.0038	0.0020	0.0032

Table 7.2: R' value and uncertainty for the weighted mean of the SBS-8 kinematic setting.

Acceptance-Averaged Kinematic Quantities

Kine	E_{Beam} (GeV)	$\langle Q^2 \rangle$ (GeV/c)^2	$\langle \epsilon \rangle$	$\langle \theta_e \rangle$ (rad)	$\langle \theta_e \rangle$	$\langle p_N \rangle$ (GeV/c)
SBS-8	5.975	4.48	0.799	0.4619	26.47°	3.192
SBS-9	4.019	4.476	0.518	0.8506	48.74°	3.186

Table 7.3: Acceptance-averaged kinematic quantities for SBS-8 and SBS-9.

For a given kinematic of the G_M^n and nTPE experiments, event-by-event distributions of the quantities Q^2, ϵ, θ_e, and p_N can be produced. The distributions of these kinematic quantities have a definite range, due to the acceptances of the BigBite and Super BigBite spectrometers. Figures 7.1 and 7.2 present the distributions for these quantities from the SBS-8 70% and SBS-9 70% kinematic and SBS magnet settings, respectively. For the

extractions of elastic neutron to proton cross-section ratios, R' values, acceptance-averaged values of kinematic quantities are used. These are determined by taking the average value of the distribution for all events passing the final event selection criteria. The acceptance-averaged quantities, denoted with $\langle\rangle$, are summarized in Tab. 7.3.

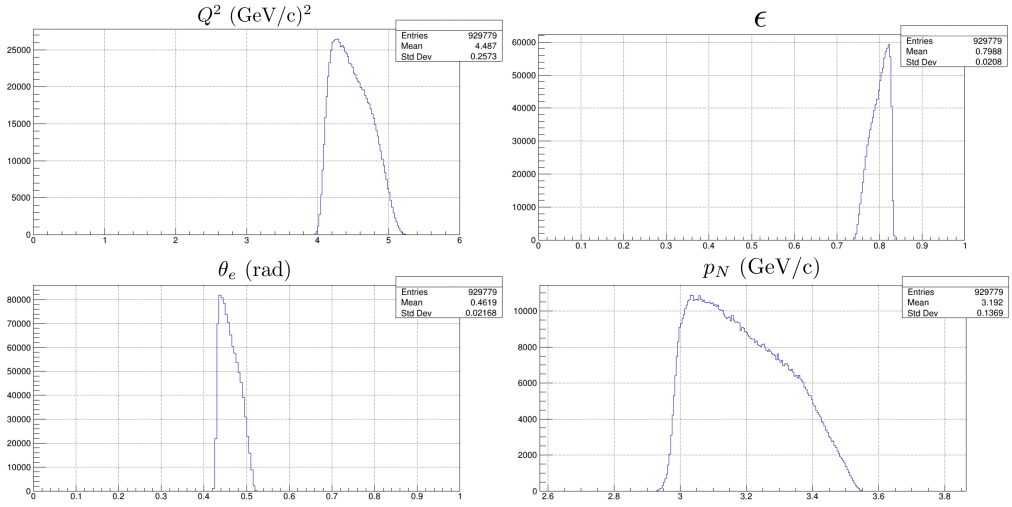

Figure 7.1: Distributions for the kinematic quantities: Q^2, ϵ, θ_e, and p_N produced from the data set corresponding to the SBS-8 kinematic and 70% SBS magnet setting. All event selection criteria, as described in Secs. 6.2 and 6.4.2, are applied to these distributions. The other SBS magnet settings from the SBS-8 kinematic show very similar distributions for these kinematic quantities.

7.2 Extraction of G_M^n from R'

7.2.1 G_M^n Extraction Formalism

The method for extracting the neutron magnetic form factor, G_M^n, is presented in Sec. 3.2.2 of this dissertation and ultimately leads to Eq. 3.5. We can update Eq. 3.5 to incorporate Eq. 6.44 and directly present G_M^n in terms of experimental observables as

$$\begin{aligned} G_M^n &= \sqrt{R' \times \frac{\epsilon_n(1+\tau_n)}{\tau_n}\frac{\tau_p}{\epsilon_p(1+\tau_p)}\left(\frac{d\sigma}{d\Omega}\right)_{\text{reduced,p}} - \frac{\epsilon_n}{\tau_n}\left(G_E^n\right)^2}. \\ &= \sqrt{R_{sf}^{n/p}R'_{\text{sim}} \times \frac{\epsilon_n(1+\tau_n)}{\tau_n}\frac{\tau_p}{\epsilon_p(1+\tau_p)}\left(\frac{d\sigma}{d\Omega}\right)_{\text{reduced,p}} - \frac{\epsilon_n}{\tau_n}\left(G_E^n\right)^2}. \end{aligned} \tag{7.2}$$

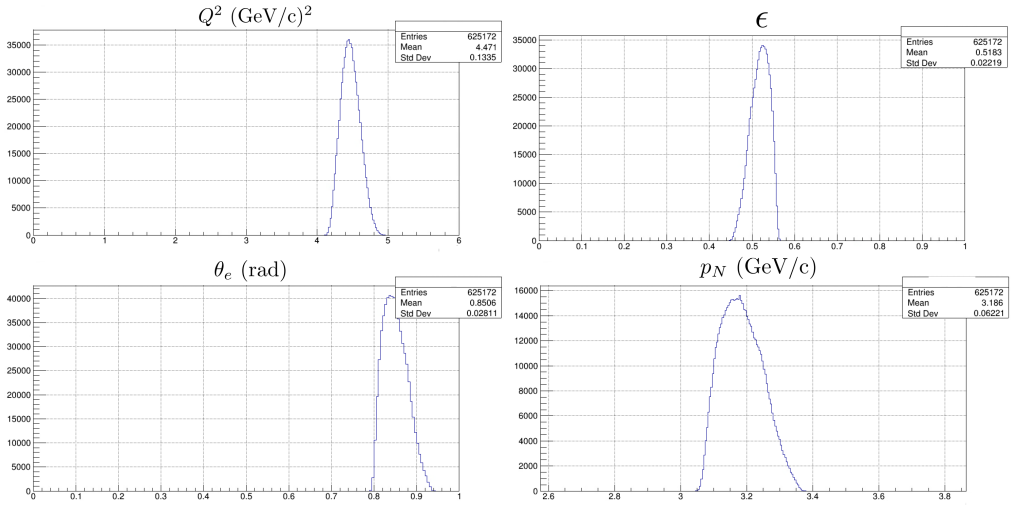

Figure 7.2: Distributions for the kinematic quantities: Q^2, ϵ, θ_e, and p_N produced from the data set corresponding to the SBS-9 kinematic and 70% SBS magnet setting. All event selection criteria, as described in Secs. 6.2 and 6.4.2, are applied to these distributions.

For the terms presented in Eq. 7.2, for a given data set, R' will be one of the values in Sec. 7.1, the reduced proton cross-section, $\left(\frac{d\sigma}{d\Omega}\right)_{\text{reduced,p}}$, and G_E^n will calculated from available parameterizations to the nucleon electromagnetic form factor world data. The Ye *et al.* [31] parameterization was used to determine values for $\left(\frac{d\sigma}{d\Omega}\right)_{\text{reduced,p}}$, in the form of Eq. 2.11, and G_E^n. Any ϵ or τ terms will be determined from acceptance-averaged kinematic quantities.

7.2.2 G_M^n Uncertainty Propagation

The value of R' was empirically extracted from the data analysis in this dissertation, as such it is independent of the Ye *et al.* parameterization. For the Ye *et al.* parameterization, the fits to the world data for the proton electric and magnetic form factors are known to be correlated and represented by a covariance matrix. The extraction of the fits to the world data for the individual neutron electric and magnetic form factors is conducted in an uncorrelated manner, as such the individual neutron form factors can be considered independent of one another. Moreover, the individual neutron electric and magnetic form factors can be considered independent of the proton form factors. Given these documented

conditions of the Ye *et al.* parameterization, the uncertainty on the extracted neutron magnetic form factor, ΔG_M^n is the relation

$$\Delta G_M^n = \sqrt{\left(\frac{\partial G_M^n}{\partial R'}\Delta R'\right)^2 + \left(\frac{\partial G_M^n}{\partial \sigma_{\text{reduced,p}}}\Delta\sigma_{\text{reduced,p}}\right)^2 + \left(\frac{\partial G_M^n}{\partial G_E^n}\Delta G_E^n\right)^2}, \tag{7.3}$$

where $\sigma_{\text{reduced,p}}$ is a short-hand notation for $\left(\frac{d\sigma}{d\Omega}\right)_{\text{reduced,p}}$. For each term in ΔG_M^n we can evaluate each partial derivative as follows

$$\frac{\partial G_M^n}{\partial R'} = \frac{\epsilon_n(1+\tau_n)}{\tau_n}\frac{\tau_p}{\epsilon_p(1+\tau_p)}\left(\frac{d\sigma}{d\Omega}\right)_{\text{reduced,p}}\frac{1}{2G_M^n}, \tag{7.4}$$

$$\frac{\partial G_M^n}{\partial \sigma_{\text{reduced,p}}} = \frac{\epsilon_n(1+\tau_n)}{\tau_n}\frac{\tau_p}{\epsilon_p(1+\tau_p)}R'\frac{1}{2G_M^n}, \tag{7.5}$$

and

$$\frac{\partial G_M^n}{\partial G_E^n} = -\frac{\epsilon_n}{\tau_n}\frac{G_E^n}{G_M^n}. \tag{7.6}$$

The uncertainty on the extracted elastic neutron-to-proton cross-section ratio, $\Delta R'$, corresponding to each relevant analysis setting has been presented in Sec. 7.1. The uncertainty on the proton reduced cross-section, $\Delta\sigma_{\text{reduced,p}}$, is calculated by propagating individual parameterization uncertainties on G_E^p and G_M^p with Eq. 2.11. This uncertainty propagation assumes that the two proton form factors are uncorrelated, which is not the most accurate representation as the Ye *et al.* parameterization describes the fitting process for the proton form factors as correlated, without providing a covariance matrix. Treating the uncertainties on G_E^p and G_M^p as uncorrelated slightly increases the uncertainty on the proton reduced cross-section. The uncertainty on the neutron electric form factor, ΔG_E^n, was directly taken as the parameterization uncertainty provided by Ye *et al.*. By appropriately combining the respective partial derivatives and quantity uncertainties, as described in Eq. 7.3, we can reasonably estimate the value for ΔG_M^n.

7.2.3 Neutron Magnetic Form Factor Preliminary Results

The preliminary values and uncertainties for $G_M^n/\mu_n G_D$ extracted from the data analysis presented in this dissertation are shown in Tab. 7.4. Fig. 7.3 shows a plot of the existing $G_M^n/\mu_n G_D$ world data with the preliminary results extracted from the analysis in this dissertation superimposed. A zoomed-in version of Fig. 7.3 is presented as Fig. 7.4, which allows for a more straightforward depiction of the preliminary $G_M^n/\mu_n G_D$ results.

Setting	$\langle Q^2 \rangle$	$\frac{G_M^n}{\mu_n G_D}$	$\Delta\left(\frac{G_M^n}{\mu_n G_D}\right)_{\text{total}}$	$\Delta\left(\frac{G_M^n}{\mu_n G_D}\right)_{\text{stat}}$	$\Delta\left(\frac{G_M^n}{\mu_n G_D}\right)_{\text{sys}}$
SBS-8 50%	4.48	0.958	0.014	0.004	0.014
SBS-8 70%	4.48	0.956	0.013	0.001	0.013
SBS-8 100%	4.48	0.952	0.014	0.003	0.014
SBS-8 Weighted Mean	4.48	0.955	0.013	0.001	0.013
SBS-9 70%	4.476	0.956	0.011	0.002	0.011

Table 7.4: Extracted preliminary $G_M^n/\mu_n G_D$ values and uncertainties for each relevant SBS-8 and SBS-9 kinematic and SBS magnet setting.

7.3 Extraction of Neutron Rosenbluth Slope from R'

7.3.1 Neutron Rosenbluth Slope Extraction Formalism

The technique for extracting the neutron Rosenbluth slope is described in Sec. 3.2.3 and culminates to the relation presented in Eq. 3.19. For ease of understanding, we will restate Eq. 3.19, and present a version which incorporates Eq. 6.44 to write it in terms of

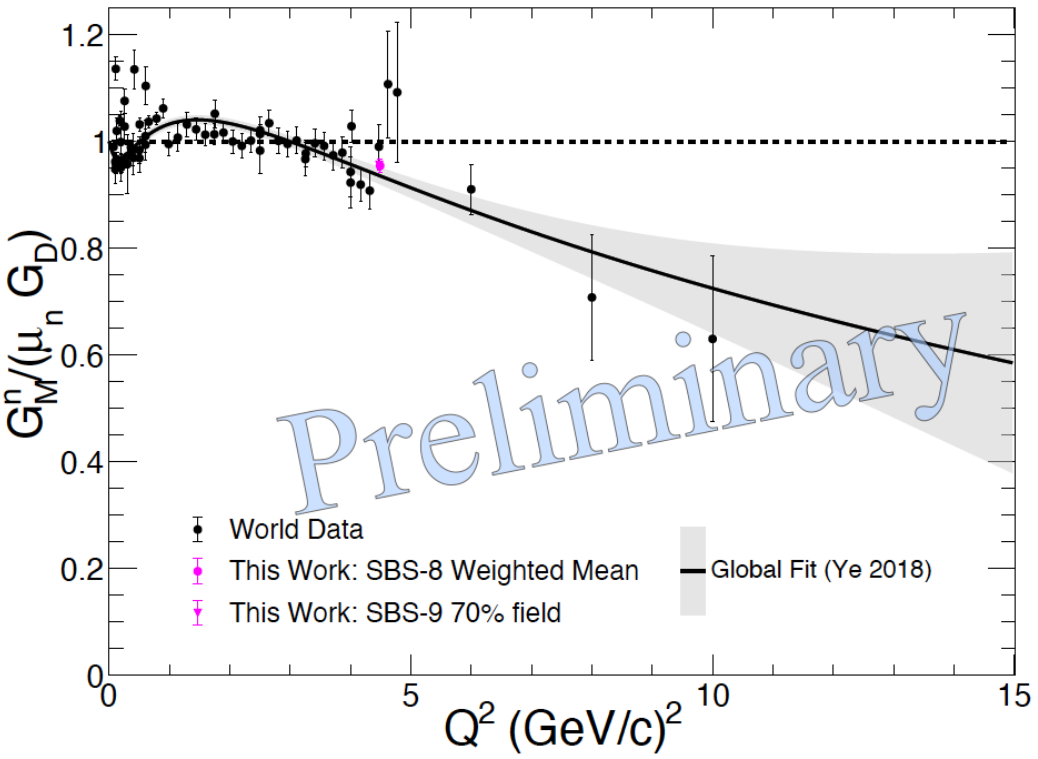

Figure 7.3: $G_M^n/\mu_n G_D$ world data along with the preliminary results extracted in this dissertation, represented by a magenta circle and magenta inverted triangle. Our preliminary values do not include any corrections for any two-photon exchange effects. The world plot is adapted from Ref. [28]. The global fit to the world data is from Ref. [31], and the details of the parameterization are summarized in Sec. 2.5.1.

experimental observables

$$
\begin{aligned}
S^n &= \frac{1}{\Delta\epsilon}\frac{\frac{\tau_{p,\epsilon_1}}{\epsilon_{1,p}(1+\tau_{p,\epsilon_1})}}{\frac{\tau_{n,\epsilon_1}}{\epsilon_{1,n}(1+\tau_{n,\epsilon_1})}}\frac{\frac{\tau_{n,\epsilon_2}}{\epsilon_{2,n}(1+\tau_{n,\epsilon_2})}}{\frac{\tau_{p,\epsilon_2}}{\epsilon_{2,p}(1+\tau_{p,\epsilon_2})}}\frac{\sigma^p_{T,\epsilon_1}}{\sigma^n_{T,\epsilon_1}}\frac{\sigma^n_{T,\epsilon_2}}{\sigma^p_{T,\epsilon_2}}\frac{1+\epsilon_{1,p}S^p_{\epsilon_1}}{1+\epsilon_{2,p}S^p_{\epsilon_2}} \\
&\left(\frac{R'_{\epsilon_1}}{R'_{\epsilon_2}} - \frac{\frac{\tau_{n,\epsilon_1}}{\epsilon_{1,n}(1+\tau_{n,\epsilon_1})}}{\frac{\tau_{p,\epsilon_1}}{\epsilon_{1,p}(1+\tau_{p,\epsilon_1})}}\frac{\frac{\tau_{p,\epsilon_2}}{\epsilon_{2,p}(1+\tau_{p,\epsilon_2})}}{\frac{\tau_{n,\epsilon_2}}{\epsilon_{2,n}(1+\tau_{n,\epsilon_2})}}\frac{\sigma^n_{T,\epsilon_1}}{\sigma^p_{T,\epsilon_1}}\frac{\sigma^p_{T,\epsilon_2}}{\sigma^n_{T,\epsilon_2}}\frac{1+\epsilon_{2,p}S^p_{\epsilon_2}}{1+\epsilon_{1,p}S^p_{\epsilon_1}}\right), \\
&= \frac{1}{\Delta\epsilon}\frac{\frac{\tau_{p,\epsilon_1}}{\epsilon_{1,p}(1+\tau_{p,\epsilon_1})}}{\frac{\tau_{n,\epsilon_1}}{\epsilon_{1,n}(1+\tau_{n,\epsilon_1})}}\frac{\frac{\tau_{n,\epsilon_2}}{\epsilon_{2,n}(1+\tau_{n,\epsilon_2})}}{\frac{\tau_{p,\epsilon_2}}{\epsilon_{2,p}(1+\tau_{p,\epsilon_2})}}\frac{\sigma^p_{T,\epsilon_1}}{\sigma^n_{T,\epsilon_1}}\frac{\sigma^n_{T,\epsilon_2}}{\sigma^p_{T,\epsilon_2}}\frac{1+\epsilon_{1,p}S^p_{\epsilon_1}}{1+\epsilon_{2,p}S^p_{\epsilon_2}} \\
&\left(\frac{\left(R^{n/p}_{sf}\right)_{\epsilon_1}\left(R'_{\text{sim}}\right)_{\epsilon_1}}{\left(R^{n/p}_{sf}\right)_{\epsilon_2}\left(R'_{\text{sim}}\right)_{\epsilon_2}} - \frac{\frac{\tau_{n,\epsilon_1}}{\epsilon_{1,n}(1+\tau_{n,\epsilon_1})}}{\frac{\tau_{p,\epsilon_1}}{\epsilon_{1,p}(1+\tau_{p,\epsilon_1})}}\frac{\frac{\tau_{p,\epsilon_2}}{\epsilon_{2,p}(1+\tau_{p,\epsilon_2})}}{\frac{\tau_{n,\epsilon_2}}{\epsilon_{2,n}(1+\tau_{n,\epsilon_2})}}\frac{\sigma^n_{T,\epsilon_1}}{\sigma^p_{T,\epsilon_1}}\frac{\sigma^p_{T,\epsilon_2}}{\sigma^n_{T,\epsilon_2}}\frac{1+\epsilon_{2,p}S^p_{\epsilon_2}}{1+\epsilon_{1,p}S^p_{\epsilon_1}}\right).
\end{aligned}
\tag{7.7}
$$

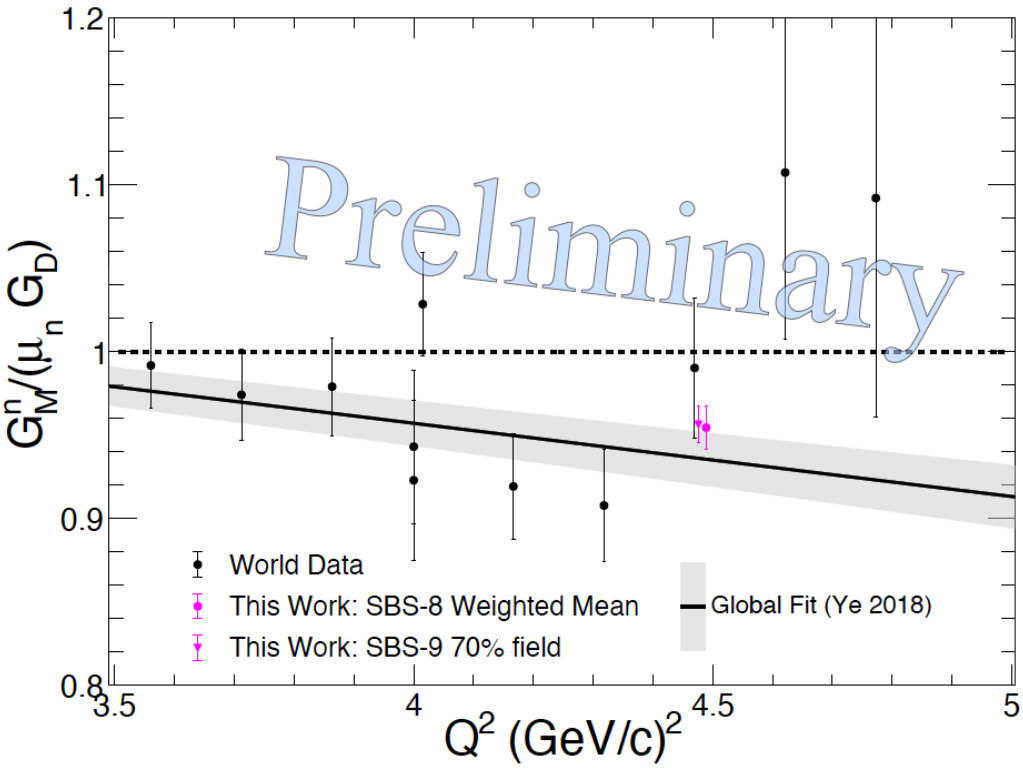

Figure 7.4: Zoomed-in $G_M^n/\mu_n G_D$ plot, including some world data along with the preliminary results extracted in this dissertation, represented by a magenta circle and magenta inverted triangle. Our preliminary values do not include any corrections for any two-photon exchange effects. The world plot is adapted from Ref. [28]. The global fit to the world data is from Ref. [31], and the details of the parameterization are summarized in Sec. 2.5.1.

However, the form in which S^n is presented in Eq. 7.7 is not ideal for explaining the extraction process. As such, we will now introduce (or reintroduce) terms to present S^n in an equivalent form which allows a more straightforward description of the extraction of preliminary results. The "super-ratio" quantity A was defined in Eq. 3.11 as the ratio of the individual elastic electron-neutron to electron-proton cross-sections at the same value of Q^2 and the two different values of the virtual photon polarization, denoted ϵ_1 and ϵ_2. The "super-ratio" quantity A will be incorporated in this new representation of S^n and A

is restated here, for clarity, as

$$A \equiv \frac{R'_{\epsilon_1}}{R'_{\epsilon_2}} = \frac{\left(R_{sf}^{n/p}\right)_{\epsilon_1} \left(R'_{\text{sim}}\right)_{\epsilon_1}}{\left(R_{sf}^{n/p}\right)_{\epsilon_2} \left(R'_{\text{sim}}\right)_{\epsilon_2}}. \tag{7.8}$$

For extraction of the neutron Rosenbluth slope, it is important to note that the empirical contribution from this data analysis is encapsulated in the super-ratio quantity A. The value for super-ratio A will be directly determined from values of extracted elastic neutron to proton cross-section ratios, which are summarized in Sec. 7.1, and its determination will be presented later in this section. We will now introduce a quantity, denoted as B, which encompasses the $\tau_{n,\epsilon_1(\epsilon_2)}$ and $\tau_{p,\epsilon_1(\epsilon_2)}$ ratio terms, the transverse cross-section ratio terms, and the proton Rosenbluth slope terms, and is defined as

$$B \equiv \frac{\frac{\tau_{n,\epsilon_1}}{\epsilon_{1,n}(1+\tau_{n,\epsilon_1})}}{\frac{\tau_{p,\epsilon_1}}{\epsilon_{1,p}(1+\tau_{p,\epsilon_1})}} \frac{\frac{\tau_{p,\epsilon_2}}{\epsilon_{2,p}(1+\tau_{p,\epsilon_2})}}{\frac{\tau_{n,\epsilon_2}}{\epsilon_{2,n}(1+\tau_{n,\epsilon_2})}} \frac{\sigma_{T,\epsilon_1}^{n}}{\sigma_{T,\epsilon_1}^{p}} \frac{\sigma_{T,\epsilon_2}^{p}}{\sigma_{T,\epsilon_2}^{n}} \frac{1+\epsilon_{2,p}S_{\epsilon_2}^{p}}{1+\epsilon_{1,p}S_{\epsilon_1}^{p}}. \tag{7.9}$$

It is important to note that if the value of Q^2 was exactly the same between data sets for the two different cross-section ratios R'_{ϵ_1} and R'_{ϵ_2}, the τ ratio terms and the transverse cross-section ratio terms would be exactly identical and as such would individually approach unity in the quantity B. However, as described Sec. 7.1, the value of $\langle Q^2 \rangle$ is not exactly identical between the SBS-8 and SBS-9 kinematics. As such, the τ ratio terms and the transverse cross-section ratio terms in B will be retained in this extraction and a value-determination will be provided. Additionally, values for the transverse cross-section ratio and the proton Rosenbluth slope terms of B will not be determined from experimental observables extracted from this data analysis. Rather, the values for these specific terms of B will be calculated from the most recent parameterizations to the world data for the nucleon electromagnetic form factors. The $\Delta\epsilon$ term in Eq. 7.8, will remain as it was defined in Sec. 3.2.3; for convenience it is restated here as

$$\Delta\epsilon = \epsilon_{1,n} - \epsilon_{2,n}. \tag{7.10}$$

By restating the super-ratio A and the $\Delta\epsilon$ terms from Sec. 3.2.3, and defining the quantity B we can provide an equivalent representation of S^n as follows

$$S^n = \frac{(A - B)}{B\Delta\epsilon}. \tag{7.11}$$

The version of S^n in Eq. 7.11 will be used when describing the value-determination of preliminary results and for discussions of uncertainty propagation.

7.3.2 Neutron Rosenbluth Slope Uncertainty Propagation

The value of the super-ratio A will be determined from empirically extracted observables from the data analysis in this dissertation, which were presented in Sec. 7.1. The values contributing to the quantity B will be calculated from known parameterizations of the nucleon electromagnetic form factor world data. Given these two conditions, it is evident that respective components of A and B are independent of one another. The uncertainty propagation on S^n will be conducted using an independent parameter analysis. The $\Delta\epsilon$ term is taken to be known sufficiently, from individual acceptance-averaged values of ϵ, such that any variation on $\Delta\epsilon$ does not introduce a significant relative variation on S^n, compared to the uncertainties associated with A and B (i.e. ΔA and ΔB). From the described considerations, the uncertainty on S^n will be calculated from the relation

$$\Delta S^n = \sqrt{\left(\frac{\partial S^n}{\partial A}\Delta A\right)^2 + \left(\frac{\partial S^n}{\partial B}\Delta B\right)^2} \tag{7.12}$$

We can evaluate the partial derivatives on A and B, respectively, which are

$$\frac{\partial S^n}{\partial A} = \frac{1}{B\Delta\epsilon}, \tag{7.13}$$

and

$$\frac{\partial S^n}{\partial B} = \frac{-A}{B^2\Delta\epsilon}. \tag{7.14}$$

Substituting both partial derivatives into the original equation for ΔS^n leads to the simplified relation

$$\Delta S^n = \sqrt{\left(\frac{1}{B\Delta\epsilon}\Delta A\right)^2 + \left(\frac{-A}{B^2\Delta\epsilon}\Delta B\right)^2}. \tag{7.15}$$

The uncertainty on S^n as presented in Eq. 7.15, will be used for determining the neutron Rosenbluth slope preliminary result.

7.3.3 Determination of the Neutron Rosenbluth Slope

The neutron Rosenbluth slope, S^n, value will be determined from the form presented in Eq. 7.11. We will first provide determinations and uncertainties of the components of S^n.

Super-Ratio A

The super-ratio A follows from Eq. 7.8 and is determined from individual elastic neutron to proton cross-section ratios extracted from the analysis presented in this dissertation. The ϵ_1 configuration is the SBS-8 kinematic and the associated R' value and uncertainty is taken as the weighted mean from Tab. 7.2. The ϵ_2 configuration is the SBS-9 kinematic and 70% SBS magnet setting and its associated R' value and uncertainty is presented in Tab. 7.1. These extracted R' values, the configuration labels, and relevant kinematic information as summarized in Tab. 7.5. The uncertainties on the respective $R'_{\epsilon_1(\epsilon_2)}$ are taken as independent, since the studies of the systematic uncertainties on the experimental observable $R_{sf}^{n/p}$ did not demonstrate any definitive correlations between the SBS-8 and SBS-9 kinematics. As such, the uncertainty on A is computed as

$$\Delta A = |A|\sqrt{\left(\frac{\Delta(R'_{\epsilon_1})}{R'_{\epsilon_1}}\right)^2 + \left(\frac{\Delta(R'_{\epsilon_2})}{R'_{\epsilon_2}}\right)^2}. \tag{7.16}$$

Any systematic effects associated with discrepancies in absolute HCal nucleon detection efficiency are highly-likely to cancel in the super-ratio. From considerations of MC HCal nucleon detection efficiency, as presented in Sec. 6.3.1, the momentum of the respective scattered nucleon should be identical for the SBS-8 and SBS-9 kinematics. However,

	Kine	$\langle Q^2 \rangle$ $(\mathrm{GeV/c})^2$	$\langle \epsilon \rangle$	R'	$\Delta\left(R'\right)_{\mathrm{total}}$
R'_{ϵ_1}	SBS-8	4.48	0.799	0.3908	0.0038
R'_{ϵ_2}	SBS-9	4.476	0.518	0.3875	0.0032

Table 7.5: Information necessary for the determination of the super-ratio A. The acceptance-averaged Q^2 and ϵ values are included. The necessary R' values and total uncertainties are summarized.

distributions of the nucleon momentum from the data suggest slightly different acceptance-averaged central values and demonstrate different shapes in these distributions. Slight variations in the nucleon momentum would suggest slightly different values in the MC HCal nucleon detection efficiency, as shown in Fig. 6.17. However, Fig. 6.17 presents smooth and similar efficiency values for the SBS-8 and SBS-9 nucleon momentum. Furthermore, comparisons of position-dependent relative-rate distributions, as described in Sec. 6.3.4, of neutron-selected and proton-selected events from deuterium data demonstrate reasonable qualitative agreement between SBS-8 and SBS-9. Therefore from these justifications from both MC and experimental data, any slight discrepancy between the SBS-8 and SBS-9 HCal nucleon detection efficiencies would likely have a small impact on the super-ratio A, so no additional uncertainty is assigned. The value of the super-ratio A is

$$A = 1.0085 \pm 0.0129.$$

Quantity B

The quantity B, as defined by Eq. 7.9, is composed of three subterms which correspond to the $\tau_{n,\epsilon_1(\epsilon_2)}$ and $\tau_{p,\epsilon_1(\epsilon_2)}$ ratio, the transverse cross-section ratios, and the proton Rosenbluth slope terms $S^p_{\epsilon_1(\epsilon_2)}$. We will summarize the values for the three subterms and the value of B in Tab. 7.6, used for the S^n extraction. Additionally we will provide details describing how each subterm of B was determined.

The ratio subterm containing $\tau_{n(p),\epsilon_1(\epsilon_2)}$ and $\epsilon_{1(2),n(p)}$ kinematic quantities are directly calculable from known acceptance-averaged kinematic quantities. The $n(p)$ notation is

Quantity	Value	Total Uncertainty
$\frac{\frac{\tau_{n,\epsilon_1}}{\epsilon_{1,n}(1+\tau_{n,\epsilon_1})}\frac{\tau_{p,\epsilon_2}}{\epsilon_{2,p}(1+\tau_{p,\epsilon_2})}}{\frac{\tau_{p,\epsilon_1}}{\epsilon_{1,p}(1+\tau_{p,\epsilon_1})}\frac{\tau_{n,\epsilon_2}}{\epsilon_{2,n}(1+\tau_{n,\epsilon_2})}}$	1.00044	———
$\frac{\sigma^n_{T,\epsilon_1}}{\sigma^p_{T,\epsilon_1}}\frac{\sigma^p_{T,\epsilon_2}}{\sigma^n_{T,\epsilon_2}}$	0.99927	0.00017
$\frac{1+\epsilon_{2,p}S^p_{\epsilon_2}}{1+\epsilon_{1,p}S^p_{\epsilon_1}}$	0.98344	0.0028
B	0.98315	0.00281

Table 7.6: Information necessary for the determination of the quantity B. The values and uncertainties for the three subterms are also included.

included to distinguish whether the neutron(proton) mass is considered in the calculation. Similarly, the $\epsilon_1(\epsilon_2)$ denotes the kinematic configuration the quantity was calculated from. Since the effects on experimental observables due to variations in kinematic quantities was not studied in this analysis, an uncertainty on the τ and ϵ ratio term is not provided. It is expected that any variation on the kinematic quantities in this term leads to a negligible effect on B.

The subterm composed of transverse cross-section ratios is calculated from the parameterization to the nucleon electromagnetic form factor world data from by Ye *et al.* [31], described in Sec. 2.5.1. The Ye *et al.* parameterization provides uncertainties for each nucleon form factor. However within the ratios, the individual neutron and proton transverse cross-sections, $\sigma^{n(p)}_{T,\epsilon_1}$ and $\sigma^{n(p)}_{T,\epsilon_2}$, respectively, will have correlated uncertainties since they are at slightly different values of $\langle Q^2 \rangle$ but are calculated from the same parameterization. The Ye *et al.* parameterization provides direct assess to individual fit parameter values and uncertainties. However, any covariance matrices describing correlations between fit parameter and their associated uncertainties is not assessable from the article nor its supplementary materials. Therefore the uncertainty on an individual neutron or proton transverse cross-section ratio, $\sigma^n_{T,\epsilon_1}/\sigma^n_{T,\epsilon_2}$ or $\sigma^p_{T,\epsilon_2}/\sigma^p_{T,\epsilon_1}$ was estimated using the following technique:

1. For each neutron(proton) magnetic form factor parameterization central value, $\left(G_M^{n(p)}\right)_{\epsilon_1(\epsilon_2)}$, add the value of the parameterization uncertainty, $\Delta\left(G_M^{n(p)}\right)_{\epsilon_1(\epsilon_2)}$ to the form factor

as follows

$$\left(G_M^{n(p)}\right)_{\epsilon_1(\epsilon_2)}^{+1} = \left(G_M^{n(p)}\right)_{\epsilon_1(\epsilon_2)} + \Delta\left(G_M^{n(p)}\right)_{\epsilon_1(\epsilon_2)}. \tag{7.17}$$

2. Square the new form factor values, denote each as $\left(\left(G_M^{n(p)}\right)_{\epsilon_1(\epsilon_2)}^{+1}\right)^2$.

3. Calculate the new neutron and proton transverse cross-section ratios individually, that is $\left((G_M^n)_{\epsilon_1}^{+1}\right)^2 / \left((G_M^n)_{\epsilon_2}^{+1}\right)^2$ and $\left((G_M^p)_{\epsilon_2}^{+1}\right)^2 / \left((G_M^p)_{\epsilon_1}^{+1}\right)^2$.

4. Calculate the absolute value of the difference between the central and new values for the individual neutron and proton transverse cross-section ratios, in each case that is

$$\left| \frac{(G_M^n)_{\epsilon_1}^2}{\left(G_M^n\right)_{\epsilon_2}^2} - \frac{\left((G_M^n)_{\epsilon_1}^{+1}\right)^2}{\left((G_M^n)_{\epsilon_2}^{+1}\right)^2} \right|, \tag{7.18}$$

and

$$\left| \frac{(G_M^p)_{\epsilon_2}^2}{\left(G_M^p\right)_{\epsilon_1}^2} - \frac{\left((G_M^p)_{\epsilon_2}^{+1}\right)^2}{\left((G_M^p)_{\epsilon_1}^{+1}\right)^2} \right|. \tag{7.19}$$

5. Steps 1. through 4. are repeated, under the condition that the value of the parameterization uncertainty is subtracted from the central value of each neutron(proton) form factor as follows

$$\left(G_M^{n(p)}\right)_{\epsilon_1(\epsilon_2)}^{-1} = \left(G_M^{n(p)}\right)_{\epsilon_1(\epsilon_2)} - \Delta\left(G_M^{n(p)}\right)_{\epsilon_1(\epsilon_2)}. \tag{7.20}$$

6. We then compare the individual neutron and proton absolute value differences between the central and both new $+1$ and -1 considerations. The absolute value differences with the greatest value, between the two conditions, is taken as the correlated uncertainty on the individual neutron or proton transverse cross-section ratio. The uncertainty on the total transverse cross-section ratio, as present in B, is taken as the quadrature sum of the individual neutron and proton transverse cross-section ratio uncertainties taken from the greatest value of the absolute difference.

The combined description of the value-determination and the correlated uncertainty estimation are used to produce the value of the transverse cross-section ratios subterm in Tab. 7.6.

The remaining term in the quantity B is the term composed of proton Rosenbluth slopes at the two different ϵ configurations. To properly extract the neutron Rosenbluth slope, we must determine $S^p_{\epsilon_1(\epsilon_2)}$ from data and parameterizations which are only derived from extractions of electron-proton cross-sections (i.e. not using form factors from polarization-transfer data). The most recent parameterization of the electron-proton cross-section world data, in the form of the proton Rosenbluth slope, is available from Christy *et al.* [38]. Christy *et al.* presents values and a parameterization of the proton Rosenbluth slope in the following form

$$RS = \frac{\left(\mu_p G_E^p\right)^2}{\left(G_M^p\right)^2}. \tag{7.21}$$

The parameterization of the proton Rosenbluth slope as presented by Christy *et al.* is the relation

$$RS = 1 + c_1\tau + c_2\tau^2, \tag{7.22}$$

where $c_1 = -0.456299 \pm 0.124409$, $c_2 = 0.121065 \pm 0.10032$, and $\tau = Q^2/4M_p^2$. From the Christy *et al.* article and supplementary material it is possible to reconstruct the uncertainty on RS, denoted ΔRS, from the provided covariance matrix properly accounting for the correlations between the individual parameters by

$$\Delta RS = \sqrt{\left(\frac{\partial RS}{\partial c_1}\Delta c_1\right)^2 + \left(\frac{\partial RS}{\partial c_2}\Delta c_2\right)^2 + 2\frac{\partial RS}{\partial c_1}\frac{\partial RS}{\partial c_2}cov(c_1, c_2)}, \tag{7.23}$$

where $\frac{\partial RS}{\partial c_1} = \tau$, $\frac{\partial RS}{\partial c_2} = \tau^2$, and $cov(c_1, c_2) = -0.778\Delta c_1 \Delta c_2$. For this extraction of S^n we require the values of the proton Rosenbluth slope in the form

$$S^p = \frac{\left(G_E^p\right)^2}{\tau_p \left(G_M^p\right)^2}, \tag{7.24}$$

and therefore any values obtained from the Christy *et al.* parameterization need to be

properly adjusted. The values of $S^p_{\epsilon_1(\epsilon_2)}$, as determined from the Christy *et al.* parameterization and in the form necessary for this extraction are summarized in Tab. 7.7. From the values summarized in Tab. 7.7, it is straightforward to obtain the value of $\frac{1+\epsilon_{2,p}S^p_{\epsilon_2}}{1+\epsilon_{1,p}S^p_{\epsilon_1}}$ as shown in Tab. 7.6. However, it is not clear from the Christy *et al.* article, how to

Quantity	Value	Total Uncertainty
$(RS)_{\epsilon_1}$	0.615	0.107
$S^p_{\epsilon_1}$	0.0619	0.0108
$(RS)_{\epsilon_2}$	0.616	0.107
$S^p_{\epsilon_2}$	0.0619	0.0107

Table 7.7: Values of the proton Rosenbluth slope at both values of ϵ. The values directly from the Christy *et al.* parameterization, as well as the adjusted versions necessary for this extraction are presented.

properly propagate the correlated uncertainties on the individual $S^p_{\epsilon_1(\epsilon_2)}$ to the uncertainty associated with $\frac{1+\epsilon_{2,p}S^p_{\epsilon_2}}{1+\epsilon_{1,p}S^p_{\epsilon_1}}$. To estimate the uncertainty propagated to $\frac{1+\epsilon_{2,p}S^p_{\epsilon_2}}{1+\epsilon_{1,p}S^p_{\epsilon_1}}$, we will employ the following technique:

1. Add to each proton Rosenbluth slope central value, $S^p_{\epsilon_1(\epsilon_2)}$, one standard deviation of the parameterization uncertainty, $\Delta S^p_{\epsilon_1(\epsilon_2)}$ as follows

$$\left(S^p_{\epsilon_1(\epsilon_2)}\right)^{+1} = S^p_{\epsilon_1(\epsilon_2)} + \Delta S^p_{\epsilon_1(\epsilon_2)}. \tag{7.25}$$

2. Calculate the relevant proton Rosenbluth slope ratio with the new values determined from step 1. as follows

$$\frac{1+\epsilon_{2,p}\left(S^p_{\epsilon_2}\right)^{+1}}{1+\epsilon_{1,p}\left(S^p_{\epsilon_1}\right)^{+1}}. \tag{7.26}$$

3. Calculate the absolute value of the difference between the central value and the new value of the relevant proton Rosenbluth slope ratio as

$$\left|\frac{1+\epsilon_{2,p}S^p_{\epsilon_2}}{1+\epsilon_{1,p}S^p_{\epsilon_1}} - \frac{1+\epsilon_{2,p}\left(S^p_{\epsilon_2}\right)^{+1}}{1+\epsilon_{1,p}\left(S^p_{\epsilon_1}\right)^{+1}}\right|. \tag{7.27}$$

4. Repeat steps 1. through 3. for a similar condition where one standard deviation of the parameterization uncertainty is instead subtracted from the central value, denoted as

$$\left(S^p_{\epsilon_1(\epsilon_2)}\right)^{-1} = S^p_{\epsilon_1(\epsilon_2)} - \Delta S^p_{\epsilon_1(\epsilon_2)}. \tag{7.28}$$

5. Compare the absolute values as determined in step 3. for both the +1 and -1 conditions of the relevant proton Rosenbluth slope ratio. The larger value quantity is taken as the uncertainty on $\frac{1+\epsilon_{2,p}S^p_{\epsilon_2}}{1+\epsilon_{1,p}S^p_{\epsilon_1}}$, propagated from the correlated uncertainties of $S^p_{\epsilon_1(\epsilon_2)}$.

To determine the value for B, as presented in Tab. 7.6, we multiply the values of the three subterms together in accordance with Eq. 7.9. The process used for estimating the uncertainty on B reasonably attempts to account for the correlated uncertainties from the relevant parameterizations. The quoted uncertainty on B is estimated by taking the quadrature sum of individual subterm uncertainties, in a manner that accounts for the multiplication of independent quantities.

$\Delta\epsilon$ Term

The determination of $\Delta\epsilon$ follows directly from Eq. 7.10 and the individual ϵ values from each kinematic as presented in Tab. 7.5. As previously noted in Sec. 7.1, uncertainties on kinematic quantities were not evaluated for this analysis. As such, no uncertainty value is assigned to the $\Delta\epsilon$ term. The value of $\Delta\epsilon$ for the extraction of S^n is

$$\Delta\epsilon = 0.281.$$

Neutron Rosenbluth Slope Preliminary Result

Our preliminary result for the neutron Rosenbluth slope, S^n, at $Q^2 = 4.48$ (GeV/c)^2, is

$$S^n = \frac{(A-B)}{B\Delta\epsilon} \simeq \frac{(G^n_E)^2}{\tau_n \left(G^n_M\right)^2} : 0.0916 \pm 0.0476.$$

The equality of S^n to the neutron electromagnetic form factor ratio only strictly holds in the one-photon exchange approximation. However, if higher-order effects (two-photon exchange) are present a more accurate formulation of the neutron Rosenbluth slope is $S^n = (G_E^n)^2 / \tau_n (G_M^n)^2 + \text{TPE}$. This formulation represents the form factors as the OPE term plus a term due to TPE effects. Since our measurement of S^n is extracted from ratios of cross-sections, this preliminary result could be sensitive to TPE effects.

The value of S^n is directly determined from the respective values of A, B, and $\Delta\epsilon$ as presented in earlier parts of this section. The total uncertainty on S^n is quantified using Eq. 7.15 and follows the uncertainty propagation as described in Sec. 7.3.2. The uncertainty propagated to S^n from only the uncertainty on A, denoted $\Delta(S^n)_{\text{Exp}}$, is presented in Tab. 7.8. Essentially, $\Delta(S^n)_{\text{Exp}}$ quantifies the variation on S^n due only to experimental observables extracted from this analysis. Similarly, the uncertainty propagated to S^n from only the uncertainty on B, denoted $\Delta(S^n)_{\text{Param}}$, is also shown in Tab. 7.8. The variation on S^n due only to propagated uncertainties from parameterizations of the nucleon form factor world data is quantified by $\Delta(S^n)_{\text{Param}}$. It is evident that the total uncertainty

Quantity	Uncertainty Value	Percentage
$\Delta(S^n)_{\text{Exp}}$	0.0465	50.8%
$\Delta(S^n)_{\text{Param}}$	0.0104	11.4%
$\Delta(S^n)_{\text{Total}}$	0.0476	52%

Table 7.8: Uncertainty contributions from extracted experimental observables, $\Delta(S^n)_{\text{Exp}}$, and parameterization to the nucleon electromagnetic form factor world data,$\Delta(S^n)_{\text{Param}}$. The uncertainty values are compared to the total uncertainty on S^n.

on S^n is dominated by uncertainties in the experimental observables extracted in this dissertation, $\Delta(S^n)_{\text{Exp}}$. Therefore it is useful to understand how individual experimental sources of uncertainty contribute to the total uncertainty on S^n. To compare the individual uncertainty sources, we isolated a particular type of uncertainty source for both the SBS-8 Weighted Mean and SBS-9 $R_{sf}^{n/p}$ values, as described in Sec. 6.4.4, and propagated the given uncertainty through the S^n extraction. Table 7.9 summarizes the impact of each isolated source of uncertainty on the neutron Rosenbluth slope. From Table 7.9 it is evident

that the two largest sources of uncertainty are those caused by the inelastic background, $\Delta\left(S^n\right)_{\text{Ine}}$, and the cut selection regions, $\Delta\left(S^n\right)_{\text{Cut}}$.

Quantity	Uncertainty Value	Percentage
$\Delta\left(S^n\right)_{\text{Stat}}$	0.0144	15.8%
$\Delta\left(S^n\right)_{\text{HCDENU}}$	0.0182	19.9%
$\Delta\left(S^n\right)_{\text{Cut}}$	0.0227	24.8%
$\Delta\left(S^n\right)_{\text{Ine}}$	0.0317	34.7%
$\Delta\left(S^n\right)_{\text{Exp}}$	0.0465	50.8%

Table 7.9: The propagated uncertainty on S^n from $R_{sf}^{n/p}$, for each uncertainty source evaluated in this dissertation. $\Delta\left(S^n\right)_{\text{Stat}}$ represents the statistical uncertainty. $\Delta\left(S^n\right)_{\text{HCDENU}}$ represents the uncertainty due to effects of HCal nucleon detection efficiency non-uniformity. $\Delta\left(S^n\right)_{\text{Cut}}$ represents effects due to cut selection regions. $\Delta\left(S^n\right)_{\text{Ine}}$ represents effects due to the inelastic background.

From the neutron Rosenbluth slope, S^n, presented in this section we can extract a preliminary result for the neutron electromagnetic form factor ratio, $\mu_n G_E^n/G_M^n$, at $Q^2 = 4.48$ $(\text{GeV/c})^2$, as

$$\mu_n \frac{G_E^n}{G_M^n} \simeq \mu_n \sqrt{S^n \tau_n} : 0.652 \pm 0.160.$$

Figure 7.5 shows a plot of the existing $\mu_n G_E^n/G_M^n$ world data with the preliminary result extracted from the analysis in this dissertation superimposed. The preliminary value of $\mu_n G_E^n/G_M^n$ in this dissertation is extracted from measurements of cross-section ratios and as such is sensitive to higher-order radiative effects, most notably two-photon exchange. In the extraction of this preliminary $\mu_n G_E^n/G_M^n$ value, no corrections for two-photon exchange were applied and as such do not provide the most accurate value for the neutron electromagnetic form factor ratio, represented by the OPE diagram.

7.4 Discussion of Results and Outlook

The preliminary value of S^n, as presented in Sec. 7.3.3, is the first measurement of the Rosenbluth slope for the neutron. From this slope, an extraction of the neutron electromagnetic form factor ratio, $\mu_n G_E^n/G_M^n$, was performed for the first time from cross-section

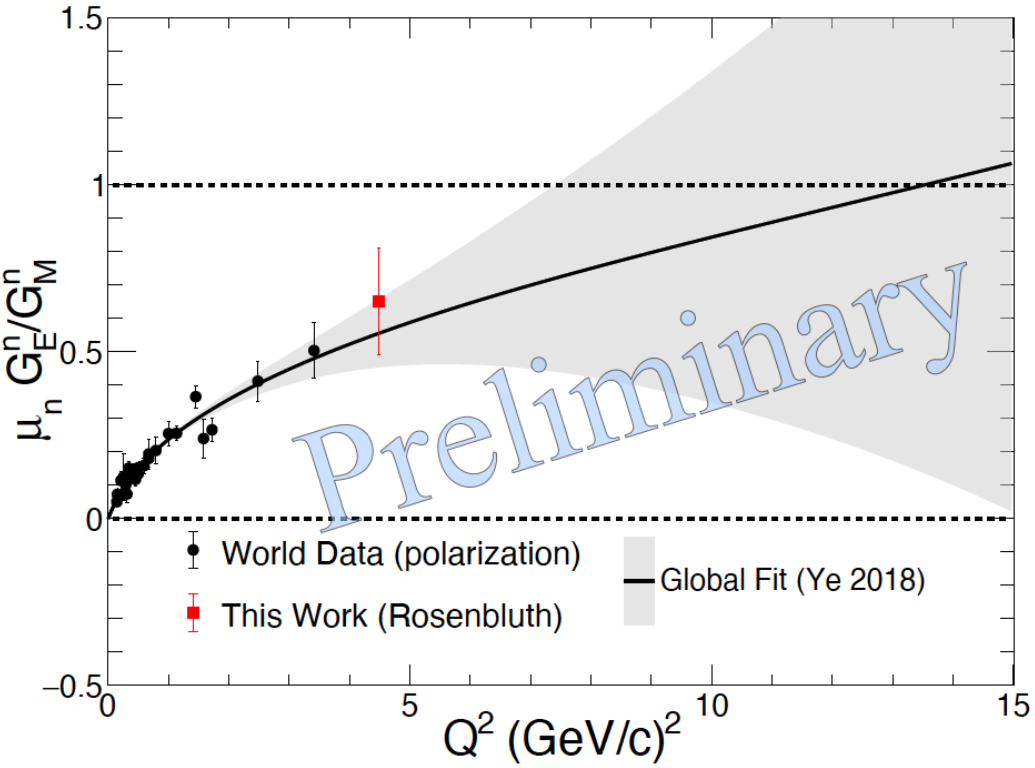

Figure 7.5: $\mu_n G_E^n/G_M^n$ world data along with the preliminary result extracted in this dissertation, represented by the red square. Our preliminary value does not include any corrections for any two-photon exchange effects. The world plot is adapted from Ref. [28]. The global fit to the world data is from Ref. [31], and the details of the parameterization are summarized in Sec. 2.5.1.

measurements, at a value of Q^2 higher than existing world data. The preliminary value for the extracted $\mu_n G_E^n/G_M^n$ ratio is presented in Fig. 7.5. Extracted $G_M^n/\mu_n G_D$ values for two experimental kinematic settings are summarized in Tab. 7.4, and shown in Figs. 7.3 and 7.4. It is important to note that the physics results presented in this dissertation are preliminary and are not the final results of the SBS nTPE (E12-20-010) and G_M^n (E12-09-019) experiments. The preliminary results for S^n and $G_M^n/\mu_n G_D$, and the extracted R' values, presented in this chapter, reflect the work of the author. All preliminary results presented in this dissertation are extracted from measurements of quasi-elastic electron-nucleon cross-section ratios. The determination made in this dissertation neglects correc-

tions to the cross-sections for high-order terms beyond the OPE diagram, most notably TPE effects.

To improve on the extractions of S^n and $G_M^n/\mu_n G_D$, obtained in this dissertation, several necessary tasks remain which could effect both the nTPE and G_M^n analyses. As discussed in Sec. 6.1.2, there are many conditions necessary for constructing a simulation which realistically models the observed physics. The MC files used in this analysis have known discrepancies involving apparatus geometries, which have since been resolved in the SBS simulation software. Appropriately modeling the radiative corrections in the SIMC generators is an ongoing development; the current simulation has a framework for radiating the incoming and scattered electrons, and protons. However, implementing appropriate radiative correction models for the neutron requires further development. The MC files used in this analysis have radiative corrections applied for the incoming and scattered electrons. Furthermore, there are initial studies of varying radiative correction models within the simulation framework to begin to address systematic effects on experimental observables. To reach final extractions of S^n and $G_M^n/\mu_n G_D$, at least one more mass generation of MC files is necessary to include these simulation developments. In the data analysis, the HCal timing calibration needs optimization to account for time-of-flight differences between neutrons and protons as evident in Fig. B.4 and suggested by the author of Ref. [140]. These improved HCal timing calibration would require an additional mass replay of the data.

It is important to note that the uncertainties extracted in this dissertation for both S^n and $G_M^n/\mu_n G_D$ do not include contributions for final state interactions nor uncertainties in the absolute HCal nucleon detection efficiency. Individual studies for each of these two effects need to be conducted to quantify any systematic effects on experimental observables or extracted results. Understanding final state interactions requires theoretical models for nucleon-nucleon interactions over the relevant momentum range. Potential ways to study effects due to absolute HCal nucleon detection efficiency are described in Sec. 6.3.6. It is thought the final state interactions and absolute HCal nucleon detection efficiency effects

will have a larger impact on $G_M^n/\mu_n G_D$ values, as they are directly extracted from a single elastic neutron-to-proton cross-section ratio. Conversely, the value of the neutron Rosenbluth slope will likely be less sensitive to final state interactions and absolute HCal nucleon detection efficiency effects. This expected insensitivity is because the neutron Rosenbluth slope is extracted from a super-ratio of elastic nucleon cross-section ratios, which are under extremely similar kinematic conditions.

The preliminary $G_M^n/\mu_n G_D$ values are obtained within a range of 1.15% to 1.5% total uncertainty, and this uncertainty range is consistent with the original proposed measurement. These total uncertainties will likely increase when contributions due to final state interactions and absolute HCal nucleon detection efficiency effects are quantified. The Ye *et al.* [31] parameterization $G_M^n/\mu_n G_D$ values are 0.9356 ± 0.0160, for $Q^2 = 4.48$ (GeV/c)^2, and 0.9362 ± 0.0159, for $Q^2 = 4.476$ (GeV/c)^2. The preliminary $G_M^n/\mu_n G_D$ values are consistent, within 1σ, with the values from the world data parameterization from Ye *et al.*. The preliminary $G_M^n/\mu_n G_D$ values are more precise than the existing world data in this Q^2 regime and will be essential for validating $G_M^n/\mu_n G_D$ at higher-Q^2 data points, from other analyses of the SBS G_M^n data, as efforts converge towards publication.

For the proton electromagnetic form factor ratio, $\mu_p G_E^p/G_M^p$, there is a well-known discrepancy between values obtained from Rosenbluth slope and polarization transfer measurements, particularly at large Q^2. Two-Photon Exchange is largely believed to be the cause of this discrepancy for the different proton measurement types, Refs. [26, 27] provide experimental and theoretical motivations for this claim. The preliminary values for the neutron Rosenbluth slope, S^n, and the neutron electromagnetic form factor ratio, $\mu_n G_E^n/G_M^n$, extracted in this analysis, are consistent with an extrapolation of the recent world data parameterization from Ye *et al.* [31]. The G_E^n values used in the Ye *et al.* parameterization are found using polarization-based measurements. Two-photon exchange corrections have not yet been experimentally established for the neutron. The consistency of the preliminary results for S^n and $\mu_n G_E^n/G_M^n$ with the extrapolation from the Ye *et al.* parameterization implies that our data are not yet precise enough to expose TPE effects

and corrections for the neutron. This preliminary result is consistent with the absence of large TPE corrections for the neutron.

One theoretical calculation is available for two-photon exchange contributions to the unpolarized electron-neutron elastic scattering cross-section, by Blunden, Melnitchouk, and Tjon [180]. They found that the sign and slope with Q^2 of the two-photon exchange correction for the neutron was opposite that of the proton. The sign change is attributed to the negative anomalous magnetic moment of the neutron. Additionally, the magnitude of the two-photon exchange contribution to unpolarized electron-neutron elastic scattering cross-section was approximately 3 times smaller than for the proton. The impact of TPE effects, as calculated by Blunden *et al.*, on the ratio $\mu_n G_E^n/G_M^n$ are shown in Fig. 7.6. At a value of $Q^2 = 4.5$ (GeV/c)^2 using a Rosenbluth slope technique (LT separation), Fig. 7.6 suggests the neutron electromagnetic form factor ratio could increase by approximately 30%, when corrections for TPE are applied. If the neutron TPE correction from Blunden *et al.* was applied to the preliminary result extracted for $\mu_n G_E^n/G_M^n$, in this dissertation, that would increase the central value by approximately 30%. If the uncertainty on the preliminary $\mu_n G_E^n/G_M^n$ remained the same, the inclusion of the TPE correction would cause the increased central value to be about 2σ away from the Ye *et al.* extrapolated value.

If the total uncertainties on the preliminary results for S^n and $\mu_n G_E^n/G_M^n$ could be reduced by a factor of two, these results would likely be more sensitive to TPE effects or corrections for the neutron. The largest contributions to the neutron Rosenbluth slope total uncertainty, as presented in Tabs. 7.8 and 7.9, are from experimental uncertainties associated with the inelastic contamination and the cut stability regions. The uncertainty contribution due to the inelastic background potentially could be studied further, likely a reduction could be achieved by incorporating a background functional form using high-statistics simulated events from the inelastic generator. Additionally, data-driven anti-cuts (side-band analysis) that more accurately captures events for the inelastic background could improve the associated uncertainty. Further iterations of cut region optimization or

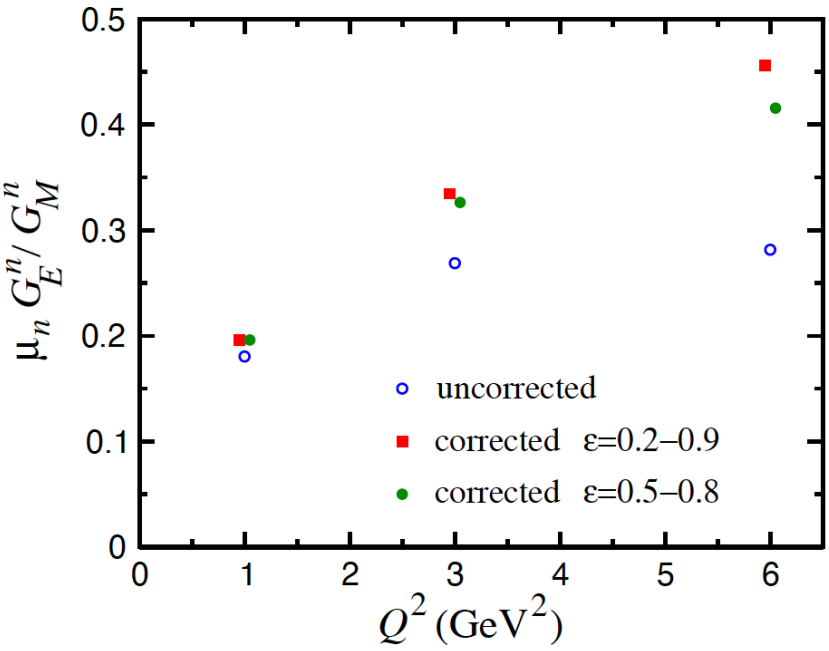

Figure 7.6: Effect of two-photon exchange on the neutron electromagnetic form factor ratio, $\mu_n G_E^n/G_M^n$, using LT separation. This plot is reproduced from Ref. [180]. The uncorrected points, open circles with blue borders, are from the form factor parameterization in Ref. [181]. The points corrected for TPE as obtained from Ref. [180] for ranges of the virtual photon polarization of $\varepsilon = 0.2 - 0.9$, red squares, and $\varepsilon = 0.5 - 0.8$, green circles, respectively. The points corrected for TPE are offset for clarity.

systematic studies of cut stability may improve the associated uncertainty. Investigation of particular cut parameters which contribute the largest to the total cut region uncertainty would be necessary.

In summary, preliminary extractions provide a first measurement of the neutron Rosenbluth slope and the ratio $\mu_n G_E^n/G_M^n$ from cross-section measurements. The preliminary results of the neutron Rosenbluth slope and the ratio $\mu_n G_E^n/G_M^n$ indicate our data are not yet precise enough to expose TPE effects and corrections for the neutron. The preliminary $G_M^n/\mu_n G_D$ values are extracted to higher precision than the existing data in this Q^2 regime. A comprehensive interpretation and refinement of these preliminary results will likely contribute to an improved understanding of the neutron's internal structure.

Appendix A

Supplementary GEM Information

A.1 GEM Specific Information for Front-End Electronics Low-Voltage Power Supply Systems

A description of the low-voltage power supplies used for the UVA and INFN GEMs during the SBS G_M^n and nTPE experiments. The information in this section provides more details than Sec. 5.4.1.

UVA GEMs

A single UVA XY GEM layer as described in Sec. 5.2.1 contains 88 instrumented APV cards. From the APV cards alone, the nominal power consumption of a single UVA XY GEM layer is approximately 26 W of power. Based on an estimate of the maximum current draw of an APV25 chip and to provide sufficient power consumption headroom, a single UVA XY GEM layer a maximum power consumption is 72 W [160]. For the low-voltage power supply units associated with the UVA GEMs, multiple custom supplies were produced by the Jefferson Lab Electronics group. Each power supply system was capable of delivering approximately 30% more power than the maximum APV25 power consumption of the entire GEM front-end electronics system.

INFN GEMs

A single INFN XY GEM layer as described in Sec. 5.2.3 has 54 instrumented APV cards. If considering only APV cards under nominal power conditions, a single INFN XY GEM layer has a power consumption of approximately 16 W. To meet the voltage specifications and power consumption of the front-end readout electronics the commercial power supply called TTi CPX400DP [182] was selected. A single channel of this dual-channel power supply is capable of providing 420 W of power, which allows for either a maximum of 60 V or 20 A of DC electricity. The CPX400DP has other relevant control, safety, and feedback features and make this particular power supply ideal for instrumentation with the INFN XY GEM layers.

A.2 Extracting GEM Clusters and Hits from Raw Data

This appendix will describe in some detail the raw signals from the GEM readout electronics, the low-level diagnostic software useful for operational testing, the pedestal information, online GEM analysis, and offline GEM analysis. The online GEM analysis will includes pedestal subtraction, common mode subtraction, and online zero suppression. The offline analysis will comprise the calorimeter search region, 1-dimensional cluster formation, 2-dimensional hit association, and the track-finding algorithm. The appendix will start with the raw GEM signals and cover analysis features up to track reconstruction.

A.2.1 Raw APV25 Signal

For one single triggered event corresponding to a one APV25 card the 128 strips/channels are sampled multiple times. Two examples of digitized data (also called raw data or raw data-frames) from the APV25 card are presented in Figs. A.1a and A.1b. The raw data comes directly from the MPDs, after the analog signal of the APV25 cards has been digitized and before any online data reduction has occurred. For the SBS program, the MPD firmware is programmed to sample data 6 times. Each individual time sample is 25

ns long so the entire sample window is 150 ns. Each plot in Figs. A.1a and A.1b has the channel amplitude in ADC units in the vertical axis. The 128 channel numbers over the six time samples are shown on the horizontal axis. There are 5 long vertical lines present in both these figures; these have been artificially implemented to denote the location of the 6 different time samples.

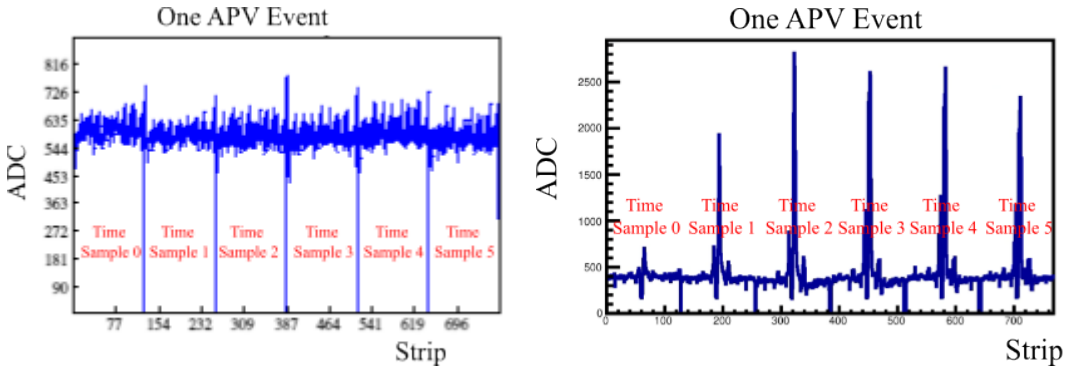

(a) (b)

Figure A.1: Examples of digitized signals for one event of a single APV25 card. There are 6 time samples per event. Each time sample is 25 ns long. The time samples are artificially separated by vertical lines in each plot. Left: An example of one event for one APV25 card during pedestal data collection. Right: An example of one event for one APV25 card in the presence of an ionization event in the GEM module.

In Fig. A.1a no ionization event is present in this data-frame; when this data was collected the high voltage of the GEM detector was off. When no ionization amplification is present in the raw data, as in Fig. A.1a, these data are commonly referred as "pedestal data" or "noise signals." The pedestal data is important because it is used to characterize the channels of the GEM modules before real signals are extracted. The raw data-frame presented in Fig. A.1b represents a case where good ionization signals are detected on multiple strips/channels of the APV25 card. This type of raw data frame still has the pedestal data, though seen on a smaller scale compared to the signal from amplified ionizing particles. The shape of the raw data in Fig. A.1b is consistent with the effect the pulse shaper circuit on the APV25 chip has on the charged collected from the GEM strips as the readout electronics generates a signal. A common term that will be used during the

discussion about GEM data analysis is "occupancy," which is defined as the fraction of total strips that contains a signal.

A.2.2 Low-Level Diagnostics

The low-level diagnostic tests and plots, for a VME based readout, were developed by collaborators from INFN named Evasito Cisbani, Roberto Perrino, and Paulo Musico. The low-level diagnostic software was further developed by Bryan Moffit to account for SSP and VTP based readout modes. The low-level diagnostic software consists of two primary modes: one is a histogram mode and the second is a sampling mode. The purpose of the histogram mode is to assess if each APV25 card properly communicates with the corresponding MPD module without the implementation of a complex data acquisition system or trigger. The function of the sampling mode is to determine the clock-phase and FIR coefficients for a particular MPD module with the corresponding set of connected APV25 cards. The clock-phase parameter accounts for the time it takes a signal to transfer along the HDMI cables between the MPD module and the APV25 cards; inherently, this parameter is dependent on the length of the HDMI cables. The FIR coefficients are filter coefficients which can be enabled/implemented in the firmware of the MPD modules to resolve noise in the APV25 electronics due to any impedance mismatch between HDMI cables.

The remainder of this section will describe each of the low-level diagnostic modes, providing more detail about the histogram and sampling modes. Both common and unique electronics troubleshooting or failure modes will be characterized using information from the low-level diagnostic software.

Histogram Mode Plots

The low-level histograms are a representation of the raw data from the APV25 card; an example of a typical histogram is shown in Fig. A.2b. If one starts with the raw APV25 signal over time as shown in Fig. A.2a and projects the vertical axis as a histogram,

then the result is the histogram such as that in Fig. A.2b. Specifically, the level 0 and analog channel signals will populate ADC values less than 500, while the digital header and level 1 signals will populate ADC values around 2500-3000. The plot in Fig. A.2b is a typical example of a properly functioning APV25 card and as such it can be used as a reference to diagnose connection and signal problems at a low-level of data acquisition. The main advantage of the low-level diagnostic program is it does not require a complex

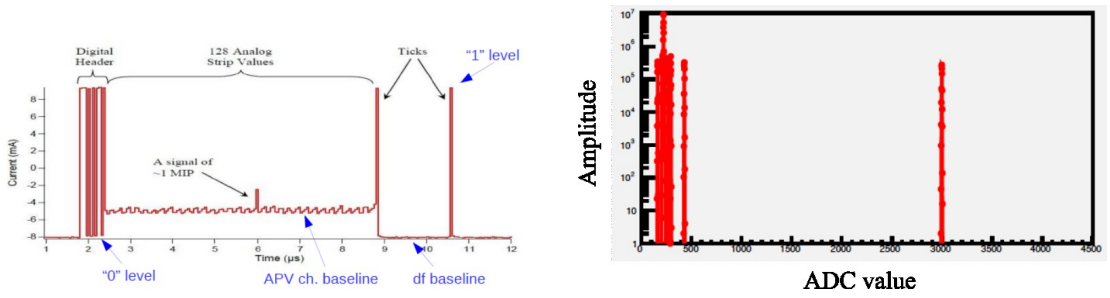

(a) (b)

Figure A.2: Information and plots related to the histogram mode of the low-level diagnostic software. Left: A diagram of raw data from a single APV25 card for one time sample of one event. The level 0 signals correspond to signals in the digital header which have a current value between -6 and -8 mA. Whereas, the level 1 signals will have a current value of approximately 8 mA. The time on the horizontal axis of this plot is not the real sample time (25 ns) of the APV25 chip. Rather it is the pipelined readout time, which has a 40 MHz readout clock frequency. Right: An example of a typical histogram mode low-level plot for a single APV25 card.

data acquisition (like CODA) and can be rapidly/iteratively performed to evaluate signals between the APV25 cards and the MPD modules, via the HDMI cables. In the histogram mode test the MPD module repeatedly sends a signal to the APV25 cards across both digital and analog HDMI cables, and then records the returned signals. These recorded signals are then represented as one histogram per APV25 card, like the example presented in A.2b.

Sample Mode Plots

The low-level samples are a representation of the raw data from an APV25 card; a typical example of a sample graph is shown in Fig. A.3. If one considers the raw APV25 data over

time as shown in Fig. A.2a the 0 level and analog signals will populate ADC values less than 500 and the 1 level signals will populate the plot with an ADC value greater than 500. The reason for this is that the low-level sample program varies the synchronized pulse of the APV25 cards. The purpose of these sample plots is the evaluation of the clock-phase parameter, which is dependent on the HDMI cable length between the MPD module and the APV25 cards. One can determine the optimal clock-phase value from a sample plot by finding the greatest difference between the level 0 and level 1 signals that is also stable (horizontally flat in A.3). For an ideal plot like in Fig. A.3, an optimal clock-phase value is in the range of 40-48 for this APV25 card.

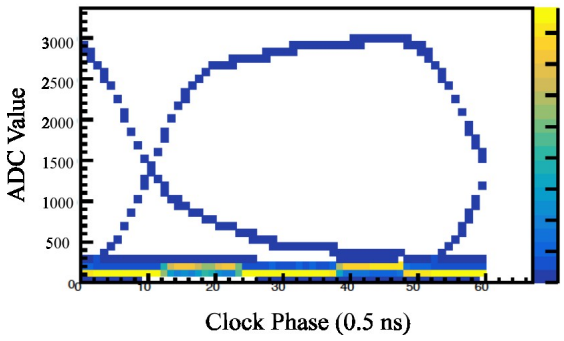

Figure A.3: Typical sample mode low-level plot for a single APV25 card (sometimes called a "fish plot"). The optimal clock-phase (see text) is between 40 and 48 in units of 0.5 ns.

Common Electronics Troubleshooting

A key component of testing, installing, or commissioning GEM detectors is ensuring the proper function of the readout electronics. For the GEMs in the SBS program the process of evaluating the proper function of the readout electronics starts with the low-level diagnostic tests. The low-level diagnostic software and plots, as described in the preceding sections, are used to identify any potential issues with HDMI cable connections or individual malfunctioning electronic components. As part of the G_M^n and nTPE GEM installation and commissioning periods, common GEM electronics troubleshooting was characterized

from empirical observation by the GEM experts. The characterization and patterns of the electronics in common failure modes, using the low-level diagnostic software, will be described in this section. The motivation for including these failure modes in this dissertation is to make available the experience and information so that it may be useful to future Jefferson Lab experiments which use GEM detectors, APV25 cards, MPDs, and the low-level diagnostic software.

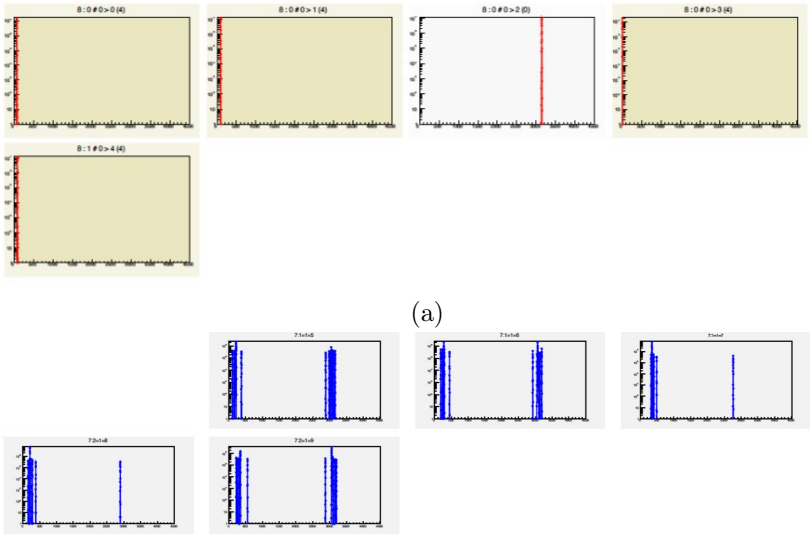

(a)

(b)

Figure A.4: Two examples of low-level histograms with digital HDMI cable connection issues. Top: A set of 5 histograms, corresponding to one backplane of 5 APV25 cards, with a particular digital HDMI cable connection problem. Bottom: A set of 5 histograms corresponding to APV25 cards with a different digital HDMI cable connection problem.

The most likely locations for a disconnection of the readout electronics from the HDMI cables are at patch panels, near the GEM detectors, near the front-end APV25 backplanes, or at the MPD modules. For the SBS GEM detectors, the HDMI cables serve the purpose of conveying either analog or digital signals.

If a digital HDMI cable is partially or fully disconnected, then it will appear as the low-level histograms in Figs. A.4a or A.4b. For either of these digital HDMI cable connection problems, if compared to the ideal low-level histogram in A.2b, these problematic histograms seem distorted or altered but still retain some of the ideal structure. Typically

partially or fully disconnected digital HDMI cables will manifest in groups equal to the number of APV25 cards on a given type of GEM backplane. This digital HDMI cable connection problem is very likely to affect multiple APV25 cards and not likely to only affect a single APV25 card. The different types of APV25 backplanes used for the SBS GEM detectors are described in Sec. 5.2. The nominal solution to the digital HDMI cable connection problems, as shown Figs. A.4a or A.4b, is to track down the exact disconnection corresponding to a particular set of APV25 cards on a backplane and then reconnect the specific HDMI cable either near the GEM detector or at the MPD module. In rare circumstances the HDMI cable connector or HDMI cable itself has failed, and the cable then needs to be replaced. In many considerations, swapping the potentially problematic HDMI cable either at the patch panel or at the MPD module with a known good set of APV25 cards helps to isolate the malfunctioning electronics faster.

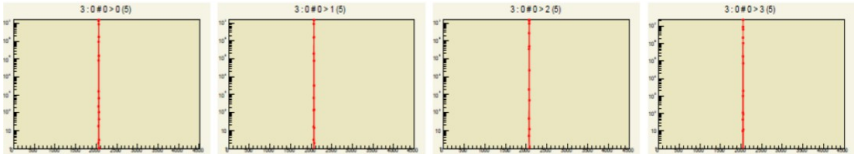

Figure A.5: An example of low-level histograms with analog HDMI cable connection issues. An example set of 4 histograms, corresponding to APV25 cards, with an analog HDMI cable connection problem.

For an analog HDMI cable which is partially or fully disconnected, the corresponding histograms will be similar to those in Fig. A.5. By comparing the case of a problematic analog HDMI cable connection to the ideal low-level histogram in Fig. A.2b, the improper histograms have no structure at all due to an absence of signal altogether. This overall lack of analog signal for the raw data of the APV25 card would be due to the APV25 card having zero current over time, which is represented as an approximate value of 2000 ADC units. This approximate value in the histogram representation is based on the inclusion of the positive and negative current values of the APV25 raw data. Or described differently, since there is no analog signal present, the low-level software can not determine the differences between the various current levels of the APV25 raw data. Typically, partially or fully

disconnected analog HDMI cables will manifest in groups equal to the number of APV25 cards on a given type of GEM backplane. The different types of APV25 backplanes used for the SBS GEM detectors are described in Sec. 5.2. The nominal solution to the analog HDMI cable connection problems, as shown in Fig. A.5, is a similar process and diagnostic task as described for the digital HDMI cable connection solution in order to isolate the disconnection.

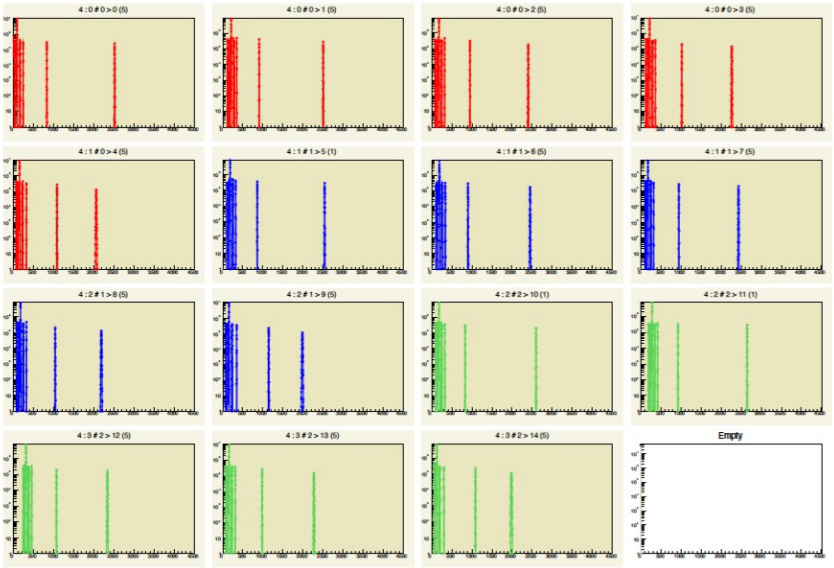

Figure A.6: An example of a 15 histograms corresponding to APV25 cards, each with an improper clock-phase parameter. The notable feature indicating the improper clock-phase parameter is that the ADC value difference between the analog signals and the level 1 signals is significantly less, compared to the ideal case of Fig. A.2b.

As described previously in this section related to the Sample Mode, part of preparing the GEM readout electronics is optimizing the clock-phase for the APV25 cards associated with a particular MPD module. The clock-phase parameter is set for a given MPD module and is not adjustable on an APV25 card basis. As a result of this electronics implementation, if the clock-phase parameter is improperly set, this issue will also be observable from the low-level histograms, not just the sample mode plots. Most, if not all, histograms representing APV25 cards will display similar behavior as shown in Fig. A.6. The distinguishing feature for these particular histograms is that the ADC value difference between

the analog signals and the level 1 signals is significantly less. This narrowing effect between the analog signals and the level 1 signals is even more pronounced when comparing to the ideal reference histogram in Fig. A.2b. The remedy for the condition of an unoptimized clock-phase parameter is to perform the low-level sample mode software and to adjust the MPD configuration files accordingly. The adjustment in the clock-phase parameter should also be evident in the low-level histograms as well.

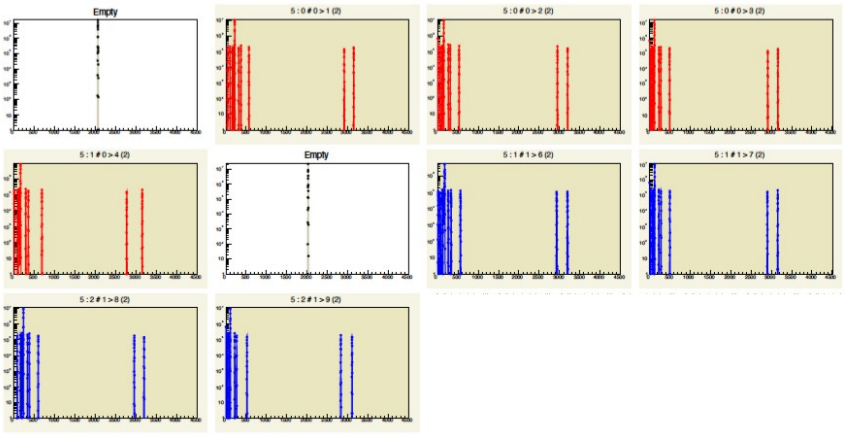

Figure A.7: An example of a 8 histograms, corresponding to two backplanes (denoted by difference in color) each with 4 APV25 cards connected. The plots most probably indicate a mismatch in digital HDMI cable connections, i.e. the digital HDMI cable associated with the first backplane (red) is actually connected to the second backplane (blue) and vice versa.

A common occurrence during installation or replacement of detectors, due to the large number of GEM channels, is the mismatch of HDMI cables with GEM electronics. Particularly, what this means is that the readout electronics within close physical proximity can have HDMI cables not connected in the proper ordering either at patch panels or the MPD module. This HDMI cable mismatch can occur for either digital and analog HDMI cables.

For the case of a mismatch of digital HDMI cables one will typically see low-level histograms similar to those presented in Fig. A.7. The distinguishing feature with this issue is that APV25 cards connected to two (or potentially more) backplanes with demonstrate a double amplitude, rather than a single amplitude, for the level 1 signals. The level 0 and

analog signals will appear as for the ideal case, and generally do not correlate to this cable mismatch problem. The double amplitude affect arises from the digital header and level 1 signals being improperly transmitted between the MPD module and APV25 cards. The typical way to correct this digital HDMI cable misordering is to carefully isolate either near the GEM detector or at the MPD module where the digital HDMI cables are mismatched in their proper order.

A similar condition can occur where the analog HDMI cables are mismatched, a direct example of these histograms is not available. If analog HDMI cables are mismatched one would observed two or more backplanes of histograms (multiple colors) similar to those presented in Fig. A.5. Diagnosing an analog HDMI cable mismatch is more difficult, than the digital mismatch case, as it tends to mimic a different analog HDMI cable problem. The low-level histograms for an analog HDMI cable mismatch manifest plots very similar to analog HDMI cables which simply disconnected (at least two cables, possibly more). Resolving this connection problem requires first ruling out simply a disconnection of analog HDMI cables. Then evaluating the ordering of the analog HDMI cables both near the GEM detector or at the MPD module to find the mismatched analog HDMI cables and connecting them in proper order.

Unique Readout Electronics Failure Modes

The focus of this section will be to encapsulate instances of unique and more rare failure modes that were observed with the GEM readout electronics. These unique failure modes only occurred a couple of times throughout the entire installation, commissioning, and operation of the GEMs during the the G_M^n and nTPE experiments. This section will not be an exhaustive list of all unique failure modes. Rather its purpose is to document observed less-frequent failure modes.

The MPD module manufacturing and physical features are generally robust. Only very rarely during the experimental run period did an MPD module fail. The set of histogram plots in Fig. A.8 corresponds to one such failed MPD module, and serves as one example.

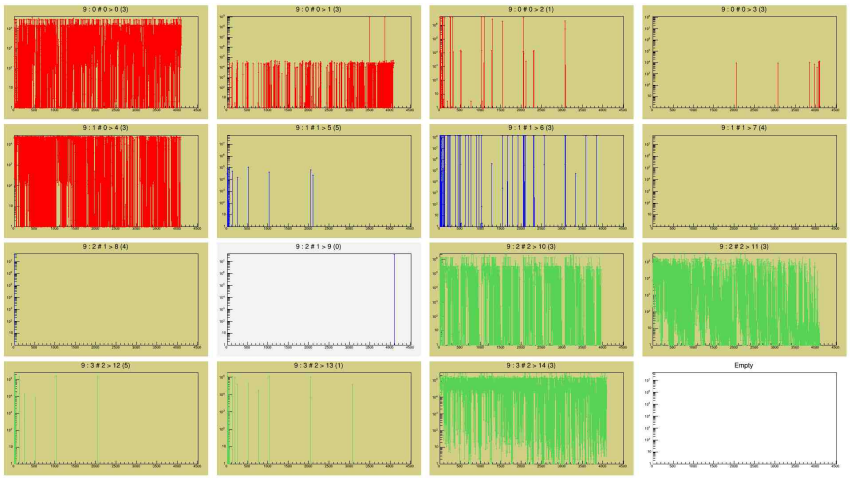

Figure A.8: An example of the 15 low-level histograms representing APV25 cards for a failed MPD module.

One clear characteristic from Fig. A.8 is that the signals for most APV25 cards, connected to multiple different backplanes, are not properly being digitized and managed. This indicates that the MPD module is potentially the source of the problem. The solution to this failed MPD module, is to replace the MPD with a known good spare and to have the failed module undergo further diagnostic testing to be repaired.

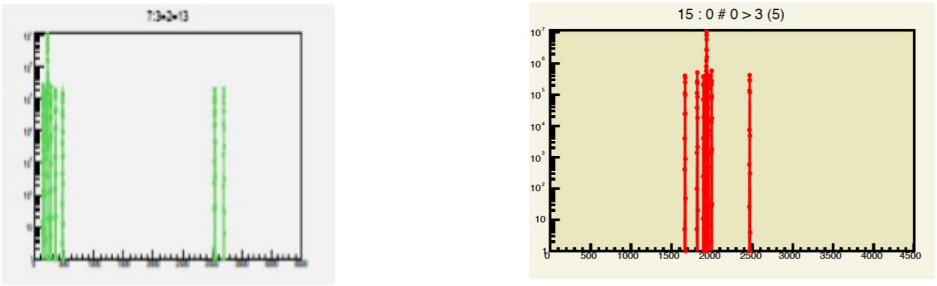

(a) (b)

Figure A.9: Example low-level histograms for a single failed APV25 card, failed APV25 card connector, failed backplane connector, or disconnected APV25 card at backplane.

The APV25 cards and backplane boards typically are well manufactured and physically sturdy. In rare instances it has been observed that either the backplane connector on the APV25 card or the APV25 connector on the backplane physically decouples from the respective electronics. Alternatively, the APV25 card can have electronics components

fail which render it inoperable, or the APV25 card can become disconnected from the backplane board. If any of these considerations occur, then plots such as those in Figs. A.9a or A.9b are typically observed. Since this failure mode on-average only affects a single APV25 card/backplane position, it is generally isolated by affecting only one histogram. Disentangling the exact source of failure can be difficult. It is best to proceed by first evaluating the connection between the APV25 card and the backplane. Then, if unresolved, carefully replacing respective pieces of electronics until signal readout is successful.

A necessary feature of pipelined or multi-crate (most modern) readout electronics systems is a clock source or clock signal, to properly manage the time in which data are collected. The GEM readout electronics are no exception and the MPD modules are able to either receive clock signals from a ROC module or to generate internal clock signals on an individual MPD basis. During the experimental running period an external clock from a ROC module is sent to the MPDs so that the clock signal is uniform for all GEM readout electronics. If a clock signal is not available to the APV25 readout cards, then data will not be able to be collected and this issue will manifest in the low-level histograms. The plots presented in Figs. A.10a and A.10b demonstrate how a set of 15 histograms, corresponding to 15 APV25 cards, would appear in the cases of either a distorted/problematic clock signal or a lack of clock signal altogether, respectively. Furthermore a clock signal problem typically will affect the entire readout electronics system at either the MPD or VTP levels. Thus one would expect to potentially see multiple sets of 15 low-level histograms affected by this failure mode. The remedy for a clock signal distribution problem is to carefully trace the clock signal using an oscilloscope throughout the entire connection from the ROC to the APV25 card, until one finds a disconnection.

A unique failure mode observed during commissioning of one of the INFN GEM layers was the failure of one APV25 card corrupting the signals of all the other connected readout cards. In this instance, the localized high voltage interacted with the APV25 card causing failure of some components and thereby rendering this particular APV25 card inoperable. The plots presented in Figs A.11a and A.11b demonstrate the signal distortion of all APV25

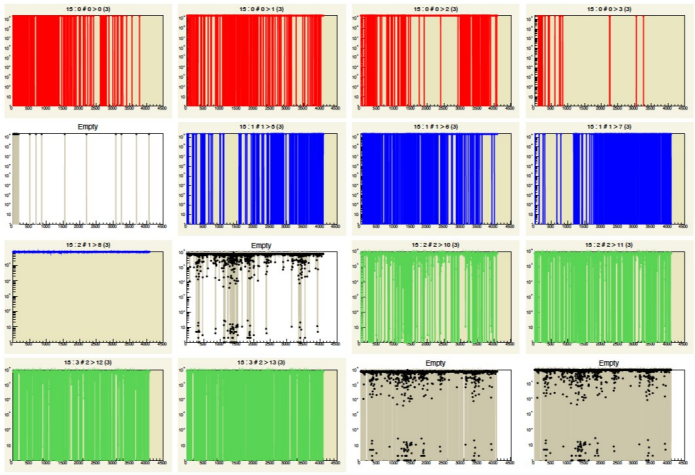

(a)

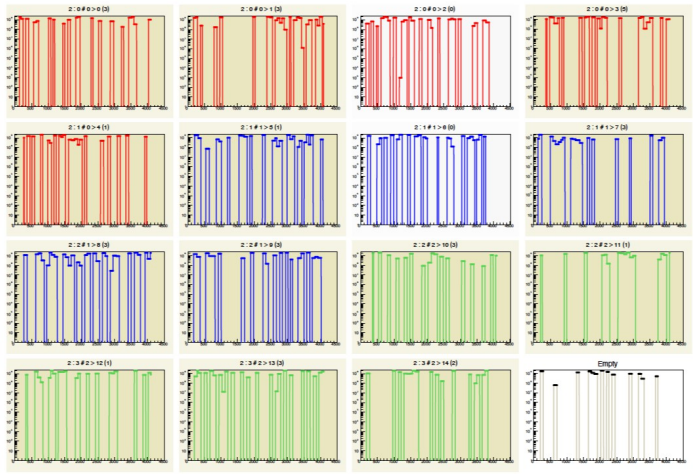

(b)

Figure A.10: A set of 15 low-level histograms associated with APV25 cards that have issues with the clock signal distribution. Top: An example of 15 low-level histograms with a distortion of the clock signal. Bottom: An example of 15 low-level histograms with no clock signal present at the MPD module or APV25 cards.

cards connected to the one failed readout card. This unique failure mode is being included in the characterization because one APV25 card malfunctioning was able to corrupt the signals of all the other APV25 cards connected to the same MPD module, and thus is difficult to diagnose. This particular APV25 card problem is difficult to evaluate as it can manifest as more common HDMI cable connection problems, which were described in the previous section. In this specific case the failed APV25 card was physically replaced. The

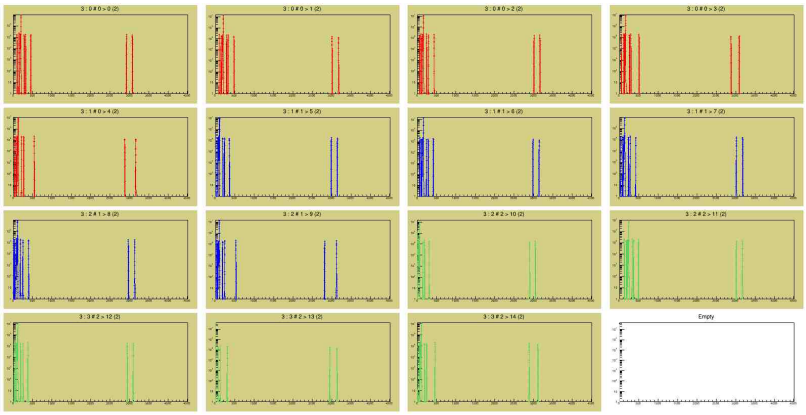

(a)

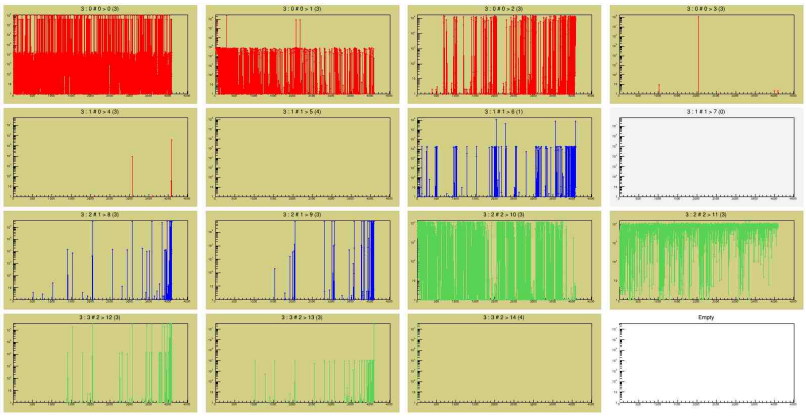

(b)

Figure A.11: Examples of sets of 15 low-level histograms which have corrupted signals from one failed APV25 card. In this case the APV25 card failed because the high voltage from a nearby GEM module interacted with the APV25 card. Top: An example of 15 low-level histograms with corrupted signals from one failed APV25 card, however, the histograms mask the issue. Bottom: An example of 15 low-level histograms with clearly distorted signals, due to one APV25 card having failed and corrupted the signals from the other cards.

GEM high voltage board was also instrumented with further electrically isolating materials.

A.2.3 Common Mode Fluctuation

For a single APV25 card all 128 channels typically fluctuate by a constant offset on a time sample-by-time sample and event-by event-basis. This offset, or shared channel shift, is referred to as the "common mode (CM)." An example of a raw data-frame where the CM

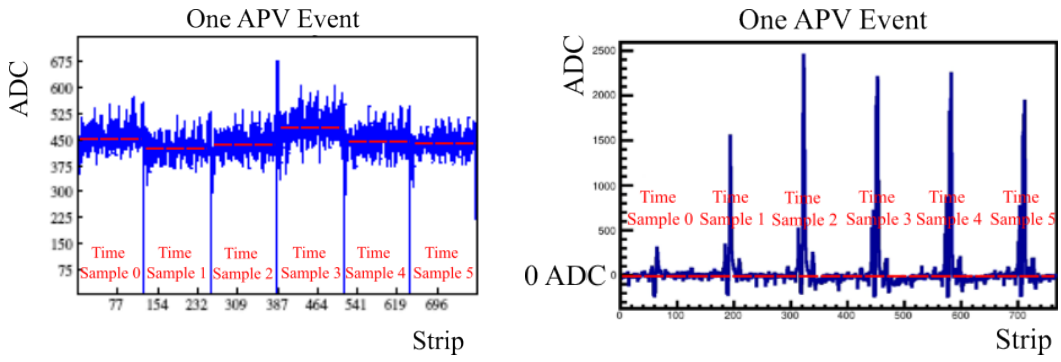

(a) (b)

Figure A.12: An example of digitized signals for one event of a single APV25 card. There are 6 time samples per event. Left: An example of a raw data-frame including dashed red lines to indicate where the CM fluctuation is different for each time sample. Right: An example of a raw data-frame in which common mode subtraction has been applied. This is evident since the baseline value is uniform and at zero ADC value for all 6 time samples. This raw data-frame is in the presence of an ionizing particle in the GEM detector.

has significantly shifted is presented in Fig. A.12a, and the value of the CM for each time sample is represented by the dashed red lines. The CM shift is quite substantial. Therefore the CM must be corrected for each time sample per event for every APV25 card in order to properly extract any amplified signals from ionizing particles in the GEM detectors. This common offset correction is referred to as the "common mode subtraction." Fig. A.12b shows an example of an event with the common mode subtraction applied in the presence of an ionization event in the GEM module.

The common mode algorithm is programmed into the VTP, which actively calculates the CM in real time during data collection. In the case similar to the data frame presented in Fig. A.12a, where no strips in the GEM module detect a charged particle, the CM calculation for a single time sample is straightforward and it would simply be the arithmetic mean of the 128 channels of a given APV25 card. However, for a consideration similar to the data frame shown in Fig. A.12b, where some strips have detected the presence of an ionization event in the GEM module, the CM calculation is nontrivial, in order for the actual ionization data to not bias the CM calculation. The GEM group for the SBS program studied multiple different CM algorithms before implementing one during

data collection. These CM algorithms include the Sorting Method, Danning Method, and Histogramming Method. For a complete description of each of these different methods see Ref. [161]. Each of these methods will be briefly summarized here.

For a given time sample, the Sorting Method ranks all 128 channels of the APV25 card from lowest to highest ADC value. Then based on experiment-specific properties of the GEM detectors, the method drops extremely low and high ADC values. The CM calculation is then the mean of the remaining strips, which have not been removed. Some negative features of the Sorting Method include bias towards higher CM values in high occupancy environments and that requires more memory than available in the VTP module during online data collection.

A more lightweight and less memory-intensive CM algorithm was developed and is referred to as the "Danning Method" [183]. The Danning Method requires that a set of parameters are calculated from a dedicated "pedestal run," data ("pedestal data") from the pedestal run must be taken before the collection of physics data and uploaded to the VTP module. A complete description of pedestal runs, data, and studies will be provided in Sec. A.2.4. By analyzing the pedestal data for a single event, for each APV25 card, a CM mean, μ_{CM}, and CM standard deviation, σ_{CM} are calculated using the Sorting Method. For a given APV25 card, the CM mean and standard deviation are determined from the average of the CM distribution across the six time samples. The CM distributions are obtained by analyzing 5000 events of data from the pedestal run. For each APV25 card the CM mean, μ_{CM}, and CM standard deviation (σ_{CM}) are uploaded to the VTP module for online use. Additionally, for every channel of each APV25 card the pedestal standard deviation, σ_{ped} (explained in A.2.4), is uploaded to the VTP module. The first step in the Danning Method is to consider all of the channels within the range $\mu_{\text{CM}} \pm 5\sigma_{\text{CM}}$ and calculate the average value, denote as μ_{CMi}, for each time sample. The value of this range is chosen to capture channels which did not have an associated signal. The second step is to calculate a second average for each time sample, called μ_{Danning}, for every channel within the range $\mu_{\text{CMi}} \pm n\sigma_{\text{ped}}$, where n is a multiplicative factor determined empirically

and is dependent on the number of time samples in the GEM data stream. The second step ensures that a majority of channels associated with a signal are excluded. This second average, μ_{Danning}, is used as the common mode value for the entire APV25 card for the given time sample. The third step of the Danning Method is to repeat the second step through multiple iterations to obtain a more accurate calculation of the common mode. During the G_M^n and nTPE experiments three iterations of this step were implemented. The Danning Method does not require the channel information to be saved in memory and therefore is ideal to be utilized by the VTP during real time operation. This algorithm was tested to be approximately a factor of 4 faster than the Sorting Method [183]. This method has some shortcomings, which were identified during operation; this includes the CM value shifting over long periods of time throughout the entire run period. Causing the initial $\mu_{\text{CM}} \pm 5\sigma_{\text{CM}}$ range to be invalid, thereby impacting the online CM calculation by either biasing the calculation or resulting in inaccurate CM values. The Danning Method was used by the VTPs for online CM subtraction during G_M^n, nTPE, and G_E^n-II experiments.

To address the shortcomings of the Danning Method, a new method was developed by Andrew Puckett and Sean Jeffas, called the "Histogramming Method." A complete description of the Histogramming Method is included in Ref. [161]. In this dissertation we will not describe the Histogramming Method, as it is an experimental improvement on the Danning Method which was developed during the G_E^n-II experiment but not yet implemented for any online CM subtraction. Furthermore it is not necessary for understanding any data analysis.

A.2.4 Pedestal Offset and Pedestal Standard Deviation

To characterize the electronic noise unique to a single readout channel of a given APV25 card, two key parameters are considered. These key parameters are known as the pedestal offset, μ_{ped}, and the pedestal standard deviation, σ_{ped}. To determine pedestal information, dedicated "pedestal runs" (referred to as "pedestal data") were necessary to be taken throughout the experimental run period. Data for a pedestal run is collected with a random

pulse trigger when both the GEM high voltage is off and the accelerator beam is not being transported to Hall A. Pedestal runs were taken regularly to account for changes in the pedestal profile due to radiation damage, electronics aging, or changes in the environment. Alternatively, if any electronics component along the data acquisition chain from the GEM detector to the VTP was manipulated or replaced (this includes the GEM, APV25 card, MPD, VTP, or any cable) a pedestal run was taken to account for any potential changes in GEM pedestal information. Pedestal information for the GEM detectors was regularly monitored for changes in the pedestal profile during experimental operations.

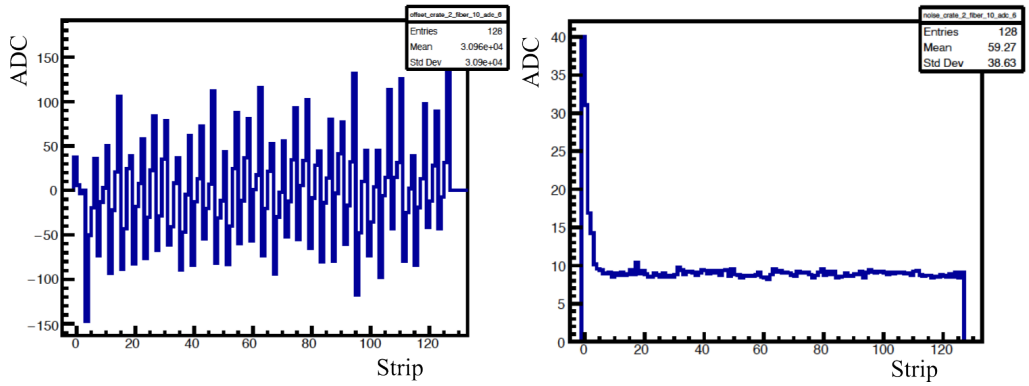

Figure A.13: Pedestal profile for all 128 channels of a single APV25 card, under nominal conditions. Left: Example of a pedestal offset plot. Right: Example of a pedestal standard deviation plot. Note that the standard deviation for most of the 128 channels is approximately constant at an ADC value of 10. For the approximately first 8 channels the pedestal standard deviation has larger value (at maximum about 40 ADC in this plot), which is due to the impedance mismatch of the HDMI cables and is correlated to the cable length.

For a specific readout channel of an APV25 card, it is empirically observed that signals stay at a constant "offset" with respect to the common mode value, with a distribution around the value of the offset. Pedestal distributions for all the GEM detector channels are determined by taking at least several thousands (typically 5000) events of pedestal data. From the pedestal data the distributions for each channel are formed by taking the average value of the common-mode-subtracted signals from each of the six time samples. The mean of this distribution is interpreted as the pedestal offset, μ_{ped}, and distribution

about this offset value is quantified as the standard deviation of the distribution, σ_{ped}. An example of a pedestal offset and pedestal standard deviation for all 128 channels of a single APV25 card, under nominal conditions, are shown in the left and right plots, respectively, of Fig. A.13. The key feature of the pedestal standard deviation plot is the approximately constant ADC value of 10, across most readout channels.

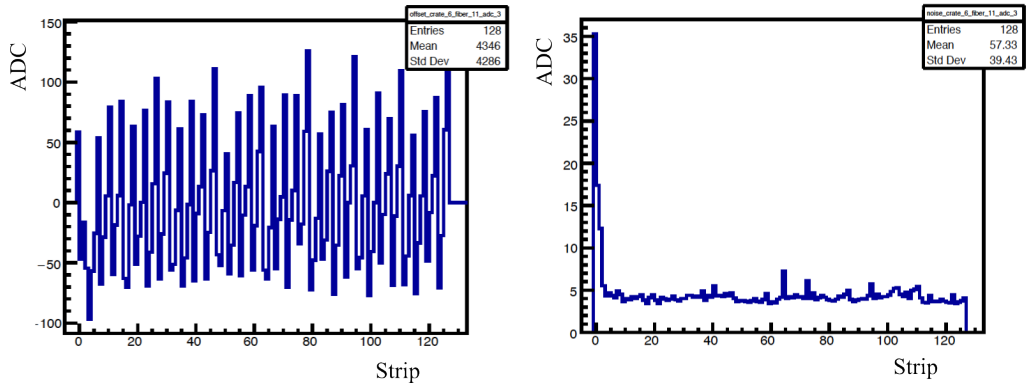

Figure A.14: Typical pedestal profile for all 128 channels of a single disconnected APV25 card. This APV25 card was disconnected from the GEM detector entirely and was not connected to any GEM strips. Left: Pedestal offset plot. Right: Pedestal standard deviation plot. Note that the standard deviation for most of the 128 channels is approximately constant at an ADC value of 5.

In the data analysis the raw signals from the APV25 card are corrected for both the pedestal offset and the common mode value, (both quantities are subtracted from the raw signal). The remaining value of the signal is compared with the pedestal standard deviation, above a certain multiplicative threshold, to determine if a channel has detected an ionization event (known as "fired") or not. If the signal value is above the threshold and has therefore fired, this signal will be moved forward in the online analysis as a "true" signal from a channel in a GEM detector.

By empirically studying the electronic noise through the pedestal offset and pedestal standard deviation plots, one is able to characterize some qualitative diagnostics of the GEM readout electronics. In the remainder of this section we will describe some common GEM readout electronics circumstances and the corresponding pedestal information. As

a reference point, presented in Fig. A.13, a single APV25 card functioning in nominal conditions and fully connected to the GEM detector has a pedestal standard deviation of approximately constant value of 10 ADC units for most of the 128 readout channels. Though not a common diagnostic occurrence, rather for completeness, a single APV25 card functioning in nominal conditions and entirely disconnected from GEM readout strips is shown in Fig. A.14. The pedestal standard deviation for this disconnected APV25 card is characterized as having an approximately constant value of 5 ADC units for most of the 128 channels; this ADC information represents the electronic noise of the APV25 card, backplane, MPD, and VTP module. A somewhat more common failure mode for the

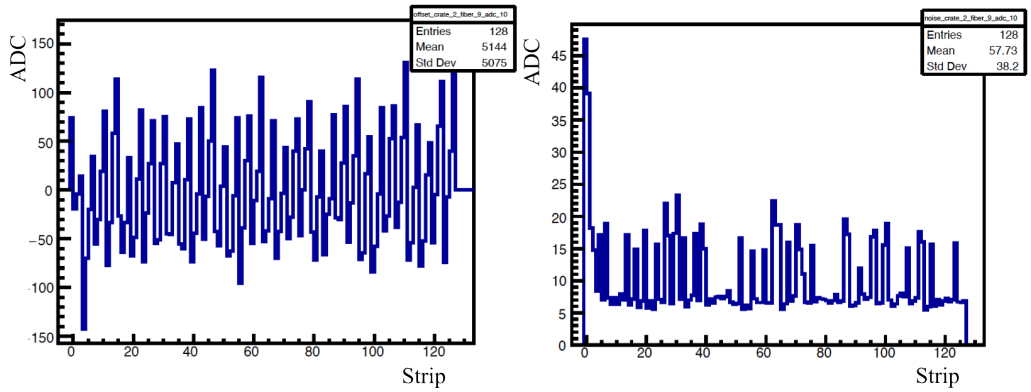

Figure A.15: Pedestal profile for all 128 channels of a single APV25 card. This example pedestal profile corresponds to an APV25 card that has one of the following conditions: damaged readout strips, damaged readout connector, or is partially connected to readout strips. Left: Pedestal offset plot. Right: Pedestal standard deviation plot. Note that the standard deviation for a selection of the readout channels is still varying around the baseline value of 10 ADC units. However, some of the readout channels see a larger standard deviation compared to the baseline.

GEM readout electronics is a single APV25 card which most likely has one of the following conditions: a partial connection to the GEM readout strips, damaged strip connectors at the APV25 card, or damaged strips at the GEM detector connector. The pedestal information for such an APV25 card is presented in Fig. A.15. The notable feature of this type of diagnostic condition is that the pedestal standard deviation has larger amplitude and more distorted features of the signal varying around the nominal baseline value of

$\simeq$ 10 ADC units. One of the most common failure modes for the GEM data acquisition components is some quantity of APV25 cards connected to one or more backplanes having partially or fully disconnected HDMI cables along the electronics path from the APVs on backplanes to the MPDs, including any HDMI patch panels. An example of the pedestal information associated with one such APV25 card is presented in Fig. A.16. However, plots similar to Fig. A.16 generally manifest in consecutive groups equal to or less than the total number of slots on a given APV25 backplane. The notable feature for this example of partially or fully disconnected HDMI cables is that the pedestal standard deviation has large amplitude distortions around the baseline of 5 ADC units which corresponds to a fully disconnected APV25 card. The pedestal information presented in Fig. A.16 is only one example of how the signal is distorted due to improperly connected HDMI cables; other plot characterizations exist and thus the general idea of large signal distortion should be considered.

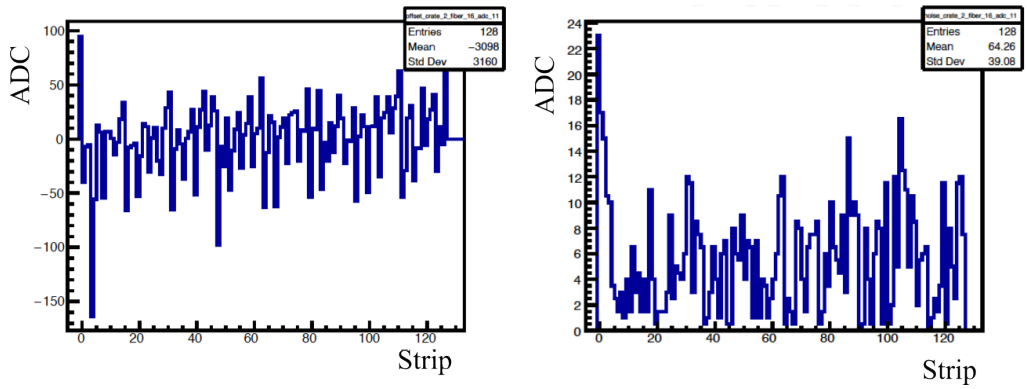

Figure A.16: Pedestal profile for all 128 channels of a single APV25 card. This example APV25 card had issues with improperly connected HDMI cables. When these plots manifest they generally occur in quantities equal to or less than the total number of slots on a given GEM backplane. Left: Pedestal offset plot. Right: Pedestal standard deviation plot. Note that the standard deviation for most of the 128 channels is distorted or amplified around the baseline value for a fully disconnected APV25 card. This standard deviation value is significantly different compared to the pedestal standard deviation under nominal conditions as presented in Fig. A.13.

A.2.5 Online Zero Suppression

In the online data processing, both CM subtraction (as described in Sec. A.2.3) and pedestal subtraction (as described in Sec. A.2.4) were applied to the raw GEM signals in the data collected. The implementation of both of these subtractions cause the baseline ADC values to be near zero. The purpose of online zero suppression is to not record in data any low ADC value channels, which represent signals due only to electronics noise. First, for a given APV25 channel and event, the sum of all 6 time samples is computed and compared to $n\sigma_{ped}$; for the case of G_M^n and nTPE $n = 5$. For any APV25 channels where the sum of 6 time samples is greater than $5\sigma_{ped}$, these channels are considered to have fired from an ionization event and the VTP forwards their data into the data stream where they are recorded. For any APV25 channels where the sum of 6 time samples is below the $5\sigma_{ped}$ threshold, the data are discarded. Thus as any channels within 5 sigma of the pedestal

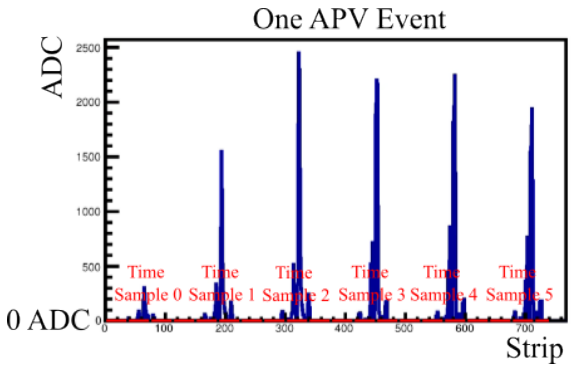

Figure A.17: An example of digitized signal for one event of one APV25 card in the presence of an ionization event in the GEM module. In this case online zero suppression was enabled during data collection. The notable features of online zero suppression are both pedestal and common mode subtraction. For each channel present in the plot the ADC sum per channel must be greater than a value of $5\sigma_{ped}$ to be recorded in the data stream.

noise are not considered a "true" signal and thus not recorded. This process of comparing APV25 channel signals per event in real time to a multiplicative factor of the pedestal standard deviation is known as "online zero suppression." Fig. A.17 shows a GEM data-frame that contains channels that have fired due to the presence of an ionization event in a

GEM module, when online zero suppression is enabled in the data stream. By comparing Figs. A.1b and A.17, one is able to see the significant data reduction provided by the zero suppression. During the GMn/nTPE experiments the implementation of the online zero suppression reduced the data read out from the GEM detectors by an approximate factor of 4 or 5"

A.2.6 Offline GEM Analysis

After the GEM decoding of the raw data, higher order analyses are performed, including 1D clustering, 2D hit association, and track-finding. These analyses are completed after data have been collected and as such are known as "offline" analyses. The entire GEM offline analysis, and the analysis of other detector systems, are completed using a software package called SBS-Offline [169]. The SBS-Offline software package inherits important key libraries from the Hall A standard analysis software package [168]. A summary of the important details of the calorimeter search region, 1D clustering, 2D hit association, and track-finding algorithm software will be provided in the remainder of this section.

Calorimeter Search Region

During the G_M^n and nTPE experiments there were, at most, 41,984 GEM readout channels and the GEM detectors were subject to a high occupancy environment. Given these conditions, considering the entire active areas of all the GEM detectors within the BigBite Spectrometer would make the clustering and track-finding algorithms computationally difficult. An event display for the GEM detectors in the BigBite Spectrometer for a single triggered event is presented in Fig. A.18. In Fig. A.18, the fired strips on each GEM module are shown as a particular color, a color gradient corresponding to the ADC value is included. From this example event, it is evident that the number of strip combinatorics is unmanageable if the active areas for all GEM modules are considered. To make the higher-order GEM detector analysis computationally functional, a calorimeter search region (or calorimeter constraint) was implemented. The calorimeter search region is defined

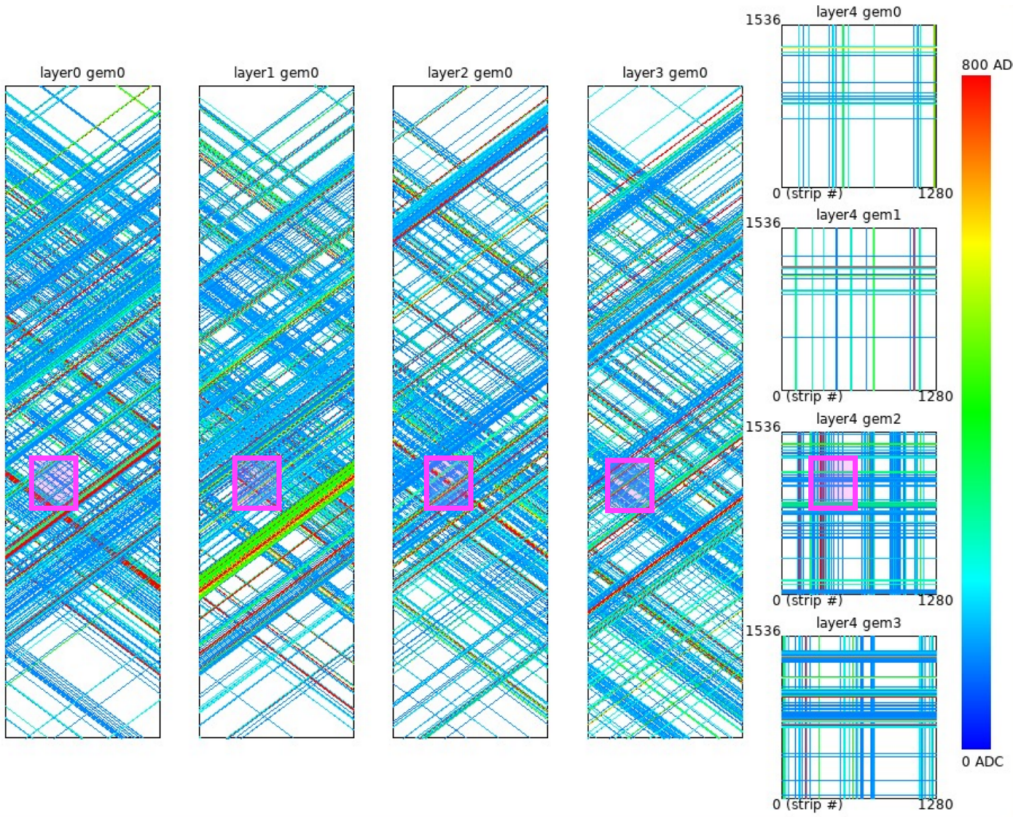

Figure A.18: A GEM event display showing an example of a single triggered event in the BigBite GEM detectors, during the G_M^n and nTPE experiments. Each GEM layer with fired strips is presented; the strips are assigned a color gradient corresponding to their ADC value. The overlayed magenta squares represent the calorimeter search region, which is defined by the highest-energy cluster in BBCal. Only strips within this calorimeter search region are considered in the tracking algorithm.

by the highest energy cluster in BBCal and enforces that the GEM cluster or strip must be within a particular distance in the transverse direction from the x,y location of the BBCal cluster. The calorimeter search region is defined to be conservative and effectively forms a square spatial constraint on valid hits for each GEM layer. The calorimeter search region is shown as overlayed magenta squares in Fig. A.18. The calorimeter search region serves an important role in the GEM data analysis, as it ensures computationally expensive processes (like track reconstruction and 2D Hit association) are only performed in this region of each GEM layer.

1-Dimensional Clustering

As described in Sec. 5.1.5, GEM detectors have two strip axes. The first step after GEM raw data decoding is a search for one dimensional clusters of strips along each axis. A complete documentation of the GEM Clustering algorithm is embedded within the source code which is available in Ref. [169]. A complete technical summary of the 1D Clustering algorithm is also presented in Ref. [161]. This section will describe the essential features of the SBS GEM 1D clustering algorithm.

First, for a given strip direction, the local strip maxima are determined from the ADC sum over all time samples. Determining the local strip maxima involves ensuring the local strip maxima are above an ADC sum threshold and within a time window. Multiple steps in the clustering algorithm involve iteratively evaluating the properties of the local strip maxima and the neighboring strips, and ensuring that additional strips pass certain ADC, timing, and strip location cuts. After this iterative cut evaluation, local strip maxima and the neighboring strips which pass this determination are used to form 1D clusters. The cluster position is then checked to see if the cluster in the calorimeter search region; any clusters not in the search region are discarded. More specifically, the evaluation of the cluster in the calorimeter search region involves projecting, in three-dimensions, the cluster position of the calorimeter to each GEM layer and determining if strips with 1D clusters are in the projected search region on a given GEM layer. Any clusters that are not above the ADC sum threshold or are made from only one strip are removed. The 1D clusters are formed along both sets of readout strips for a particular GEM module. A typical minimum ionizing particle will create clusters along one strip direction in the range from two (minimum cluster size enforced) to five, typically; sometimes clusters can be even larger.

2-Dimensional Hit Association

For any clusters passing the 1-dimensional cluster analysis phase, 2-dimensional cluster formation is considered from these 1D clusters. These 2D clusters will be referred to as "hits" or "hit associations." For every possible 2D combination, the first step is to evaluate if the GEM strip positions associated with a cluster are within the calorimeter search region as projected to a given GEM layer. The remaining steps evaluate ADC and timing correlations between the two strip axes 1D clusters. For all sets of 1D clusters passing these requirements, 2D Hit associations are formed for each GEM module on an event-by-event basis.

Track-Finding Algorithm

A comprehensive description of the GEM track-finding algorithm is within the source code and is available in Ref. [169]. A technical summary of the GEM track-finding algorithm is also provided in Ref. [161]. This section will summarize the important components of the track-finding algorithm and how "good tracks" are determined from 2D hit associations. After the completion of the 2D hit association, for each GEM layer, a set of 2D hits are available as potentially being on a track. From this set of hits, given the multiple GEM layers, an iterative search process evaluates combinations of (x,y,z) hits that form a straight line through the GEM layers to form tracks.

A prerequisite check for a given event, before any track finding processes, is to ensure a minimum number of GEM layers have hits. For the G_M^n and nTPE experiments, the minimum number of GEM layers with hits is three. The first step in the track finding process is segmenting the active area of each GEM layer into small grid bins. The next step is to iteratively select all possible combinations of hits between the front and back tracking GEM layers and form potential tracks from each combination. At this phase of track finding, the potential track is also projected back to the target and forward to the calorimeter search region in BBCal. With valid hit combinations identified as those going

through both the front and back tracking layers, these potential tracks are looped through to identify any intermediate layers with hits near the location of the projected track. Now that there are potential hits on all of the GEM layers, straight 3D line fits are performed on the hit combinations and the fit with the best χ^2 per degree of freedom is determined as the track. After this last step a set of good tracks has been determined, that can be used for later physics analysis.

Appendix B

Supplementary Data Analysis Information

B.1 Cut Region Optimization Supplemental

This section provides example plots, for every cut variable, for the analysis procedures described in Sec. 6.4.2. Figure B.1 shows example plots used for optimizing cut regions for good electron cut variables. Figure B.2 shows example plots used for optimizing cut regions for quasi-elastic event selection cut variables. For a comprehensive set of plots associated with cut region optimization for every relevant kinematic and SBS magnet field setting see Ref. [178].

B.2 Cut Systematic Supplemental

This section provides example graphs and plots used for quantifying systematic effects for cut variables not explicitly described in Sec. 6.4.2. Figure B.3 shows $R_{sf}^{n/p}$ graphs for the remaining single boundary cut variables: E_{PS}, N_{GEMhits}, and E_{HCal}. Figures B.4, B.5, and B.6 show $R_{sf}^{n/p}$ graphs for both boundary variations for the remaining separate double boundary cut variables: Δt, W^2, E_{BBCal}, $x_{\text{HCal}}^{\text{exp}}$, $y_{\text{HCal}}^{\text{exp}}$, x_{BB}, and y_{BB}. Figure B.7 shows the $R_{sf}^{n/p}$ graph for the Δy, and is the only remaining symmetric double boundary cut vari-

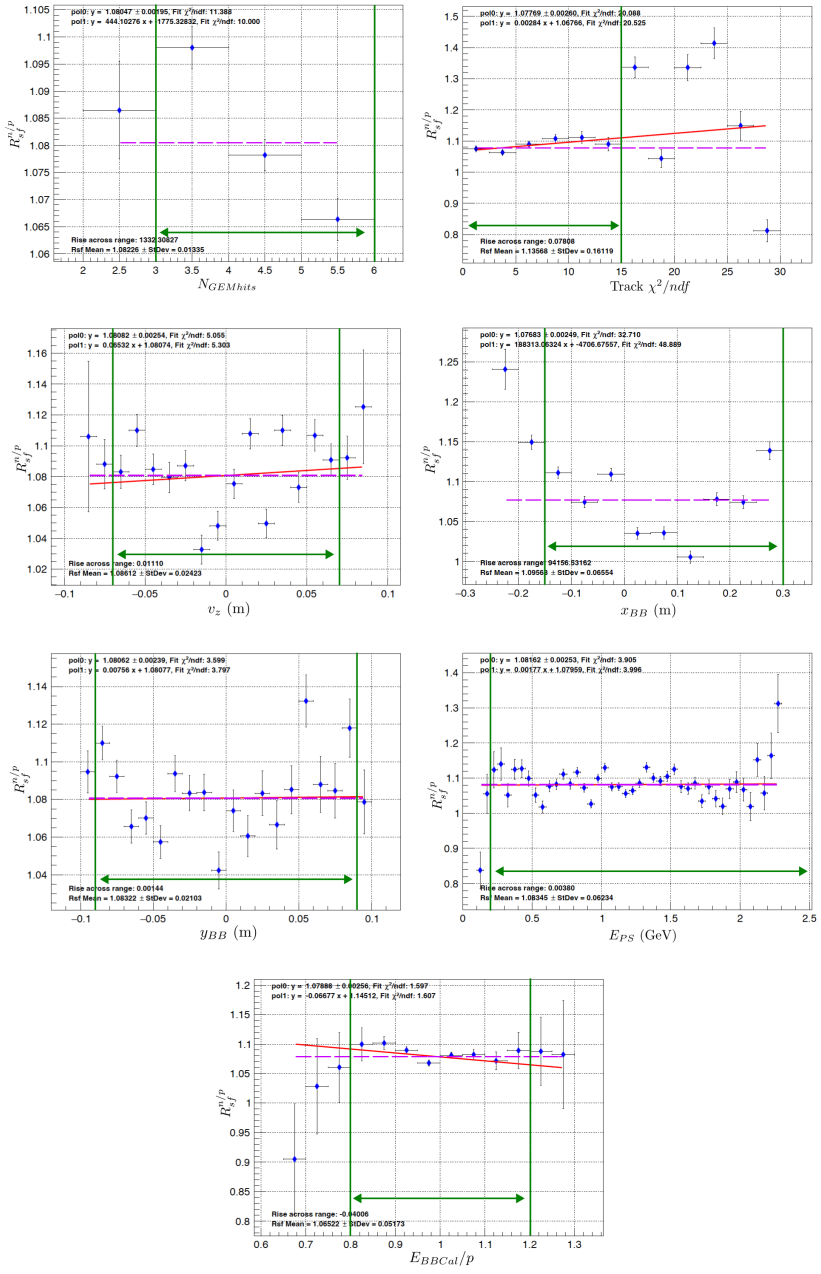

Figure B.1: Example plots used for determining optimal cut regions. The cut variables presented in these plots correspond to good electron cuts. These plots are produced from data and MC information from the SBS-8 ($Q^2 = 4.5$ (GeV/c)^2) kinematic and SBS magnet 70% field setting. General details about the information presented in a given plot will be described in Sec. 6.4.2.

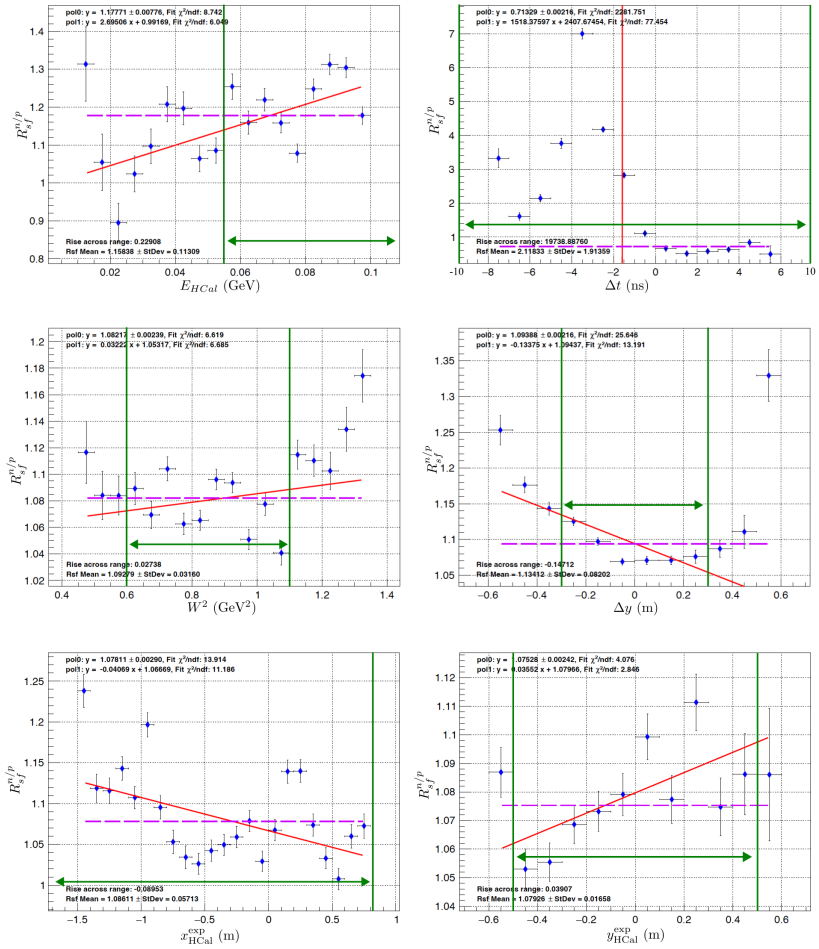

Figure B.2: Example plots used for determining optimal cut regions. The cut variables presented in these plots correspond to cuts which are typically more sensitive to selecting quasi-elastic nucleons. These plots are produced from data and MC information from the SBS-8 ($Q^2 = 4.5$ (GeV/c)^2) kinematic and SBS magnet 70% field setting. General details about the information presented in a given plot will be described in Sec. 6.4.2.

able. For a comprehensive set of plots associated with cut region systematic quantification for every relevant kinematic and SBS magnet field setting see Ref. [178].

B.3 Compromised HCal Modules

Figure B.8 shows the channel (or module) map of the top and bottom structures of HCal with channels whose ADC spectra had abnormal distributions.

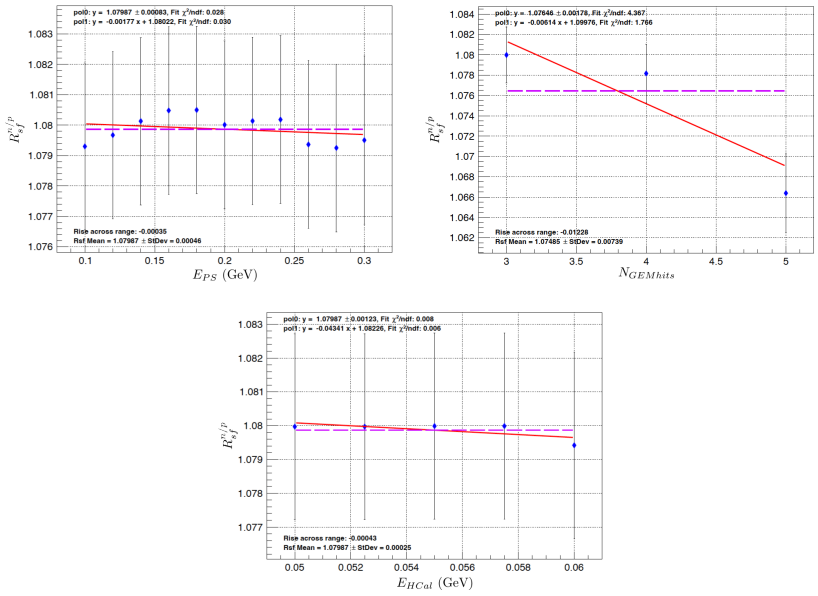

Figure B.3: Example plots for the remaining cut variables which are in the single boundary (or threshold) category for systematic quantification. These plots are produced from data and MC information from the SBS-8 ($Q^2 = 4.5$ (GeV/c)^2) kinematic and SBS magnet 70% field setting. General details about the information presented in a given plot will be described in Sec. 6.4.2.

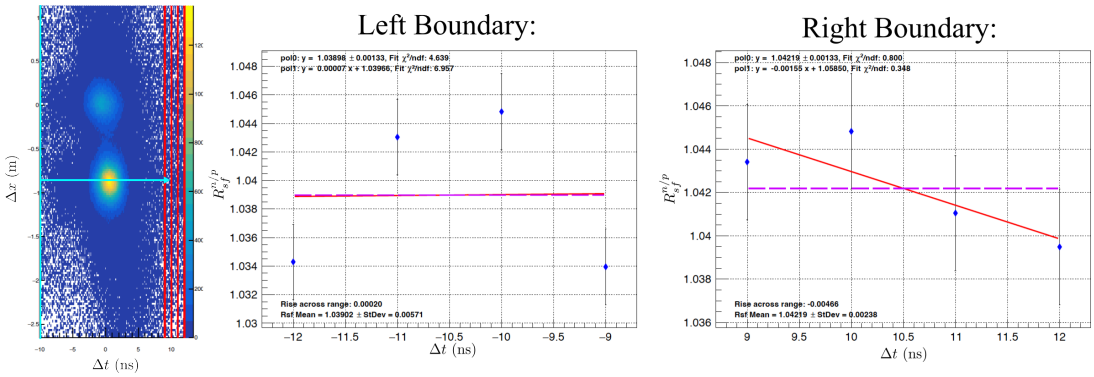

Figure B.4: Example plots for the Δt cut variable used for the systematic quantification. The 2D plot is present to show the variation of the right boundary condition. Both boundary $R_{sf}^{n/p}$ graphs are presented. These plots are produced from data and MC information from the SBS-8 ($Q^2 = 4.5$ (GeV/c)^2) kinematic and SBS magnet 70% field setting. General details about the information presented in a given plot will be described in Sec. 6.4.2.

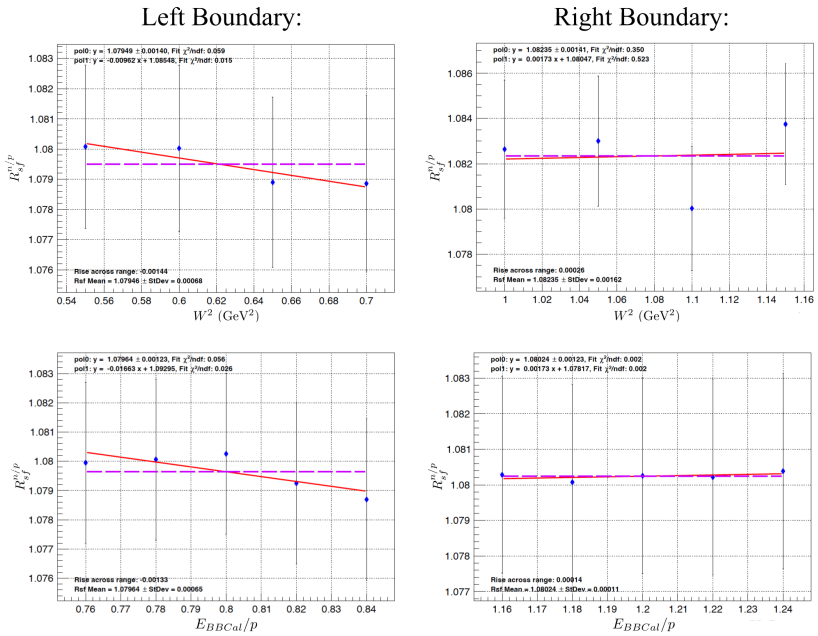

Figure B.5: Example $R_{sf}^{n/p}$ graphs for both boundary variations of the cut variables W^2, and E_{BBCal}/p. These plots are produced from data and MC information from the SBS-8 ($Q^2 = 4.5$ (GeV/c)^2) kinematic and SBS magnet 70% field setting. General details about the information presented in a given plot will be described in Sec. 6.4.2.

B.4 Data/MC Total Fit Shift Parameters

The parameters which account for shifts in the centroids of the MC neutron and proton distributions during the data/MC comparison procedure are presented in Tab. B.1.

Setting	δ_n shift parameter (m)	δ_p shift parameter (m)
SBS-8 50%	0.0064	-0.0375
SBS-8 70%	0.0086	-0.0388
SBS-8 100%	0.0155	-0.0375
SBS-9 70%	-0.0271	-0.0475

Table B.1: The parameters from the total fit procedure, described in Sec. 6.4.1, which account for the shifting centroids of MC neutron and proton distributions.

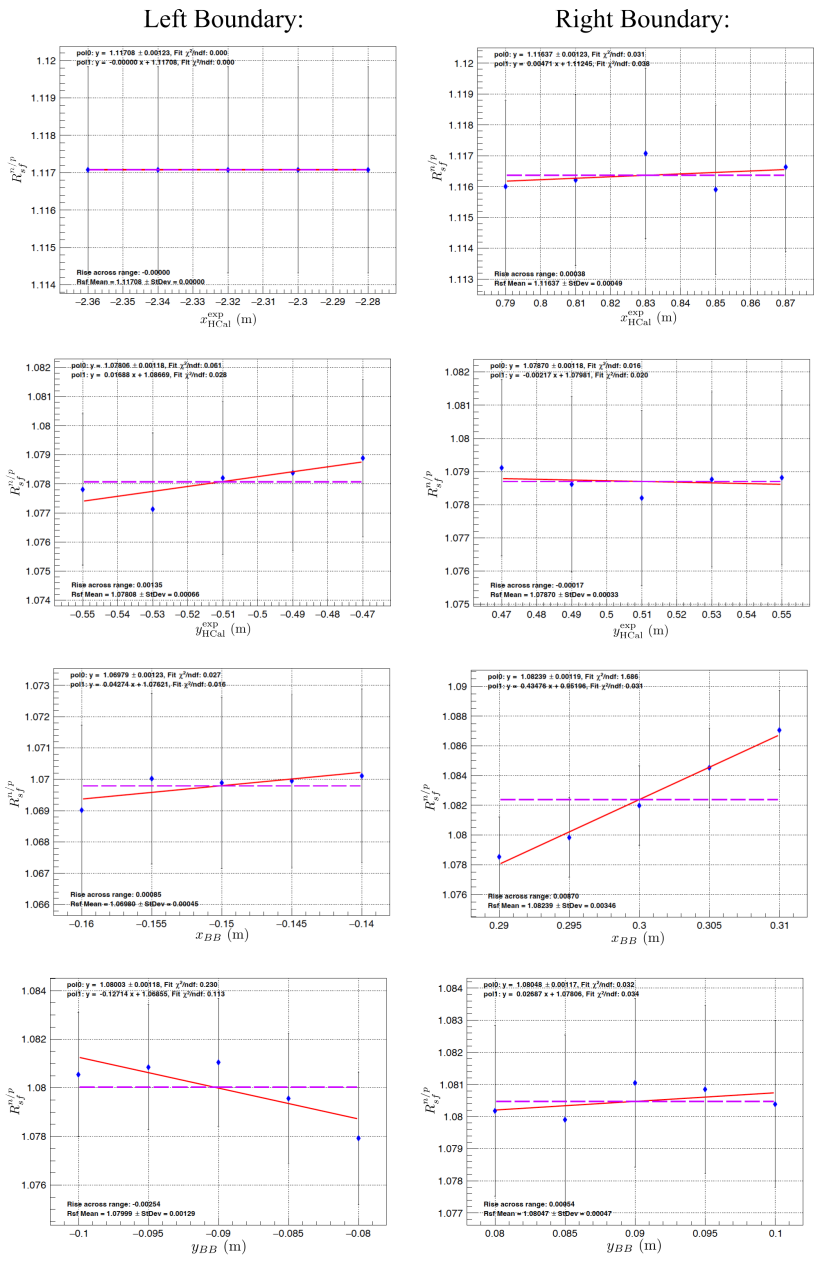

Figure B.6: Example $R_{sf}^{n/p}$ graphs for both boundary variations of the cut variables $x_{\mathrm{HCal}}^{\mathrm{exp}}$, $y_{\mathrm{HCal}}^{\mathrm{exp}}$, x_{BB}, and y_{BB}. These plots are produced from data and MC information from the SBS-8 ($Q^2 = 4.5$ (GeV/c)^2) kinematic and SBS magnet 70% field setting. General details about the information presented in a given plot will be described in Sec. 6.4.2.

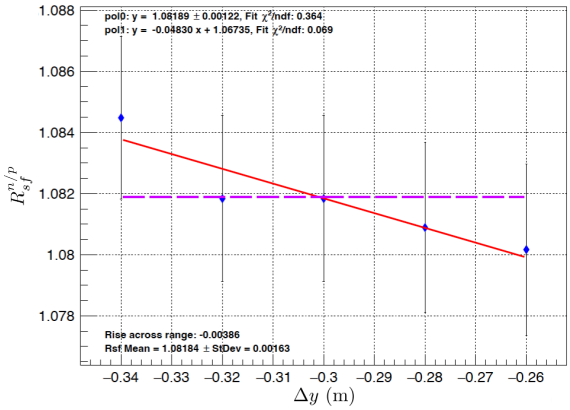

Figure B.7: Example $R_{sf}^{n/p}$ graph for the symmetric double boundary the cut variable Δy. These plots are produced from data and MC information from the SBS-8 (Q^2 = 4.5 (GeV/c)^2) kinematic and SBS magnet 70% field setting. General details about the information presented in a given plot will be described in Sec. 6.4.2.

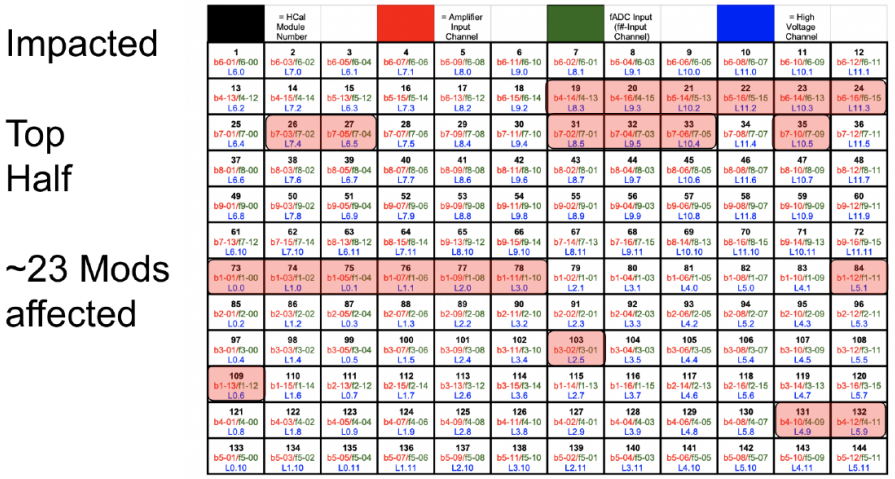

(a) Top Half of HCal

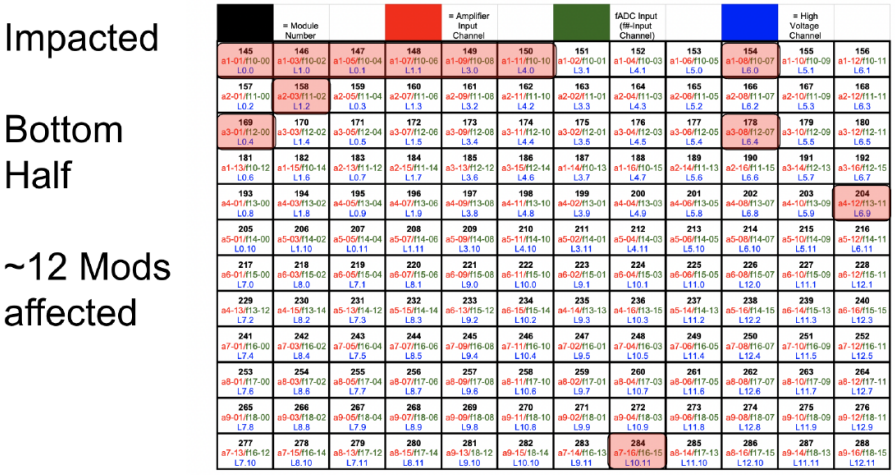

(b) Bottom Half of HCal

Figure B.8: A map for all of the channels (modules) of the HCal detector, separated into top and bottom halves. Any channels which are shaded in red are associated with abnormal distributions for ADC spectra. The studies of HCal ADC spectra and the aggregated information were conducted and completed by S. Seeds. These plots are reproduced from Ref. [140].

References

[1] J. J. Thomson, Cathode rays, The London, Edinburgh, and Dublin Philosophical Magazine and Journal of Science **44**, 293 (1897).

[2] H. Gegier and E. Marsden, On a diffuse reflection of the α-particles, Proceedings of the Royal Society of London. Series A, Containing Papers of a Mathematical and Physical Character **82**, 495 (1909).

[3] E. Rutherford, The scattering of α and β particles by matter and the structure of the atom, Philosophical Magazine **92**, 379 (1911).

[4] E. Rutherford, Collision of α particles with light atoms. iv. an anomalous effect in nitrogen, Philosophical Magazine **90**, 31 (1919).

[5] J. Chadwick, The existence of a neutron, Proceedings of the Royal Society of London. Series A, Containing Papers of a Mathematical and Physical Character **136**, 692 (1932).

[6] P. A. M. Dirac, The quantum theory of the electron, Proceedings of the Royal Society of London. Series A, Containing Papers of a Mathematical and Physical Character **117**, 610 (1928).

[7] I. Estermann, R. Frisch, and O. Stern, Magnetic moment of the proton, Nature **132**, 169 (1933).

[8] L. W. Alvarez and F. Bloch, A quantitative determination of the neutron moment in absolute nuclear magnetons, Physical review **57**, 111 (1940).

[9] R. Hofstadter, Electron scattering and nuclear structure, Reviews of Modern Physics **28**, 214 (1956).

[10] S. Navas *et al.* (Particle Data Group Collaboration), Review of particle physics, Phys. Rev. D **110**, 030001 (2024).

[11] A. Arbey and F. Mahmoudi, Dark matter and the early Universe: A review, Progress in Particle and Nuclear Physics **119**, 103865 (2021).

[12] F. Halzen and A. D. Martin, *Quarks And Leptons: An Introductory Course In Modern Particle Physics* (John Wiley & Sons, 1984).

[13] M. E. Peskin and D. V. Schroeder, *An Introduction to Quantum Field Theory* (Addison-Wesley, 1995).

[14] A. Denig and G. Salmè, Nucleon electromagnetic form factors in the timelike region, Progress in Particle and Nuclear Physics **68**, 113 (2013).

[15] F. J. Ernst, R. G. Sachs, and K. C. Wali, Electromagnetic Form Factors of the Nucleon, Phys. Rev. **119**, 1105 (1960).

[16] R. G. Sachs, High-Energy Behavior of Nucleon Electromagnetic Form Factors, Phys. Rev. **126**, 2256 (1962).

[17] L. N. Hand, D. G. Miller, and R. Wilson, Electric and Magnetic Form Factors of the Nucleon, Rev. Mod. Phys. **35**, 335 (1963).

[18] V. Punjabi, C. F. Perdrisat, M. K. Jones, E. J. Brash, and C. E. Carlson, The structure of the nucleon: Elastic electromagnetic form factors, Eur. Phys. J. A **51**, 10.1140/epja/i2015-15079-x (2015).

[19] A. I. Akhiezer and M. P. Rekalo, Polarization Phenomena in Electron Scattering by Protons in the High-Energy Region, Soviet Physics Doklady **13**, 572 (1968).

[20] A. I. Akhiezer and M. P. Rekalo, Polarization effects in the scattering of leptons by hadrons, Sov. J. Particles Nucl. **4**, 277 (1974).

[21] N. Dombey, Scattering of Polarized Leptons at High Energy, Rev. Mod. Phys. **41**, 236 (1969).

[22] R. G. Arnold, C. E. Carlson, and F. Gross, Polarization transfer in elastic electron scattering from nucleons and deuterons, Phys. Rev. C **23**, 363 (1981).

[23] G. Cates *et al.*, Measurement of the neutron electromagnetic form factor ratio G_E^n/G_M^n at high Q^2, Jefferson Lab experiment proposal E12-09-016 (2009).

[24] G. Cates *et al.*, Measurement of the neutron electromagnetic form factor ratio G_E^n/G_M^n at high Q^2, Jefferson Lab experiment proposal E12-09-016 (2009).

[25] J. Arrington, P. Blunden, and W. Melnitchouk, Review of two-photon exchange in electron scattering, Progress in Particle and Nuclear Physics **66**, 782 (2011).

[26] A. Afanasev, P. G. Blunden, D. Hasell, and B. A. Raue, Two-photon exchange in elastic electron–proton scattering, Progress in Particle and Nuclear Physics **95**, 245 (2017).

[27] A. Afanasev *et al.*, Radiative corrections: from medium to high energy experiments, Eur. Phys. J. A **60**, 91 (2024).

[28] F. Gross *et al.*, 50 years of quantum chromodynamics, Eur. Phys. J. C **83**, 1125 (2023).

[29] S. Galster, H. Klein, J. Moritz, K. Schmidt, D. Wegener, and J. Bleckwenn, Elastic electron-deuteron scattering and the electric neutron form factor at four-momentum transfers 5 $fm^{-2} < q^2 < 14$ fm^{-2}, Nuclear Physics B **32**, 221 (1971).

[30] J. J. Kelly, Simple parametrization of nucleon form factors, Phys. Rev. C **70**, 068202 (2004).

[31] Z. Ye, J. Arrington, R. J. Hill, and G. Lee, Proton and neutron electromagnetic form factors and uncertainties, Physics Letters B **777**, 8 (2018).

[32] G. Lee, J. R. Arrington, and R. J. Hill, Extraction of the proton radius from electron-proton scattering data, Phys. Rev. D **92**, 013013 (2015).

[33] J. C. Bernauer *et al.* (A1 Collaboration), Electric and magnetic form factors of the proton, Phys. Rev. C **90**, 015206 (2014).

[34] J. C. Bernauer *et al.* (A1 Collaboration), High-precision determination of the electric and magnetic form factors of the proton, Phys. Rev. Lett. **105**, 242001 (2010).

[35] W. Xiong *et al.*, A small proton charge radius from an electron–proton scattering experiment, Nature **575**, 147 (2019).

[36] P. N. Kirk *et al.*, Elastic Electron-Proton Scattering at Large Four-Momentum Transfer, Phys. Rev. D **8**, 63 (1973).

[37] A. F. Sill *et al.*, Measurements of elastic electron-proton scattering at large momentum transfer, Phys. Rev. D **48**, 29 (1993).

[38] M. E. Christy *et al.*, Form Factors and Two-Photon Exchange in High-Energy Elastic Electron-Proton Scattering, Phys. Rev. Lett. **128**, 102002 (2022).

[39] T. Janssens, R. Hofstadter, E. B. Hughes, and M. R. Yearian, Proton Form Factors from Elastic Electron-Proton Scattering, Phys. Rev. **142**, 922 (1966).

[40] C. Berger, V. Burkert, G. Knop, B. Langenbeck, and K. Rith, Electromagnetic form factors of the proton at squared four-momentum transfers between 10 and 50 fm^{-2}, Physics Letters B **35**, 87 (1971).

[41] L. E. Price, J. R. Dunning, M. Goitein, K. Hanson, T. Kirk, and R. Wilson, Backward-Angle Electron-Proton Elastic Scattering and Proton Electromagnetic Form Factors, Phys. Rev. D **4**, 45 (1971).

[42] W. Bartel, F. Büsser, W. Dix, R. Felst, D. Harms, H. Krehbiel, P. Kuhlmann, J. McElroy, J. Meyer, and G. Weber, Measurement of proton and neutron electromagnetic form factors at squared four-momentum transfers up to 3 $(\mathrm{GeV/c})^2$, Nuclear Physics B **58**, 429 (1973).

[43] F. Borkowski, G. Simon, V. Walther, and R. Wendling, Electromagnetic form factors of the proton at low four-momentum transfer, Nuclear Physics B **93**, 461 (1975).

[44] L. Andivahis *et al.*, Measurements of the electric and magnetic form factors of the proton from Q^2=1.75 to 8.83 $(\mathrm{GeV/c})^2$, Phys. Rev. D **50**, 5491 (1994).

[45] M. E. Christy *et al.*, Measurements of electron-proton elastic cross sections for 0.4 $< Q^2 <$ 5.5 $(\mathrm{GeV/c})^2$, Phys. Rev. C **70**, 015206 (2004).

[46] I. A. Qattan *et al.*, Precision Rosenbluth Measurement of the Proton Elastic Form Factors, Phys. Rev. Lett. **94**, 142301 (2005).

[47] B. D. Milbrath *et al.* (Bates FPP Collaboration), Comparison of polarization observables in electron scattering from the proton and deuteron, Phys. Rev. Lett. **80**, 452 (1998).

[48] M. K. Jones *et al.*, G_{Ep}/G_{Mp} ratio by polarization transfer in $\vec{e}p \to e\vec{p}$, Physical Review Letters **84**, 1398 (2000).

[49] O. Gayou *et al.* (The Jefferson Lab Hall A Collaboration), Measurements of the elastic electromagnetic form factor ratio $\mu_p G_{\mathrm{ep}}/G_{\mathrm{mp}}$ via polarization transfer, Phys. Rev. C **64**, 038202 (2001).

[50] T. Pospischil *et al.*, Measurement of G_{Ep}/G_{Mp} via polarization transfer at $Q^2 = 0.4$ $(\mathrm{GeV/c})^2$, Eur. Phys. J. A 10.1007/s100500170046 (2001).

[51] O. Gayou *et al.* (Jefferson Lab Hall A Collaboration), Measurement of G_{E_p}/G_{M_p} in $\vec{e}p \to e\vec{p}$ to $Q^2 = 5.6$ GeV^2, Phys. Rev. Lett. **88**, 092301 (2002).

[52] V. Punjabi *et al.* (Jefferson Lab Hall A Collaboration), Proton elastic form factor ratios to $Q^2 = 3.5$ GeV^2 by polarization transfer, Phys. Rev. C **71**, 055202 (2005).

[53] G. MacLachlan *et al.*, The ratio of proton electromagnetic form factors via recoil polarimetry at $Q^2 = 1.13$ (GeV/c)^2, Nuclear Physics A **764**, 261 (2006).

[54] A. J. R. Puckett *et al.*, Recoil Polarization Measurements of the Proton Electromagnetic Form Factor Ratio to $Q^2 = 8.5$ GeV^2, Phys. Rev. Lett. **104**, 242301 (2010).

[55] M. Paolone *et al.* (E03-104 Collaboration), Polarization Transfer in the ^{4}He$(\vec{e}, e' \vec{p})^3$**H** Reaction at $Q^2 = 0.8$ and 1.3 (GeV/c)^2, Phys. Rev. Lett. **105**, 072001 (2010).

[56] M. Meziane *et al.* (GEp2γ Collaboration), Search for Effects Beyond the Born Approximation in Polarization Transfer Observables in $e\vec{p}$ Elastic Scattering, Phys. Rev. Lett. **106**, 132501 (2011).

[57] G. Ron *et al.* (The Jefferson Lab Hall A Collaboration), Low-Q^2 measurements of the proton form factor ratio $\mu_p G_E/G_M$, Phys. Rev. C **84**, 055204 (2011).

[58] X. Zhan *et al.*, High-precision measurement of the proton elastic form factor ratio $\mu_p G_E/G_M$ at low Q^2, Physics Letters B **705**, 59 (2011).

[59] A. J. R. Puckett *et al.* (The Jefferson Lab Hall A Collaboration), Final analysis of proton form factor ratio data at $Q^2 = 4.0$, 4.8, and 5.6 GeV^2, Phys. Rev. C **85**, 045203 (2012).

[60] A. J. R. Puckett *et al.*, Polarization transfer observables in elastic electron-proton scattering at $Q^2 = 2.5$, 5.2, 6.8, and 8.5 GeV^2, Phys. Rev. C **96**, 055203 (2017).

[61] M. K. Jones *et al.* (Resonance Spin Structure Collaboration), Proton G_E/G_M from beam-target asymmetry, Phys. Rev. C **74**, 035201 (2006).

[62] C. B. Crawford *et al.*, Measurement of the Proton's Electric to Magnetic Form Factor Ratio from $^1\overrightarrow{\mathrm{H}}\,(\overrightarrow{e}, e' p)$, Phys. Rev. Lett. **98**, 052301 (2007).

[63] A. Liyanage *et al.* (SANE Collaboration), Proton form factor ratio $\mu_p G_E^p / G_M^p$ from double spin asymmetry, Phys. Rev. C **101**, 035206 (2020).

[64] G. Simon, C. Schmitt, F. Borkowski, and V. Walther, Absolute electron-proton cross sections at low momentum transfer measured with a high pressure gas target system, Nuclear Physics A **333**, 381 (1980).

[65] A. V. Gramolin and D. M. Nikolenko, Reanalysis of rosenbluth measurements of the proton form factors, Phys. Rev. C **93**, 055201 (2016).

[66] I. Passchier *et al.*, Charge Form Factor of the Neutron from the Reaction $^2\overrightarrow{\mathrm{H}}(\vec{e}, e'n)p$, Phys. Rev. Lett. **82**, 4988 (1999).

[67] H. Zhu *et al.*, Measurement of the Electric Form Factor of the Neutron through $^2\overrightarrow{d}\,(\vec{e}, e'n)p$ at $Q^2 = 0.5$ (GeV/c)^2, Phys. Rev. Lett. **87**, 081801 (2001).

[68] G. Warren *et al.* (Jefferson Lab E93-026 Collaboration), Measurement of the Electric Form Factor of the Neutron at $Q^2 = 0.5$ and 1.0 (GeV/c)^2, Phys. Rev. Lett. **92**, 042301 (2004).

[69] E. Geis *et al.* (The BLAST Collaboration), Charge Form Factor of the Neutron at Low Momentum Transfer from the $^2\overrightarrow{\mathrm{H}}(\vec{e}, e'n)$H Reaction, Phys. Rev. Lett. **101**, 042501 (2008).

[70] J. Becker *et al.*, Determination of the neutron electric form factor from the reaction $^3\mathrm{He}\,(e, e'n)$ at medium momentum transfer, The Eur. Phys. J. A **6**, 329 (1999).

[71] J. Bermuth *et al.*, The neutron charge form factor and target analyzing powers from $^3\overrightarrow{\mathrm{He}}\,(\vec{e}, e'n)$ scattering, Physics Letters B **564**, 199 (2003).

[72] S. Riordan *et al.*, Measurements of the Electric Form Factor of the Neutron up to Q^2 = 3.4 GeV^2 Using the Reaction $^3\overrightarrow{\mathrm{He}}\,(\vec{e}, e'n)\,pp$, Phys. Rev. Lett. **105**, 262302 (2010).

[73] B. S. Schlimme *et al.*, Measurement of the Neutron Electric to Magnetic Form Factor Ratio at Q^2 = 1.58 GeV^2 Using the Reaction $^3\overrightarrow{\mathrm{He}}\,(\vec{e}, e'n)\,pp$, Phys. Rev. Lett. **111**, 132504 (2013).

[74] V. Sulkosky *et al.* (Jefferson Lab Hall A Collaboration), Extraction of the neutron electric form factor from measurements of inclusive double spin asymmetries, Phys. Rev. C **96**, 065206 (2017).

[75] C. Herberg *et al.*, Determination of the neutron electric form factor in the $d(e, e'n)p$ reaction and the influence of nuclear binding, Eur. Phys. J. A **5**, 131 (1999).

[76] D. I. Glazier *et al.*, Measurement of the electric form factor of the neutron at Q^2 = 0.3-0.8 (GeV/c)^2, Eur. Phys. J. A **24**, 101 (2005).

[77] B. Plaster *et al.* (Jefferson Laboratory E93-038 Collaboration), Measurements of the neutron electric to magnetic form factor ratio G_{En}/G_{Mn} via the $^2\overrightarrow{\mathrm{H}}(\vec{e}, e'\vec{n})^1\mathrm{H}$ reaction to $Q^2 = 1.45$ (GeV/c)^2, Phys. Rev. C **73**, 025205 (2006).

[78] L. Durand, Inelastic electron-deuteron scattering cross sections at high energies, Phys. Rev. **115**, 1020 (1959).

[79] H. Anklin *et al.*, Precision measurement of the neutron magnetic form factor, Physics Letters B **336**, 313 (1994).

[80] E. E. W. Bruins *et al.*, Measurement of the neutron magnetic form factor, Phys. Rev. Lett. **75**, 21 (1995).

[81] H. Anklin *et al.*, Precise measurements of the neutron magnetic form factor, Physics Letters B **428**, 248 (1998).

[82] G. Kubon *et al.*, Precise neutron magnetic form factors, Physics Letters B **524**, 26 (2002).

[83] J. Lachniet *et al.* (CLAS Collaboration), Precise Measurement of the Neutron Magnetic Form Factor G_M^n in the Few-GeV^2 Region, Phys. Rev. Lett. **102**, 192001 (2009).

[84] H. Gao *et al.*, Measurement of the neutron magnetic form factor from inclusive quasielastic scattering of polarized electrons from polarized ^{3}He, Phys. Rev. C **50**, R546 (1994).

[85] W. Xu *et al.*, Transverse Asymmetry A_T from the Quasielastic $^3\overrightarrow{\mathrm{He}}\,(e,e'n)$ Process and the Neutron Magnetic Form Factor, Phys. Rev. Lett. **85**, 2900 (2000).

[86] W. Xu *et al.*, Plane-wave impulse approximation extraction of the neutron magnetic form factor from quasielastic $^3\mathrm{He} \to (e,e')$ at $Q^2 = 0.3$ to 0.6 (GeV/c)^2, Phys. Rev. C **67**, 012201 (2003).

[87] B. Anderson *et al.* (Jefferson Lab E95-001 Collaboration), Extraction of the neutron magnetic form factor from quasielastic $^3\overrightarrow{\mathrm{He}}\,(e,e'n)$ at Q^2=0.1-0.6 (GeV/c)^2, Phys. Rev. C **75**, 034003 (2007).

[88] S. Rock *et al.*, Measurement of elastic electron-neutron scattering and inelastic electron-deuteron scattering cross sections at high momentum transfer, Phys. Rev. D **46**, 24 (1992).

[89] A. Lung *et al.*, Measurements of the electric and magnetic form factors of the neutron from Q^2=1.75 to 4.00 (gev/c)^2, Phys. Rev. Lett. **70**, 718 (1993).

[90] P. Markowitz *et al.*, Measurement of the magnetic form factor of the neutron, Phys. Rev. C **48**, R5 (1993).

[91] S. Xu, C. Mondal, J. Lan, X. Zhao, Y. Li, and J. P. Vary (BLFQ Collaboration), Nucleon structure from basis light-front quantization, Phys. Rev. D **104**, 094036 (2021).

[92] E. L. Lomon, Effect of recent R_p and R_n measurements on extended Gari-Krümpelmann model fits to nucleon electromagnetic form factors, Phys. Rev. C **66**, 045501 (2002).

[93] M. Diehl, T. Feldmann, R. Jakob, and P. Kroll, Generalized parton distributions from nucleon form factor data, Eur. Phys. J. C **39**, 1 (2005).

[94] F. Gross, G. Ramalho, and M. T. Peña, Pure s-wave covariant model for the nucleon, Phys. Rev. C **77**, 015202 (2008).

[95] J. Segovia, I. C. Cloët, C. D. Roberts, and S. M. Schmidt, Nucleon and Δ Elastic and Transition Form Factors, Few-Body Systems **55**, 1185 (2014).

[96] I. C. Cloët and G. A. Miller, Nucleon form factors and spin content in a quark-diquark model with a pion cloud, Phys. Rev. C **86**, 015208 (2012).

[97] R. Gilman, R. J. Holt, and P. Stoler, Transition to perturbative QCD, J. Phys. Conf. Ser. **299**, 012009 (2011).

[98] A. V. Belitsky, X. Ji, and F. Yuan, Perturbative QCD Analysis of the Nucleon's Pauli Form Factor $F_2(Q^2)$, Phys. Rev. Lett. **91**, 092003 (2003).

[99] Z.-Q. Yao, D. Binosi, Z.-F. Cui, and C. D. Roberts, Nucleon charge and magnetisation distributions: flavour separation and zeroes (2024), arXiv:2403.08088 .

[100] M. Diehl and P. Kroll, Nucleon form factors, generalized parton distributions and quark angular momentum, Euro. Phys. J. C **73**, 2397 (2013).

[101] G. D. Cates, C. W. de Jager, S. Riordan, and B. Wojtsekhowski, Flavor Decomposition of the Elastic Nucleon Electromagnetic Form Factors, Phys. Rev. Lett. **106**, 252003 (2011).

[102] G. Cates, Nucleon electromagnetic form factors and quark content, in *Proceedings of the Sixth International Conference on Quarks and Nuclear Physics (QNP2012). April 16-20* (2012) p. 20.

[103] C. D. Roberts, M. S. Bhagwat, A. Höll, and S. V. Wright, Aspects of hadron physics, Euro. Phys. J. ST **140**, 53 (2007).

[104] B. Wojtsekhowski *et al.*, Precision Measurement of the Neutron Magnetic Form Factor up to Q^2= 18.0 $(GeV/c)^2$ by the Ratio Method, Jefferson Lab experiment proposal E12-09-019 (2008).

[105] E. Fuchey *et al.*, Measurement of the Two-Photon Exchange contribution to the electron-neutron elastic scattering cross section, Jefferson Lab experiment proposal E12-20-010 (2020).

[106] J. Annand *et al.*, Measurement of the Ratio G_E^n/G_M^n by the Double-polarized $^2\overrightarrow{H}(\vec{e},e'\vec{n})$ Reaction, Jefferson Lab experiment proposal PR12-11-001 (2010).

[107] C. F. Perdrisat *et al.*, Large Acceptance Proton Form Factor Ratio Measurements at 13 and 15 $(GeV/c)^2$ Using Recoil Polarization Method, Jefferson Lab experiment proposal E12-07-109 (2007).

[108] B. Wojtsekhowski *et al.*, Measurement of the Semi-Inclusive π and K electro-production in DIS regime from transversely polarized ^{3}He target with the SBS & BB spectrometers in Hall A, Jefferson Lab experiment proposal E12-09-018 (2008).

[109] C. Keppel *et al.*, Measurement of Tagged Deep Inelastic Scattering (TDIS), Jefferson Lab experiment proposal PR12-14-010 (2014).

[110] B. Wojtsekhowski *et al.*, A Search for a Nonzero Strange Form Factor of the Proton at 2.5 $(GeV/c)^2$, Jefferson Lab experiment proposal PR12-22-005 (2022).

[111] B. Wojtsekhowski *et al.*, Measurement of the Nucleon Axial Vector Form Factor at Q^2 = 1 $(GeV/c)^2$, Jefferson Lab experiment letter of intent LOI12-24-009 (2024).

[112] C. W. Leemann, D. R. Douglas, and G. A. Krafft, The Continuous Electron Beam Accelerator Facility: CEBAF at the Jefferson Laboratory, Annual Review of Nuclear and Particle Science **51**, 413 (2001).

[113] P. A. Adderley *et al.*, The Continuous Electron Beam Accelerator Facility at 12 GeV, Phys. Rev. Accel. Beams **27**, 084802 (2024).

[114] A. P. Freyberger, Commissioning and Operation of 12 GeV CEBAF, in *IPAC 2015* (USDOE Office of Science, 2015).

[115] Y. Wang, A. S. Hofler, and R. Kazimi, Commissioning of the 123 MeV injector for 12 GeV CEBAF, in *IPAC 2015* (USDOE Office of Science, 2015).

[116] R. Rimmer, R. Bundy, G. Cheng, G. Ciovati, W. Clemens, E. Daly, J. Henry, W. Hicks, P. Kneisel, S. Manning, *et al.*, JLab CW Cryomodules for 4th Generation Light Sources, in *13th Workshop on RF Superconductivity* (USDOE Office of Science, 2008).

[117] M. Battaglieri *et al.*, Dark matter search in a Beam-Dump eXperiment (BDX) at Jefferson Lab (2016), proposed to JLab PAC 44, arXiv:1607.01390 [hep-ex] .

[118] A. Zec, *Compton Polarimetry for Neutral Weak Form Factor Measurements in 208Pb and 48Ca*, Ph.D. thesis, University of Virginia (2022).

[119] The Hall A Collaboration, *2017 Version: Jefferson Lab Hall A Standard Equipment Manual*, Thomas Jefferson National Accelerator Facility (TJNAF), Newport News, VA (2023).

[120] J.-C. Denard, A. Saha, and G. Laveissiere, High Accuracy Beam Current Monitor System for CEBAF's Experimental Hall A, in *PACS2001*, Vol. 3 (IEEE, 2001) pp. 2326–2328.

[121] J. Alcorn *et al.*, Basic instrumentation for Hall A at Jefferson Lab, Nucl. Instrum. Methods Phys. Res., Sect. A **522**, 294 (2004).

[122] D. King, D. Jones, C. Gal, D. Gaskell, W. Henry, A. Kaplan, J. Napolitano, S. Park, K. Paschke, R. Pomatsalyuk, and P. Souder, Precision Møller polarimetry for PREX-2 and CREX, Nucl. Instrum. Methods Phys. Res., Sect. A **1045**, 167506 (2023).

[123] D. Meekins, *Hall A Target Configuration October 2021 to February 2022*, Tech. Rep. TGT-RPT-22-002 (Thomas Jefferson National Accelerator Facility (TJNAF), Newport News, VA, 2022).

[124] D. de Lange, J. Steijger, H. de Vries, M. Anghinolfi, M. Taiuti, D. Higinbotham, B. Norum, and E. Konstantinov, A large acceptance spectrometer for the internal target facility at NIKHEF, Nucl. Instrum. Methods Phys. Res., Sect. A **406**, 182 (1998).

[125] M. Satnik, *Precision Measurement of the Neutron Magnetic Form Factor via the Ratio Method at Jefferson Lab Hall A*, Ph.D. thesis, William & Mary (2025).

[126] T. D. Averett, H. Yao, and B. Wojtsekhowski, *GRINCH Detector Technical Document v.11*, Tech. Rep. (College of William & Mary, 2012).

[127] F. Anghinolfi, P. Jarron, A. Martemiyanov, E. Usenko, H. Wenninger, M. Williams, and A. Zichichi, NINO: an ultra-fast and low-power front-end amplifier/discriminator ASIC designed for the multigap resistive plate chamber, Nucl. Instrum. Methods Phys. Res., Sect. A **533**, 183 (2004).

[128] B. Raydo, *Description and Technical Information for the VXS-based Electron Trigger and Readout Card (VETROC)*, Tech. Rep. (Thomas Jefferson National Accelerator Facility, 2014).

[129] F. Barbosa *et al.*, *A VME64x, 16-Channel, Pipelined 250 MSPS Flash ADC With Switched Serial (VXS) Extension*, Tech. Rep. (Thomas Jefferson National Accelerator Facility, 2007).

[130] I. Adam *et al.*, The DIRC particle identification system for the BaBar experiment, Nucl. Instrum. Methods Phys. Res., Sect. A **538**, 281 (2005).

[131] GRINCH Mirror Coating, (2012), the application of the mirror coating to the Lexan sheets was completed by a company called Evaporated Coatings Inc.

[132] R. M. M. III, *Performance and Commissioning of the BigBite Timing Hodoscope for Nucleon Form Factor Measurements at Jefferson Lab*, Ph.D. thesis, University of Glasgow (2023).

[133] G. Penman, R. Montgomery, D. Hamilton, R. Marinaro, and O. Jevons, *Hall A: Bigbite Timing Hodoscope Calibration*, Tech. Rep. (University of Glasgow, 2024).

[134] P. Datta, *Precision Measurements of the Neutron Magnetic Form Factor to High Momentum Transfer using Durand's Method*, Ph.D. thesis, University of Connecticut (2024).

[135] H. Avakian *et al.*, Performance of the electromagnetic calorimeter of the HERMES experiment, Nucl. Instrum. Methods Phys. Res., Sect. A **417**, 69 (1998).

[136] G. Akopdzhanov, A. Inyakin, and P. Shuvalov, Photomultiplier short-term instability, Nucl. Instrum. Methods **161**, 247 (1979).

[137] T. S. Collaboration and J. Russ, Recent Results from SELEX (2000), arXiv:hep-ex/0010011 [hep-ex] .

[138] P. Datta, A. Tadepalli, and M. Jones, *Study of the Linear Region of Operation for all the Electronic Modules involved in BigBite Calorimeter Circuit*, Tech. Rep. (Thomas Jefferson National Accelerator Facility, 2021).

[139] C. de Jager, J. Hansen, M. Jones, J. LeRose, L. Pentchev, B. Wojtsekhowski, G. Cates, N. Liyanage, V. Nelyubin, S. Riordan, *et al.*, The Super-bigbite Spectrometer for Jefferson Lab Hall A, Conceptual Design Report (2009).

[140] S. A. Seeds, *The Two-Photon Exchange Contribution to Electron-Neutron Elastic Scattering (nTPE) and Extraction of G_M^n at $Q^2 = 4.5\ GeV^2$ in Hall A at Jefferson National Lab*, Ph.D. thesis, University of Connecticut (2024).

[141] N. V. Vlasov, O. P. Gavrishchuk, N. A. Kuz'min, V. V. Kukhtin, A. N. Maksimov, P. K. Man'yakov, Y. V. Mikhailov, I. A. Savin, V. K. Semenov, A. B. Shalygin, and A. I. Yukaev, A calorimeter for detecting hadrons with energies of 10–100 GeV, Instruments and Experimental Techniques **49**, 41 (2006).

[142] V. Brio, V. Bellini, C. Petta, L. Re, C. Sutera, F. Tortorici, B. Wojtsekhowski, J. Cornejo, G. Franklin, and B. Quinn, HCAL-J: hadron calorimeter for the study of nucleon form factors at Jefferson Lab, Radiation Effects and Defects in Solids **173**, 857 (2018).

[143] F. Barbosa, E. Jastrzembski, J. Wilson, and J. Proffitt, *F1TDC A High-Resolution, Multi-Hit, VME64x Time-to-Digital Converter*, Tech. Rep. (Thomas Jefferson National Accelerator Facility, 2005).

[144] J. W. Gu, *Description and Technical Information for Version 4 Trigger Supervisor (TS) Module*, Tech. Rep. (Thomas Jefferson National Accelerator Facility, 2017).

[145] J. W. Gu, *Description and Technical Information for the VME Trigger Distribution (TD) Module*, Tech. Rep. (Thomas Jefferson National Accelerator Facility, 2016).

[146] J. W. Gu, *Description and Technical Information for the VME Trigger Interface (TI) Module*, Tech. Rep. (Thomas Jefferson National Accelerator Facility, 2024).

[147] Data Acquistion Group, *CODA: CEBAF On-line Data Acquisition User's Manual*, Tech. Rep. (Thomas Jefferson National Accelerator Facility, 1993).

[148] EPICS documentation (2004).

[149] Panguin documentation (2018).

[150] F. Sauli, GEM: A new concept for electron amplification in gas detectors, Nucl. Instrum. Methods Phys. Res., Sect. A **386**, 531 (1997).

[151] F. Sauli, The gas electron multiplier (GEM): Operating principles and applications, Nucl. Instrum. Methods Phys. Res., Sect. A **805**, 2 (2016).

[152] M. Titov and L. Ropelewski, Micro-pattern gaseous detector technologies and RD51 collaboration, Mod. Phys. Lett. A **28**, 1340022 (2013).

[153] B. Ketzer, Q. Weitzel, S. Paul, F. Sauli, and L. Ropelewski, Performance of triple GEM tracking detectors in the COMPASS experiment, Nucl. Instrum. Methods Phys. Res., Sect. A **535**, 314 (2004), proceedings of the 10th International Vienna Conference on Instrumentation.

[154] L. Hallermann, *Analysis of GEM properties and development of a GEM support structure for the ILD time projection chamber*, Ph.D. thesis, Hamburg University (2010).

[155] W. R. Leo, *Techniques for Nuclear and Particle Physics Experiments: A How-To Approach* (Springer, 1994).

[156] A. Buzulutskov, L. Shekhtman, A. Bressan, A. Mauro, L. Ropelewski, F. Sauli, and S. Biagi, Gem operation in pure noble gases and the avalanche confinement, Nucl. Instrum. Methods Phys. Res., Sect. A **433**, 471 (1999).

[157] F. Simon, *Commissioning of the GEM Detectors in the COMPASS Experiment*, Ph.D. thesis, Physik-Department E18 Technische Universitat Munchen (2001).

[158] R. Guida, B. Mandelli, and M. Corbetta, Effects of gas mixture quality on gem detectors operation, Journal of Physics: Conference Series **1498**, 012036 (2020).

[159] J. A. B. III, *Measurements of the Neutron Magnetic Form Factor and the Two-Photon Exchange Contribution to the Electron-Neutron Elastic Scattering Cross Section*, Ph.D. thesis, University of Virginia (2024).

[160] A. D. R. Mudiyanselage, *Measurement of the Neutron Magnetic Form Factor at Large Momentum Transfer Using the Super-Bigbite Apparatus in Jefferson Lab Hall-A*, Ph.D. thesis, University of Virginia (2024).

[161] S. P. Jeffas, *Measurement of the Neutron Electromagnetic Form Factor Ratio at High Momentum Transfer*, Ph.D. thesis, University of Virginia (2024).

[162] L. G. Re, *Characterization of the GEM Chambers for the SBS/BB Front Tracker at JLab Hall A*, Ph.D. thesis, Università Delgi Studi Di Catania (2019).

[163] M. French, L. Jones, Q. Morrissey, A. Neviani, R. Turchetta, J. Fulcher, G. Hall, E. Noah, M. Raymond, G. Cervelli, *et al.*, Design and results from the APV25, a deep sub-micron CMOS front-end chip for the CMS tracker, Nucl. Instrum. Methods Phys. Res., Sect. A **466**, 359 (2001).

[164] P. Musico, *MPD Specifications*, INFN Genova, 2nd ed. (2018).

[165] B. Raydo, *VTP Manual*, Jefferson Lab Nuclear Physics Division Fast Electronics Group (2016).

[166] L. Jones, *APV25-S1 User Guide Version 2.2* (2001).

[167] N. Boetti, F. Faccio, and P. Jarron, *A radiation hardened voltage regulator for LHC and space applications*, Tech. Rep. (CERN, 2000).

[168] Hall A Collaboration, Hall A Analyzer Software Package (2025).

[169] SBS Collaboration, SBS-Offline Software Package (2025).

[170] SBS Collaboration, SBS-Replay Software Package (2025).

[171] Hall C Collaboration, SIMC Software Package (2025).

[172] SBS Collaboration, G4SBS Software Package (2025).

[173] M. E. Christy and P. E. Bosted, Empirical fit to precision inclusive electron-proton cross sections in the resonance region, Physical Review C **81**, 10.1103/physrevc.81.055213 (2010).

[174] P. E. Bosted and M. E. Christy, Empirical fit to inelastic electron-deuteron and electron-neutron resonance region transverse cross sections, Physical Review C **77**, 10.1103/physrevc.77.065206 (2008).

[175] SBS Collaboration, LIBSBSDIG Software Package (2025).

[176] Ezekiel Wertz, GMn and nTPE physics analysis Software Package (2025).

[177] E. Wertz, Supplementary material: Nucleon detection efficiency (2025).

[178] E. Wertz, Supplementary material: Cut stability and systematic studies (2025).

[179] E. Wertz, Supplementary material: Background shape studies (2025).

[180] P. Blunden, W. Melnitchouk, and J. Tjon, Two-photon exchange in elastic electron-nucleon scattering, Physical Review C—Nuclear Physics **72**, 034612 (2005).

[181] P. Mergell, U.-G. Meißner, and D. Drechsel, Dispersion-theoretical analysis of the nucleon electromagnetic form factors, Nuclear Physics A **596**, 367 (1996).

[182] Thurlby Thandar Instruments, *CPX400DP Instruction Manual* (2008).

[183] D. Di, *High Momentum Transfer Nucleon Elastic Electromagnetic Form Factor Measurements Using Super BigBite Spectrometer at Jefferson Lab*, Ph.D. thesis, University of Virginia (2019).